REVIEW ARTICLE

Development of the indirect-drive approach to inertial confinement fusion and the target physics basis for ignition and gain

John Lindl
Lawrence Livermore National Laboratory, Livermore, California 94551

(Received 14 November 1994; accepted 14 June 1995)

Inertial confinement fusion (ICF) is an approach to fusion that relies on the inertia of the fuel mass to provide confinement. To achieve conditions under which inertial confinement is sufficient for efficient thermonuclear burn, a capsule (generally a spherical shell) containing thermonuclear fuel is compressed in an implosion process to conditions of high density and temperature. ICF capsules rely on either electron conduction (direct drive) or x rays (indirect drive) for energy transport to drive an implosion. In direct drive, the laser beams (or charged particle beams) are aimed directly at a target. The laser energy is transferred to electrons by means of inverse bremsstrahlung or a variety of plasma collective processes. In indirect drive, the driver energy (from laser beams or ion beams) is first absorbed in a high-Z enclosure (a hohlraum), which surrounds the capsule. The material heated by the driver emits x rays, which drive the capsule implosion. For optimally designed targets, 70%–80% of the driver energy can be converted to x rays. The optimal hohlraum geometry depends on the driver. Because of relaxed requirements on laser beam uniformity, and reduced sensitivity to hydrodynamic instabilities, the U.S. ICF Program has concentrated most of its effort since 1976 on the x-ray or indirect-drive approach to ICF. As a result of years of experiments and modeling, we are building an increasingly strong case for achieving ignition by indirect drive on the proposed National Ignition Facility (NIF). The ignition target requirements for hohlraum energetics, radiation symmetry, hydrodynamic instabilities and mix, laser plasma interaction, pulse shaping, and ignition requirements are all consistent with experiments. The NIF laser design, at 1.8 MJ and 500 TW, has the margin to cover uncertainties in the baseline ignition targets. In addition, data from the NIF will provide a solid database for ion-beam-driven hohlraums being considered for future energy applications. In this paper we analyze the requirements for indirect drive ICF and review the theoretical and experimental basis for these requirements. Although significant parts of the discussion apply to both direct and indirect drive, the principal focus is on indirect drive.

TABLE OF CONTENTS

I. ICF OVERVIEW

Inertial confinement fusion (ICF) is an approach to fusion that relies on the inertia of the fuel mass to provide confinement.[1–3]

To achieve conditions under which inertial confinement is sufficient for efficient thermonuclear burn, high-gain ICF targets have features similar to those shown in Fig. 1. A capsule generally is a spherical shell filled with low-density gas (≤ 1.0 mg/cm^3). The shell is composed of an outer region, which forms the ablator, and an inner region of frozen or liquid deuterium–tritium (DT), which forms the main fuel. As shown in Fig. 2, the cross section[4] for DT fusion reactions is approximately two orders of magnitude larger than that for the next largest reaction in the relevant temperature range, up to about 40 keV. Hence, ignition and high-gain targets planned for the near term use DT fuel. Many of the near-term targets discussed later, which only use neutrons for diagnostic purposes, contain deuterium–deuterium (DD) fuel.

Energy from a driver is delivered rapidly to the ablator, which heats up and expands. As the ablator expands outward,

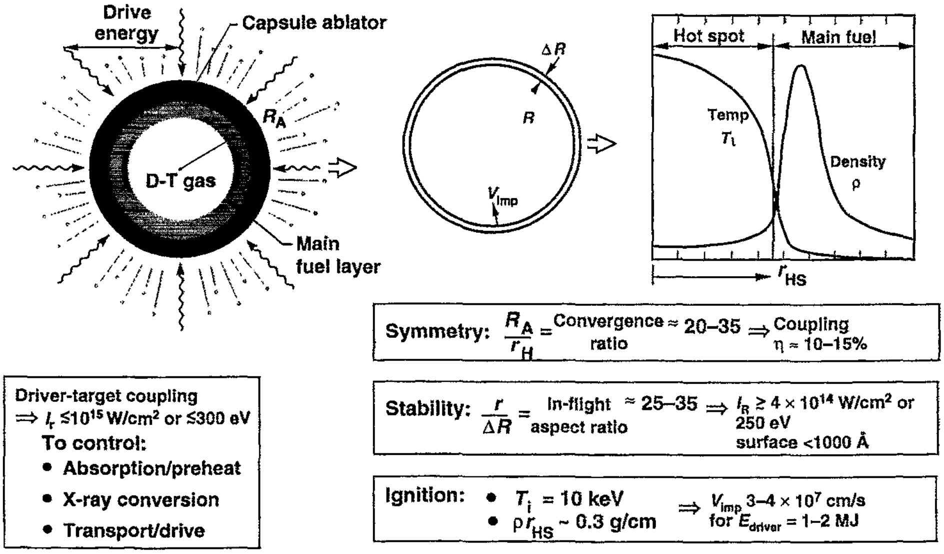

FIG. 1. The target physics specifications on current ICF ignition targets include constraints on drive intensity, symmetry, stability, and ignition.

the rest of the shell is forced inward to conserve momentum. The capsule behaves as a spherical, ablation-driven rocket. The efficiency with which the fusion fuel is imploded typically lies in the range of 5%–15%. The work that can be done on the imploding fuel is the product of the pressure generated by the ablation process times the volume enclosed by the shell. Hence, for a given pressure, a larger, thinner shell that encloses more volume can be accelerated to a higher velocity than can a thicker shell of the same mass. The peak achievable implosion velocity determines the minimum energy (and mass) required for ignition of the fusion fuel in the shell.

In its final configuration, the fuel is nearly isobaric at pressures up to ~200 Gbars but consists of two effectively distinct regions—a central hot spot, containing ~2%–5% of the fuel and a dense main fuel region comprising the remaining mass. Fusion initiates in this central region, and a thermonuclear burn front propagates radially outward into the main fuel, producing high gain. The efficient assembly of the fuel into this configuration places stringent requirements on

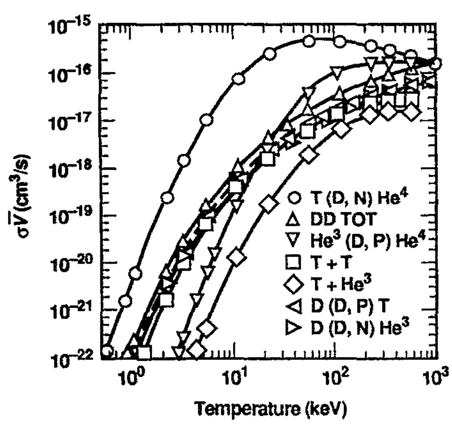

FIG. 2. Thermonuclear reaction rates are strongly temperature dependent, and DT is by far the easiest fuel to ignite.

the details of the driver coupling, including the time history of the irradiance and the hydrodynamics of the implosion.

In the implosion process, several features are important. The in-flight aspect ratio (IFAR) is defined as the ratio of the shell radius R as it implodes to its thickness ΔR, which is less than the initial thickness because the shell is compressed as it implodes. Hydrodynamic instabilities,[5] similar to the classical Rayleigh–Taylor (RT) fluid instability, impose an upper limit on this ratio, which results in a minimum pressure or absorbed driver irradiance. For $25<\text{IFAR}<35$, peak values are ~100 Mbars and $\sim 10^{15}$ W/cm² for megajoule-scale drivers. These minimum values depend on the required implosion velocity, which is determined by the capsule size. Minimum velocities are in the range of $3-4\times 10^7$ cm/s for megajoule scale lasers. Control of RT-induced mix of hot and cold fuel is crucial to the successful formation of the central hot spot.

The convergence ratio C_r as defined in Fig. 1 is the ratio of the initial outer radius of the ablator to the final compressed radius of the hot spot. Typical convergence ratios to the hot spot for an ignition or high-gain target design are 30–40. If a target with an initial radius R_A and average acceleration g has a location on its surface with acceleration perturbation δg, then the deviation from sphericity as it implodes is given by

$$\delta R = \frac{1}{2}\,\delta g\, t^2 = \frac{\delta g}{g}\, r(C_r - 1). \tag{1}$$

An asymmetric implosion will convert less of the available kinetic energy into compression and heating of the fuel. The tolerable degree of asymmetry depends on the excess of available kinetic energy above the ignition threshold, which is discussed later. If we require that this deviation δR be less than $r/4$, where r is the final compressed radius, we have

$$\frac{\delta g}{g} \approx \frac{\delta v}{v} < \frac{1}{4(C_r - 1)}, \tag{2}$$

TABLE I. Total energy released will determine energy output, but only charged-particle energy is available for self-ignition of ICF-size capsules.

	E (MeV)	E^* (MeV) (charged particle)	Energy/ gram
$D+T \rightarrow He^4(3.52\ \text{MeV})+n(14.06\ \text{MeV})$	17.58	3.52	3.39×10^{11}
$D+D \rightarrow He^3(0.82)+n(2.45\ \text{MeV})$			
$D+D \rightarrow T(1.01\ \text{MeV})+p(3.03\ \text{MeV})$	3.6	2.4	8.67×10^{10}
$D+He^3 \rightarrow He^4(3.67\ \text{MeV})+p(14.67\ \text{MeV})$	18.34	18.34	3.53×10^{11}
$T+T \rightarrow He^4+n+n$	11.32		1.82×10^{11}

where v is the implosion velocity. Since $30 \leqslant C_r \leqslant 40$ is typical, we require accelerations and velocities that are uniform to about 1%.

The fuel conditions that must be achieved for efficient burn and a high yield relative to the driver energy can be obtained readily from an analysis of the burn of an inertially confined fuel mass. The number of thermonuclear reactions n per second is given by

$$\frac{dn}{dt}=N_D N_T \langle \sigma v \rangle, \tag{3}$$

where $\langle \sigma v \rangle$ is the reaction cross section averaged over a Maxwellian distribution of particles, and for an equimolar DT mixture,

$$N_D=N_T=\left(\frac{1}{2} N_0-n\right), \tag{4}$$

where $N_0$is the initial total number density. If we define the burn fraction by $\phi=2n/N_0$, then we have

$$\frac{d\phi}{dt}=\frac{N_0}{2}(1-\phi)^2\langle \sigma v \rangle. \tag{5}$$

If we assume that the Maxwell averaged cross section is nearly constant over the burn duration, then we can integrate this equation to obtain

$$\frac{\phi}{1-\phi}=\frac{N_0 \tau}{2}\langle \sigma v \rangle, \tag{6}$$

where τ is the confinement time. In inertial confinement, burn of an ignited fuel mass typically is quenched by hydrodynamic expansion. (For a capsule below the ignition threshold, such as those on Nova, electron conduction usually cools the fuel before hydroexpansion occurs, as discussed in Sec. III.) From the outside of the fuel, a rarefaction moves inward at the speed of sound, C_s. By the time this rarefaction has moved a fraction of the radius r, the fuel density in most of the fuel mass has dropped significantly, and the fuel no longer burns efficiently. If we choose

$$\tau \approx \frac{r}{3C_s}, \tag{7}$$

which would allow time for a rarefaction wave to propagate across the dense main fuel layer in Fig. 1, we can write the burn efficiency as

$$\frac{\phi}{1-\phi}=N_0\langle \sigma v \rangle \frac{r}{6C_s}. \tag{8}$$

For DT between 20 and 40 keV, which is typical of the burn of ICF capsules, the ratio of the cross section to the sound speed is nearly constant, and we have approximately

$$\phi=\frac{\rho r}{\rho r+6(\text{g/cm}^2)} \approx \frac{N_0 \tau}{N_0 \tau+5\times10^{15}(\text{s/cm}^3)}, \tag{9}$$

where we have related number density N_0 to the mass density ρ by

$$N_0=6.02\times10^{23}\frac{Z}{A}\rho \approx 2.4\times10^{23}, \quad \text{for DT.} \tag{10}$$

Equation (9) compares well with detailed numerical simulations of most high-gain ICF targets.[6,7] We need $\rho r=3$ g/cm^2 for a 33% burnup. As indicated in Eq. (9), the ρr requirement for ICF is equivalent to the $N\tau$ requirement generally quoted for magnetic fusion energy (MFE) plasmas. The factor of 5×10^{15} in the $N\tau$ formula uses the DT cross section at 20 keV. At 40 keV, the factor becomes 3×10^{15}. We can use this burn efficiency formula to compare the fusion burn requirements of MFE with those of ICF.

Both ICF and MFE refer to "ignition" of the plasma, but ignition has different meanings for these two approaches to fusion.

In MFE, which requires steady-state or near steady-state operation for most energy production approaches, ignition is defined in terms of power balance. In this approach, ignition occurs when energy deposition from thermonuclear burn products during one energy confinement time equals the energy required to heat the plasma to thermonuclear burn temperatures. When this occurs in steady state, the plasma can sustain itself indefinitely with no external heating.

The energy per gram required to heat a DT plasma is given by

$$E_{\text{DT heating}}=0.1152\times10^9 T\ \text{(J/g)}=2.3\times10^9\ \text{(J/g)},$$
$$\text{at 20 keV,} \quad \text{with } T_e=T_i, \tag{11}$$

where T_e is electron temperature and T_i is ion temperature. The thermonuclear burn products and energy content of various thermonuclear fuels is given in Table I. In general, only the charged-particle reaction products are available to heat the fuel since most of the neutrons escape the plasma without interacting. For DT, the alpha particle energy ($E_\alpha=3.5$ meV) from the reaction is about 20% of the total energy produced. If we assume that all of the alphas are deposited, then the energy per gram deposited in the fuel is given by

$$E_{\text{thermonuclear } \alpha \text{ particle}} = \frac{6.68\times10^{10} n\tau}{n\tau+5\times10^{15}} \text{ (J/g)},$$

$$\text{at } 20 \text{ keV}. \tag{12}$$

If we set $E_{\text{DT heating}}=E_{\text{thermonuclear } \alpha \text{ particle}}$ in this simple model, ignition occurs for $n\tau>1.7\times10^{14}$ or $\rho r=0.21$ and corresponds to a burn efficiency of about 3.4%.

Ignition in this sense is adequate for a MFE plasma if the energy required to maintain the magnetic confinement is much less than the energy to heat the plasma. Since the magnetic-field energy is much greater than the plasma energy in magnetic confinement devices, it is generally assumed that superconducting magnets would be used to minimize the dissipation of magnetic field energy.

As a measure of the fusion power performance for a MFE device, the fusion power gain is defined by $Q=P_f/P_i$, where P_f is the fusion power and P_i is the input power. The fusion power is given by

$$P_f=\int E_{TN}\frac{d\phi}{dt}\,dV, \tag{13}$$

and the input power is given by

$$P_i=\frac{1}{\tau_E}\int E_{\text{DT heating}}\,dV-\frac{1}{5}P_f, \tag{14}$$

where the integrals are over the plasma volume, $E_{TN}=3.34\times10^{11}$J/g is the energy per gram produced by DT fusion reactions, and $E_{\text{DT heating}}$ is the heat capacity of DT from Eq. (11). In Eq. (14), one-fifth of P_f, which is all of the α-particle energy, is assumed to be deposited in the plasma. The energy confinement time τ_E characterizes the rate at which energy is lost from the plasma by cross-field transport and radiation. Ignition occurs when $P_i=0.0$ or when $Q=\infty$. An actual MFE reactor would run somewhat below the ignition limit, to maintain a stable operating regime, so that a $Q\approx20$ is desirable.[8] Recent experiments[9] with DT plasmas have achieved $Q\approx\frac{1}{4}$.

In ICF, which is inherently pulsed, ignition occurs when energy production and α deposition from the central hot spot are sufficient to initiate a self-sustaining burn wave that propagates into the surrounding main fuel. To compensate for driver and implosion inefficiencies, ICF targets must have a high burn efficiency, and most of the fuel must be heated by the burn wave propagating outward from the hot spot.

Target gain, defined as the ratio of thermonuclear energy produced to driver energy on target,is the closest equivalent to Q in MFE. A described in Sec. XIV, energy production in ICF requires target gains high enough that the product of gain times driver efficiency is $\sim$10. Depending on driver efficiency, target gains of 30–100 or more are required to satisfy this condition.

Compression of the DT fuel mass makes it feasible, in the laboratory, to achieve the $\rho r=3$ g/cm^2 necessary for a burn efficiency of $\frac{1}{3}$, about a factor of 10 higher burn efficiency than for an ignited MFE plasma. For a sphere, we have

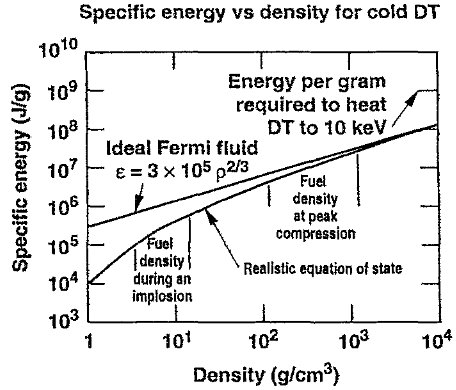

FIG. 3. For densities of interest to ICF, Fermi-degenerate compression requires much less energy than does ignition.

$$M=\frac{4\pi}{3}\frac{(\rho r)^3}{\rho^2}. \tag{15}$$

Hence, the mass (and also driver energy at fixed coupling efficiency) required for $\rho r=3$ g/cm^2 scales as $1/\rho^2$. At a normal liquid density of 0.21 g/cm^3, more than 2.5 kg of DT is required. If this much mass were ignited, it would yield about 3×10^{14} J or 70*kt*. On the other hand, at a density of 400 g/cm^3, a spherical shell with a thickness $r/2$ and radius r would have $\rho r=3$ with a mass of 5 mg. This mass would have a yield of about 6×10^8 J and is readily contained. At five to six pulses per second, such targets could drive a 1 GW reactor for power production.

As shown in Fig. 3, if the DT remains nearly Fermi degenerate during compression, then compression is economical because the energy required for compression is small compared to that required for ignition of the same mass of fuel. The Fermi compression energy can be obtained from a simple estimate. Every Fermi particle occupies a phase space volume of h^3. Then N particles in a volume V must occupy a phase space volume given by

$$\sum_s\int_V\int_{P_f}d^3x\,d^3p=(2s+1)\,V\,\frac{4\pi}{3}\,P_f^3=Nh^3. \tag{16}$$

The sum is over spin states that are 2 for spin $s=\frac{1}{2}$ particles. The Fermi energy is defined by $\epsilon_f\equiv P_f^2/2m$, where P_f is the momentum of the highest energy particle or

$$\epsilon_f(\text{eV})=\frac{\hbar^2}{2m_e}\left(\frac{6\pi^2}{2s+1}\frac{N}{V}\right)^{2/3}=14\rho^{2/3}(\text{g/cm}^3). \tag{17}$$

The average energy per particle is just $0.6\epsilon_f$, and the specific energy per gram of DT, ϵ_{DT}, is given by

$$\epsilon_{\text{DT}}(\text{J/g})=3\times10^5\rho^{2/3}(\text{g/cm}^3). \tag{18}$$

When there is a finite temperature, Eq. (18) becomes[10]

$$\epsilon_{\text{DT}}=3\times10^5\rho^{2/3}\left[1+0.02\left(\frac{T_e^2(\text{eV})}{\rho^{4/3}}\right)\right]. \tag{19}$$

Equation (19) shows that the temperature of DT at a density of 1 g/cm^3 must remain below a few electron volts, or the finite temperature corrections start becoming significant. Equations (18) and (19) ignore ion contributions and molecular effects that affect the real equation of state for DT. Equation (18) is plotted in Fig. 3 for comparison with the specific energy from a more accurate equation of state, such as that given in the *Sesame Tables.*[11]

Although compression is energetically attractive and reduces the driver size required for efficient burn, high gain also requires hot-spot ignition. For example, it takes 6.5×10^4 J to compress 5 mg to 400 g/cm^3. But to heat that mass to 5 keV would require about 3×10^6 J. If the implosion had an overall efficiency of 5%, the driver size would have to be about 6×10^7 J. This is near the upper limit of what could be considered for a laboratory driver, yet the target gain for a burn efficiency of $\frac{1}{3}$ would be only 10. On the other hand, if the target can be ignited from a central hot spot containing about 2% of the total mass, then the energy required to heat this mass would be only about 6×10^4 J. The total energy invested in compression and ignition would be about 1.25×10^5 J (2.5×10^7 J/g), the driver size would be 2.5×10^6 J, and the gain would be greater than 200. Depending on the driver efficiency, target gains of 30–100 generally are required for most ICF applications. The hot spot forms during compression from material at the center of the fuel, which is on a high isentrope. The hot-spot temperature will increase as long as the energy gained due to the PdV work done by the imploding main fuel material and charged-particle energy deposition exceed energy lost due to radiation and electron thermal conduction,[12] as described in Sec. III. Once ignition occurs, heating of the surrounding main fuel layer from electron conduction and α-particle deposition results in a thermonuclear burn wave that propagates outward into the main fuel layer. The typical configuration of the compressed fuel at ignition is shown in Fig. 1.

For effective self-heating, the hot spot ρr must exceed the α-particle range. The range energy relationship for α particles[13] is approximated by Fraley[14] as

$$\frac{dU}{dx}=-26.9\left(\frac{\rho}{\rho_0}\right)\frac{U^{1/2}}{T_e^{1/2}}\left\{1+0.168\ \ln\left[T_e\left(\frac{\rho_0}{\rho}\right)^{1/2}\right]\right\}$$
$$-0.055\left(\frac{\rho}{\rho_0}\right)\frac{1}{U}\left\{1+0.075\ \ln\left[T_e^{1/2}\left(\frac{\rho_0}{\rho}\right)^{1/2}U^{1/2}\right]\right\}, \tag{20}$$

where the first term is the interaction with electrons and the second term is the interaction with ions. Here $U\equiv E_\alpha/3.5$ MeV and $\rho_0=0.25$ g/cm^3 is the density of solid DT. Figure 4(a) is a plot of the α-particle range as a function of T_e (keV) at various densities. At low temperature, most of the α-particle energy is deposited into the electrons, as shown in Fig. 4(b). For solid-density DT, most of the energy goes into the electrons below a temperature of about 32 keV. Fraley *et al.* find that the α-particle range $\rho\lambda_0$ (g/cm^2) in solid-density DT can be approximated by

$$\rho\lambda_\alpha(\mathrm{g/cm^2})=\frac{1.5\times10^{-2}T_e^{5/4}}{1+8.2\times10^{-3}T_e^{5/4}}, \tag{21}$$

where the electron temperature T_e is in keV. At 10 keV, for typical hot-spot densities of 10–100 g/cm^3, the α particles have a range of about 0.3 g/cm^2. As discussed in Sec. III, a

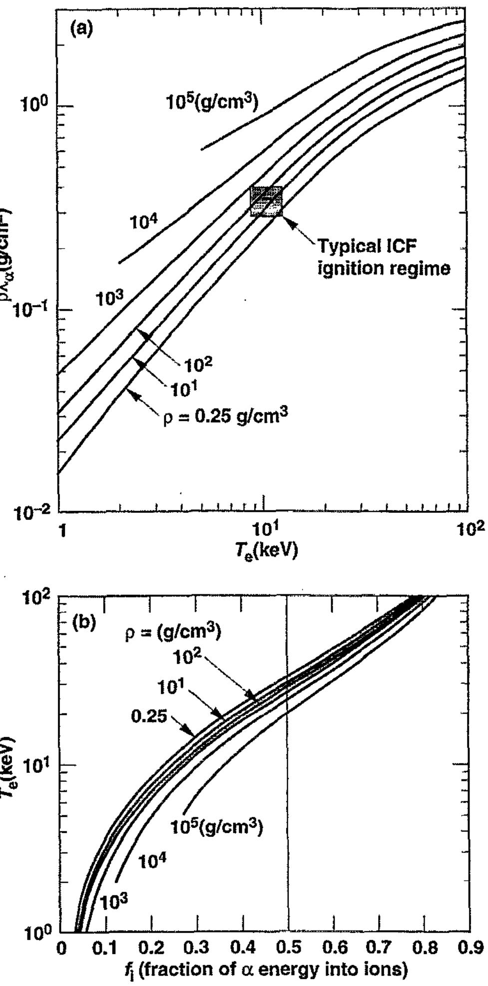

FIG. 4. Efficient alpha capture requires $\rho r\approx0.3$ g/cm^2. (a) Alpha-particle range $\rho\lambda_\alpha$ vs T_e; (b) alpha-energy absorption.

hot spot at a temperature of about 10 keV with a $\rho r\approx0.3$ g/cm^2 is required for ignition of a self-sustaining burn wave for typical high-gain ICF capsules. Ignition and propagating burn are discussed further in Sec. XIII for targets being designed for the NIF.

The implosion of an ICF capsule can be described by a rocket equation:[15]

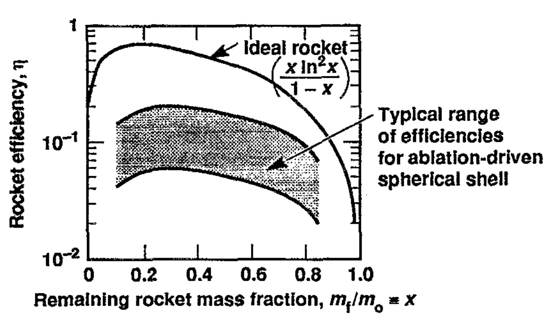

FIG. 5. Subsonic ablation follows an isothermal rocket equation. Radiation-driven implosions typically have an efficiency of 15%–20%. Direct-drive efficiency depends on laser wavelength and illumination geometry, but is typically 5%–10%; $x=m_f/m_0$ is the ratio of the final shell mass m_f to the initial mass m_0.

$$V_{\mathrm{shell}}=\frac{P_a}{\dot{m}}\ln\left(\frac{m_0}{m_f}\right)\equiv V_{\mathrm{exhaust}}\ln\left(\frac{m_0}{m_f}\right). \tag{22}$$

In this equation, P_a is the ablation pressure, $\dot{m}$ is the mass ablation rate per unit area, m_0 is the initial shell mass, and m_f is the fuel or payload mass. The rocket efficiency versus m_f/m_0 is shown in Fig. 5 for both an ideal rocket and an ablation-driven rocket. The peak efficiency of an ablation-driven rocket is typically a factor of 4 or more smaller than that of an ideal rocket because the exhaust is continually heated by the incident flux driving the implosion. This is further discussed in Sec. V on implosion dynamics.

ICF capsules rely on either electron conduction (direct drive) or x rays (indirect drive) for energy transport to drive an implosion.

In direct drive, the laser beams (or charged particle beams) are aimed directly at a target. The laser energy is transferred to electrons by means of inverse bremsstrahlung or a variety of plasma collective processes. This absorption occurs at a particle density equal to or less than the plasma critical density $n_c(\mathrm{cm}^{-3})=10^{21}/\lambda^2$, where λ is the laser wavelength in μm. Electron conduction must transport the energy to the ablation front, which typically has an electron density of about $10^{24}/\mathrm{cm}^3$. Uniformity of the flux must be obtained by direct overlap of a large number of very uniform beams, or by lateral electron conduction smoothing. Until it was shut down in December 1992, the Omega laser[16,17] at the University of Rochester Laboratory for Laser Energetics (LLE) was the principal facility for direct-drive implosion experiments in the United States. Omega was a 24-beam, glass laser facility capable of delivering 2–3 kJ of 0.35 μm light in a 0.6 ns pulse. Lawrence Livermore National Laboratory (LLNL), in collaboration with Rochester, is conducting planar experiments on the Nova laser[18,19] at LLNL to investigate hydrodynamic instabilities and beam smoothing in direct drive. These experiments use a single beam of Nova delivering 2–3 kJ of energy in about 3 ns. GEKKO XII at Osaka University in Japan is the principal facility outside the United States for conducting direct-drive experiments. The 12-beam GEKKO laser[20] can deliver about 10 kJ of energy in 1 ns at either 0.5 or 0.35 μm. Rochester has completed construction of a 60-beam upgrade to Omega. The Omega Upgrade[21,22] has achieved over 40 kJ of energy in a variety of pulse shapes. The Naval Research Laboratory (NRL) is constructing a KrF laser called NIKE,[23,24] which is designed to deliver 2–3 kJ of energy in a 3–4 ns pulse. This laser is primarily intended as a testbed for a NRL beam-smoothing technique called *echelon-free ISI* and as a technology development program for kilojoule-scale KrF lasers with the precision needed for ICF applications. NIKE is scheduled to begin target experiments in 1995.

Because of relaxed requirements on laser-beam uniformity and reduced sensitivity to hydrodynamic instabilities, the U.S. ICF Program has concentrated most of its effort since 1976 on the x-ray or indirect-drive approach to ICF. In indirect drive, the driver energy, from laser beams or ion beams, is first absorbed in a high-Z enclosure, a "hohlraum," which surrounds the capsule. The material heated by the driver emits x rays, which drive the capsule implosion. For optimally designed targets, 70%–80% of the driver energy can be converted to x rays. The optimal hohlraum geometry depends on the driver.

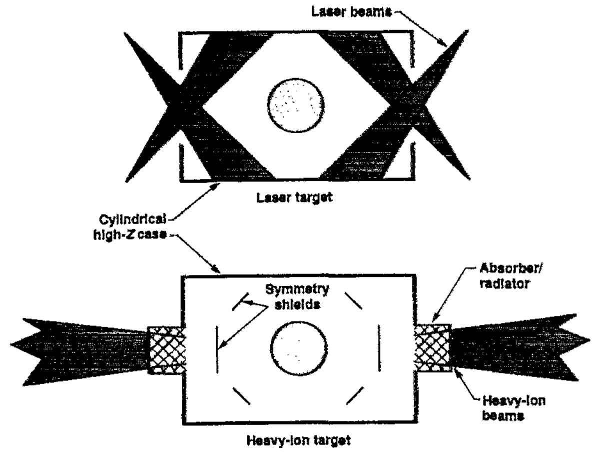

FIG. 6. For indirect-drive targets, Nova and National Ignition Facility experiments are relevant to both laser and heavy-ion targets. Capsule implosion and burn physics, as well as hohlraum energetics and x-ray transport, are essentially driver independent.

Schematic hohlraums for a laser and heavy-ion-beam driver are shown in Fig. 6. The specific details of geometry are chosen to achieve flux uniformity on the capsule. The symmetry requirement will dictate driver beam placement and hohlraum geometry, including such issues as the ratio of capsule size to case size, hohlraum internal structure, and various other details, as discussed in Sec. IX.

In general, laser-driven hohlraums designed to achieve radiation symmetry with two laser entrance holes (LEHs) are elongated with a length-to-diameter ratio greater than unity. Such a geometry arises from the need to balance the absence of x-ray emission from the LEH by locating the laser beams, which have higher emission than the rest of the hohlraum wall, relatively close to the LEH. In a spherical geometry, proper placement of the beams would result in very high angles of incidence as the beam pass through the LEHs. Such high angles can result in clipping of the beam on the LEH or a very large LEH. Alternatively, in a sphere, the beams can be aimed past the capsule toward the opposite LEH. This can work for short pulses, but capsule blowoff interferes with beam propagation for longer pulses. There are some spherical laser-driven hohlraums that have more than two holes. These designs must balance the increased LEH radiation losses with a potentially smaller case.

Ion-driven hohlraums, such as that shown in Fig. 6, are elongated because of the need to place internal shields for symmetry control. Some spherical ion-driven hohlraums, discussed in Sec. XIV, use more than two radiators.

The target physics specifications for laser-driven indirect-drive ignition targets are shown in Fig. 1. Driver–target coupling issues, which include laser absorption, x-ray conversion, and transport, limit the x-ray temperature of laser-driven hohlraums. This limitation is primarily the result of laser-driven parametric instabilities,[25] which result in scattering of laser light and production of high-energy electrons. Light scattering degrades symmetry, and high-energy elec-

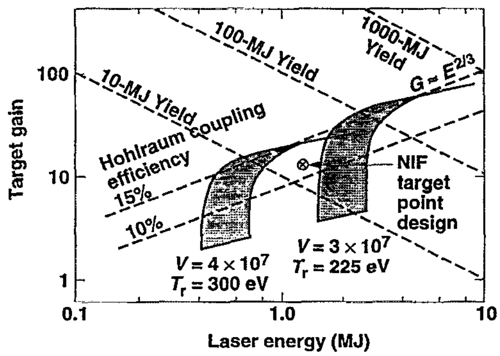

FIG. 7. The National Ignition Facility (NIF) is being designed to demonstrate ICF capsule ignition and propagating burn.

FIG. 8. Nova laser bay.

trons cause capsule preheat, which reduces the achievable compression. For the typical ignition target designs described in Sec. XIII, the hohlraum temperature is limited to about 300 eV or an equivalent x-ray intensity of about 10^{15} W/cm^2. As discussed in Sec. XI, "Hohlraum Plasma Conditions," this temperature constraint limits the plasma density in the laser propagation path to about 10% of the electron critical density for 0.35 μm laser light.

Given the x-ray flux limitations and the implosion velocity required for ignition, the flux onto the capsules must be sufficiently uniform to allow the capsules to converge by a factor of 25–35, as discussed above. For a capsule to converge this far and remain nearly spherical, x-ray fluxes must be uniform to 1%–2%. To achieve this level of x-ray flux uniformity requires a hohlraum that is large compared to the capsule dimension. In current hohlraum designs, hohlraum areas are typically 15–25 times that of the initial capsule area. Such a large-area hohlraum limits the coupling efficiencies of driver energy to the capsule to 10%–15%, as discussed in Sec. VIII. It should ultimately be possible to achieve a coupling efficiency of 20%–25% through the use of optimal driver and hohlraum geometries that minimize hohlraum and LEH area.

The achievable implosion velocity, which is the primary determinant of the minimum-size driver for ignition, is determined by a combination of the allowable capsule IFAR and the maximum achievable x-ray flux. Shown in Fig. 7 are gain curves at implosion velocities of 3 and 4×10^7 cm/s, under the assumption of a fixed hohlraum coupling efficiency of 10%–15%. If the capsule IFAR is limited to about 30, an implosion velocity of 3×10^7 cm/s requires a hohlraum temperature of about 225 eV, whereas an implosion velocity of 4×10^7 cm/s requires a higher temperature—about 300 eV. This near-linear relationship between radiation temperature and implosion velocity is discussed in Sec. V. At any given velocity, capsules below a certain energy will fail to ignite because the hot spot will not achieve sufficient ρr and temperature. The shaded bands correspond to a minimum cutoff energy, which depends on hydrodynamic instability levels and capsule surface quality. The left-hand edge of each band corresponds to the gain for perfectly uniform implosions. The right-hand edge of each band corresponds to the gain for targets with surface finishes of 500–1000 Å. As seen in Fig. 7, capsules on the proposed NIF (described more completely in Sec. XIII), which is being designed to deliver 1.8 MJ of energy, must reach implosion velocities approaching 4×10^7 cm/s, and have hohlraum temperatures of approximately 300 eV.

The ICF program has used data from laboratory experiments and from underground nuclear experiments. A joint Los Alamos/LLNL program using underground nuclear experiments, called *Halite* at LLNL and *Centurion* at Los Alamos (collectively called H/C), demonstrated excellent performance, putting to rest fundamental questions about the basic feasibility of achieving high gain.[26] It performed inertial fusion experiments using nuclear explosives at the Nevada Test Site at higher energies than those available in the laboratory.

Since its completion in 1985, the Nova laser[18,19] at LLNL has been the primary U.S. laboratory facility for radiation-driven experiments. Figure 8 is a picture of the laser hall, showing some of Nova's ten beams. Figure 9 shows the Nova experimental area as it was before any diagnostics were installed. The laser beams are arranged so that five beams located along the rim of a 100° cone irradiate each end of a hohlraum, such as that shown in Fig. 10. Nova can deliver about 30–40 kJ in 1 ns at an output wavelength of 0.35 μm. This energy can also be delivered with a wide variety of pulse shapes. Figure 10 is a typical 1.6 mm diam hohlraum used on Nova for implosion experiments. For ease

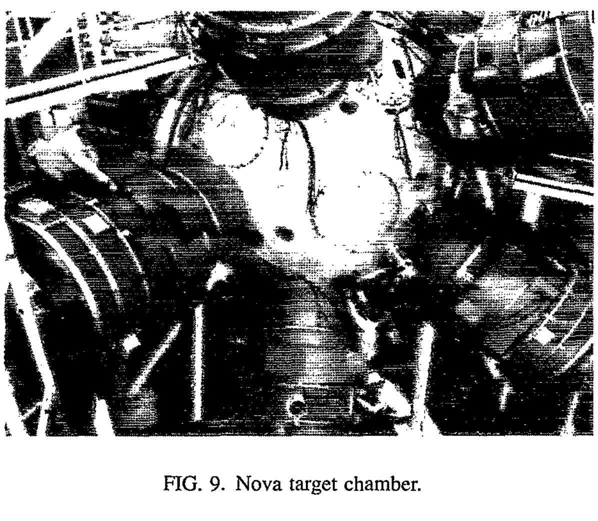

FIG. 9. Nova target chamber.

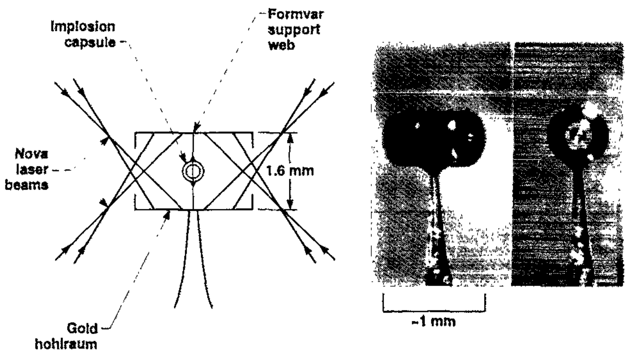

FIG. 10. Nova implosion target, illustrating beam geometry. Five Nova beams irradiate each side of the hohlraum. The beams are uniformly distributed around the rim of a 100° cone.

of fabrication, the hohlraum wall for this target is made of gold, but other high-Z materials such as tungsten and uranium are also used. The capsule shown inside is a plastic microballoon about $\frac{1}{2}$ mm in diameter.

Outside of the United States, GEKKO XII and the Phebus laser at Limeil have been the primary facilities for experiments on radiation-driven ICF. Hohlraums[27] used on GEKKO XII have been about half the scale of the Nova hohlraums shown in Fig. 10. Experiments on Phebus,[28] which is the equivalent of two beams of Nova, have used a variety of hohlraum geometries, including spheres ranging in size from 1 to 2 mm in diameter and targets with beam shields for implosions, as shown in Fig. 11. In Russia, the ISKRA-5 laser[29] at Arzamus-16 has been used for indirect drive. ISKRA-5 is an iodine laser operating at a 1.315 μm laser wavelength. In typical experiments, this facility can focus 10–15 kJ in a 0.25 ns pulse into a spherical cavity with six LEHs. Other facilities being used for indirect drive include the Asterix III laser[30] at Garching and the Shengguang laser facility[31] in Shanghai. The Shengguang facility is a two-beam facility currently capable of delivering up to 800 J in a 0.1–1.2 ns pulse at 1.06 μm.

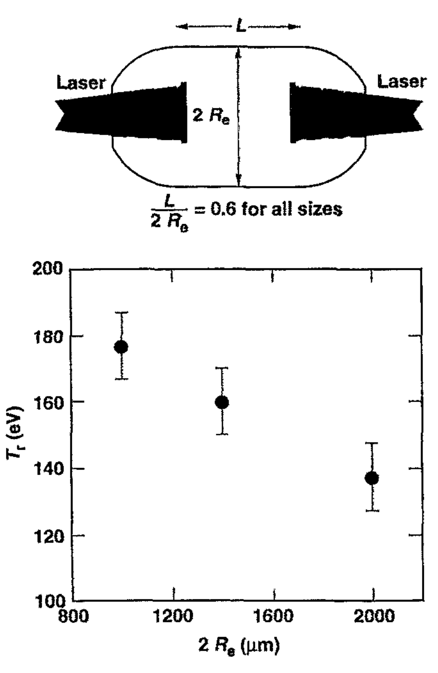

FIG. 11. Hohlraum drive on the Phebus laser[28] has been measured at 0.35 μm, E_{laser}=6 kJ in 1.3 ns, as a function of cavity diameter.

The primary alternatives to laser drivers for indirect drive are ion-beam machines. Sandia National Laboratories has developed a succession of pulsed-power, light-ion drivers. The primary challenge for ion beams has been, and continues to be, achieving the required focused intensity. Completed in 1985, the current Sandia facility is PBFA II,[32] which can deliver[33] about 100 kJ of lithium ions at 1–2 TW/cm^2. Sandia has begun conducting preliminary hohlraum and beam-coupling experiments.

Heavy-ion drivers are also being developed for ICF. Of the current ICF drivers, both the 1990 National Academy of Science (NAS)[26] and the Fusion Policy Advisory Committee (FPAC)[34] reviews concluded that because of their potential efficiency, durability, and rep rate, heavy-ion drivers have the greatest potential as drivers for future inertial fusion power plants. The heavy-ion driver work in the United States is supported primarily by the Office of Fusion Energy (OFE). The U.S. program in heavy-ion drivers focuses on induction accelerators. The experimental work has been carried out primarily at Lawrence Berkeley Laboratory. Although induction accelerator technology has had a variety of applications, primarily for electron beams, a heavy-ion driver using space-charge-dominated beams for ICF currently is the least mature of the major driver approaches. In contrast to the laser case, a typical ion-driven hohlraum, which requires a certain minimum intensity to achieve good x-ray conversion,[35–37] concentrates the driver into a few radiators, as shown schematically in Fig. 6. This feature, which is attractive from a reactor-design point of view,[38] minimizes the solid angle over which beams must be distributed and allows for a wide variety of reactor designs, including liquid waterfall and ceramic granule designs, which protect the target chamber wall against the fluence of neutrons, x rays, and debris from the target.

Although significant parts of the following discussion apply to both direct and indirect drive, the principal focus will be on indirect drive.

II. HISTORICAL DEVELOPMENT OF INDIRECT DRIVE IN THE U.S. ICF PROGRAM

We are nearing completion of a two-decade program to develop the data and numerical modeling capabilities needed to accurately specify the requirements for ignition and high-gain, radiation-driven ICF targets. Although research on indirect drive in the United States has been largely classified throughout this period and some aspects remain classified, a recent DOE declassification decision[39] goes a long way toward achieving a long-time goal of research scientists in the field for more openness and international cooperation in ICF.

John Nuckolls' seminal 1972 *Nature* paper[1] was published at about the time when laser technology, diagnostic development, and numerical modeling were becoming mature enough so that an expanded ICF program could begin to evaluate the limits and requirements for the success of ICF. This publication grew out of work, initiated by Nuckolls in

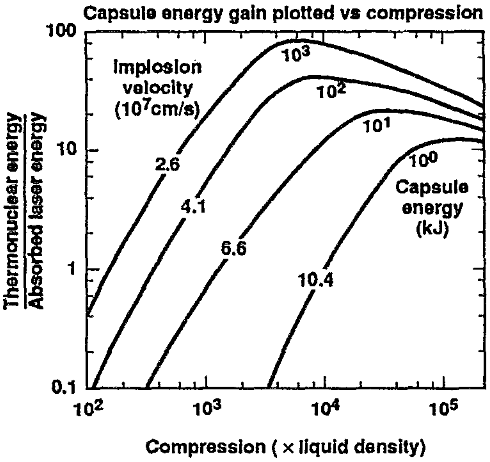

FIG. 12. The initial capsule energy estimates for ICF could be met with a factor of 2.5 increase in the achievable implosion velocity compared to velocities predicted for the NIF. The gains are plotted with the assumption that the fuel is near Fermi degenerate and that the yield is not degraded due to hot electrons, asymmetry, or hydrodynamic instability. The threshold driver energy and implosion velocity are obtained from $E_{\text{driver}}(\text{MJ}) \sim \frac{1}{2}(0.05/\eta_{\text{hydro}})\beta^{3/2}(V/(3\times 10^7))^{-5}$, with $\eta_{\text{hydro}}=5\%$.

the late 1950s, to address the challenge of creating the smallest possible fusion explosion. These early calculations were based on radiation implosions and predated invention of the laser. When the laser was invented in 1960, LLNL physicists immediately recognized its utility for inertial fusion. Sterling Colgate, Ray Kidder, and Nuckolls independently calculated various methods of using high-power lasers to implode and ignite fusion target designs.[40] Colgate and Nuckolls calculated implosions in laser-driven hohlraums. Kidder applied a spherically symmetric pulse of laser light to the target without the use of a radiation implosion. Other early work in laser-driven inertial fusion was proceeding around the world. In 1963 at the 3rd International Conference on Quantum Electronics (Paris), Basov and Krokhin[41] evaluated the laser requirements for using a laser to heat plasma to thermonuclear temperatures. This evaluation considered just direct heating of a plasma by laser irradiation and did not use an implosion.

Nuckolls' 1972 paper was based on the direct-drive implosion of bare drops or shells of DT. But, as indicated, LLNL had shifted by 1975 to radiation-driven implosions for reasons described below.

Figure 12 shows Nuckolls' original gain curves as functions of fuel compression. These curves predict that, if sufficient compression is achieved, targets driven by lasers as small as 1 kJ could achieve target gains greater than unity. Drivers of about 1 MJ were predicted to be required for high gain. Although today's estimates of the driver size required for high gain have not changed significantly, we now believe that a driver of about 1 MJ also will be required to achieve ignition.

Why has the ignition threshold increased by such a large factor while the requirements for high gain have remained fairly constant? This apparent disparity is explained by the extreme sensitivity of the ignition threshold to the implosion velocity that can be achieved in near spherical implosions in which the fuel remains nearly Fermi degenerate. A simple model for an isobaric implosion[42,43] would predict that the required energy would scale as $\beta^3 V^{-10}$, where V is the implosion velocity and β is the ratio of the pressure in the fuel to the Fermi pressure. Detailed numerical calculations[44] predict that this dependency is approximately reduced to

$$E_{\text{capsule}}(\text{MJ}) = \frac{1}{2}\left(\frac{0.05}{\eta_{\text{hydro}}}\right)\beta^{3/2}\left(\frac{V}{3\times 10^7}\right)^{-5}, \tag{23}$$

where η_{hydro} is the hydrodynamic efficiency and V is in units of cm/s. The reduction in the velocity dependence from an ideal isobaric model is the result of several factors, including an increase in the required hot-spot temperature as the target size decreases, and an increase in the fractional mass in the hot spot that self-consistently occurs during compression and results in reduced compression and hot-spot coupling efficiency. The effects of hydrodynamic instability and asymmetry will result in an increase above the energy predicted by Eq. (23). As discussed in Sec. VI, these deviations from a uniform spherical implosion result in a factor of 2–3 increase in the minimum capsule energy required for ignition.

The strong dependence of the minimum energy on the achievable implosion velocity means that only a factor of about 4 increase in the implosion velocity is required to go from a minimum energy of about 1 MJ to a minimum energy of 1 kJ, as shown in Fig. 12. The velocity indicated in Fig. 12 depends on the ignition margin required to overcome the effects of mix during the process of assembling the hot spot.

The dependence of gain on implosion velocity is much weaker. To lowest order, the reduction in gain with reduction in target size, or increase in implosion velocity, occurs primarily because less mass is imploded per Joule of energy coupled to the target. For equal burn efficiency, the gain would scale as V^{-2} so that there would be about an order of magnitude less gain at 1 kJ than at 1 MJ, as shown in the curves of Nuckolls. Once a target with a DT pusher ignites, it is expected to burn as calculated. In practice, compressions achieved in self-consistent implosions are lower than the optimal compression indicated in Fig. 12, and the gain is a stronger function of energy as discussed in Sec. VII.

We now believe that implosion velocities are limited to between about 3 and 4×10^7 cm/s because of two constraints: (1) the physics governing the hydrodynamic instability of an ICF implosion; and (2) the maximum intensity allowed by efficient laser plasma coupling.

Higher implosion velocities are possible in certain types of high-entropy implosions, in which the high-density shell is heated rapidly to high temperature and then explodes. In a so-called "exploding pusher target," the center of mass of the shell or "pusher" is almost stationary as it explodes. The radius of the boundary between the inner edge of the shell and the fuel typically converges only a factor of 3 or 4. Such targets are quite insensitive to asymmetry. The direct-drive, electron-conduction-driven exploding pusher target[45–49] was the most common early ICF target and was the first type of target to produce thermonuclear neutrons.[47,48] However, it does not scale to high gain, because all of the mass of the target is on a high isentrope, which precludes high compression.

To obtain gain at laser sizes much smaller than about 1 MJ, Nuckolls[1] used a very optimistic model for RT instability in the presence of ablation. As described in Sec. VI on hydrodynamic instabilities, this model, coupled with an assumption that implosions with absorbed laser intensities approaching 10^{17} W/cm^2 would be feasible, was required to obtain ignition at laser energies approaching 1 kJ. In 1972, computers and numerical models were just becoming powerful enough to allow detailed evaluation of the effects of hydrodynamic instability and the limits that laser plasma instabilities would place on the allowable intensity. Over the next few years, experiments indicated that laser intensities would be limited to between 10^{14} and a few times 10^{15} W/cm^2, depending on the laser wavelength. Numerical calculations provided most of the guidance for the growth of RT instability until the quantitative data discussed in Sec. VI became available in the late 1980s and the early 1990s.

By 1974, numerical calculations[50] using the LASNEX code[51] indicated that direct-drive capsules would have much higher instability growth rates than were assumed in Nuckolls' 1972 paper. In addition, new experiments using neodymium glass lasers indicated that reduced absorption and hot electron production would severely degrade direct-drive implosions at the high intensities required for ignition with lasers in the 1–100 kJ range. The quality of the laser beam also was much worse than could be tolerated for the implosion uniformity required for direct drive. For direct-drive implosions, beam nonuniformities provide a source of small-spatial-scale perturbations (referred to as imprinting), which are further amplified during the implosion.

Much progress has been made since the 1970s toward solving the irradiation-uniformity problem for direct drive. A series of clever optical inventions, both in the United States and Japan,[52–54] traded off laser-beam coherence for laser-beam uniformity so that it is now possible to obtain beams that are uniform to a few percent. The overlap of a large number of beams, and further optical innovation should allow nonuniformity to be reduced to less than 1%, estimated to be required for direct drive. With optimization of density gradient stabilization effects, as discussed in Sec. VI, the direct-drive ignition threshold is now estimated to be about 1 MJ.[55] In the United States, the Omega Upgrade laser[21,22] at the University of Rochester is designed to answer these questions, and the NIF conceptual design (see Sec. XIII) will permit adding a direct-drive option. In Japan, the 300 kJ Kongoh laser project,[56,57] an upgrade to GEKKO XII is being proposed to study direct-drive ignition. Although the beam-smoothing techniques that have been developed greatly reduce the level of these effects, imprinting is still a major concern for direct drive.

Calculations carried out in 1975 showed that it is possible, with proper design, to achieve high gain with radiation-driven targets[58] such as those in Fig. 1. These targets are very similar to direct-drive targets, except that the choice of ablator material must be properly matched to the x-ray drive spectrum in order to control RT instability and ensure that the fuel can be kept in a near-Fermi-degenerate state. From one point of view, implosions driven by soft x rays could be considered as being driven by a laser with a very short wavelength and a very broad frequency bandwidth.

Compared to direct drive, these calculations for indirect drive showed a dramatically reduced growth of perturbations due to RT instability. As discussed in Sec. VI, this reduced level of instability—one of the principal advantages of radiation-driven implosions—occurs because radiation-driven implosions have much higher ablation rates and hence lower growth rates and thicker shells.

In addition, because the laser beams are absorbed far from the capsule, as indicated schematically in Fig. 6, radiation-driven implosions are unaffected by small-scale nonuniformities in the laser beam.

As discussed in Sec. XII, "Hot Electron Preheat," indirect-drive targets are less sensitive to the effects of hot electrons produced by laser-driven parametric instabilities because of solid-angle effects and because radiation-driven capsules are thicker than directly driven capsules.

A potential disadvantage of indirect drive for lasers, compared to direct drive, is the longer scale length of plasma traversed by the laser as it propagates from the LEH to the hohlraum wall. Under some conditions, very large levels of parametric instabilities can be generated in this plasma. Controlling the level of parametric instabilities places limits on laser wavelength and intensity. In practice, both direct drive and indirect drive are optimized by using short-wavelength lasers with $\lambda \leq 0.5$ μm, and intensities typically are limited to about 10^{15} W/cm^2.

For indirect drive, the capsules and such issues as radiation transport and hohlraum wall loss are essentially independent of the driver. This means that the ICF Program could use underground experiments driven by nuclear explosives to test aspects of ICF capsules at much higher energy than could be tested by available laboratory sources. As mentioned previously, the H/C program (from 1978 to 1988) laid to rest fundamental questions about the feasibility of high-gain ICF.[26]

Because much of the physics of indirect drive is independent of the driver, many of the results learned with lasers carry over to other drivers such as heavy-ion beams. This synergism is particularly important for heavy-ion-beam drivers. Indirect-drive laser experiments provide a key element of the database required to ensure that targets driven by heavy-ion beams will work when the accelerators are available.[34,59]

Because of the reduced level of hydrodynamic instability, capsule energy requirements for ignition at a given x-ray intensity are very close to the projections in Nuckolls' 1972 paper. However, there is a substantial energy penalty incurred in producing x rays and transporting them symmetrically to a capsule. Further, because of limits to the achievable x-ray intensity, the minimum driver energy for indirect drive is about 0.5–1 MJ, as shown in Fig. 7. The upper edge of the band in Fig. 7 allows for the effects of asymmetry and the mixing of hot and cold fuel while the hot spot is being assembled.

Hence, the currently projected minimum energy for ignition and burn propagation is quite similar for both direct and indirect drive. However, because of relaxed beam-

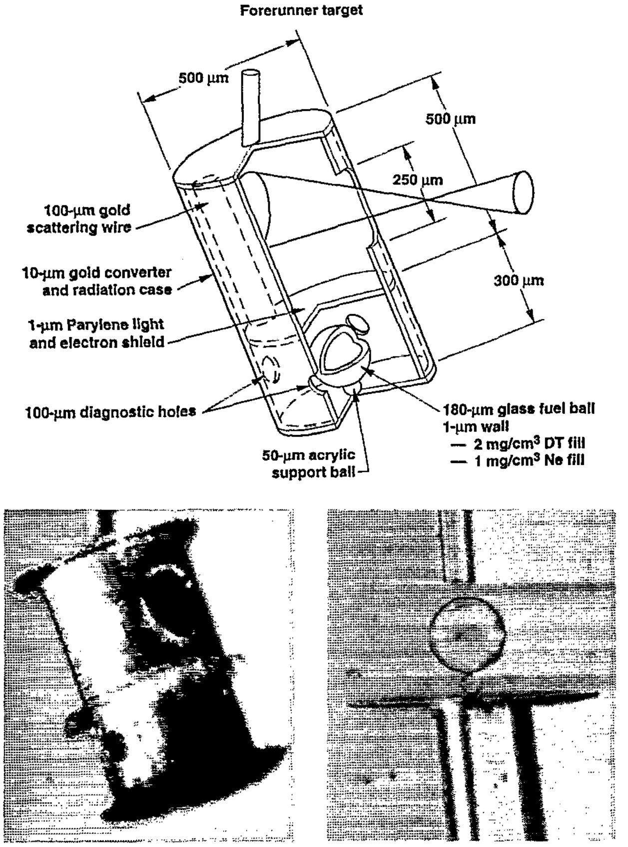

FIG. 13. The first indirect-drive, laser-driven implosion was achieved on the Cyclops laser at LLNL in 1976 using a target called a Forerunner.

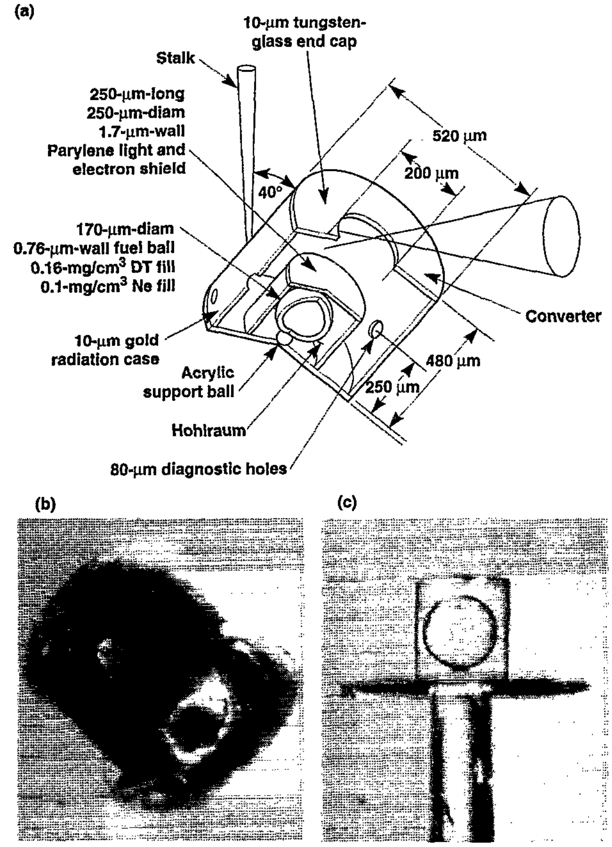

FIG. 14. Improved version of Forerunner target: (a) engineering drawing, (b) assembled target, and (c) fuel capsule and Parylene cover mounted on end cap prior to assembly.

quality requirements and reduced sensitivity to RT instability, it has been possible over the past two decades to make more rapid progress toward obtaining the radiation-drive database required to quantitatively specify the driver requirements for ignition. In the United States, a comparable database for direct drive will not be available until the experiments planned for the Omega Upgrade are completed, sometime after the end of the 1990s.

Between March and May 1976, LLNL carried out the first series of laser-driven radiation implosion experiments. Target designs for these experiments required about 100 J of 1.06 μm light. They were fielded on the Cyclops laser[60] at LLNL. Figures 13 and 14 show the two principal types of targets fielded in these experiments.[61] To simplify fabrication, gold radiation cases were used for these targets and for most radiation-driven implosion targets since then. For the first few radiation implosions, leaded glass microballoons were used as radiation cases, but gold was a far superior material and could be shaped easily from available tubing or electroplated onto mandrels of arbitrary shape. For these first radiation-driven targets, with calculated radiation temperatures of about 100 eV, thin glass microballoons were used for capsules. The radiation mean-free path in these capsules was comparable to the shell thickness. The targets became nearly isothermal and behaved as exploding pusher targets. The targets shown in Fig. 13 had yields of about 10^4 neutrons, whereas the target in Fig. 14, which was designed to couple radiation to the capsule more efficiently, had a yield between 1 and 2×10^5 neutrons. Yields for both types of targets were predicted correctly. These results, which made us optimistic about radiation drive, resulted in a shift of the 20 beam, 10 kJ Shiva laser from a uniform-illumination scheme to a two-sided irradiation scheme for indirect drive and formed the basis for the early optimism about the possibilities for achieving breakeven on a 200 kJ laser operating at 1.06 μm.

However, as we attempted the higher drive temperatures needed for high-density implosions and higher yields, laser-driven parametric instabilities in the hohlraum plasmas generated high levels of energetic electrons. Also, coupling difficulties hampered progress in the LLNL program on both Argus[62] (a two-beam laser capable of delivering 1–2 kJ of 1.06 μm light that served as a prototype for the laser hardware in Shiva) and Shiva[63] as we worked to achieve a DT fuel density equal to $100\times$ liquid DT fuel density (about 20 g/cm^3).

In the initial Cyclops hohlraum experiments, the presence of high-energy electrons, which we later determined were produced primarily by stimulated Raman scattering (SRS), showed up as noise in the neutron detectors.[61] Besides the 500 μm diam target shown in Fig. 13, we tested 300 and 400 μm diam versions of this target. The smaller two hohlraums generated such large signals (from high-energy electrons) in the neutron detectors that they could not be used for implosions. Therefore, we did the implosion experiments in the larger, lower-temperature hohlraum, which

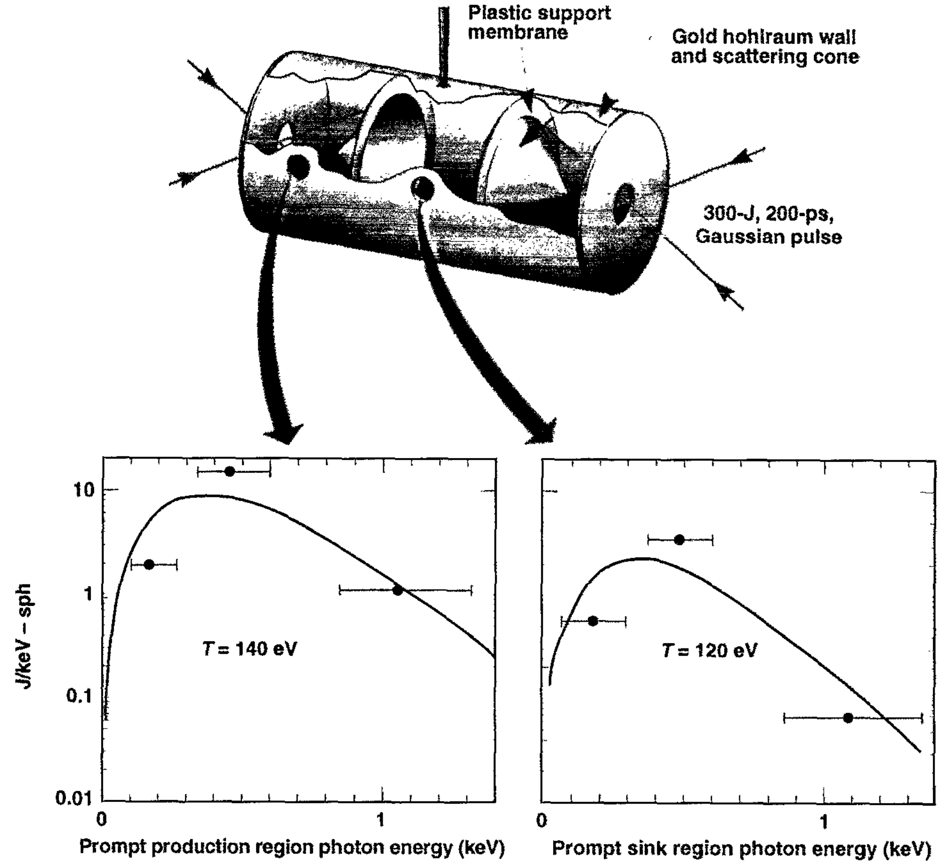

FIG. 15. Time-resolved x-ray spectroscopy, showing energy loss and temperature gradient between production and sink regions of Cairn targets on the Argus laser at LLNL (1978).

had low noise levels. As discussed in Sec. XI, "Hohlraum Plasma Conditions," laser plasma parametric instabilities strongly limit the hohlraum temperature that can be achieved with a laser of a given size and wavelength.

Because we lacked adequate models for certain key pieces of the physics, including non-LTE (local thermodynamic equilibrium) or NLTE atomic physics for the high-Z hohlraum walls, and adequate understanding of the laser–plasma interactions below critical density inside the hohlraum, we believed that absorption would be high in hohlraums for 1 μm light and that conversion to x rays would be very high. In addition, we had few measurements to quantify target performance: no quantitative measurement of x-ray drive, inadequate information about high-energy x rays from energetic electrons, and no measurements of the spectral distribution of scattered light that could have identified Raman scattering. We fully expected to achieve 100× liquid density on Argus and go on to more aggressive implosions on Shiva. In 1977 and 1978, hohlraum experiments were performed with increasingly sophisticated targets, as shown in Figs. 15–17. Figures 15 and 16 show 1978 Argus laser targets designed to measure radiation temperature and x-ray preheat.[64] Figure 17 shows a hohlraum for capsules designed to achieve 10 to 100×liquid density[65,66] on Argus. Because of high-energy electron production, we were unsuccessful in all attempts to obtain measurable yields from capsules designed to achieve a density >10×liquid on Argus.

Throughout 1978 and 1979, we tested a wide variety of targets designed to achieve high density on Shiva.[67] A sketch of the Cairn Mod-B hohlraum, which achieved the highest densities, is shown in Fig. 18(a). The capsules were glass microballoons with diameters of ~150 μm and wall thick-

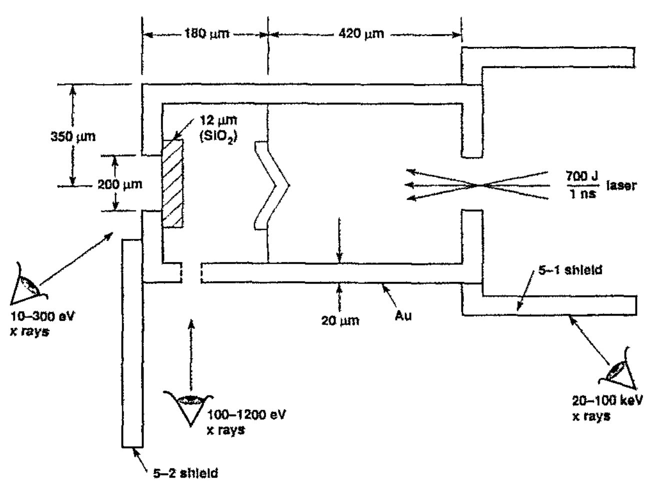

FIG. 16. Target setup for a coupling experiment on the Argus laser. We measured the coupling of radiation (burnthrough) and superthermals (preheat) to a 12 μm slab of glass (100×-like target) in a 100×-like environment (half-Cairn).

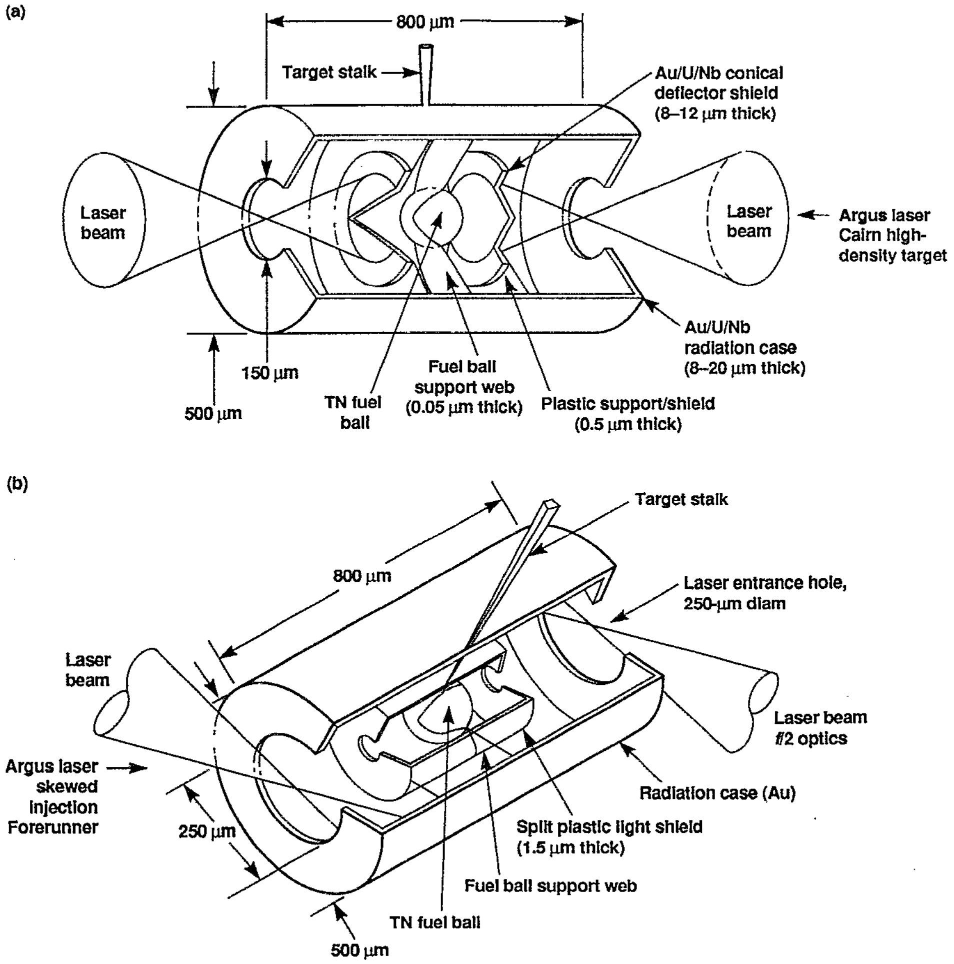

FIG. 17. By 1977, sophisticated hohlraum implosion targets were being fielded on the two-beam Argus laser: (a) Cairn high-density target; (b) Forerunner exploding pusher target.

nesses of 5–10 μm. These capsules were coated with either Teflon ($CF_{1.4}$) or CH_2. The illumination geometry for the Cairn-B target is shown in Fig. 18(b). Shiva's inner cone of beams was focused on the gold shine shields, while the outer cone of beams was focused to pass beyond the capsule and illuminate the opposite hohlraum wall and endcap. Figure 19 shows the variety of Cairn hohlraum types tested in the high-density campaigns on Shiva. Figure 20 is a plot of the density, obtained by neutron activation[68] of the glass pusher surrounding the fuel, and neutron yields obtained with these designs. In general, the neutron yield anticorrelated with density. The more open geometries, which allowed more efficient transport of energy to the capsule, also provided less preheat shielding against the large fluxes of hot electrons produced in these experiments. Most of the Cairn implosion experiments were designed to operate with radiation temperatures near 200 eV. Under these conditions, high-energy x-ray measurements indicated that up to 50% of the absorbed laser light ended up in hot electrons. The presence of these high-energy electrons, which generally had a temperature of 50–60 keV, degraded the achievable density and neutron yield. In general, it proved quite difficult to calculate the performance of these targets with large fractions of hot electrons, although the trends were understandable.

On the basis of an examination of the plasma conditions calculated for the Shiva hohlraums and an improved understanding of SRS,[25] a model was developed for the limitations on hohlraum temperatures based on filling hohlraums to densities near $\frac{1}{4}$ critical density.[69] At this density, the Raman instability—which couples an incident photon, a scattered photon, and a plasma wave—is an absolute instability with very high gain. The plasma wave has a high phase velocity and produces energetic electrons when it undergoes Landau damping. A series of scaling experiments,[70] which varied the hohlraum size and energy, gave hot-electron fractions that scaled well with the fraction of energy remaining in the pulse after the hohlraum filled to an average density of $\frac{1}{4}$ critical, as shown in Fig. 21. In addition to measuring the hot-electron fraction, we also measured Raman-shifted backscattered light. The magnitude of this scattering, as well as the time delay before large levels of scattering occurred, also were consistent with the model of hohlraum filling as the source of plasma responsible for producing hot electrons. The time delay before the onset of hot-electron production is shown in Fig.22 and is consistent with the calculated time delay for filling to $\frac{1}{4}$ critical density.[69] A Cairn scale 1, referenced to the initial Argus experiments, was 500 μm in diameter and 800 μm long. Most Shiva implosion experiments, such as the Cairn-B shown in Fig. 18, were a scale 2. Because of the

(a)

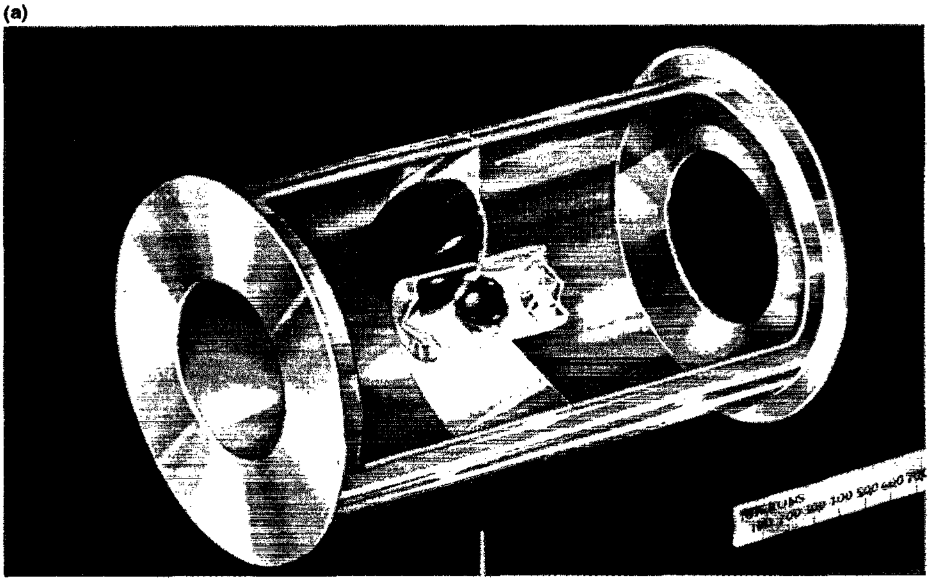

(b)

FIG. 18. (a) Cairn Mod-B, one of a series of targets that use radiation-driven, ablative compression of the fuel capsule. (b) Mod-B irradiation geometry for 20-beam Shiva laser.

relatively low critical density of 10^{21} cm^{-3} for 1.06 μm laser light, hohlraum experiments on Shiva at this wavelength were limited to between 130 and 140 eV before significant levels of hot electrons were produced, with the 1 ns pulses required for implosions.

Low-preheat hohlraums are required for imploding capsules with fuel regions that remain nearly Fermi degenerate. To test our ability to predict the performance of ablatively driven capsules in a low-preheat hohlraum, we designed the Nova Precursor Implosion Research Experiments (NPIRE),[71] which were designed to implode capsules at 130–140 eV and that used the two types of hohlraums shown in Figs. 23(a) and 23(b) with the capsules shown in Fig. 23(c). The capsules performed as predicted, with a neutron yield of 10^7, as indicated in Fig. 23. This gave us confidence that capsules driven by radiation ablation in low-preheat hohlraums would behave as predicted. With diagnostic and alignment shields, these targets are quite complex to fabricate, as shown by the assembled targets in Fig. 24.

From 1976 to 1981, we investigated both single- and double-shell targets as potential high-gain targets. Compared to single-shell targets such as those in Fig. 1, double-shell targets reach ignition conditions at lower implosion velocities. Figure 25 shows a high-gain, double-shell target.[72] In all double-shell targets, called "Apollo" targets, the main fuel is part of the outer shell. During the implosion, the outer shell collides with the much lighter inner shell and accelerates it to a higher velocity. In the limiting case of the inner shell's mass being negligible compared to that of the outer shell and the collision being elastic, the inner shell can reach a velocity twice that of the outer shell. Since compression to the high density required for high gain generally requires a lower velocity than that required to ignite the hot spot, this velocity multiplication can, in principle, result in a factor-of-4 higher

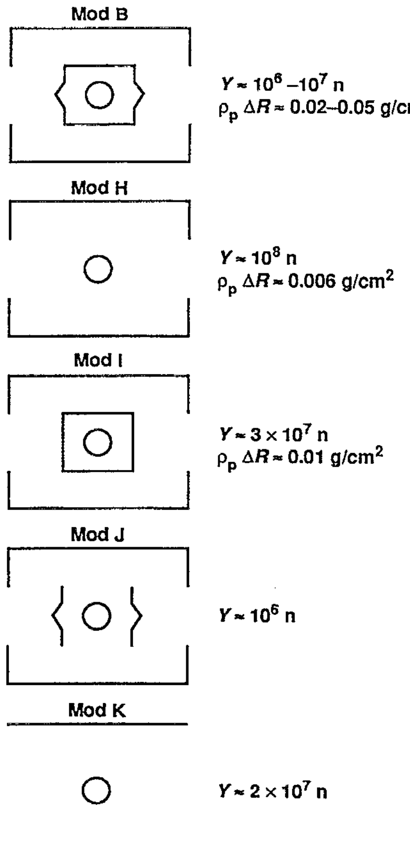

FIG. 19. Radiation cases for five Cairn targets: the Mod-B, H, I, J, and K. When irradiated, they provided a variety of drive and preheat environments for the Cairn capsules, most of which were SiO_2 microshells, 5 μm wall thickness, 150 μm diam, overcoated with 15 μm of Teflon, and filled with about 10 mg/cm^3 of DT.

gain for a double shell compared to a single shell. The inner shell must be high Z for efficient high-density compression of the fuel contained within it. Because this shell starts out at a density of nearly 20 g/cm^3, it can tolerate the high-pressure shock generated during the collision and still achieve high density. Because it is high Z, such a shell also contains the radiation emission from the fuel as it compresses and further lowers the ignition threshold. Early projections of ignition on a "200 kJ," 20-beam Nova laser were based largely on

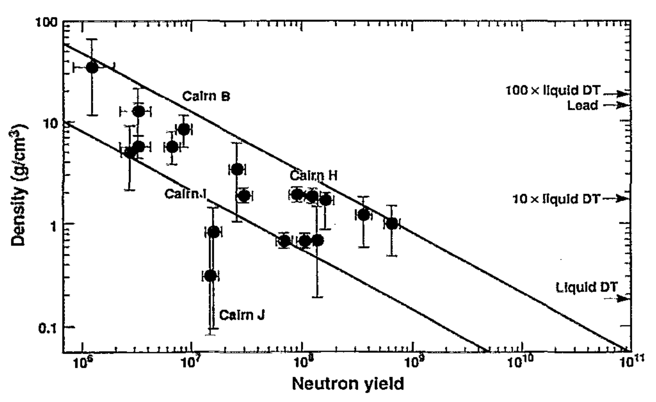

FIG. 20. Fuel density at burn time versus neutron yield for various Cairn hohlraum geometries.

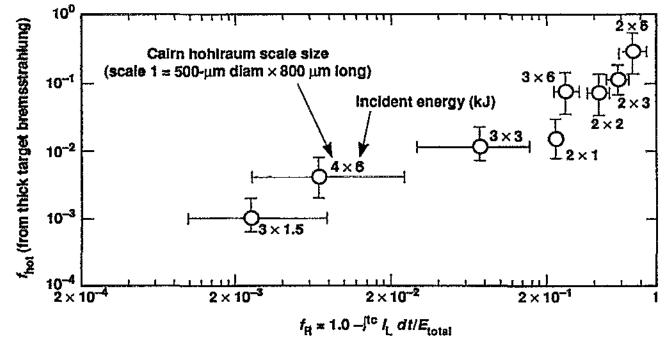

FIG. 21. The experimental hot-electron fraction f_{hot} in 1.06 μm hohlraum scales with the fraction of energy remaining in the pulse f_r at time t_c when the average hohlraum density reaches quarter-critical.

double-shell target designs[72,73] such as those shown in Fig. 26. The two capsules shown in Fig. 26 are labeled "subsonic" and "transonic" to characterize the velocity of the radiation front (Marshak wave) relative to the velocity of the shock generated by the ablation. In the subsonic capsule, the shock propagates ahead of the Marshak wave during most of the ablation process. In the transonic capsule, the Marshak wave and shock propagate through the LiH ablator at nearly the same speed until the radiation wave is slowed by the TaCOH layer. In this transonic regime, the compression caused by the shock in the ablator depends on radiation temperature and decreases as the temperature increases. This negative feedback results in a reduced sensitivity to radiation flux asymmetry because the pressure on the TaCOH shell is proportional to $\rho_s T$, where ρ_s is the shocked ablator density and T is the radiation temperature. These transonic capsules could tolerate 5%–10% flux asymmetry, versus 1% for the subsonic capsules.

However, the potential advantages of velocity multiplication ignore the effects of hydrodynamic instability during the collision of the two shells. When these types of targets were proposed, little was known about the growth of the turbulent instability layer that is produced during the collision and acceleration of the inner shell. More detailed analy-

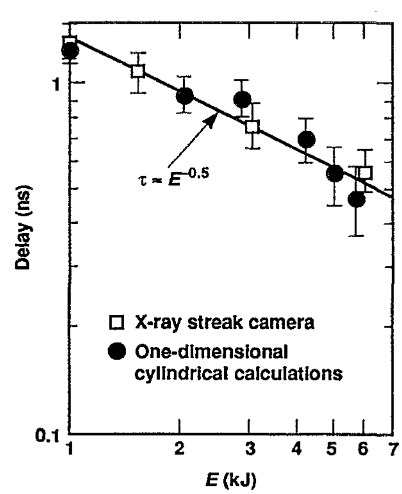

FIG. 22. High-energy electron time delay versus energy for Shiva 2.0-scale Cairn target (1000 μm diam by 1600 μm long) hohlraum (2 ns pulse).

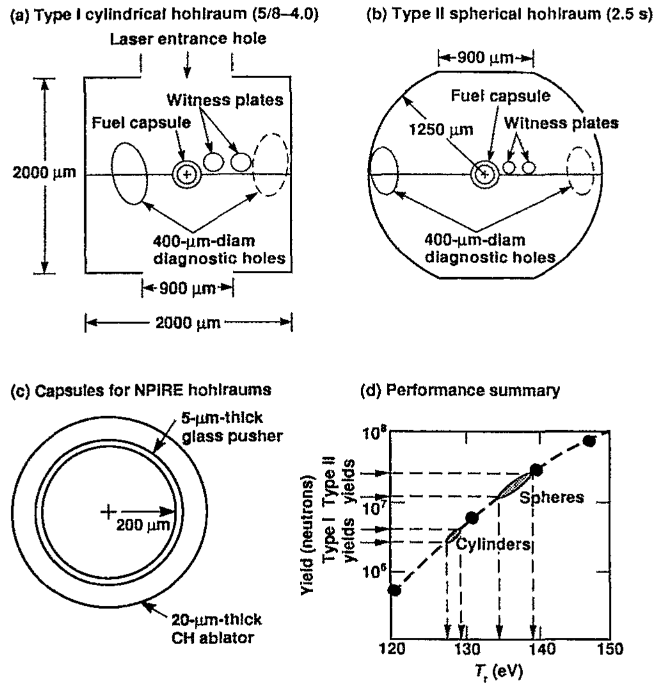

FIG. 23. The NPIRE hohlraums on the Shiva laser were designed to operate at a low radiation temperature of (130–140 eV) in order to minimize hot-electron preheat problems.

sis of this instability, and experiments[74] make it clear that the inner shell cannot be pushed the required distance before being penetrated by this turbulent layer. We now believe that the minimum size for successful ignition of double-shell targets makes it uninteresting for ICF applications.

On Shiva,[75–77] we fielded a few double-shell targets such as those shown in Fig. 27. The inner shell was a 180 μm diam, 20 μm thick glass shell, and the outer shell was a 360 μm diam, 50 μm thick CH shell formed from a pair of hemishells glued to the few-hundred-angstroms-thick film that held the inner shell in place. These Apollo targets had a higher calculated density than did the single-shell Cairn targets. However, the low neutron yields of $<10^7$ resulted in poor statistics for the neutron activation measurement of the glass pusher areal density, which was our only density diagnostic.

The model of hohlraum temperatures limited by plasma filling predicted that we would be able to achieve the temperature required for high-gain, single-shell targets if the proposed Nova laser were built to produce the third harmonic of the neodymium glass laser. This became practical because of efficient conversion schemes, using nonlinear conversion in potassium dihydrogen phosphate (KDP) crystals, initially devised by the University of Rochester.[78] In 1981, the improved coupling in hohlraums was demonstrated at the 100 J level in a series of experiments at 0.53 and 0.35 μm on the Argus laser.[79] In these experiments, the hot-electron levels dropped to open-geometry levels, and the fraction of the incident light that was absorbed in the hohlraum increased to nearly 100%, as shown in Fig. 28(a). These results are consistent with those seen in 1988 experiments reported by Sakabe *et al.*,[80,30] as shown in Fig. 28(b). Hohlraum absorption greater than 90% also has been typical

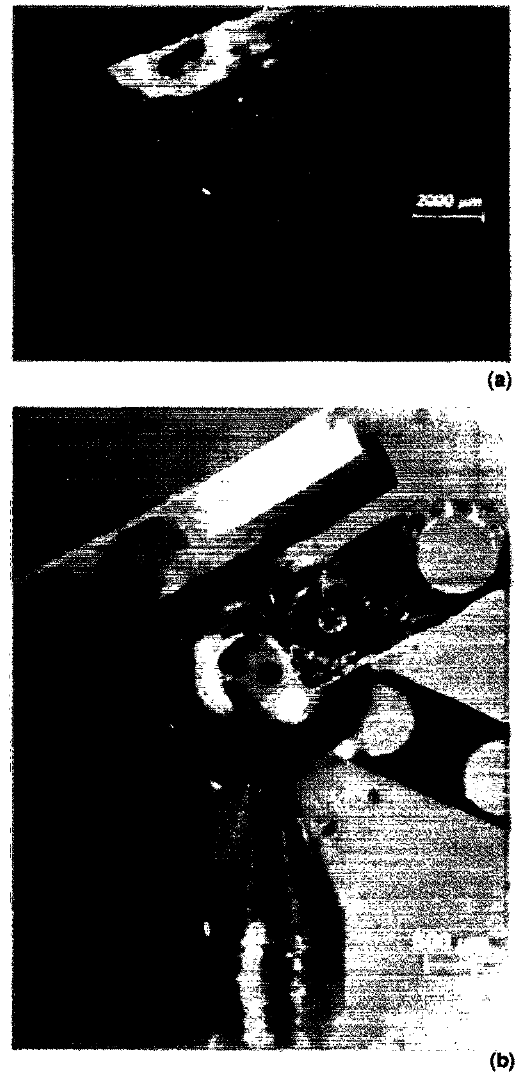

FIG. 24. The NPIRE targets: (a) cylindrical Cairn NPIRE after final assembly; (b) spherical NPIRE after final assembly.

of most short-wavelength hohlraum experiments on larger laser systems. The limitations to this high absorption are discussed in Sec. XI on hohlraum plasma conditions.

Using these estimates of the achievable radiation temperatures and an estimate of the hohlraum coupling efficiency that could be achieved consistent with the required implosion symmetry, we estimated the single-shell target gains[81] shown in Fig. 29. These gains are very similar to those now estimated for the proposed NIF.

In 1979, when it became clear that ignition would not be achieved on Nova, we devised a strategy for obtaining the database that would be required for ignition on a future facility.[82] This strategy tests the physics of high-gain targets by using a series of Nova experiments on targets that are as close as possible to being "hydrodynamically equivalent targets" (HETs), and by using a series of underground nuclear experiments (Halite/Centurion) at much higher energy. This combination of experiments and modeling was devised to provide the basis for the facility that ultimately would be required for ignition and high gain.

Since 1979, the LLNL ICF program has focused on developing the quantitative modeling tools, diagnostics, and

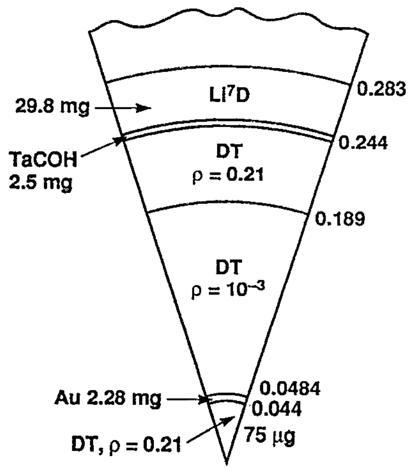

FIG. 25. High-gain Apollo double shell. This target had capsule absorbed energy=0.8 MJ, yield=313 MJ, maximum gold pusher velocity=1.9×10^7 cm/s, peak spark-plug fuel $\rho r\approx0.68$ g/cm^2, peak Au pusher $\rho r\approx3.6$ g/cm^2, peak main fuel DT $\rho r\approx0.96$ g/cm^2, and peak TaCOH $\rho r\approx0.11$ g/cm^2 (preheat shield).

experimental techniques required to provide this quantitative physics basis. This strategy was endorsed by the Foster Review[83] in October, 1979, along with the recommendation that Nova be a smaller, ten-beam laser with 2ω (0.53 μm wavelength) and 3ω (0.35 μm) capability. These recommended changes were implemented, and Nova has proved to be an extremely successful facility.[84]

In 1983, the first two beams of Nova were constructed as a laser test bed in an experimental facility called Novette, which gave us our first multikilojoule experience with 2ω

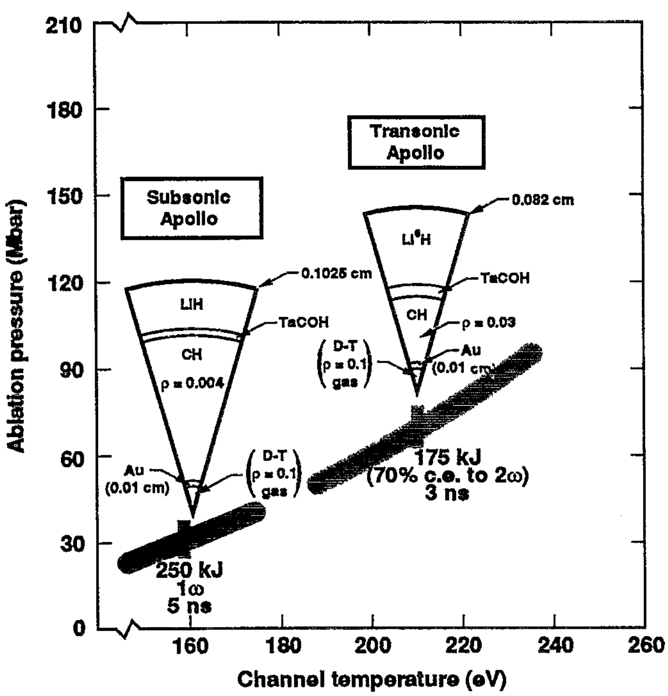

FIG. 26. Calculations in 1979, which predicted ignition for a 20-beam "200 kJ Nova," required high hohlraum coupling efficiency and near 1-D performance of double-shell targets. Both capsules had $E_{\mathrm{cap}}\doteq50$ kJ, $V(\mathrm{TaCOH})=2\times10^7$ cm/s, $V(\mathrm{Au})=3\times10^7$ cm/s. Capsule yields were about 100 kJ.

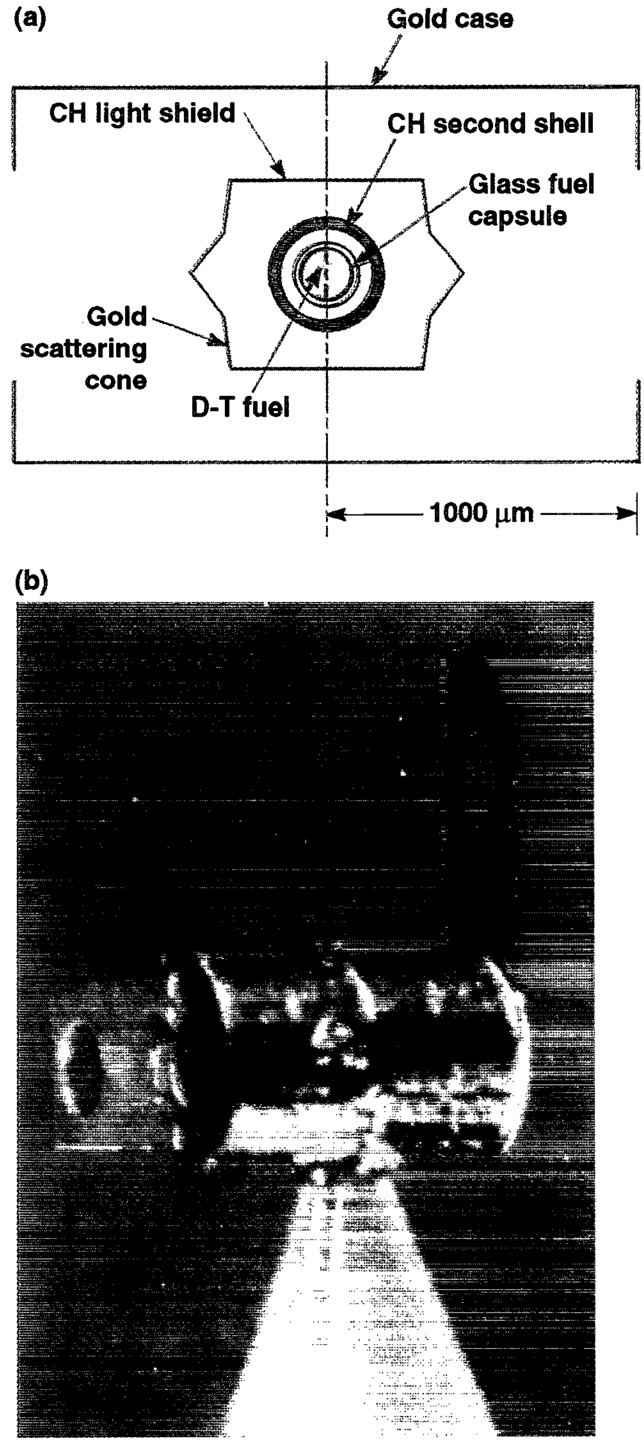

FIG. 27. (a) Apollo version B constructed for laser experiments on the Shiva laser during 1979. (b) Completed Apollo target. Outer shell and inner fuel capsule are visible through a diagnostic hole.

light. ICF experiments on this facility lasted only about three months, but indicated that we were very likely to achieve our hohlraum temperature goals on Nova. Implosions on Novette[85,86] used hohlraums such as those shown in Fig. 30. With 7–9 kJ of 2ω laser light, these hohlraums reached temperatures of 150–160 eV. For hohlraums that were four-fifths the size of those in Fig. 30 (scale 0.8), the temperatures were about 20 eV higher. The most accurate temperature measure-

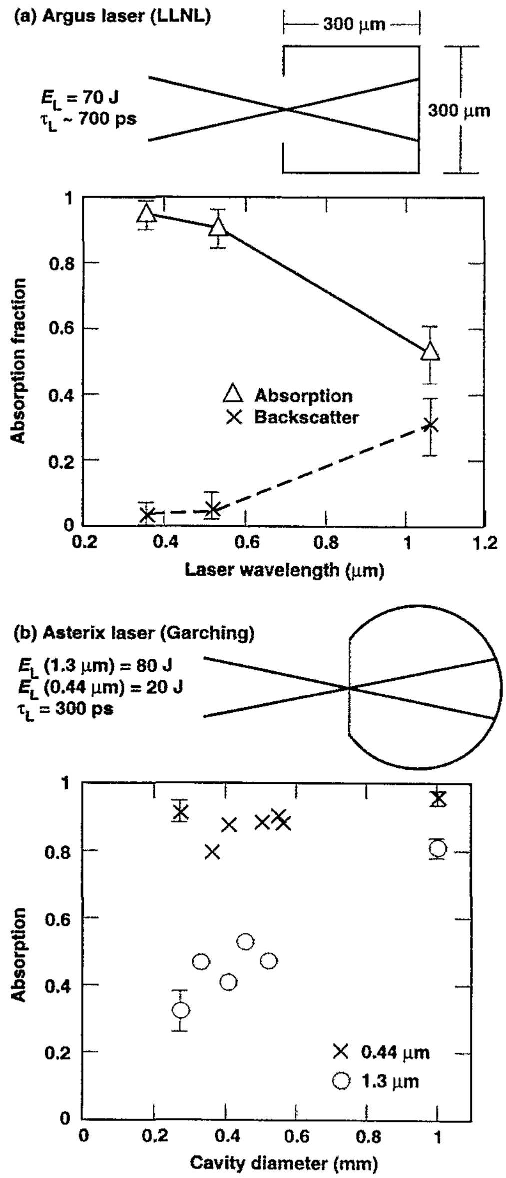

FIG. 28. Small-target hohlraum experiments showed efficient coupling with short-wavelength laser light. (a) Results from 1981 Argus laser experiments at LLNL using 0.35, 0.53, and 1.06 μm light. (b) Asterix laser (Garching, 1988) results using 0.44 and 1.3 μm light.

ment for these hohlraums was obtained by using an aluminum "witness plate" on a reentrant tube in "megaphone" hohlraums[87] such as shown in Fig. 31. The witness plates used on Novette had steps of two different thicknesses mounted on the end of a gold reentrant tube. By looking at optical emission when the radiation-driven shock breaks through the aluminum step and recording the time difference between the two steps, we obtain a shock velocity that can be related to x-ray drive. As indicated in Fig. 31 for a scale-0.8 hohlraum with 7.2 kJ of laser light, the hohlraum temperature reached 172 eV with only about 3% of the absorbed energy in hot electrons. (These results are consistent with the results achieved on the Phebus laser,[28] as shown in Fig. 11.)

We also carried out some 4ω (0.265 μm) experiments[87] with greater than 1.5 kJ of energy in a 1 ns pulse. Witness-plate measurements on the 4ω experiments indicated a hohlraum temperature of 210 eV with only 0.08% of the energy in hot electrons in a half-scale Novette hohlraum (Fig. 32) using 1.63 kJ of energy.

Although we did not carry out 3ω experiments on Novette (the appropriate KDP crystal arrays were not available), these results gave us confidence that Nova could meet or exceed its temperature goals of 200–225 eV. In principle, Nova could have been configured to produce 4ω light instead of 3ω , but we concluded that the decreased performance from optical damage would more than offset the benefits of the increased margin of safety in laser plasma interaction effects.

The NAS review[88] chaired by Dr. William Happer occurred just as Nova was becoming fully operational at the end of 1985. Soon after its activation, Nova achieved its initial temperature goals of 200–225 eV with low levels of hot electrons.[89] We had established this goal as the temperature that would be required for high gain with a 5–10 MJ laser. The DOE labeled such a facility the Laboratory Microfusion Facility (LMF).[90] The NAS review continued to endorse the HET approach, but made the H/C program the highest priority.

Between 1986 and 1990, LLNL made rapid progress on indirect-drive target physics. Nova experiments and quantitative modeling demonstrated symmetry control,[91,92] the first quantitative RT instability experiments,[93,94] the expected benefits of pulse shaping,[95,96] and the radiation-drive tem-

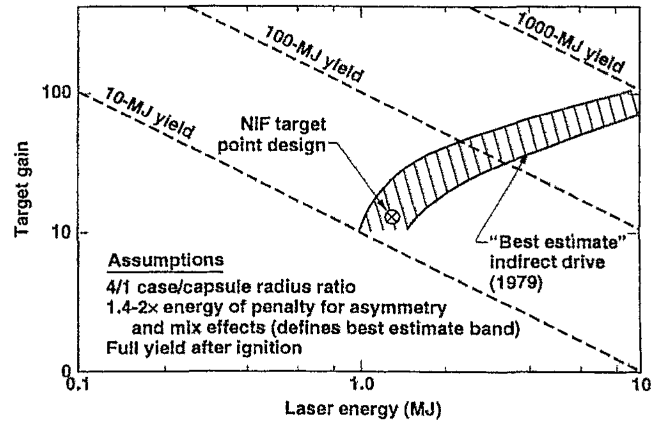

FIG. 29. By 1979, "best estimate" gains for single-shell, radiation-driven targets were comparable to today's estimates.

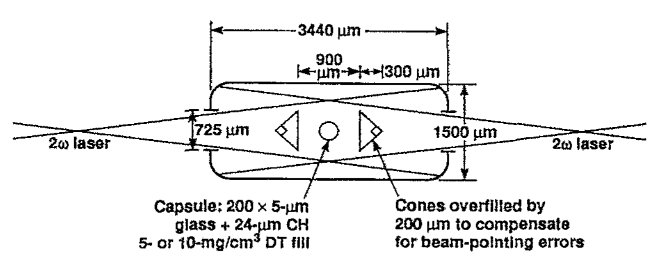

FIG. 30. Laser-target configuration for the two-beam Novette laser implosion campaign in 1983. These dimensions define a scale-1 Novette target.

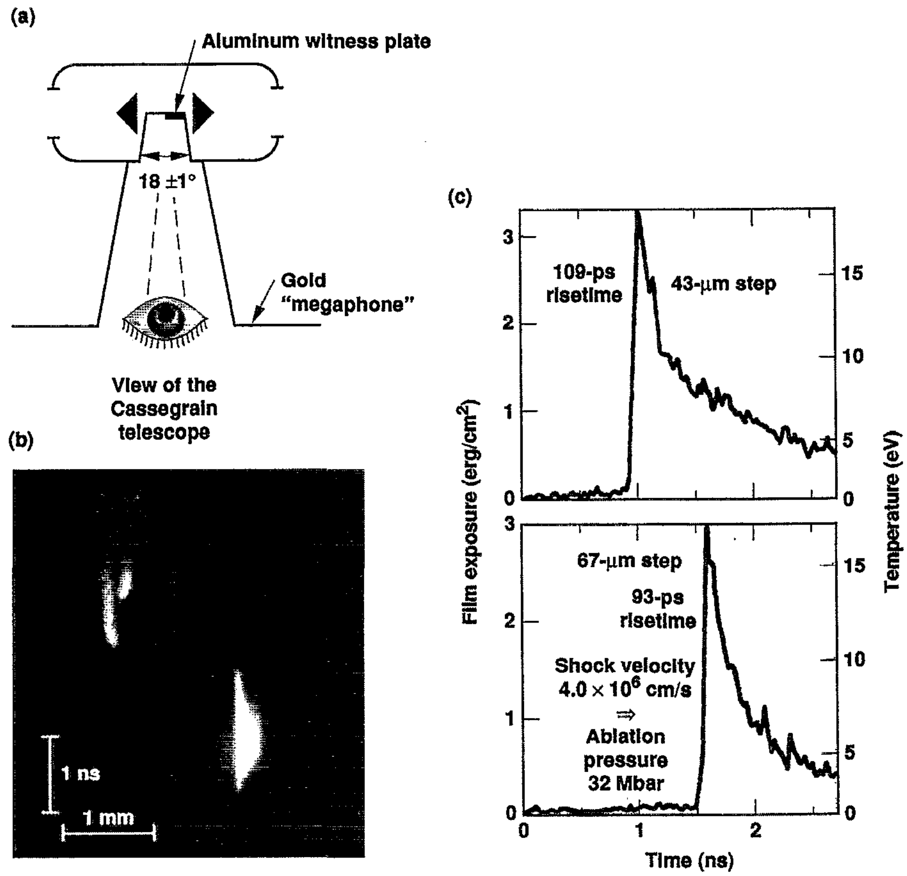

FIG. 31. Novette Megaphone 0.8-scale Cairn target used to measure the shock velocity of the drive at the center of the secondary. Target: 2487 μm long, 1198 μm in diameter, with 696 μm LEH. Laser beam: 7.2 kJ, 5270 Å, 1 ns pulse, $f/4.3$ diverging beam spot at cone. Aluminum witness plate for incident flux temperature: 43 μm step, 990 ps; 67 μm step, 1590 ps; $u_s=4.0\times10^6$ cm/s$\rightarrow P=32$ Mbars, $T_R=172$ eV. Hot electrons: 200 J of 34 keV electrons$\rightarrow T_{\mathrm{preheat}}=1.3$ eV for 43 μm step, 0.3 eV for 67 μm step. X-ray diode reemission flux temperature: $T_R=155$ eV.

perature scaling of implosions.[97] These experiments and their more recent equivalent are discussed later in this paper.

Based on the Nova and H/C progress, it was recommended that DOE begin considering the LMF based on glass-laser technology. This recommendation initiated a series of internal DOE reviews in 1988 and a request from Congress for an external review of the ICF Program, which was carried out by the NAS in 1989–1990. In its January 1990 interim report, the NAS committee, under the chairmanship of Professor Steven Koonin, commended the

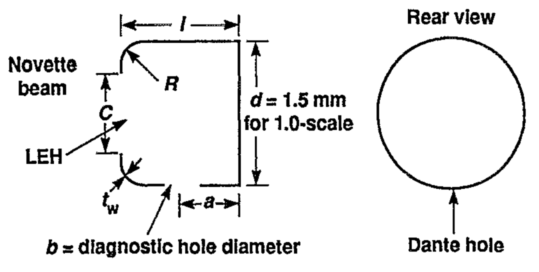

FIG. 32. Half-Cairn targets for Novette scaling experiments. Dimensions: d=outside diameter of cylinder=1500 μm for 1.0 scale; l=length of cylinder=$(5/6)d$; a=distance from back wall to center of Dante hole=$(13/30)d$; b=diameter of Dante hole=$(4/15)d$; c=LEH diameter=$0.5d$; t_w=wall thickness; R=radius of front corner=$0.25d$; g=back corner angle $=90\pm2°$.

progress that had been made in ICF, but concluded that the LMF, with proposed yields of 200–1000 MJ, was too large for the next step and encouraged the laboratories to explore a step between Nova and the LMF.[26] In addition, Koonin's committee concluded that the H/C program had achieved its principal objectives and recommended that the remaining issues regarding the feasibility of ICF be resolved on Nova.

Analysis of the relationship between implosion velocity, hydrodynamic instability, and hohlraum temperature indicated that ignition and modest gain would be possible with a 1–2 MJ laser if hohlraum temperatures of 300 eV, and implosion velocities of 4×10^7 cm/s could be achieved.[98,99] At this implosion velocity, the capsule has sufficient ignition margin to accommodate the expected level of degradation from hydrodynamic instability and asymmetry. At a laser energy of 1.8 MJ, which is the NIF baseline, there also is a sufficient margin to account for uncertainty in the achievable hohlraum coupling efficiency. Early in 1990, using the increased power and energy that had become available when Nova's laser glass was replaced with improved platinum-free material, we were able to demonstrate 300 eV hohlraums with less than 1% of the absorbed energy in hot electrons.

Based on experimental and modeling results, both the September 1990 final report[26] of Koonin's NAS committee and the DOE Fusion Policy Advisory Committee (FPAC) report[34] recommended construction of a 1–2 MJ glass laser for demonstrating ignition and modest gain within about a decade. The NAS noted that ignition demonstration is the natural next step in the ICF program. This recommendation was made contingent upon successful completion of a series of experiments to be carried out on Nova. These experiments and modeling in hohlraum and laser plasma interaction physics (HLP) and hydrodynamically equivalent physics (HEP) constitute the Nova Technical Contract (NTC).[26]

The HLP experiments address the issues of the effects of hohlraum plasma conditions on implosion symmetry, and the scaling of a variety of plasma collective effects (including parametric instabilities) in hohlraums.

The HEP experiments address the issues of hydrodynamic instability and mix, as well as the effects of flux asymmetry on capsules that are scaled as closely as possible to ignition capsules (hydrodynamic equivalence). Several improvements to the Nova laser, including improved power balance and pointing accuracy, were required to carry out some of these experiments. These requirements resulted in the "Precision Nova Project,"[100] which was completed in 1993.

Except for cryogenic implosions, which are not now planned for Nova, the experiments of the NTC will complete the goals established for Nova in 1981.

As part of its conclusions, the Koonin committee recommended that Los Alamos become an integral part of the Nova physics program. That work has been pursued jointly by LLNL and LANL since the end of 1990.

In early 1993, DOE endorsed the mission need for the NIF and authorized development of a conceptual design report (CDR) for the facility. Demonstration of ignition and burn propagation would complete the physics basis for ICF and open the door for ICF applications, including fusion power production.

The following sections review in more detail the theoretical and experimental progress in ICF, with an emphasis on Nova and the NTC, and summarize the expected performance of the proposed NIF. Included are a wide variety of analytic scaling laws that serve an important role in illuminating key physics issues.

III. IGNITION PHYSICS

Figure 1 shows the typical configuration of the compressed fuel at ignition. As a capsule implodes, $P\,dV$ work and α-particle deposition from thermonuclear burn of DT act to heat the central hot-spot region. Electron conduction from the hot spot to the cold surrounding fuel, as well as radiative losses, act to cool the hot spot. As the shell of main fuel compresses the hot spot, pressure increases, and densities of both the hot spot and the main fuel increase. If conduction and radiative losses from the hot spot are too large, ignition never occurs. To achieve ignition by the time the implosion process has stopped, the hot spot must have a ρr equal to about 0.3 g/cm^2 and must achieve a central temperature of about 10 keV. Under these conditions, α-particle deposition can overcome electron conduction losses from the hot spot, and a self-sustaining burn wave will be generated.

A simple analytic model demonstrates these requirements.[12,101,102] To estimate the rate of mechanical work per unit volume, P_w, done on the hot spot, we assume that the main fuel acts as a piston on a gas with uniform pressure:

$$\begin{aligned} P_w &= \frac{P(dV/dt)}{V} = \frac{PAv}{V} = \frac{3Pv}{r} \\ &= 2.3\times 10^{15}\,\frac{\rho T(v/10^7)}{r}\ \ (\text{W/cm}^3), \end{aligned} \tag{24}$$

where ρ is the hot-spot density in g/cm^3, P is the pressure, A is the surface area of the hot spot, V is its volume, r is its radius in cm, v is the implosion velocity in cm/s, and T is the matter temperature in keV. Electrons and ions are assumed to be in equilibrium. The thermonuclear heating rate per unit volume P_α is obtained from the burn rate and the fractional alpha particle deposition:

$$\begin{aligned} &P_\alpha = \rho\dot{\phi}\epsilon_\alpha F_\alpha, \\ &\dot{\phi} = \tfrac{1}{2}(1-\phi)n_0\langle\sigma v\rangle \approx 1.2\times 10^{23}\rho\langle\sigma v\rangle, \\ &\epsilon_\alpha = 0.67\times 10^{11}\ \ (\text{J/g}), \\ &P_\alpha = 8\times 10^{16}\rho^2\left\langle\frac{\sigma v}{10^{-17}}\right\rangle F_\alpha\ \ (\text{W/cm}^3). \end{aligned} \tag{25}$$

In this equation, $\dot{\phi}$ is the rate of change of the burnup fraction, ϵ_α is the α-particle energy per gram of DT, n_0 is the total number density of particles, $\langle\sigma v\rangle$ (cm^3/s) is the Maxwell-averaged cross section, and F_α is the α-particle deposition fraction. Efficient α-particle capture requires a ρr greater than the α-particle range shown in Fig. 4. The radiation loss, P_r, is assumed to be bremsstrahlung emission that escapes the fuel:

$$P_r = 3.0\times 10^{16}\rho^2 T^{1/2}\ \ (\text{W/cm}^3). \tag{26}$$

Conduction losses P_e are obtained assuming Spitzer[103] conductivity with a steady-state temperature profile determined by balancing volume heating and conduction losses:

$$\begin{aligned} &Q = -k\,\nabla T = \frac{-9.4\times 10^{12}S(Z)}{Z\cdot\ln\Lambda}\,T^{5/2}\,\nabla T\ \ (\text{W/cm}^2), \\ &4\pi r^2 Q = \frac{4\pi}{3}\,r^3(P_\alpha + P_w - P_R) \rightarrow Q = \text{const}\times r, \\ &\rightarrow T = T_0\left[1-\left(\frac{r}{r_0}\right)^2\right]^{2/7} \quad \text{and} \quad T^{5/2}\,\nabla T(r_0) = \frac{4}{7}\,\frac{T_0^{7/2}}{r_0}, \\ &P_e = \frac{QA}{V} = \frac{3Q}{r} \\ &\quad = 8\times 10^{12}\,\frac{T^{7/2}}{r^2}\ (\text{W/cm}^3), \quad \text{for } \ln\Lambda = 2, Z = 1. \end{aligned} \tag{27}$$

Here $S(Z) = \delta(z)\epsilon(z)/[\delta(z=1)\epsilon(z=1)]$ is from Spitzer. In addition, $S(Z)$ varies from 1.0 at $Z=1$ to about 4.0 at $Z=\infty$. Table II gives δ and ϵ at several different values of Z. Here T_0 is the central temperature of the hot spot and r_0 is its outer radius. The subscripts are dropped in Eq. (27). In obtaining the temperature, the implosion velocity within the hot spot is assumed to be proportional to the radius r at each point. This is necessary to maintain a constant density, which is a typical

TABLE II. We use Spitzer values of δ and ϵ for electron thermal conductivity.

Z	1	2	3	4	α
δ	0.225	0.356	0.513	0.791	1
ϵ	0.419	0.410	0.401	0.396	0.4

characteristic of the hot spot, as seen in Fig. 1. The Coulomb logarithm $\ln \Lambda$ is also assumed to be a constant, and the temperature at the edge of the hot spot is taken to be zero for simplicity. The temperature profile obtained under these assumptions is close to that seen in detailed numerical simulations at ignition for a typical high-gain target.

Equations (24)–(27) provide a qualitative picture of the gain and loss terms in the hot spot, but detailed numerical simulations are required for quantitative accuracy.

Energy gain in the hot spot occurs for $f=P_w+P_\alpha-P_e-P_r>0$. The $f=0$ boundary is a quadratic in ρr:

$$(\rho r)^2\left(\left\langle\frac{\sigma v}{10^{-17}}\right\rangle F_\alpha-\frac{T^{1/2}}{2.6}\right)+\rho r\left(\frac{T(V/10^7)}{35}\right)-\frac{T^{7/2}}{10^4}=0. \tag{28}$$

This boundary separates regions in which the hot spot gains energy as it is compressed from those regions in which it loses energy. The regions of gain and loss are plotted in Fig. 33 for a velocity of 3×10^7 cm/s. At this velocity, there are uninterrupted trajectories in the energy gain region, from low temperature and low ρr to ignition conditions. Plotted in Fig. 33 are the boundaries that specify the regions in which the various terms of the energy equation dominate. Above a line given by

$$T=15.5(\rho r)^{2/3}\ \ (\mathrm{keV}), \tag{29}$$

the electron conduction loss rate exceeds the radiative loss rate. Typical ICF capsule implosions proceed entirely above this line, for DT with no impurities. It is also clear that PdV work is the dominant energy gain term below $0.1<\rho r<0.2$ g/cm^2 and temperatures of several keV.

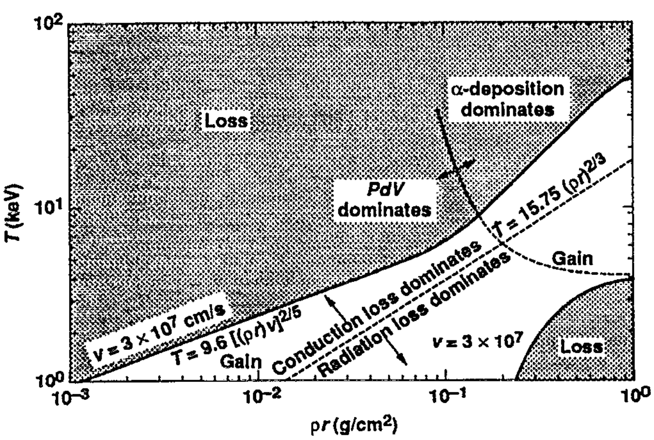

FIG. 33. With sufficient implosion velocity, PdV work will implode a hot spot until α deposition can propagate the burn.

The existence of a loss region at high ρr and a temperature of a few keV is caused by the fact that radiative losses scale as ρ^2 whereas PdV work scales only as ρ. The ratio of the PdV work to the radiative loss is given by

$$\frac{P_w}{P_r}=0.767\,\frac{T^{1/2}(v/10^7)}{\rho r}. \tag{30}$$

For any given v, this ratio is less than unity at sufficiently high ρr. However, at high ρr, the radiation no longer escapes, and the loss rates are not as high as assumed in this model. This region of energy loss at high ρr extends only up to the so-called "ideal ignition temperature," the temperature at which the α-particle production rate equals the radiation loss rate. In DT without any impurities, this temperature is 4.3 keV. Since both the bremsstrahlung and alpha production rates scale as ρ^2 and are independent of r, the alpha production results in energy gain above this temperature at sufficiently high ρr.

Along the boundaries defined by $f=0$, the gain and loss terms exactly balance, so a capsule cannot implode exactly along this boundary. For the region in which electron conduction and PdV work dominate the energy balance, there is an implosion trajectory toward which all possible implosion trajectories will be "attracted."[104] To show this, we write, for the time rate of change of the temperature,

$$\begin{aligned}
&C_v\rho\,\frac{dT}{dt}=\sum P=P_w+P_\alpha-P_e-P_r,\\
&\frac{dT}{dt}=\frac{dT}{d(\rho r)}\,\frac{d(\rho r)}{dt}=2\rho v\,\frac{dT}{d(\rho r)},\\
&\frac{dT}{d(\rho r)}=\frac{\Sigma P}{2C_v\rho^2 v}\approx a\,\frac{T}{\rho r}\left(1-\frac{bT^{5/2}}{\rho r}\right);\\
&b=\frac{3.5\times 10^{-3}}{[v/(3\times 10^7)]},\quad a=1.0.
\end{aligned} \tag{31}$$

If we assume $T=\delta^{2/5}(\rho r)^{2/5}/b$, where $\delta=1$ defines $f=0$ for small ρr and T, then we have a solution for

$$\delta=1-\frac{2}{5a}=0.60$$

or

$$T=0.815\,\frac{(\rho r)^{2/5}}{b}=7.8\left((\rho r)\,\frac{v}{3\times 10^7}\right)^{0.4}. \tag{32}$$

This solution parallels the $f=0$ boundary, but is 18.5% lower in temperature. Capsules that begin their implosion away from this trajectory gradually tend toward it. For example, suppose a capsule had a $\rho r=0.01$ g/cm^2 and $T=1$ keV in Fig. 33. Under these conditions, the ratio of the PdV work to the conduction loss is almost a factor of 10 when the implosion velocity is 3×10^7, so the implosion would be almost adiabatic. For an adiabatic implosion, we have

$$\frac{T}{T_0}=\left(\frac{\rho}{\rho_0}\right)^{\gamma-1}=\left(\frac{\rho}{\rho_0}\right)^{2/3}. \tag{33}$$

For a sphere of mass M, we have $M=(4\pi/3)[(\rho r)^3/\rho^2]$ or for constant mass, $\rho r\propto\rho^{2/3}$. From Eq. (33) we then have

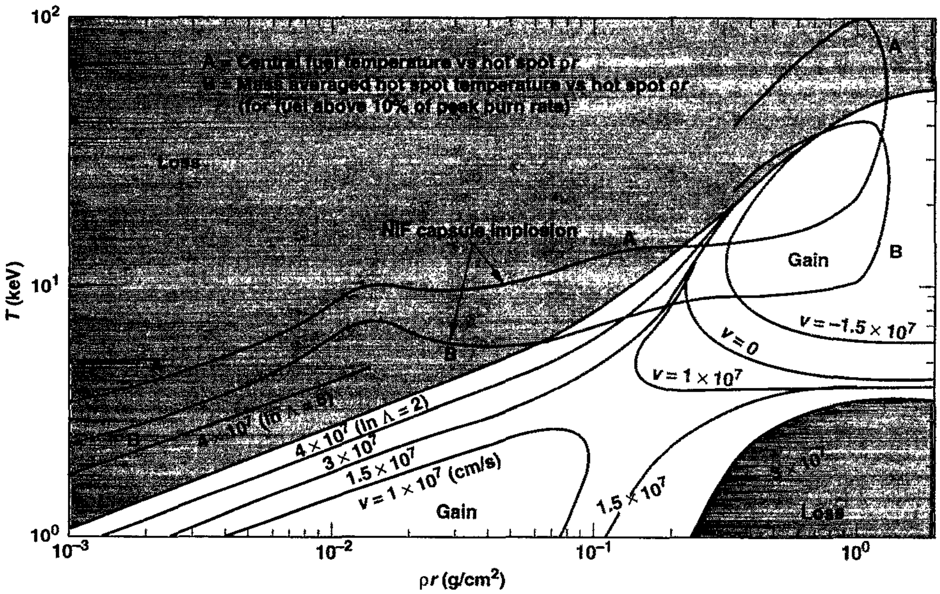

FIG. 34. The calculated NIF capsule trajectory in T_i vs ρr space is qualitatively consistent with a simple model of fuel energy gain and loss, but the fuel hot spot achieves a higher temperature at preignition values of ρr.

$$\frac{T}{T_0}=\left(\frac{\rho r}{\rho r}\right)_0 . \tag{34}$$

The T vs ρr curve would have a slope of unity, which would approach the "stable attractor" curve from below. The trajectory could not cross that of the "stable attractor," since the slope from below asymptotically approaches the same value as the "stable attractor." The same process occurs in reverse for a capsule that starts out with too high a temperature for a given ρr. Most ICF capsules start out on this latter type of trajectory since the shock that sets the initial adiabat often establishes a higher temperature than can be sustained by the corresponding implosion velocity.

Figure 34 is an implosion trajectory from a numerical simulation of the NIF capsule (see Fig. 107, Sec. XIII). Time is implicit in the trajectory and increases as the temperature and ρr change from left to right across the figure. The contours labeled with different velocities are the $f=0$ boundaries at the indicated velocities. This capsule has an implosion velocity of 4×10^7 cm/s at the time it started decelerating. As seen in Fig. 34, the hot-spot temperature increases somewhat more rapidly during compression than this simple model would predict. This is at least partly because electron conduction losses are not into a surrounding cold heat sink but into DT, which is at a finite temperature so that conduction losses are reduced. Also, during the low-ρr hot-spot assembly stage, $\ln \Lambda \approx 6$, which results in smaller conduction loss compared to Eq. (27), which used $\ln \Lambda=2$. The line in Fig. 34, with $V=4\times 10^7$ cm/s and $\ln \Lambda=6$, is close to the trajectory followed by the mass-averaged hot-spot temperature of the NIF capsule.

Figure 35 shows the calculated fuel temperature and density versus ρr for a 0.2 MJ capsule that could be driven by the NIF and a larger 2 MJ capsule. Although the capsule energies differ by an order of magnitude, the fuel configuration in temperature and ρr space, the variables that determine burn propagation are nearly identical. The smaller capsule has larger density to make up for the reduced mass and energy in the fuel.

A key to the predicted success of capsules that are being designed to ignite on NIF is the use of a pure DT cryogenic fuel pusher. Of all possible materials that could be used for a pusher to compress the central hot spot to ignition conditions, DT has the least susceptibility to the effects of mix, which can occur at the hot/cold boundary. This mix of hot and cold material can quench ignition because of increased radiative and electron conduction losses and because of increased heat capacity in the hot-spot region. DT will not suffer increased radiative losses compared to the hot spot and will burn to essentially full yield, independent of mix if ignition is achieved. As discussed in Sec. VI, DT also has the least amount of hydrodynamic instability growth at the hot/cold interface during decompression.

Once ignition occurs, the burn wave in these DT cap-

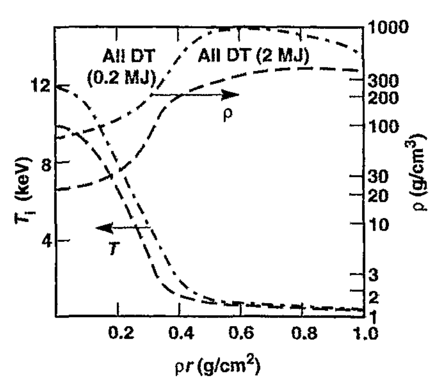

FIG. 35. Laboratory ignition and high-gain capsules have very similar ignition conditions. Hot-spot temperature profiles and ρr are nearly independent of size at ignition. Smaller capsules must have higher density to achieve the required hot spot $\rho r \approx 0.3$ g/cm^2.

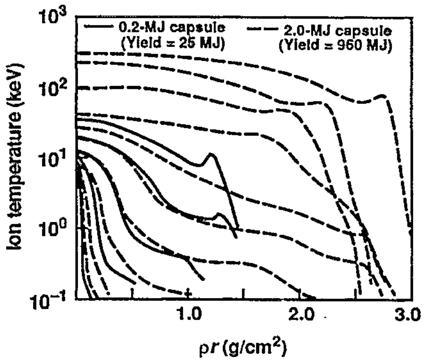

FIG. 36. Burn propagation in small capsules tracks that in larger capsules until decompression begins. Pairs of curves are temperature contours at a series of times as the burn wave propagates through the fuel.

sules propagates in ρr and temperature space in a way that is essentially independent of size. Figure 36 shows the temperature-versus-ρr conditions for a 0.2 MJ NIF and the larger 2.0 MJ capsule as the burn wave propagates into the fuel. The two capsules track each other until the smaller capsule starts to decompress. Thus, a demonstration of ignition and burn on the NIF will determine the requirements for high gain with a larger driver.

IV. PULSE SHAPING

Precise and flexible pulse shaping is required to achieve the high densities indicated in Fig. 35. To achieve the required hot-spot and pusher densities with minimal energy, the pusher must remain nearly Fermi degenerate.

The change in fuel entropy, $\Delta s = \Delta Q/T$ determines its compressibility. The heat ΔQ can come from a variety of sources, including shocks, electron conduction, photon preheat, and hot electrons from plasma instabilities. For ignition capsules being designed for the NIF, shocks are typically the largest source of entropy.

To see how compressibility changes with the addition of entropy, the equation of state tables for DT (e.g., from the Los Alamos *Sesame Library*[11]) can be used to generate a family of isentropes[105] in the pressure-versus-density plane, as shown in Fig. 37. The number labeling each curve also gives the specific entropy along that isentrope, relative to the initial cryogenic value, in units of 10^8 J/keV/g. Since only changes in entropy are meaningful, we have, for convenience, put $s=0$ when $T=11.6$ K and $\rho=0.25$ g/cm^3, the density of solid DT.

For $\rho \geqslant 5.0$ g/cm^3, curves 1, 2, 3, and 4 are seen to nearly coalesce. This coalescence is just above the so-called Fermi-degenerate adiabat, where the pressure is due almost entirely to the degeneracy pressure of the electrons ($kT_e \leqslant \epsilon_{\rm Fermi}$). (For $\rho \leqslant 5.0$ g/cm^3, the $\Delta s=0$ adiabat curves down from $P \propto \rho^{5/3}$ because the equation of state of DT at these densities and low temperatures is dominated by atomic and molecular binding and is poorly approximated by a Fermi gas.) There is a fairly abrupt transition at $\Delta s=4$. For $\Delta s<4$, the adiabatic compressibility is a very weak function of s. However, above that threshold, the pressure at a given density increases exponentially with increasing entropy:

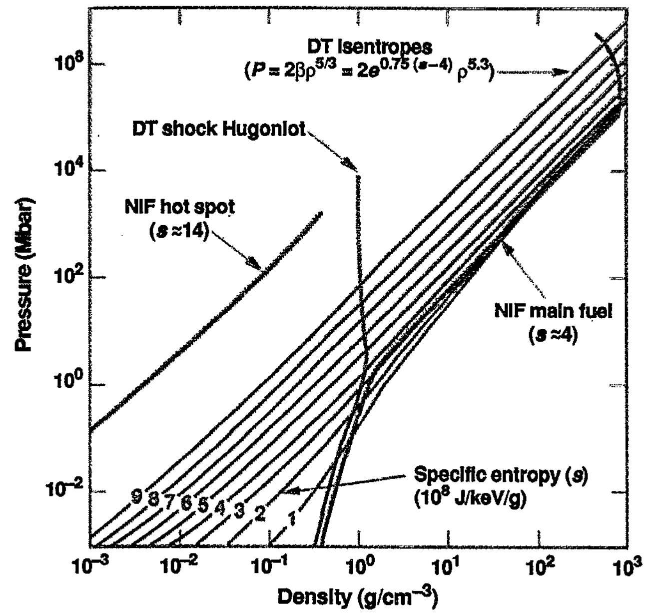

FIG. 37. DT isentropes and shock Hugoniot. The initial state for the shock Hugoniot is $\rho=0.25$ g/cm^3, $T=11.6$ K. Each isentrope is labeled by its specific entropy(s) relative to that initial state in units of 10^8 J/g/keV.

$$P_{\rm DT}(\text{Mbar}) = 2\ \exp[0.75(\Delta s - 4)]\rho^{5/3}(\text{g/cm}^3) = 2\beta\rho^{5/3}$$

or

$$\beta = \exp[0.75(\Delta s - 4)], \tag{35}$$

where β is the ratio of the pressure at a given density to the Fermi pressure at that density. From Eq. (35), we see that, for every change in entropy of $\Delta s=1$ above $\Delta s=4$, the pressure at a given density increases by about a factor of 2. To avoid this reduction in compressibility, the optimal ICF capsule should have $\Delta s<4$ from all sources.

Also plotted in Fig. 37 is the shock Hugoniot for DT from an initial solid density of 0.25 g/cm^3. The shock Hugoniot represents the set of possible final states reached in a single shock from the initial state. For a $\gamma=5/3$ gas such as DT, the density at high pressures asymptotically approaches[106] a compression

$$\eta_\infty = \frac{\gamma+1}{\gamma-1} = 4. \tag{36}$$

Typical implosion pressures for an ICF capsule are 100 Mbars or more. If the driving pressure were turned on suddenly, producing a 100 Mbar shock, the entropy generated in the fuel would be $\Delta s=9$, as shown in Fig. 37. From Eq. (35), compression to a given density would require a pressure about 42 times the Fermi pressure. Figure 37 shows that a single shock of 2 Mbars gives the fuel an entropy of $\Delta s=4$. If we start an implosion at this initial pressure, the subsequent pressure history must be tailored such that almost no entropy is generated as the driving pressure increases from 2 to 100 Mbars or more.

If the pressure profile is generated from a series of shocks of increasing pressure, we can use the Hugoniot relationships[106,107] to determine the allowable pressure ratios

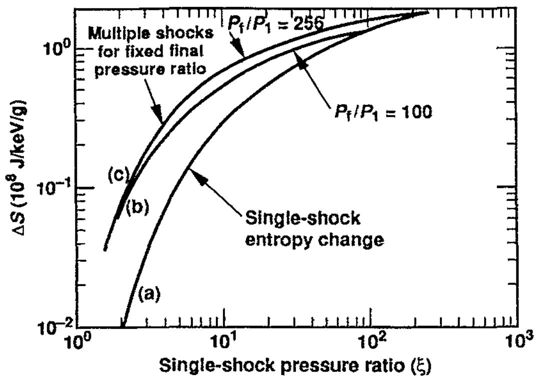

FIG. 38. Entropy changes in shocked DT: (a) for single shock; (b) multiple shocks versus individual shock pressure ratio with fixed final-to-initial pressure ratio $P_f/P_1=100$; (c) multiple shocks versus individual shock pressure ratio with $P_f/P_1=256$.

that will result in an acceptable fuel entropy level. For a γ-law gas, we have

$$\xi \equiv \frac{P_2}{P_1} = \frac{2\gamma M^2-(\gamma-1)}{(\gamma+1)} = \frac{5}{4}M^2 - \frac{1}{4}, \tag{37}$$

$$\eta_s \equiv \frac{\rho_2}{\rho_1} = \frac{\xi\eta_\infty - 1}{\xi+\eta_\infty}, \tag{38}$$

$$\frac{T_1}{T_2} = \frac{[(\gamma+1)^2/2(\gamma-1)]M^2}{\{1+[(\gamma-1)/2]M^2\}\{[2\gamma/(\gamma-1)]M^2-1\}} = \frac{16M^2}{(3+M^2)(5M^2-1)}, \tag{39}$$

$$\Delta s(10^8\ \text{J/keV/g}) = 2.5R \ln \frac{T_2/T_1}{(P_2/P_1)^{(\gamma-1)/\gamma}} = 0.96 \ln\left(\frac{T_2/T_1}{(P_2/P_1)^{0.4}}\right). \tag{40}$$

In these relationships, subscript 1 (2) refers to conditions downstream (upstream) from the shock, and a $\gamma=5/3$ has been used. Here R is the gas constant per unit mass. The Mach number, M, is the ratio of the shock speed to the sound speed.

For a pressure ratio ξ, Eq. (38) can be compared to an isentropic compression:

$$\eta_I = \xi^{1/\gamma} = \xi^{0.6}, \tag{41}$$

which can be obtained from Eq. (35)

These relationships are reasonably accurate for DT above an entropy of 4. Figure 38 shows the entropy generated as a function of the pressure ratio for a single shock. Also plotted is the total entropy change for a series of shocks with a total pressure ratio of 100 and 256 as a function of the single-shock pressure ratio. In the limit of a very large number of shocks for a fixed pressure change, the entropy change approaches zero (i.e., the compression becomes adiabatic). For a pressure ratio of 100, the total entropy change is less than 0.3 for three shocks each, with a pressure ratio of 4.6. If we were to start with an initial pressure of 1 Mbar and proceeded to 100 Mbars with a series of three more shocks, the entropy of the fuel would remain below 4, and the fuel would remain essentially Fermi degenerate.

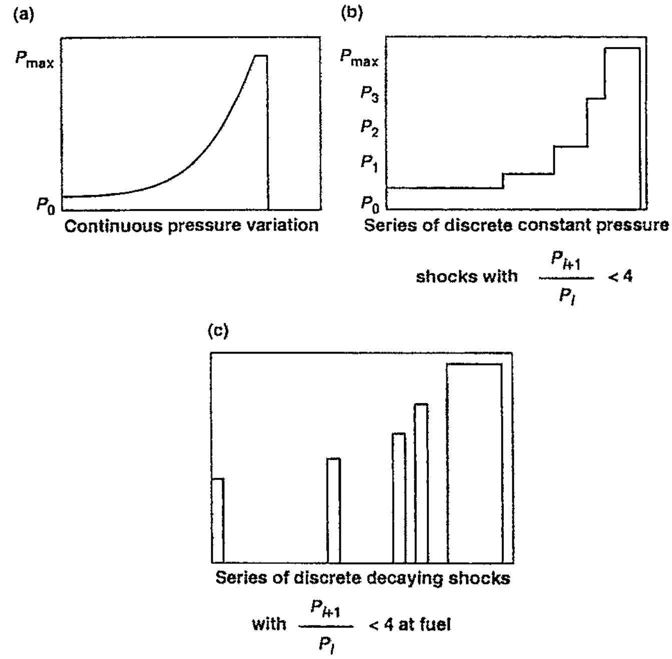

FIG. 39. A variety of equivalent pulse shapes can provide the required temporal history of pressure on the fuel: (a) continuous pressure variation; (b) a series of discrete, constant-pressure shocks with P_{i+1}/P_i less than about 4; (c) a series of discrete decaying shocks (picket fence) with P_{i+1}/P_i less than about 4 in the fuel.

From Eq. (38), the total compression ratio for three shocks with a total pressure ratio of 100 is given by $\eta_s^3=11.5$, while for a series of six shocks, the compression ratio is 15.1. From Eq. (41), the isentropic compression ratio for a pressure ratio of 100 is given by $\eta_I=15.9$

The timing of these successive shocks must be precisely controlled. Since we want to keep all but a few percent of the total fuel nearly Fermi degenerate, all shocks must be timed to coalesce near the inside surface of the fuel. If two or more shocks coalesce before reaching the inner surface of the fuel, the fuel inside the position where they coalesce will see a much larger pressure ratio, with a correspondingly higher entropy change. On the other hand, if the inner region of the fuel has a chance to decompress before all of the shocks have passed through, the region of the fuel within the rarefaction will see a larger pressure ratio and, again, a larger entropy change.

A wide variety of pulse shapes, such as those shown schematically in Fig. 39 can be used. The continuously varying pulse in Fig. 39(a) is potentially isentropic, but in practice, the rate of power change is steep enough that the pressure pulses generated by different parts of the pulse shape usually steepen into shocks before they reach the interior of the fuel. The series of steps in Fig. 39(b) generates a series of discrete shocks whose pressure ratio and timing are adjusted. In the "picket fence" pulse shape in Fig. 39(c), the laser drive is on for short pulses and off between the pulses. This launches "blast waves" (shocks followed immediately and continuously weakened by rarefactions) into the capsule. The pressure of each blast wave is chosen so that it has the desired pressure when it arrives at the fuel.

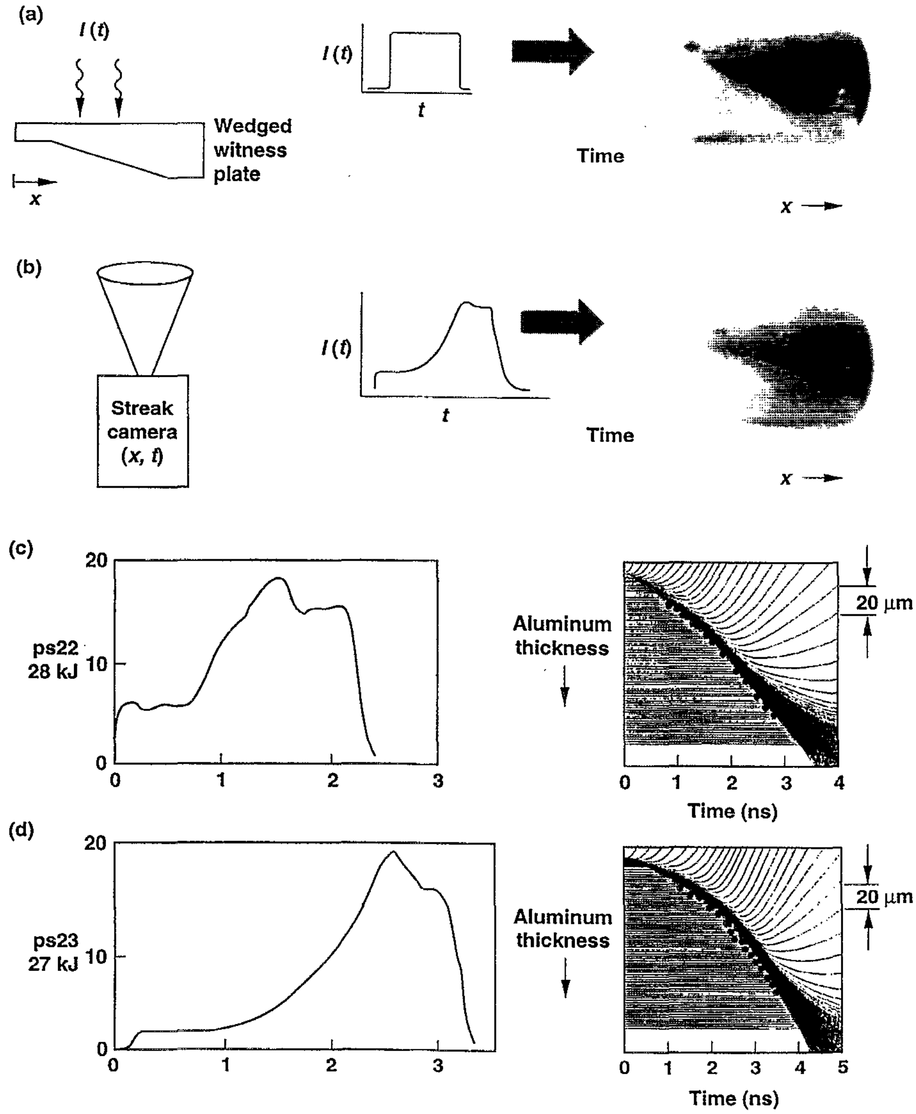

FIG. 40. Shock-wave measurements on Nova demonstrated our ability to produce the time-varying ablation pressures required for high-gain ICF.

NIF capsules, described in Sec. XIII, require pulses with a contrast that varies from about 10 to 50. The pulse shape for the NIF baseline PT target (see Figs. 106 and 107 in Sec. XIII) generates four shocks that result in an entropy change $\Delta S=4$ in the main cryogenic fuel. Figure 37 shows the P vs ρ trajectory for the NIF target main fuel region.

That Nova can deliver widely varying, precisely controlled pulse shapes has been demonstrated by using a wedge-shaped aluminum "witness plate" in the wall of a hohlraum,[108–110] as shown in Fig. 40. Radiation ablation on the hohlraum side of the witness plate generates a shock. When this shock reaches the outside of the witness plate, optical emission is generated, which we view by means of an ultraviolet streak camera at $\lambda=280$ nm, with the slit aligned along the length of the witness plate. If a constant-velocity shock is generated, position versus time, at which optical emission is first observed in the slit has constant slope, as shown in Fig. 40(a). If the radiative power driving the shock increases with time, causing a time-varying shock velocity, then the slope is not constant, as shown in Fig. 40(b). In general, when measured radiation temperature is used in the calculations, the shock velocities produced by these pulse shapes are well matched by the calculations, as indicated in Fig. 40(c) for a 2.3 ns, 3:1-contrast pulse (labeled ps22), and Fig. 40(d) for a 3.2 ns, 8:1-contrast pulse (ps23). (The dots are from experimental measurements.) In the calculations, the shock position corresponds to the edge of the dark band. These pulse shapes were used in the symmetry experiments discussed in Sec. IX.

Pulse-shaped implosions[111,112,95,96] also show the expected increase in density, as shown in Fig. 41 for a constant-power, 1 ns pulse and an implosion using ps22. The capsules were plastic shells with 50 atm DD fuel fill and 0.1 atm argon doping, as shown in Fig. 42. Figure 41(b) shows the size of the 3 keV emission from the imploded core. Some of this emission comes from the plastic pusher, so the size of the x-ray emission does not directly indicate the change in density. A more direct measure of the change in density comes from Stark broadening[113] of the argon He-β x-ray line profile, as shown in Fig. 41(c). This measurement shows that the density doubled with this modest level of pulse shaping, in agreement with calculations.

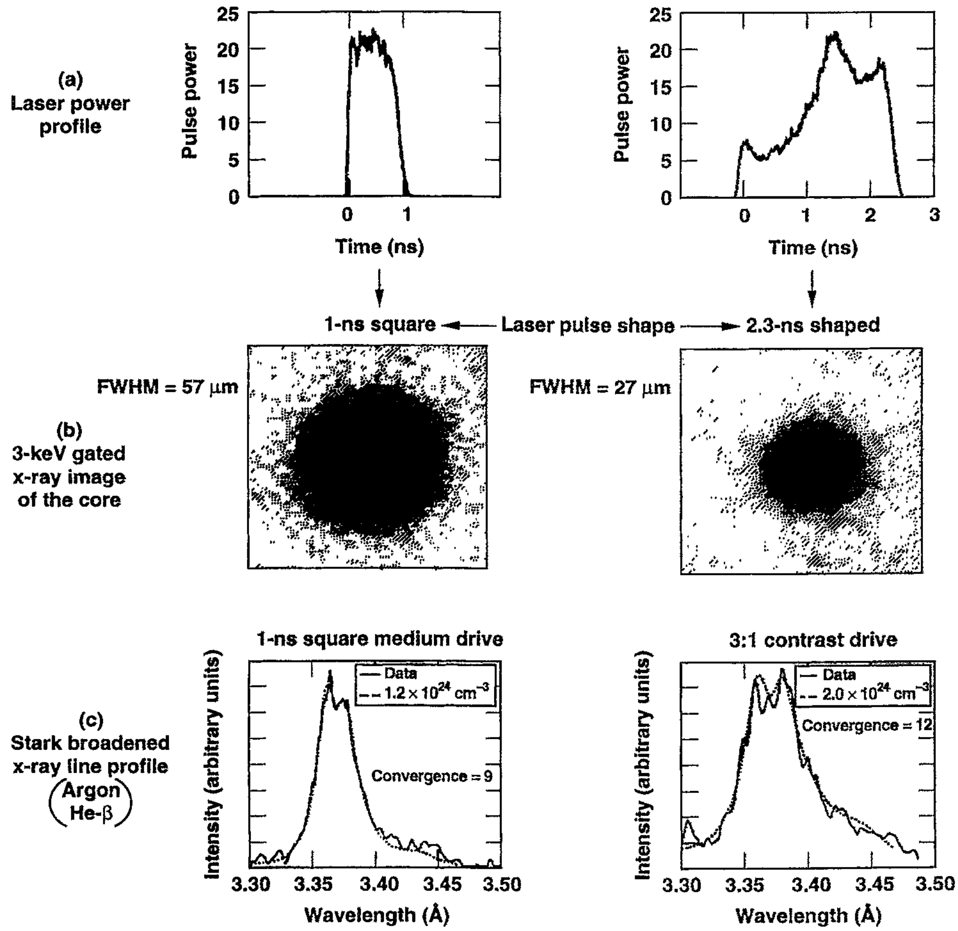

FIG. 41. Implosion experiments with shaped drive demonstrate higher convergences and fuel densities at the same peak drive pressure.

V. IMPLOSION DYNAMICS

The implosion of an ICF capsule can be described by a rocket equation, as given in Eq. (22). In an ablation-driven rocket, the exhaust, which is the target corona, is continually heated so that it remains nearly isothermal as it expands, instead of having no internal energy, as assumed for the ideal rocket.

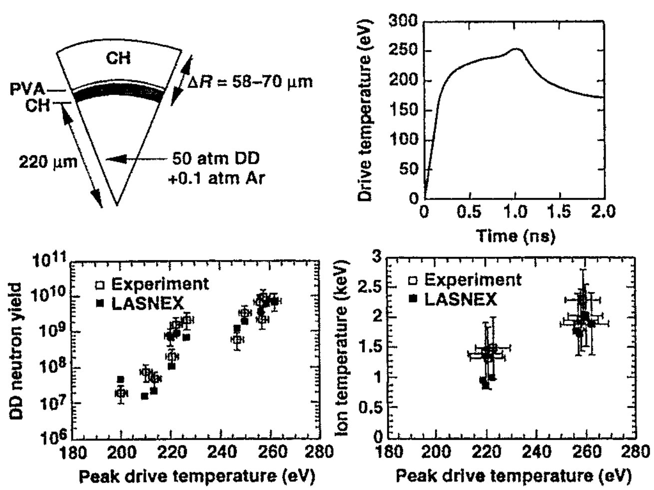

FIG. 42. Nova implosion experiments show the expected scaling of yield and fuel ion temperature with radiation temperature.

The ideal rocket has the efficiency $(x \ln^2 x)/(1-x)$, as shown in Fig. 5, where $x \equiv m/m_0$ is the ratio of the payload mass m to the initial rocket mass m_0. The band of achievable efficiencies in Fig. 5 corresponds to the range seen in numerical simulations for ICF capsules. The top of the band is typical of radiation-driven implosions, which have hydrodynamic efficiencies of 15%–20%. X rays that drive the implosion are deposited at high density near the ablation front. Laser-driven, direct-drive implosions have lower hydrodynamic efficiency than do x-ray-driven implosions because the laser energy is deposited in the target corona at a density and radius outside the ablation front. This energy must then be conducted to the ablation surface. In a spherical target, the efficiency of this conduction process decreases as the distance between the laser absorption region and the ablation front increases.[114,115] This is essentially a solid-angle effect. Hence, lasers with longer wavelengths, which have a lower critical density and are absorbed at larger radius, have lower implosion efficiencies. Direct-drive targets that use a laser wavelength of $\frac{1}{4}$–$\frac{1}{3}$ μm typically have an implosion efficiency of 5%–10%, depending on details of the target.

The minimum capsule size that will achieve ignition and propagating burn into the main fuel depends strongly on the achievable implosion velocity. This velocity, in turn, is determined primarily by the peak pressure that can be generated consistent with efficient coupling of the driver energy to the capsule and by the degree of hydrodynamic instability of the implosion process.

The pressure P generated by ablation scales as a power of the incident flux I:

$$P=P_0 I^{a_1}, \tag{42}$$

where a_1 is less than 1. The mass ablation rate $\dot{m}$ is also given by a power of the incident flux:

$$\dot{m}=\dot{m}_0 I^{a_2}, \tag{43}$$

where a_2 is also less than 1. If the pusher is imploded adiabatically, then the pressure and density ρ are related by

$$P=P_F\beta\rho^{5/3} \quad \text{or} \quad \rho=\frac{P^{3/5}}{P_F^{3/5}\beta^{3/5}}=\frac{P_0^{3/5}I^{(3/5)a_1}}{P_F^{3/5}\beta^{3/5}}, \tag{44}$$

where β is the ratio of the pressure at a given density to the Fermi pressure P_F. Equation (22) for the implosion velocity V_{imp} can be written in terms of the intensity I:

$$V_{imp}=\frac{P}{\dot{m}}\ln\frac{m_0}{m}=\frac{P_0}{\dot{m}_0}I^{a_1-a_2}\ln\frac{m_0}{m}\equiv V_{ex}\ln\frac{m_0}{m}. \tag{45}$$

The ablation velocity—the velocity with which the ablation front moves through the shell, V_{abl}—is given by the mass ablation rate divided by the shell density:

$$V_{abl}=\frac{\dot{m}}{\rho}=\frac{P_F^{3/5}\beta^{3/5}\dot{m}_0}{P_0^{3/5}}I^{a_2-(3/5)a_1}=V_{abl}^0 I^{a_2-(3/5)a_1}. \tag{46}$$

The ablation velocity is a critical quantity for evaluating the hydrodynamic instability of an imploding shell. High ablation velocities result in reduced growth from RT instabilities, as discussed in Sec VI.

Equations (42)–(46) are valid for both direct drive and indirect drive, but the coefficients differ significantly. For direct drive,[15,115,116] we have, approximately,

$$P(\text{Mbar})_{\text{D.D.}}=40\left(\frac{I_{15}}{\lambda}\right)^{2/3}, \tag{47}$$

$$\dot{m}(\text{g/cm}^2/\text{s})_{\text{D.D.}}=2.6\times10^5\left(\frac{I_{15}}{\lambda^4}\right)^{1/3}. \tag{48}$$

From these two equations, we then have

$$V_{imp}(\text{cm/s})_{\text{D.D.}}=1.5\times10^8(I\lambda^2)^{1/3}\ln\left(\frac{m_0}{m}\right) \equiv V_{ex}\ln\left(\frac{m_0}{m}\right), \tag{49}$$

$$V_{abl}(\text{cm/s})_{\text{D.D.}}=4.3\times10^4\beta^{3/5}I_{15}^{-1/15}\lambda^{-14/15}, \tag{50}$$

where we have used $P_{DT}(\text{Mbar})=2\beta\rho^{5/3}$ (g/cm^3) from Eq. (35). Intensity is in units of 10^{15} W/cm^2. Laser wavelength λ is in micrometers. We assume here that the compressibility of the ablator material has been matched to that of DT (e.g., by pulse shaping or control of x-ray preheat). The ΔR used in the following analysis is the total shell thickness, although at peak velocity, most of the shell in an optimized target will be fuel. These relationships for direct drive are valid for situations in which the laser absorption occurs predominantly near the critical density. Dependence on laser wavelength will be reduced if the intensity is low enough that significant absorption occurs well below critical density. The exponents of intensity and laser wavelength dependence can be obtained from dimensional analysis by using a simple model of the physics involved. We set the incident intensity equal to pressure times blowoff velocity at the sonic point. For direct drive, the sonic point occurs near the critical density ρ_c, so we have

$$I\approx PV_{ex}\propto\rho_c V_{th}^3\propto\frac{1}{\lambda^2}V_{th}^3\Rightarrow V_{th}\propto(I\lambda^2)^{1/3},$$

or

$$P\approx\rho_c V_{th}^2\propto\frac{1}{\lambda^2}(I\lambda^2)^{2/3}\Rightarrow P\propto\left(\frac{I}{\lambda}\right)^{2/3},$$

where V_{th} is the thermal velocity. This matches the scaling in Eq. (47). For the mass ablation rate, we have, at the critical density,

$$\dot{m}\approx\rho_c V_{th}\propto\frac{1}{\lambda^2}(I\lambda^2)^{1/3}\Rightarrow\dot{m}\propto\left(\frac{I}{\lambda^4}\right)^{1/3}.$$

This reproduces the scaling in Eq. (48). The scaling in Eqs. (49) and (50) follow from applying the definition of V_{abl} and V_{ex} to Eqs. (47) and (48).

For indirect drive,[117–119] we have, approximately,

$$P(\text{Mbar})_{\text{I.D.}}=3T_r^{3.5}=170I_{15}^{7/8}, \tag{51}$$

$$\dot{m}(\text{g/cm}^2/\text{s})_{\text{I.D.}}=3\times10^5T_r^3=10^7I_{15}^{3/4}. \tag{52}$$

From these two equations, we then have

$$V_{imp}(\text{cm/s})_{\text{I.D}}=10^7\sqrt{T_r}\ln\frac{m_0}{m}=1.8\times10^7I_{15}^{1/8}\ln\frac{m_0}{m}, \tag{53}$$

$$V_{abl}(\text{cm/s})_{\text{I.D}}=2.35\times10^5\beta^{3/5}T_r^{9/10} =6.6\times10^5\beta^{3/5}I_{15}^{9/40}. \tag{54}$$

These equations, which are written both in terms of the radiation temperatures T_r (in hundreds of eV, or "heV") and an equivalent intensity, are valid approximations for capsules for which the capsule ablator albedo (the ratio of the reemitted x-ray flux to the incident flux) is near zero. Because it is usually possible to choose a low-Z ablator that has sufficiently high opacity in its cold state to absorb the incident radiation but still have very low opacity in the heated blowoff region, this approximation is reasonable for much of the capsule implosion history. This approximation is valid longer for a sphere with diverging flow than for a planar sample. When the albedo of the capsule blowoff starts becoming significant, Eqs. (51)–(54) become time dependent. The exponents in Eqs. (51)–(54) also can be obtained by dimensional analysis of a simple model of the physics. We again set the incident flux equal to the pressure times the blowoff velocity at the sonic point. For radiation drive, the sonic-point temperature is proportional to the radiation drive temperature, and the incident intensity is proportional to T_r^4. Hence, we have

$$I \approx P V_{\mathrm{ex}} \propto T_r^{1/2} P \propto T_r^4$$

or

$$P \propto T_r^{3.5} \propto I^{7/8}.$$

This reproduces the scaling given in Eq. (51). From the rocket equation, we have

$$V_{\mathrm{imp}} = \frac{P}{\dot{m}} \ln \frac{m_0}{m} \approx V_{\mathrm{th}} \ln \frac{m_0}{m}.$$

Hence, we have

$$\dot{m} \approx \frac{P}{V_{\mathrm{th}}} \propto T^3 \propto I^{3/4}.$$

This reproduces the scaling given in Eq. (52). The coefficients in Eqs. (51) and (52) can be estimated analytically,[117] but the exact numerical values depend on details of the ablator and the pulse length and shape. The values given in Eqs. (51) and (52) are approximately valid for ablators chosen to minimize capsule albedo.

Subsonic ablation implosion experiments on Nova, which are described by Eqs. (51)–(54), have been very successful in the 200–300 eV radiation-temperature regime predicted to be required for laboratory capsules that would ignite and burn when driven by 1–10 MJ lasers. Figure 42 shows the experimental results and LASNEX simulations[97] for a variety of 1 ns experiments with drive temperatures between about 200 and 260 eV. The capsules had DD fuel. The shells were composed of a polystyrene microballoon, overcoated with a few micrometers of polyvinyl alcohol (PVA) as a permeation barrier. The capsules are then coated by plasma polymerization, with a carbon–hydrogen polymer CH_n with $n \sim 1.3$ (although the material is generally just referred to as CH). Within the limits of the laser and target diagnostics at the time, features such as bang time, ion temperature, and yield are well matched by calculations, and the predicted strong dependence on radiation temperature is observed. Other experiments on Nova have been used to measure implosion symmetry, fuel density and ρr, pusher ρr, and burn width. There is also a good correspondence between measured and calculated values for these quantities.

The shell IFAR, $R/\Delta R$, the ratio of the shell radius R to its thickness can be related to V_{imp}, V_{abl}, and V_{ex} by integrating the rocket equation. The work W done on the imploding fuel by the pressure P generated from ablation is given by

$$W = \int_{\mathrm{Vol.}} P \, dV.$$

Most of the work is done while the shell is still at a large fraction of its initial radius. Shell velocities typically approach their peak values by the time the shell reaches half its initial radius.

If we assume that the shell is accelerated over half its radius, we have

$$\int_0^{t_1} v \, dt = \frac{1}{2} R = \int_0^{t_1} V_{\mathrm{ex}} \ln \frac{m_0}{m} \, dt, \tag{55}$$

where

$$\ln \frac{m_1}{m_0} = \ln\left(1 - \frac{V_{\mathrm{abl}} t_1}{\Delta R}\right) = \frac{V_{\mathrm{imp}}}{V_{\mathrm{ex}}}$$

$$\Rightarrow \frac{R}{\Delta R} = 2 \frac{V_{\mathrm{ex}}}{V_{\mathrm{abl}}} f_1\left(\frac{V_{\mathrm{imp}}}{V_{\mathrm{ex}}}\right), \tag{56}$$

where $f_1(x) = [1 - (1+x)\exp(-x)]$.

In numerical simulations, $R/\Delta R$ varies in time. The maximum in $R/\Delta R$ typically occurs just as the compressed shell begins to accelerate. This maximum is not a representative value for $R/\Delta R$, because the shell has not moved very far, and the density has not relaxed to a more steady-state distribution. For most high-gain targets, a more representative value of $R/\Delta R$, for use in comparison with the analysis presented here, is the value at a time when the shell has moved about $\frac{1}{4}$ of the initial radius. At this time, the shell has moved about $\frac{1}{2}$ of the total acceleration distance and has experienced $1/\sqrt{2}$ of the total number of e-foldings of growth for constant acceleration.

For implosions in which most of the mass is ablated, or in other words, if the implosion velocity is greater than the rocket exhaust velocity V_{ex}, then f_1 is approximately linear in x. Since typical implosion velocities range from 2 to 4×10^7 cm/s, this case generally applies to radiation drive, as seen from Eq. (53), for radiation temperatures of a few hundred electron volts. We obtain, for the indirect-drive IFAR, $(R/\Delta R)_{\mathrm{I.D.}}$,

$$\left(\frac{R}{\Delta R}\right)_{\mathrm{I.D.}} \approx 0.56 \frac{V_{\mathrm{imp}}}{V_{\mathrm{abl}}}, \quad \text{for } 4 > \frac{V_{\mathrm{imp}}}{V_{\mathrm{ex}}} > 0.8. \tag{57}$$

If the implosion velocity is less than the rocket exhaust velocity, then f_1 is approximately quadratic in x. In this case, which applies to direct drive, as seen from Eq. (49) for typical implosion velocities and typical laser intensities of 10^{14}–10^{16} W/cm^2, the relationship between the shell IFAR, $(R/\Delta R)_{\mathrm{D.D.}}$ and the rocket parameters is somewhat more complex:

$$\left(\frac{R}{\Delta R}\right)_{\mathrm{D.D.}} = 0.70 \frac{V_{\mathrm{imp}}^2}{V_{\mathrm{abl}} V_{\mathrm{ex}}}, \quad \text{for } 0.8 > \frac{V_{\mathrm{imp}}}{V_{\mathrm{ex}}} > 0.1. \tag{58}$$

Equation (58) can be rewritten in a way that makes the physics clearer. By definition, $V_{\mathrm{abl}} = \dot{m}/\rho$. From the rocket equation, we have $P/\dot{m} = V_{\mathrm{ex}}$. Combining these two, we have

$$\frac{R}{\Delta R} \approx 0.7 \frac{\rho V_{\mathrm{imp}}^2}{P}.$$

Essentially this same result can be obtained from a simple model for implosion of a shell without ablation. If we apply a constant pressure to a shell with enclosed volume V, then the work done is just PV. If we set this work equal to the kinetic energy given to a shell of thickness Δr and density ρ, we have

$$PV=P\frac{4\pi}{3}R^3=\frac{1}{2}MV_{\rm imp}^2=\frac{1}{2}4\pi\rho R^2\,\Delta R\,V_{\rm imp}^2$$

or

$$\frac{R}{\Delta R}=\frac{3}{2}\frac{\rho V^2}{P}.$$

To within a factor of 2, this is the same as Eq. (58).

Equations (57) and (58) were obtained by assuming an ice block model for the shell density (constant density across the entire shell thickness). In an actual ICF capsule, pressure and density gradients are necessary for the shell to have a uniform acceleration. Within the accelerating shell, we have

$$\rho a=\nabla P=\frac{dP}{dr}. \tag{59}$$

If the material across the shell has constant entropy, we can use $P_{\rm DT}$ (Mbar)$=2\beta\rho^{5/3}$ (g/cm^3) from Eq. (35) to obtain

$$\frac{d}{dr}\rho^{2/3}=\text{const.} \tag{60}$$

With the boundary conditions $\rho=\rho_0$ at $r=0$ and $\int\rho\,dr=\rho_0\,\Delta R$, we obtain

$$\frac{\rho}{\rho_0}=\left(1-\frac{2}{5}\frac{r}{\Delta r}\right)^{3/2}, \tag{61}$$

where ρ_0 is the peak density in the shell. The shell thickness is usually defined as the distance between densities that are $1/e$ times the peak density. From Eq. (61), this is about $1.2\times$ that of the ice block model.

In general, radiation-driven implosions can be described as high-ablation-rate, low-exhaust-velocity implosions. This results in significant benefits for hydrodynamic stability. Direct-drive implosions are high-exhaust-velocity, low-ablation-rate implosions. In principle, this allows implosions with higher implosion velocity than is the case for radiation drive. For a particular velocity, it is instructive to compare Eqs. (57) and (58). At a velocity of 3×10^7 cm/s, we use Eq. (53) to obtain the following from Eq. (57):

$$\left(\frac{R}{\Delta R}\right)_{\rm I.D.}=\frac{21(V_{\rm imp}/3\times10^7)}{\beta^{3/5}I^{9/40}}=\frac{59(V_{\rm imp}/3\times10^7)}{\beta^{3/5}T_r^{9/10}}. \tag{62}$$

Using Eqs. (49) and (50) in Eq. (58), we obtain

$$\left(\frac{R}{\Delta R}\right)_{\rm D.D.}=\frac{80(V_{\rm imp}/3)^2}{\beta^{3/5}(I_{15}/\lambda)^{4/15}}=\frac{60(V_{\rm imp}/3\times10^7)^2}{\beta^{3/5}I_{15}^{4/15}},$$

$$\lambda=\frac{1}{3}\,\mu\text{m}. \tag{63}$$

These IFARs have been adjusted by a factor of 1.2 to account for the fact that the shell density is not a constant, as discussed above.

The IFAR scales quadratically with velocity for direct drive versus the linear relationship for indirect drive. If we choose $\frac{1}{3}\,\mu$m light for direct drive, we see that at a velocity of 3×10^7 cm/s, direct-drive shells have IFARs about a factor of 3 higher at an incident intensity of 10^{15} W/cm^2 for a given fuel adiabat. At higher velocities, direct-drive shells have IFARs that are larger by increasing factors. The IFAR of direct-drive shells can be reduced by increasing the fuel adiabat β, which makes the shell less compressible, although this reduces the target gain and increases the ignition threshold. The IFAR also can be decreased by increasing the intensity, but there is a maximum intensity that is consistent with efficient coupling and low levels of laser-driven plasma instabilities. Optimizing these two constraints is discussed further in Sec. VI.

From Eq. (62), the achievable implosion velocity for radiation-driven capsules at fixed $R/\Delta R$ will be linearly proportional to the ablation velocity or nearly linearly proportional to the radiation temperature:

$$(V_{\rm imp})_{\rm I.D.}\approx\frac{R/\Delta R}{0.56}V_{\rm abl}=5.1\times10^5\beta^{3/5}\frac{R}{\Delta R}T_R^{0.9}$$
$$=1.4\times10^6\beta^{3/5}\frac{R}{\Delta R}I_{15}^{9/40}. \tag{64}$$

Since the minimum energy for ignition depends strongly on the achievable implosion velocity, a great benefit will be derived from operating at the highest possible hohlraum temperature and IFAR. This equation also shows that achieving an implosion velocity of 3×10^7 with an IFAR-30 Fermi-degenerate shell with $\beta=1$ for indirect drive would require a minimum drive temperature of about 200 eV.

VI. HYDRODYNAMIC INSTABILITY

In general, the RT hydrodynamic instability sets an upper limit to the value of the shell IFAR, and hence to the peak implosion velocity via Eqs. (62) and (63).

As described in Sec. II, Nuckolls' 1972 paper[1] was based on the direct-drive implosion of bare drops or shells of DT. To obtain gain at laser sizes much smaller than about 1 MJ, Nuckolls used a very optimistic model for RT instability in the presence of ablation. This model, described below, with an assumption that implosions with absorbed laser intensities approaching 10^{17} W/cm^2 would be feasible, resulted in predictions that ignition at laser energies approaching 1 kJ might be feasible. Since these early optimistic predictions are frequently cited, it is instructive to examine the original assumptions and evaluate the changes that have occurred as the experimental database and numerical modeling have improved.

As described in his 1972 paper, the dispersion relation for RT instability used by Nuckolls was one based on a model of "fire polishing" during the ablation process:

$$\gamma^2=ka-k^2\frac{P_a}{\rho}=ka(1-k\,\Delta R), \tag{65}$$

where P_a is the ablation pressure, k is the wave number, and ΔR is the shell thickness. This dispersion relation predicts that all wavelengths shorter than $2\pi\,\Delta R$ are stabilized and that the maximum number of e-foldings is approximately

$$n_{\max}=\int\gamma_{\max}\,dt\approx\frac{1}{2}\sqrt{\frac{R}{\Delta R}}, \tag{66}$$

for constant acceleration and $(1/2)at^2=R/2$.

Equations (23), (63), and (66) can be combined to obtain

$$E_{\text{capsule}}(\text{MJ})=\frac{\beta^{3/2}}{2}\left(\frac{V}{3\times10^7}\right)^{-5}\approx\left(\frac{1}{2}\right)\left(\frac{n_{\max}}{10/3}\right)^{-5}I_{15}^{-2/3}, \tag{67}$$

where a typical direct-drive coupling efficiency of 5% into the compressed fuel is assumed. A laser wavelength of $\lambda=1/3\ \mu$m was chosen for this example. This transforms the minimum driver energy for direct drive into a relationship that depends only on the maximum allowed growth of hydrodynamic instabilities and the allowed laser intensity. If we let the maximum number of e-foldings equal 6, we obtain

$$E_{\text{capsule}}(\text{kJ})=26I_{15}^{-2/3}. \tag{68}$$

If we allow a maximum intensity of 10^{17} W/cm^2, then the minimum driver energy is 1 kJ. In 1972, computers and numerical models were just becoming powerful enough to begin doing detailed evaluation of the effects of hydrodynamic instability and the limits that laser plasma instabilities would place on the allowable intensity. Early experiments indicated that, because of reduced absorption and hot electron production by plasma collective processes, laser intensities would be limited to 10^{14} to a few times 10^{15} W/cm^2, depending on the laser wavelength.

Numerical calculations provided most of the guidance for the growth of RT instability until quantitative data became available in the late 1980s and the early 1990s. By 1974, numerical calculations[50] using the LASNEX code indicated that direct-drive capsules designed for ignition and gain would have much higher instability growth rates than indicated by Eq. (66).

The dispersion relations that are most widely used today are still analytic fits to numerical simulations. A widely used formula for the growth of RT perturbations is given by

$$\gamma=\sqrt{\frac{ka}{1+kL}}-\tilde{\beta}kV_a. \tag{69}$$

In this equation, k is the mode wave number, a is the acceleration, L is the density-gradient scale length in the ablation front, and $\tilde{\beta}$ is a constant between 1 and 3. Equation (69) with $\tilde{\beta}\approx1$ was obtained in 1983 from numerical simulations for radiation-driven implosions.[120] Equation (69) also applies to direct drive[121] with $\tilde{\beta}=3$.

Although $\tilde{\beta}$ is smaller for radiation drive than for direct drive, ablation velocities at a typical intensity of 10^{15} W/cm^2 are about a factor of 10 larger for radiation drive, as seen by comparing Eqs. (50) and (54), so that the stabilizing effects of ablation are larger for radiation drive. The higher ablation rates also result in thicker shells and larger density scale lengths L for radiation-driven capsules. In optimized capsules, the ablation and density scale-length effects are about equally important stabilizing effects.

There is no simple analytical derivation of the ablation stabilization given in Eq. (69), but a simple physical model reproduces this result. The kV_a term can be understood as a simple convective effect due to the fact that RT modes are surface modes. In the absence of ablation, the amplitude η of a RT mode is given by

$$\eta=e^{\gamma_0 t}e^{-kx_0}, \tag{70}$$

where γ_0 is the growth rate in the absence of ablation and x_0 is position measured relative to the initial surface of the shell. In an ablating shell, the only material that matters to the implosion is the material inside the ablation front. The ablated material disappears beyond the sonic horizon of the shell and no longer affects the implosion. When distance into the shell is referenced relative to the ablation front x_A, Eq. (70) becomes

$$\eta=e^{\gamma_0 t}e^{-(kx_0+kV_{\text{A}}t)}=e^{(\gamma_0-kV_{\text{A}})t}e^{-kx_{\text{A}}}, \tag{71}$$

and growth is effectively reduced. In this model with a uniform density shell, it makes sense to define the ablation velocity relative to the peak density, as was done earlier. However, in an actual density profile, the RT mode will not necessarily be located near peak density. The coefficient multiplying V_{A} varies by a factor of about 2 in numerical simulations, and this could be due to variations in the position of the modes relative to the peak density. The factor of 2–3 difference between direct drive and indirect drive could also be due to this effect. A more detailed analysis will be required to better understand the differences in the dispersion relation between direct and indirect drive.

The density gradient stabilization modification of the first term in Eq. (69) also occurs because RT modes have a finite spatial extent.[122,123] If there is not a sharp density discontinuity at an interface, the effective density difference across the interface is reduced and the growth rate is reduced.

For direct drive, Eq. (69) is a generalization of another formula obtained in 1985 by Takabe *et al.*:[124]

$$\gamma=0.9\sqrt{ka}-\tilde{\beta}kV_{\text{A}}, \tag{72}$$

where $\tilde{\beta}$ varies in numerical simulations but is usually 3–4.

Equation (72) is similar to a form obtained by Bodner[125] from an analytical model of ablation, with a density discontinuity at the ablation front. Both Eqs. (69) and (72) have a far weaker form of ablation stabilization than that given by Eq. (65).

Direct-drive experiments[126,127] have now been carried out that agree with the numerical simulations and are in substantial agreement with Eq. (69), although more work needs to be done.

Nova Experiments[128–130] and calculations for indirect-drive RT instability also are in substantial agreement and are consistent with Eq. (69). Figure 43 shows a typical setup for these experiments. Data are obtained by looking at an x-ray backlighter through a sample placed near the hohlraum wall. By looking face on through a perturbed sample, using either an x-ray framing camera or an x-ray streak camera, one can observe the flow of material from thin to thick regions as an increase in the contrast in x-ray transmission through the sample. Representative data and calculations are shown in Fig. 43(a). Looking edge on to a perturbed sample, one can record the shape of the perturbations on an x-ray framing camera. Representative edge-on data and calculations are shown in Fig. 43(b). By using an x-ray streak camera and

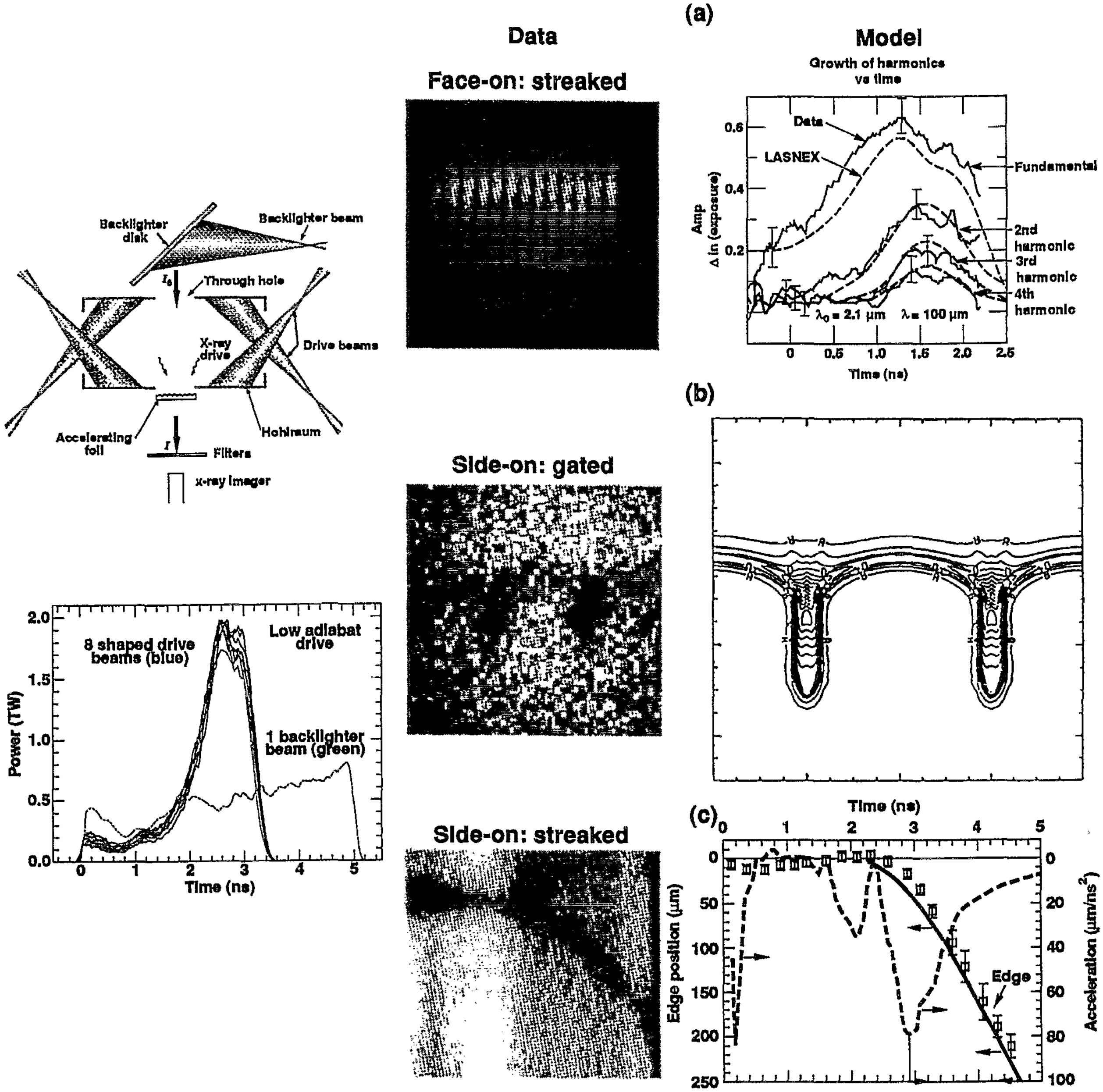

FIG. 43. Experiments[129,130] on planar targets have allowed quantitative evaluation of the growth of RT instability in the presence of radiation ablation. (a) Face-on streaked images provide a 1-D history of the time variation in the spatial distribution of the x-ray backlighter transmission through the perturbed sample. (b) Side-on gated images provide a 2-D record of the spatial distribution of the perturbed foil. (c) Side-on streaked images provide a record of the foil position as a function of time.

looking edge on, one can record sample position versus time. Representative data and calculations are shown in Fig. 43(c).

Integrating Eq. (69), the maximum number of e-foldings for direct drive is given approximately by

$$n=\int \gamma\, dt \approx \sqrt{\frac{2lx/R}{1+0.1l(\Delta R/R)}}-3l\,\frac{\Delta R}{R}\left(1-\frac{m}{m_0}\right)$$

$$\approx \sqrt{\frac{l}{1+0.1l(\Delta R/R)}}-3l\,\frac{\Delta R}{R}\left(1-\frac{m}{m_0}\right), \tag{73}$$

where $l=kR$ is the Legendre polynomial mode number. A value for the density-gradient scale length $L=0.1\ \Delta R$ has been chosen. This is near the maximum that has been achieved in calculations of direct-drive implosions designed to minimize RT instability. In doing the integral, a constant acceleration over a distance x equal to half the initial radius R is assumed. By the time the shell has moved this far, the volume inside the shell has been reduced by almost an order of magnitude, and little more PdV work can be done on the shell. As described in Sec. V, the value for ΔR in Eq. (73) is an average value of the shell thickness. In general, a value for ΔR taken from simulations at the time when the shell has accelerated to about $\frac{1}{2}$ its peak velocity, or when it has moved to about $\frac{3}{4}$ of the initial radius, is representative.

The quantity m/m_0 comes from the direct-drive rocket

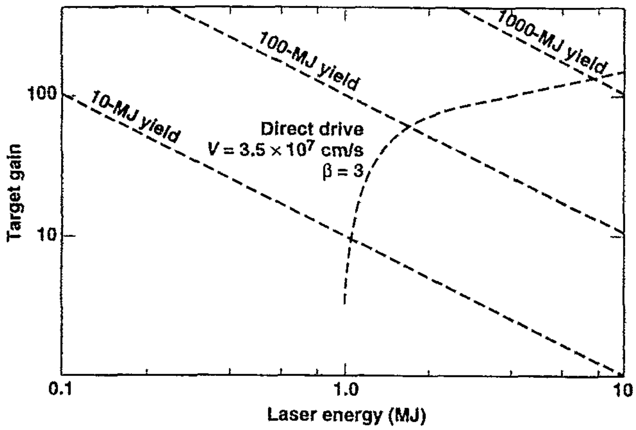

FIG. 44. Calculations[55] from the University of Rochester that constrain RT growth to 6–7 e-foldings predict about a 1 MJ threshold laser energy for direct drive.

equation, Eq. (49). For direct drive, over the range of velocities and intensities of interest to ICF,

$$\left(1-\frac{m}{m_0}\right)=1-\exp\left(\frac{-v_{\mathrm{imp}}}{v_{\mathrm{ex}}}\right)\approx 0.2\left(\frac{V}{3\times 10^7}\right)I_{15}^{-0.3}. \quad (74)$$

Using Eqs. (63) and (74) in Eq. (73) yields the approximate maximum number of e-foldings for direct drive:

$$(n_{\max})_{\mathrm{D.D.}}\approx 8.5\beta^{-2/5}\left(\frac{V}{3\times 10^7}\right)^{1.4}I_{15}^{-1/15}, \quad (75)$$

again choosing $\lambda=1/3$ μm as the laser wavelength. If this equation is combined with Eq. (23) for a 5% efficient coupling between driver and imploding fuel, the required driver energy becomes

$$E_{\mathrm{driver}}(\mathrm{MJ})_{\mathrm{D.D.}}\approx\left(\frac{1}{2}\right)\left(\frac{n_{\max}}{8.5}\right)^{-25/7}\beta^{1/14}I_{15}^{-5/21}. \quad (76)$$

Equation (76) has a much higher ignition threshold and a much weaker dependence on laser intensity than does Eq. (67) obtained from Nuckolls' more optimistic model for RT instability.

If we allow a maximum amplification of 1000 (6.9 e-foldings), then we have

$$E_{\mathrm{driver}}(\mathrm{MJ})_{\mathrm{D.D.}}\approx I_{15}^{-5/21}. \quad (77)$$

This result is consistent with recent calculations[55] at the University of Rochester, as shown in Fig. 44.

For indirect drive, Eq. (73) takes on a particularly simple form that depends only on the shell IFAR, $R/\Delta R$. Because of the relatively low exhaust velocity, most of the shell mass is ablated in indirect-drive implosions to achieve the required implosion velocity. Hence, we take $(1-m/m_0)\approx 0.8$ in the integral and obtain

$$(n_{\mathrm{I.D.}})_{\mathrm{accel}}=\int\gamma\,dt\approx\sqrt{\frac{l}{1+0.2l(\Delta R/R)}}-0.8l\,\frac{\Delta R}{R}. \quad (78)$$

A constant acceleration over half the shell radius is again assumed, and $L=0.2\ \Delta R$ has been chosen for the density gradient at the ablation front. For indirect drive, values for L typically range from 0.1 to 0.5 ΔR, depending on the ablator material and the x-ray drive spectrum. Here $L\approx 0.5\ \Delta R$ is the largest gradient scale length consistent with maintaining a given peak shell density and fuel adiabat. As in Eq. (73), ΔR in Eq. (78) is an average value of the shell thickness.

The large reduction in growth for indirect-drive capsules [for Fermi degenerate implosions with $\beta=1$ in Eq. (35)] relative to direct drive was first shown in LASNEX calculations.[58] This reduction occurs because of the high ablation rates and larger density gradients at the ablation front. From one point of view, implosions driven by soft x rays could be considered as being driven by a very short wavelength, very broadband laser that penetrates to solid density and deposits energy over a significant fraction of the shell thickness.

If we limit the maximum number of e-foldings to about six, then Eq. (78) implies that $R/\Delta R\approx 30$.

Instabilities during the deceleration phase also must be controlled. For the case of greatest interest in high-gain ICF targets, the instability during deceleration occurs between the DT hot spot, at high temperature and relatively low density, and the DT main fuel. Although electron conduction provides some ablation stabilization as the hot/cold boundary moves into the cold fuel, stabilization occurs primarily because electron conduction establishes a density gradient between the hot and cold material. This gradient is typically 0.1 to $0.2r$, where r is the final compressed radius. Without deceleration, the hot/cold interface would arrive at the origin at about ignition time, so the effective deceleration distance is about equal to the compressed radius r. If just the first term in Eq. (69) is used with $L\approx 0.2r$ and constant deceleration is assumed over a distance r, the number of e-foldings of growth during deceleration n_{decel} is given by

$$n_{\mathrm{decel}}\approx\sqrt{\frac{2l}{1+0.2l}}. \quad (79)$$

Because of the density gradient from electron conduction, growth during deceleration typically is limited to about three e-foldings over a broad spectrum of modes, as seen from Eq. (79).

The source of perturbation at the hot/cold interface can be either initial perturbations on the inside of the shell, or perturbations that feed through from the outside of the shell. The RT modes are surface modes that decrease away from the surface approximately as

$$\eta=\eta_0 e^{-k\,\Delta R}=\eta_0 e^{-l\,\Delta R/R}. \quad (80)$$

Hence, the number of e-foldings on the inner surface due to feedthrough is reduced from the number on the outer surface by

$$n_{\mathrm{feedthrough}}=-l\,\frac{\Delta R}{R}. \quad (81)$$

Because feedthrough decreases exponentially with l, it will be dominated by lower-order modes.

The combined effects of acceleration, feedthrough, and deceleration result in a total number of e-foldings of amplification of perturbations given by

$$n_{\text{accel}}+n_{\text{feedthrough}}+n_{\text{decel}}$$

$$\approx \sqrt{\frac{l}{1+0.2l(\Delta R/R)}}-1.8l(\Delta R/R)+\sqrt{\frac{2l}{1+0.2l}}. \tag{82}$$

When the effects of growth during acceleration, feedthrough, and deceleration are combined with the fact that the spectral distribution of perturbations for typical capsules falls off as l increases, the principal modes that contribute to perturbations in the fuel are spherical harmonic mode numbers less than about 30 or 40. For $R/\Delta R=30$ the number of e-foldings predicted by Eq. (82) is plotted in Fig. 48(a), which is discussed below.

Equation (82) applies to the amplification of perturbations that grow initially on the outside of the shell during acceleration. Perturbations initially present on the inside also must be taken into account. However, because the growth of these perturbations is limited by Eq. (79), their initial amplitude can be larger before they degrade performance. This does become an important consideration in specifying the cryogenic layer uniformity, as discussed in Sec. XIII.

The maximum tolerable capsule aspect ratio depends on the capsule surface finish and the spectral distribution of perturbations. The effect of a whole spectrum of modes, when all of the modes remain in the linear or only weakly nonlinear regime, can be calculated by using the theory of Haan.[131] This is the case of greatest interest with regard to high-gain ICF capsules. In this regime, the primary nonlinearity is a transition from exponential growth in time to linear growth in time for those modes that exceed an amplitude $\eta \gtrsim 2\pi/k^2L=(\lambda/kL)$. This criterion, which is valid when a full spectrum of modes is present, is a generalization of the single-mode criterion of Layzer,[132] which specifies that the transition from exponential growth to linear growth occurs when $\eta \approx 0.6/k$. The factor λ/L accounts for the number of similar modes about k that can contribute to the saturation of mode k, including a density-of-states factor with periodic boundary conditions of length L. In amplitude or physical space, this correction occurs because a wave packet with small but finite spectral width cannot be distinguished over short distances from a single mode at k. We expect saturation to occur at roughly the same amplitude in both cases, or when the amplitude of each spectral component of the multimode case is given by the Haan criterion. Except for this transition to growth linear in time, all of the modes in a full spectrum of perturbations for most single-shell high-gain ICF capsules with realistic surface finishes can be treated as growing independently. The amplitude generated by a full spectrum of modes with random phases can then be calculated by taking a root-mean-square (RMS) sum over all modes. The best estimates of these effects require the use of a large number of detailed numerical simulations to calculate the growth factors for a large number of individual modes.

For a more quantitative description of the model, we define the spherical harmonic modes as

$$R_{lm}(t)=\int d\Omega\ Y_{lm}^*(\Omega)R(\Omega,t), \tag{83}$$

where $R(\Omega,t)$ is the radius at solid angle Ω and time t, and Y_{lm}^* is the complex conjugate of the l,m spherical harmonic. Initial surface characterization is used to determine $R_{lm}(0)$. Numerical simulations of one mode at a time throughout the linear regime are used to define $R_{lm}^{\text{lin}}(t)$, the amplitude to which mode l would have grown if the evolution were entirely linear. This quantity is directly proportional to $R_{lm}(0)$, with the proportionality factor determined from the simulation. Sufficient simulations are run to interpolate to all contributing modes. Given the set of quantities $R_{lm}^{\text{lin}}(t)$, we determine if the spectrum is nonlinear by comparing $R_{lm}^{\text{lin}}(t)$ to

$$S(l)=2R/l^2, \tag{84}$$

where R is the mean radius. If any modes $R_{lm}^{\text{lin}}(t)$ have amplitude larger than $S(l)$, they are replaced with an estimated nonlinear amplitude. That is,

$$R_{lm}(t)=\begin{cases} R_{lm}^{\text{lin}}(t) & \text{if } R_{lm}^{\text{lin}}(t)<S(l), \\ S(l)\{1+\ln[R_{lm}^{\text{lin}}(t)/S(l)]\}, & \text{if } R_{lm}^{\text{lin}}(t)>S(l). \end{cases} \tag{85}$$

This construction gives growth linear in time at large amplitude, with the appropriate velocity, if $R_{lm}^{\text{lin}}(t)$ grows exponentially. The mix amplitude at any time of interest is determined from the RMS sum of the modes,

$$\sigma^2(t)=\frac{1}{4\pi}\sum_{l,m}|R_{lm}(t)|^2\approx\frac{R^2}{2\pi}\int_0^\infty k|R_{lm}|^2\,dk$$
$$=\frac{1}{4\pi}\int[R(\Omega)-R_0]^2\,d\Omega. \tag{86}$$

The bubble amplitude is taken to be $\sqrt{2}\sigma$, and the spike amplitude to be $(1+A)\sqrt{2}\sigma$, where A is the Atwood number.[74]

Haan has developed a second-order mode coupling theory[133] that can be used to determine when this approximation breaks down. This theory is in generally good agreement with initial experiments[134] that impose multiple initial modes on samples and look at the growth of sum and difference modes. These results confirm that mode coupling is not important for most cases of interest in indirect-drive ICF.

Significant progress has been made toward experimentally verifying this approach to modeling hydrodynamic instabilities and the resultant effects of a whole spectrum of modes (mix) in ICF capsules. These experiments exploit controlled variations in initial capsule roughness. Capsules can be roughened intentionally via laser ablation (early experiments described later used other techniques to vary surface roughness), and the surface can be characterized in detail with atomic force microscopy (AFM). As a function of initial surface roughness, model calculations predict observables including (1) neutron yield, ρr, as inferred from neutron measurements, and (2) spectroscopic emission from dopants in the fuel and pusher. Instability growth can be varied by changing drive profiles and ablator composition.

The results shown in Fig. 45 came from a pair of 1991 Nova experiments in which the DD fuel region was doped with argon and the polystyrene pusher was doped with chlorine.[111,112,135] One of the experiments used a "smooth" capsule, and the other used a capsule with a deliberately perturbed surface. The smooth capsule had a RMS surface

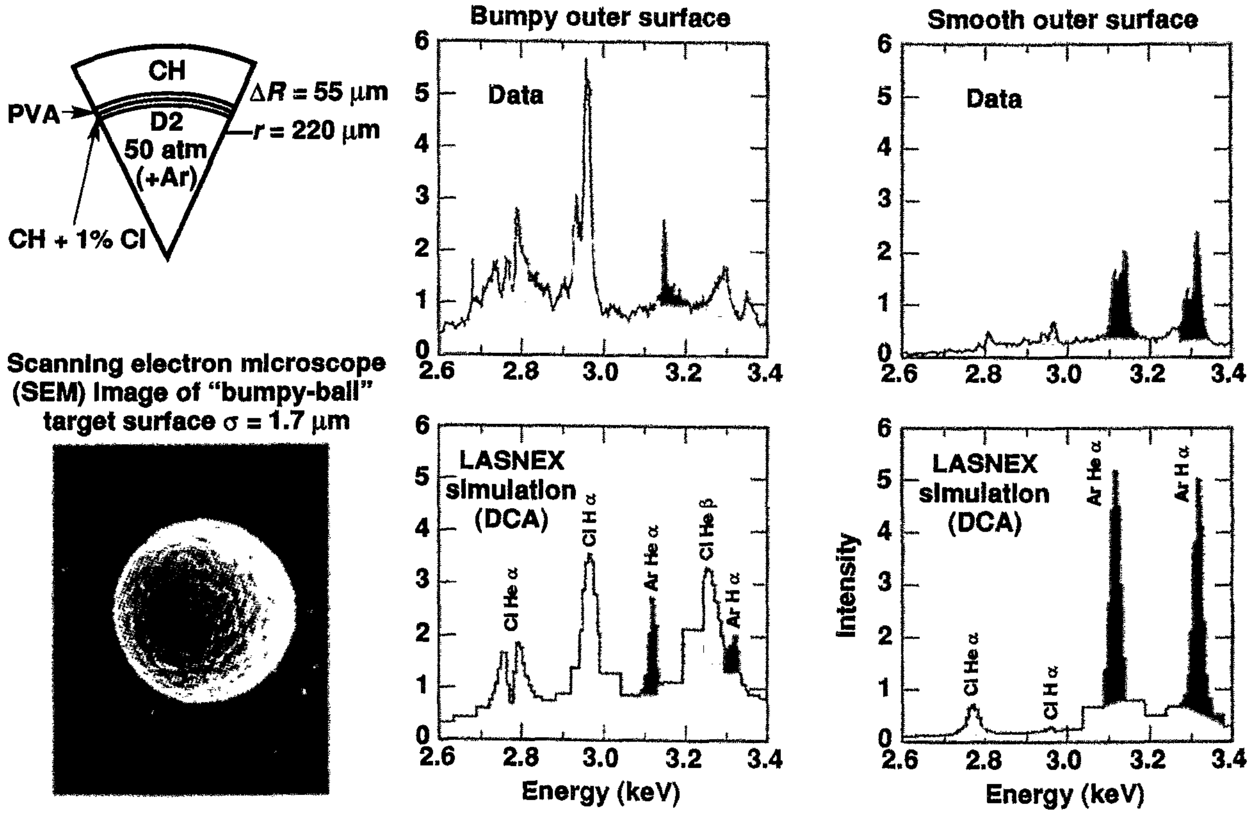

FIG. 45. Spectroscopic emission measurements[135] from smooth and bumpy-ball targets show the expected differences caused by hydrodynamic-instability-driven mix between the fuel and the surrounding pusher. Because of mix, a bumpy outer surface results in enhanced Cl emission from the pusher and reduced Ar emission from the fuel.

finish of 300–500 Å, and the rough surface had a RMS of about 1.6 μm. In this case, the rough capsule was made by coating the polystyrene mandrel with small polystyrene beads before depositing the CH ablator material. The spectroscopic signatures of the two capsules were expected to be very different. The smooth capsule was calculated to have little mix between the plastic pusher and the fuel region. In this case, the argon emission would come on early and be quite strong. Chlorine emission would be weak and would come on only later when electron conduction from the fuel region heats up the pusher. In the "bumpy ball" case, significant mix was expected, and the fuel and pusher emission would come on almost at the same time. In addition, the argon emission was weaker because the fuel was cooled by mix, and the chlorine emission was brighter because of mix. This is what is observed from a streak-camera record of the emission spectrum,[111,112] as shown in Fig. 46. More work is needed to verify that the Haan model for estimating mix in ICF capsules can be applied to ignition capsules proposed for NIF. This is the ultimate goal of the HEP experiments recommended by the NAS.

Experiments (HEP-4) are now underway on Nova that use capsules and pulse shapes (Fig. 47) that have hydrodynamic instability growth approaching that expected for NIF capsules.[136,137] These plastic capsules use bromine or germanium dopants in the ablator to suppress photon preheat and to control the density-gradient scale length at the ablation front. By varying the dopant level and pulse shape, the magnitude of instability growth can be adjusted toward that of a NIF capsule. The fuel has argon as a dopant, and the polystyrene mandrel has a titanium dopant. The variations in neutron signatures with surface roughness, as well as dopant spectroscopic signatures, can be used to quantify reduction of capsule performance due to hydrodynamic instabilities.

Figure 48(a) shows the number of e-foldings of growth, at peak burn rate for Nova and at ignition for the NIF, as a function of the spherical harmonic mode number for the HEP-4 capsule in Fig. 47 and the NIF capsule shown in Fig. 49. The simple model from Eq. (82) is a good approximation of the number of e-foldings for the modes of interest. Also shown in Fig. 48(b) for the two capsules, as a function of spherical harmonic mode number, is the running integral of the contribution to the total RMS perturbation of the capsule, using the Haan mix model and the modal amplitude spectrum shown in Fig. 48(c). Because of ablation stabilization, the effects of feedthrough, and the initial modal amplitude decrease with increasing l, only modes with $l<20$ make significant contributions to the final perturbation amplitude for these capsules.

A feature of the instability growth of all these capsules is an oscillation in the amplification as a function of spherical harmonic mode number. Oscillation of the initial shock as it propagates across the shell is largely responsible for this effect. Perturbations on the shell surface result in perturbations to the shock generated by the foot of the pulse. These perturbations are stable and oscillate as they propagate across

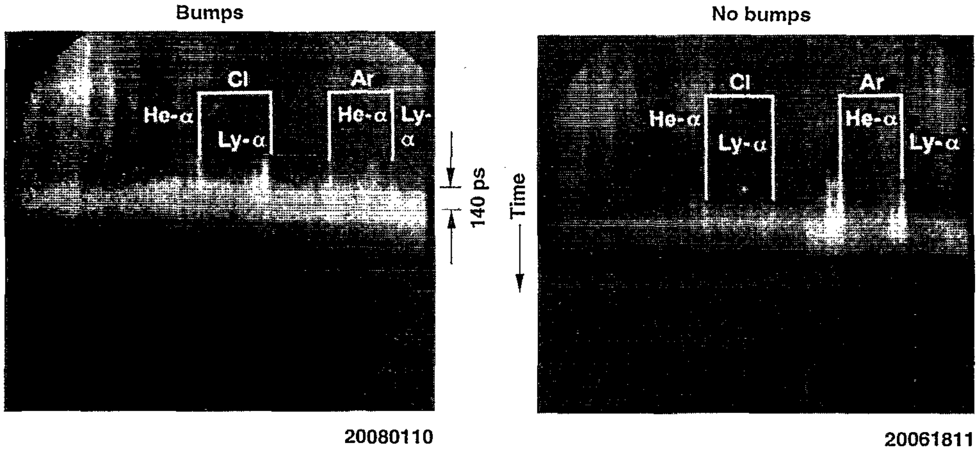

FIG. 46. Poor target surface finish increases the amount of mix, causing the Cl dopant in the ablator to heat and emit early in the compression.[111,112]

the shell. The phase of these oscillations, when the shock reaches the inner surface of the shell, depend on the shell thickness, wavelength, and shock strength. The rarefaction that propagates backward through the shell is also perturbed and has an amplitude that depends on the perturbation of the shock. When the rarefaction gets back to the ablation surface, the perturbation of the rarefaction can add to or subtract from the perturbation at the ablation front. The rapid reduction in growth of the HEP-4 capsule beyond $l=30$ is caused by this effect. Numerical calculations of amplitude versus l oscillate at larger l's than those shown in Fig. 48. This effect has recently been observed in experiments on GEKKO XII.[138]

Perturbations for the HEP-4 capsules are impressed on the capsule surface by a laser ablation process. The initial capsules have a 200–300 Å surface finish.[139] An ArF laser operating at $\lambda=0.193$ μm is then used to ablate pits on the capsule surface.[140] By controlling the size, depth, and spatial distribution of these pits, a specified spectral distribution and amplitude can be impressed on a capsule. The spectral distribution shown in Fig. 48(c) arises from a random distribution of 200 pits with a 75 μm diam Gaussian spatial profile.

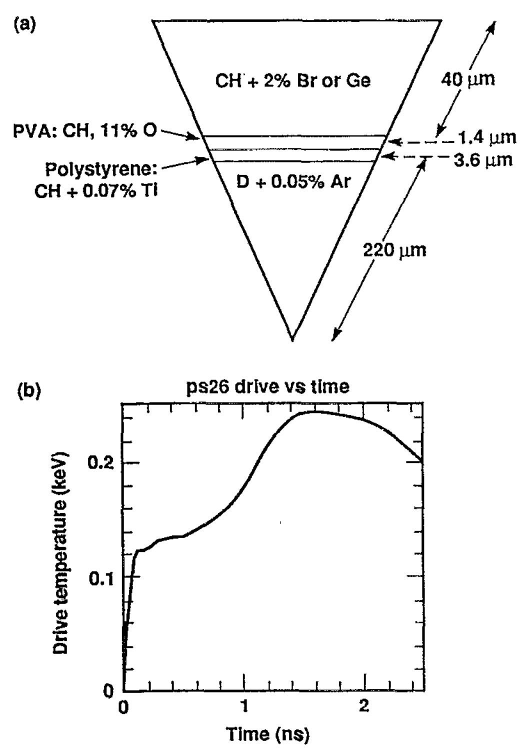

FIG. 47. (a) The HEP-4 experiments on Nova use doped ablator capsules; (b) pulse shaping (ps26) results in hydrodynamic perturbation growth (100–300) that approaches that of NIF targets.

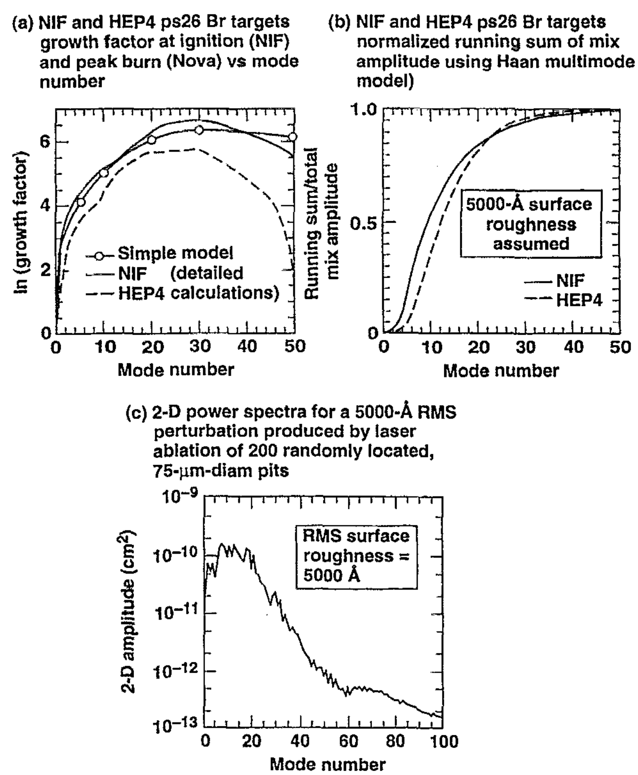

FIG. 48. Growth-factor spectrum for ps26 brominated targets compares well with NIF targets.

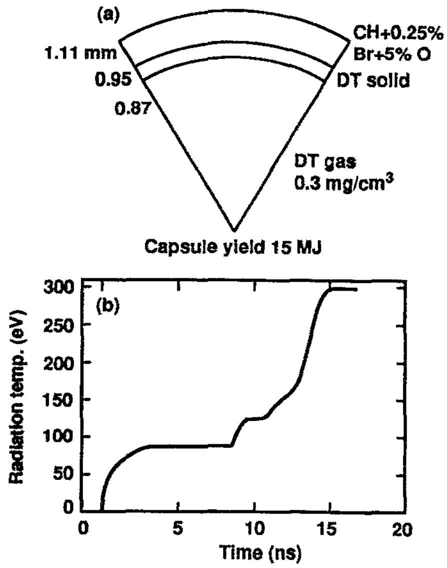

FIG. 49. The NIF baseline target absorbs 150 kJ and has robust ignition and burn-propagation characteristics: (surface finish $\leq 0.08\ \mu$m peak to valley); (b) radiation-temperature input to capsule simulations.

Figure 50 shows the yield versus RMS amplitude for capsules with this spectral distribution of perturbations. The falloff in yield with increasing perturbation amplitude is consistent with calculations using the Haan mix model. Detailed characterization of these experiments, including drive and symmetry, is still ongoing, but absolute yields are within a factor of 2–3 of that predicted from initial calculations.

Using Eq. (23) with a 15% hydroefficiency typical of indirect drive, and Eq. (64) with $R/\Delta R=30$, we obtain the minimum capsule energy:

$$E_{\text{capsule}}(\text{MJ})_{\text{I.D.}} \approx 0.035 M_{RT}\beta^{-3/2} I_{15}^{-9/8} \approx 0.045 M_{RT}\beta^{-3/2}\left(\frac{T_r}{300\ \text{eV}}\right)^{-4.5}, \tag{87}$$

$$E_{\text{laser}}(\text{MJ})_{\text{I.D.}} \approx 0.23\left(\frac{\eta}{0.15}\right) M_{RT}\beta^{-3/2} I_{15}^{-9/8} \approx 0.3\left(\frac{\eta}{0.15}\right) M_{RT}\beta^{-3/2}\left(\frac{T_r}{300\ \text{eV}}\right)^{-4.5},$$

where M_{RT} is the margin allowed for the effects of hydrodynamic instability and asymmetry in the compressed fuel volume. Equation (87) gives capsule energies very close to the projections in Nuckolls' 1972 paper, and in fact scales more favorably with intensity. Equation (87) can be compared to Eq. (77) for direct drive. If we take $M_{RT}=2$, then the minimum capsule absorbed energy is about 90 kJ, with a radiation drive temperature of 300 eV. Since 10%–15% of the driver energy can be coupled to the capsule, the minimum driver size at 300 eV is 0.6–0.9 MJ, comparable to direct drive. The baseline NIF target, shown in Fig. 49, absorbs 150 kJ. This capsule, with a velocity of 4×10^7 cm/s, can tolerate perturbations that penetrate more than 25% of the capsule radius and are 25% out of round. Below this perturbation fraction, enough hot-spot ρr remains for ignition, and the capsule gives a nearly undegraded yield.

Scaling laws for the capsule absorbed power P_{cap}, radius R_{cap}, and pulse length τ_{imp}, can be obtained using Eqs. (64) and (87). If we keep the IFAR, $R/\Delta R$, fixed, we have

$$\tau_{\text{imp}} \approx \frac{R_{\text{cap}}}{V_{\text{imp}}} \propto \frac{R_{\text{cap}}}{\beta^{3/5} T_r^{0.9}} \tag{88}$$

and

$$E_{\text{cap}} = P_{\text{cap}}\tau_{\text{imp}} \propto T_r^4 R_{\text{cap}}^2 \frac{R_{\text{cap}}}{\beta^{3/5} T_r^{0.9}} \propto \frac{T_r^{3.1}}{\beta^{3/5}} R_{\text{cap}}^3, \tag{89}$$

or

$$R_{\text{cap}} \approx \frac{\beta^{1/5} E_{\text{cap}}^{1/3}}{T_r^{1.03}}, \tag{90a}$$

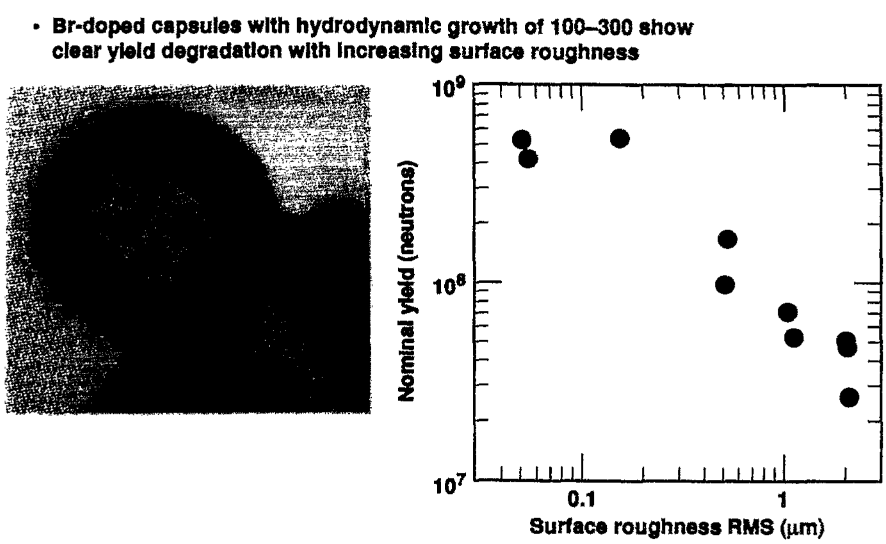

FIG. 50. Quantitative studies of implosions with large RT growth factors are now possible. For the HEP-4 capsules, surface roughness is imposed by precision laser ablation during fabrication. Precision Nova operation has dramatically reduced shot-to-shot yield variations, making these measurements possible.

$$\tau_{\rm imp} \approx \frac{E_{\rm cap}^{1/3}}{\beta^{2/5} T_r^{1.93}}, \quad (90b)$$

$$P_{\rm cap} \approx \beta^{2/5} T_r^{1.93} E^{2/3}. \quad (90c)$$

Scaled to the NIF target in Fig. 49, we have approximately

$$R_{\rm cap}({\rm cm}) = 0.65 \, \frac{\beta^{1/5} E_{\rm cap}^{1/3}}{T_r^{1.03}}, \quad (91a)$$

$$\tau_{\rm imp}({\rm ns}) = 50 \, \frac{E({\rm MJ})_{\rm cap}^{1/3}}{\beta^{2/5} T_r^{1.93}}, \quad (91b)$$

$$P_{\rm cap}({\rm TW}) = 20 \beta^{2/5} T_r^{1.93} E({\rm MJ})_{\rm cap}^{2/3}, \quad (91c)$$

where τ is the energy divided by the peak power. These quantities can be related to the laser energy if the hohlraum coupling efficiency $\eta_{\rm hohl}$ is known:

$$P_{\rm laser}({\rm TW}) = 133 \beta^{2/5} T_r^{1.93} E_{\rm cap}^{2/3} = 37.5 \beta^{2/5} T_r^{1.93} E_{\rm laser}^{2/3} \left(\frac{0.15}{\eta_{\rm hohl}} \right)^{1/3}, \quad (92)$$

$$\tau_{\rm imp}({\rm ns}) = \frac{26.5 E_{\rm laser}^{1/3}}{\beta^{2/5} T_r^{1.93}} \left(\frac{\eta_{\rm hohl}}{0.15} \right)^{1/3}. \quad (93)$$

As before, T_r is in units of 10^2 eV.

VII. CAPSULE GAIN

Equations also can be developed for the yield and gain as functions of the driver energy. The yield Y can be approximated by

$$Y \approx M_F \epsilon_{\rm T.N.} \frac{(\rho r)_F}{(\rho r)_F + 6} \approx M_F \epsilon_{\rm T.N.} \frac{(\rho r)_F}{10}, \quad (94)$$

where $\epsilon_{\rm T.N.}$ is the fusion energy per gram for DT and $(\rho r)_F$ is the areal density of the compressed fuel. The fuel mass M_F is given by

$$M_F \approx \frac{\eta_H E_{\rm cap}}{\frac{1}{2} V_{\rm imp}^2}, \quad (95)$$

where η_H is the hydrodynamic efficiency of an implosion. If we assume constant hydrodynamic efficiency and use Eq. (23), with fixed capsule adiabat, to relate $E_{\rm cap}$ and $V_{\rm imp}$, we obtain

$$M_F \propto E_{\rm cap}^{7/5}. \quad (96)$$

For the adiabatic compression of a shell of DT, we have

$$\epsilon_F = \tfrac{1}{2} V_{\rm imp}^2 = 2 \beta \rho_F^{2/3} \quad \text{or} \quad \rho_F \propto V_{\rm imp}^3, \quad (97)$$

where ϵ_F is the specific energy per gram and β is held constant.

For a sphere with mass M_F, we have

$$(\rho r)_F \propto (\rho_F^2 M_F)^{1/3} \propto E_{\rm driver}^{1/15}. \quad (98)$$

Combining Eqs. (94), (96), and (98), we obtain

$$Y \approx E_{\rm cap}^{22/15}. \quad (99)$$

This simple analysis ignores the hot spot, which typically occupies 50%–80% of the compressed radius and reduces the capsule ρr for a given compression.

Yield from LASNEX calculations scales somewhat more rapidly with energy and more closely follows

$$Y({\rm MJ}) \approx 375 E_{\rm cap}^{5/3}({\rm MJ}) = 375 \eta_{\rm hohl}^{5/3} E_{\rm laser}^{5/3}$$

or

$$\text{Gain} \approx 375 \eta_{\rm hohl}^{5/3} E_{\rm laser}^{2/3}, \quad (100)$$

where $\eta_{\rm hohl}$ is the coupling efficiency between the laser and the capsule. The two dashed lines labeled 10% and 15% in Fig. 7 use $\eta_{\rm hohl} = 10\%$ and 15%, which bracket the current NIF target designs. Issues that affect hohlraum coupling efficiency are discussed in Sec. VIII. Equation (100) holds when the capsule at each energy is imploded to a velocity equal to the minimum required to ignite for a given surface finish. This will require a minimum intensity or drive temperature at each energy, as given by Eq. (87). At any given energy, it will be possible to meet or exceed the minimum ignition velocity for all intensities or drive temperature above this minimum. For any given implosion velocity, it is possible to calculate capsule gain versus driver energy. Gain curves for indirect drive at velocities of 3×10^7 and 4×10^7 cm/s are shown in Fig. 7. These curves are calculated under the assumption of a fixed 15% hohlraum coupling efficiency of laser energy to a capsule. The shaded band at the left of each set of curves in Fig. 7 corresponds to the uncertainty in the achievable capsule surface finish. The far left edge corresponds to the gain achievable for perfectly uniform implosions. The right edge of the band corresponds to the gain for targets with surface finishes of 500–1000 Å RMS. As stated earlier, the best current Nova capsules have surface finishes of about 200–300 Å RMS. As the capsule size (or driver energy) increases, the minimum implosion velocity required to ignite a capsule decreases. If we exceed the minimum velocity at any given size, the capsules will still ignite, but there is a performance penalty for operating above the minimum velocity. The gain will drop because we will implode less mass and get less yield for a given energy. The capsules also tend to ignite earlier than optimal in the compression process. This results in reduced ρr and lower burn efficiency. Hence, the optimum strategy implies operation at the minimum implosion velocity consistent with the desired capsule size and yield. This is the strategy that follows the scaling given by Eq. (100).

VIII. HOHLRAUM COUPLING EFFICIENCY

Both the efficiency of coupling driver energy to a capsule and the physics of hohlraum symmetry are largely determined by the physics of x-ray absorption in the hohlraum wall.

In the following analysis, the hohlraum wall is approximated by a planar surface exposed to a uniform temperature of x rays, and a Lagrangian coordinate system is used for the analysis. The two independent variables are time t and a Lagrangian spatial coordinate $m = \int \rho \, dx$, which is the mass per unit area of material between the fluid particle and the surface of the hohlraum wall. Conservation of mass and momentum are given by

$$\frac{\partial U}{\partial t}=\frac{\partial v}{\partial m} \tag{101}$$

and

$$\frac{\partial v}{\partial t}=\frac{\partial P}{\partial m}, \tag{102}$$

where $U(t,m)=1/\rho$ is the specific volume, $v(t,m)$ is the fluid velocity in the rest frame of the hohlraum wall, and $P(t,m)$ is the pressure. Conservation of energy relates the heating $T\, dS$ of a fluid particle (where T is temperature and S represents specific entropy) to the thermal energy transported out of a fluid element by the energy flux F. Since $T\, dS=de+P\, dU$, where $e(t,m)$ is the internal energy per unit mass in the slab, the conservation of energy may be expressed as

$$\frac{\partial e}{\partial t}+P\frac{\partial U}{\partial t}=-\frac{\partial F}{\partial m}. \tag{103}$$

In this analysis, it is assumed that the opacity of the matter is sufficiently high that, on the time scales of interest, matter and radiation are in local thermodynamic equilibrium (LTE). More specifically, the radiation field is assumed to be nearly isotropic and of the same characteristic temperature as the matter. Although the x-ray production region, near the laser critical density, violates this assumption and must be calculated using non-LTE (NLTE) models, the hohlraum wall loss, which is at higher density and lower temperature, is near LTE conditions. The dominant heat-transport mechanism is radiation transport, and the matter is assumed to be sufficiently opaque that the diffusion approximation[141] can be used:

$$F=-\frac{4\sigma}{3K_{\mathrm{R}}}\frac{\partial T^4}{\partial m}, \tag{104}$$

where K_{R} is the Rosseland mean opacity and σ is the Stefan–Boltzmann constant.

Dimensional analysis of Eqs. (101)–(104) provides useful insight. Suppose that the source temperature, applied suddenly at $t=0$, is T_s. Let $\rho_s=1/U_s$ be the initial density of the wall, and let P_s and e_s be the pressure and energy per unit volume that the material would have if it were heated to the full source temperature T_s before it could expand to a higher specific volume than U_s.

Initially, the diffusion process described by Eqs. (103) and (104) will heat the surface of the block so rapidly that the slab material will remain stationary in comparison to the penetration speed of the heat front. When there is no hydrodynamic motion, these equations lead to a heat front that advances into the slab according to a diffusive law of the form

$$\left(\frac{m^2}{t}\right)_{\text{front}}\approx\frac{4\sigma T_s^4/3K_s}{e_s}. \tag{105}$$

The inertia of the slab material allows the pressure P_s to cause disturbances in the slab, which propagate with a sound (or shock) speed that can be estimated from Eqs. (101) and (102):

$$(m/t)_{\text{front}}\approx\sqrt{P_s\rho_s}. \tag{106}$$

At early times, the penetration speed of the thermal wave exceeds this hydrodynamic speed, but at later times, the hydrodynamic speed far exceeds the rate at which the heat wave can penetrate the wall. The critical time scale t_s at which the hydrodynamic motion begins to affect the progress of the heat front is easily estimated from the previous two relationships:

$$t_s=\left(\frac{4\sigma T_s^4}{3K_s e_s}\right)\left(\frac{1}{P_s\rho_s}\right). \tag{107}$$

The depth of the slab that has been heated at this "transition time" t_s is estimated by

$$m_s=t_s\sqrt{P_s\rho_s}. \tag{108}$$

For times $t\ll t_s$, it is safe to assume that $\rho=1/U(t,m)=\rho_s$ everywhere in the slab, which eliminates the need to solve the mass and momentum equations. (This is Marshak's "constant density" solution, which is equivalent to the classical nonlinear heat conduction problem.[142])

When $t\gg t_s$, something "in between" diffusion-wave behavior and shock-wave behavior occurs. A competition exists between Eqs. (101) and (102), which produce disturbances that propagate at constant speed, and Eqs. (103) and (104), which produce disturbances that diffusively decelerate as they progress. For example, the pressure of the heated material causes it to explode into the vacuum and decompress. If the opacity of the heated material decreases as the density drops, more of the radiation emitted by the source reaches the colder, deeper regions of the wall. Thus, the heat front can progress somewhat more rapidly than the $m\propto\sqrt{t}$ diffusive behavior, since the heated material becomes less effective at insulating the underlying unheated material. Another effect occurs if the specific energy increases with decreasing density. This means that expanding the material at constant temperature requires an energy input. This effect counteracts the effect of a drop in opacity with density.

Rosen[143] obtained an approximate similarity solution to Eqs. (101)–(104). The following analysis closely follows his solution.

First, the energy Eq. (103) is simplified by the assumption that, for slow subsonic radiation fronts, the pressure is nearly constant near the heat front. We put P inside the time derivative and deal with the enthalpy $h=e+P/\rho$. The enthalpy and Rosseland mean opacity K are then approximated by power laws of density and temperature:

$$h=h_s\left(\frac{\rho}{\rho_s}\right)^{-\epsilon}T^l \tag{109}$$

and

$$K=K_{0\mathrm{R}}\left(\frac{\rho}{\rho_s}\right)^{\mathrm{R}}T^{-n}. \tag{110}$$

As an approximate solution to the dynamics in the blowoff region, we set the density equal to that of an isothermal expansion in the blowoff region:

$$\rho=\frac{m}{C_s t}, \tag{111}$$

where the sound speed C_s is given by

$$C_s=C_0\left(\frac{\rho}{\rho_0}\right)^{-\epsilon/2} T^{l/2}. \tag{112}$$

From the definition of m, we see that the solution to Eq. (111) is $\rho=\exp(-x/C_s t)$. With these assumptions, the energy equation has similarity solutions of the form

$$m\equiv Wt^Q \tag{113}$$

and

$$T(m,t)=T_0\left(\frac{t}{t_0}\right)^P f(W), \tag{114}$$

with $f(W=0)=1$ and $f(W=\text{front})=0$ as boundary conditions. Here T_0 is the temperature at the heated surface when $t=t_0$. The parameter W provides a new coordinate system in which the temperature profile is time invariant. By a suitable choice of Q, this enables us to reduce the nonlinear differential diffusion equation for heat transport to a linear differential equation. We obtain, by substitution,

$$(lPZ+z\epsilon)f^{lz}-QW\frac{\partial}{\partial W}f^{lz}$$

$$=W^{\epsilon Z}\frac{\partial}{\partial W}\frac{D}{W^{RZ}}t^{[P\beta+r+1-Q(2+r)]}\frac{\partial}{\partial W}f^{\beta+lz}, \tag{115}$$

where

$$D=\frac{16\sigma C_0^r\rho_0^r T_0^\beta}{3K_0 h_0 t_0^{P\beta}(\beta+lZ)},$$

$$\beta\equiv n+4-l+\frac{rl}{2}, \tag{116}$$

$$Z\equiv\left(1-\frac{\epsilon}{2}\right)^{-1},$$

and

$$r\equiv Z(R-\epsilon).$$

We can eliminate the time dependence by choosing

$$Q=\frac{\beta P+1+Z(R-\epsilon)}{2+Z(R-\epsilon)}=\frac{\beta P+1+r}{2+r}. \tag{117}$$

With this choice of Q, Eq. (115) becomes

$$\frac{D}{W^r}(f^{\beta+lZ})''-\frac{ZRD}{W^{r+1}}(f^{\beta+lZ})'+QW(f^{lZ})'$$

$$-(lpZ+Z\epsilon)f^{lZ}=0. \tag{118}$$

Since W is related to the mass ablated from the surface, it increases as we move through space toward the ablation front. Near the ablation front, W will be large, R is always small, and Z and l are less than unity, so that f^{lZ} is small. We expect the gradient $(f^{lZ})'$ to be large near the wavefront, since the nonlinear radiation conductivity must result in a steep-fronted wave. Hence, we neglect the second and fourth terms of Eq. (118). Near $W=0$, we use, as a trial solution,

$$f(w)=\left[1-\left(\frac{W}{W_0}\right)^\alpha\right]^{1/\beta}, \tag{119}$$

where $\alpha=1+RZ$. Equation (118) becomes

$$\left[-\frac{D}{W^r}\frac{\beta+lZ}{\beta}\frac{\alpha}{W_0}\left(\frac{W}{W_0}\right)^{\alpha-1}+QW\right]\left\{\frac{\partial}{\partial W}\left[1-\left(\frac{W}{W_0}\right)^\alpha\right]^{lZ/\beta}\right\}$$

$$=0. \tag{120}$$

Near the front, the second term cannot be zero, because the gradient is steep. Hence, the first term must be zero. Also, near the front, $W\approx W_0$. Hence, W_0 is given by

$$W_0^{2+r}=\frac{4\sigma}{3K_0}\frac{1}{h_0}\frac{4}{Q\beta}\alpha C_0^r\rho^r\frac{T_0^\beta}{t_0^{\beta P}}, \tag{121}$$

and the mass penetrated by the radiation wave is then $m_0=W_0t^Q$,

$$\frac{\text{Loss}}{\text{Area}}=\frac{E_{wa}}{A_w}=\int_0^{m_0}(h)dm=\int_0^{m_0}h_0\left(\frac{\rho}{\rho_0}\right)^{-\epsilon}T_0^l\left(\frac{t}{t_0}\right)^{Pl}f^l(w)dm$$

$$=h_0C_0^{\epsilon Z}t^{\epsilon Z}(m_0)^{1-\epsilon Z}\left(\frac{t}{t_0}\right)^{plZ}\rho_0^{\epsilon Z}T_0^{lZ}\frac{\beta}{\beta+lZ}. \tag{122}$$

In carrying out the integral, we substituted for ρ/ρ_0 from Eq. (111) and set $m=m_0$ in the resulting term. Here E_{wa} is the energy into the hohlraum wall and A_w is the hohlraum wall area. If we do not set $m=m_0$, the right-hand side of Eq. (122) is multiplied by $(1/\alpha)\text{Beta}[(1-z\epsilon)/\alpha,\ (1+lz)/\beta]$, where $\text{Beta}(x,y)\equiv\Gamma(x)\Gamma(y)/\Gamma(x+y)$. Similar analytic solutions have been obtained by Kaiser *et al.*[144] and by numerically integrating the equation for W.[145]

To obtain specific results for gold, we use

$$K_R=6\times10^3K_0\rho^{0.3}T_{\text{heV}}^{-1.5}\ \text{cm}^2/\text{g},$$

$$h=4.2\times10^6T_{\text{heV}}^{1.6}\rho^{-0.14}\ \text{J/g}, \tag{123}$$

$$C_s=3.0\times10^6T_{\text{heV}}^{0.8}\rho^{-0.07}.$$

The Rosseland mean opacity is obtained from the super-transition-array (STA) model[146] and K_0 is an overall multiplier on the opacity. Thus, $\epsilon=0.14$, $R=0.3$, $l=1.6$, $n=1.5$, $Z=1.075$, $r=0.172$, $\beta=4.04$, and $Q=0.54+1.86P$. If these quantities are used, the energy absorbed by the hohlraum wall after a time τ is approximated by

$$E_{wa}(\text{MJ})=5.2\times10^{-3}K_0^{-0.39}(3.44P+1)^{-0.39}$$

$$\times T_0^{3.3}\tau^{0.62+3.3P}A_w, \tag{124}$$

where T_0 is the temperature at 1 ns. For a constant hohlraum temperature T_r, we have

$$E_{wa}(\text{MJ})=5.2\times10^{-3}K_0^{-0.39}T_r^{3.3}A_w\tau^{0.62}. \tag{125}$$

For a constant loss rate $\dot{E}_{wa}/A_w=S_A$, we must have $t^{-0.38+3.3P}=t^0$. Hence, $P=0.115$ and

$$(S_A)_{15}=\frac{\dot{E}_{wa}}{A_w}\ (\mathrm{MJ/cm^2/ns})=4.5\times10^{-3}T_0^{3.3}/K_0^{0.39}, \tag{126}$$

where $(S_A)_{15}$ is the absorbed flux in units of 10^{15} W/cm^2. This form for the wall loss would be appropriate, for example, for a constant-power laser pulse with a constant x-ray conversion efficiency if we ignore laser entrance hole loss. Using $T=T_0\tau^{0.115}$ and $(S_r)_{15}=0.01T^4$, we have $T^{3.3}=T_0^{3.3}\tau^{0.38}=44.7(S_R)_{15}^{0.825}$, where S_R is the flux at time τ emitted from the hohlraum wall. Hence, we can write Eq. (126) as follows:

$$(S_R)_{15}=7.0K_0^{0.47}(S_A)_{15}^{1.21}\tau(\mathrm{ns})^{0.46}. \tag{127}$$

From Eq. (127), we see that for time on the order of 1 ns and fluxes of 10^{14}–10^{15} W/cm^2, typical of ICF hohlraums, the reemitted flux from a hohlraum wall is large compared to the absorbed flux.

The mass ablated from a hohlraum wall is approximated by

$$m_0(\mathrm{g/cm^2})=1.20\times10^{-3}T^{1.86}K_0^{-0.46}\times(3.44P+1)^{-0.46}\tau^{(0.54+1.86P)}. \tag{128}$$

If we take $P=0.115$, as required for a constant loss rate, then the depth penetrated in micrometers, for gold, is given by

$$x(\mu\mathrm{m})=10^4\ m(\mathrm{g/cm^2})/\rho=0.53T_0^{1.86}\tau^{0.75}. \tag{129}$$

Thus, for time and temperature of interest to ICF, a few micrometers of wall material are heated.

To obtain the approximate hohlraum coupling efficiency, we write

$$\eta_{\mathrm{c.e.}}E_{\mathrm{laser}}=E_{wa}+E_{\mathrm{ca}}+E_h, \tag{130}$$

where $\eta_{\mathrm{c.e.}}$ is the laser-to-x-ray conversion efficiency. The LEH losses E_h and capsule absorbed energy E_{ca} are estimated by

$$E_h=10^{-2}T_r^4A_h\tau,\qquad E_{\mathrm{ca}}=10^{-2}T_r^4A_c\tau. \tag{131}$$

The assumption made here is that the capsule absorbs all of the flux incident on it. This assumption is approximately valid for times of interest to ICF capsules for suitably chosen low-Z ablators in spherical geometry. The more general case, for which the capsule will reemit a small fraction of the incident x-ray energy, is discussed below. The hohlraum wall A_w (cm^2) and entrance hole A_h (cm^2) areas used are the initial values. The capsule area A_c (cm^2) used is the initial area of the inside of the fuel layer (or the inside of the ablator if there is no fuel layer). This area is representative of the effective area during the bulk of the energy absorption. Temperature T_r (heV) is peak temperature, and the time τ (ns) used is typically the total energy divided by the peak power. For the case of constant hohlraum temperature, the ratio of the capsule absorbed energy E_{ca} to the energy delivered into the hohlraum by the driver E_{laser} is then given by[147]

$$\frac{E_{\mathrm{ca}}}{E_{\mathrm{laser}}}=\frac{\eta_{\mathrm{c.e.}}}{1+A_h/A_c+(A_w/A_c)(0.52/T^{0.7}\tau^{0.38})}=\frac{\eta_{\mathrm{c.e.}}}{1+a_h+1.625a_w/N_w}=\frac{\eta_{\mathrm{c.e.}}}{1+a_h+a_w/\tilde{N}_w}, \tag{132}$$

where a_w and a_h are the ratios of the wall or entrance hole area to the capsule area, N_w is the ratio of the wall reemission flux to the absorbed flux given by Eq. (127), and $\tilde{N}_w$ is the ratio of the energy reemitted by the wall during the pulse to the absorbed energy. Equation (132) also can be written in terms of the albedo, which is the ratio of the wall emission to the incident flux and is closely related to N_w,

$$\frac{E_{\mathrm{ca}}}{E_{\mathrm{laser}}}=\frac{\eta_{\mathrm{c.e.}}}{1+a_h+1.625a_w[(1-\alpha)/\alpha]}=\frac{\eta_{\mathrm{c.e.}}}{1+a_h+a_w[(1-\bar{\alpha})/\bar{\alpha}]}, \tag{133}$$

where α is the albedo, given by

$$\alpha=\frac{S_R}{S_R+S_A}=\frac{10^{-2}T^4}{10^{-2}T^4+\dot{E}_w}=\frac{1}{1+(0.32/T^{0.7}\tau^{0.38})}=\frac{N_w}{N_w+1}, \tag{134}$$

and $\bar{\alpha}$ is the average albedo over time τ, given by

$$\bar{\alpha}=\frac{10^{-2}T^4\tau}{10^{-2}T^4\tau+E_w}=\frac{1}{1+0.52/T^{0.7}\tau^{0.38}}. \tag{135}$$

Because the wall albedo is near unity for ICF conditions, or because the ratio of reemitted flux to absorbed flux is large, the hohlraum wall area can be much greater than the capsule and still maintain reasonable coupling efficiency.

In the more general case with finite capsule reemission E_{cr}, we can write[148]

$$E_{\mathrm{ca}}+E_{\mathrm{cr}}=(1+N_c)E_{\mathrm{ca}}=\frac{A_c}{A_w}E_{\mathrm{wr}}=\frac{N_w}{a_w}E_{wa},$$

or

$$E_{wa}=\left(\frac{1+N_c}{N_w}\right)a_wE_{\mathrm{ca}}=\frac{a_w}{n}E_{ca}, \tag{136}$$

and

$$E_h=\frac{A_h}{A_w}E_{\mathrm{wr}}=(1+N_c)a_hE_{\mathrm{ca}},$$

where N_c is the ratio of capsule reemission to capsule absorption and $n=N_w/(1+N_c)$ is the effective ratio of wall reemission to absorption.

From Eqs. (130) and (136), we obtain

$$\frac{E_{\mathrm{ca}}}{E_{\mathrm{laser}}}=\frac{\eta_{\mathrm{c.e.}}}{1+(a_w/n)+(1+N_c)a_h}. \tag{137}$$

When the capsule reemits some fraction of the incident energy, it takes longer to absorb a given amount of absorbed energy. Hence, there is more time—essentially by the ratio $(1+N_c)$—for energy to be absorbed into the wall and to leak out the LEHs.

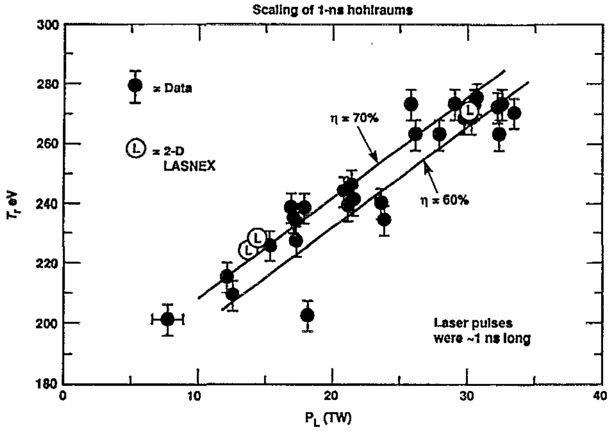

FIG. 51. Drive from gold hohlraums is in accord with 2-D LASNEX simulations.

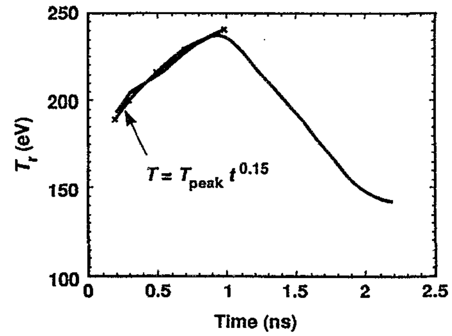

FIG. 52. Radiation-temperature profile obtained from soft x-ray diode measurements for a hohlraum driven by a 1 ns, constant-power laser pulse.

For capsules that are designed to ignite, we can relate the pulse length and temperature to the capsule energy by using Eq. (87), with a margin of 2 for hydrodynamic instabilities, and Eq. (91b). The hohlraum coupling efficiency from Eq. (132) then becomes

$$\frac{E_{\text{ca}}}{E_{\text{laser}}}=\frac{\eta_{\text{c.e.}}}{1+a_h+(a_w\beta^{0.14}/8.5E_{\text{ca}}^{0.13})}. \tag{138}$$

The coupling efficiency depends primarily on x-ray conversion efficiency, and the ratio of LEH and hohlraum wall area to capsule area. The coupling efficiency depends only weakly on capsule energy.

The LEHs must be made large enough to avoid significant absorption and refraction of the laser energy as it enters the hohlraum. The required size scales with the capsule size because the capsule size determines the pulse length. For hohlraums being investigated for ignition, the ratio of hole area to capsule area varies from about 1 to 2. The ratio of hohlraum wall area to capsule area is dictated primarily by capsule symmetry requirements, as discussed in Sec. IX. For ignition hohlraums, the ratio of case area to capsule area varies from about 15 to 30. For this range of sizes for the case and the entrance holes, Eq. (138) gives an overall coupling efficiency that varies from about 10% to 20% if the x-ray conversion efficiency is about 70%. Symmetry issues that affect the choice of hohlraum size are discussed in Sec. IX.

Figure 51 shows the experimentally measured and calculated hohlraum temperatures as functions of laser power for a series of experiments on Nova.[149] These experiments used a hohlraum that was 1600 μm in diameter and 2550 μm long with LEH diameters equal to half the diameter. This is a standard scale-1 Nova hohlraum. The data are from experiments conducted over several years and are for constant-power, 1 ns pulses. The temperatures plotted were obtained from aluminum witness-plate measurements. Temperatures were obtained from shock-velocity measurements similar to those in the pulse-shaping discussion. These are incident flux temperatures that are higher than temperatures that would be inferred from looking through a hole in the hohlraum at wall reemission away from the laser spots. The witness plate looks at both the hot laser source regions and the cooler reemitting wall. The incident flux temperature, T_I, can be related to the reemission flux temperature, T_R, from the definition of the albedo in Eq. (134):

$$T_I=\frac{(S_R+S_A)^{1/4}}{(0.01)^{1/4}}=\frac{T_R}{\alpha^{1/4}}=T_R\left(1+\frac{0.32}{T_R^{0.7}\tau^{0.38}}\right)^{1/4}$$

$$\approx T_R+0.08\,\frac{T_R^{0.3}}{\tau^{0.38}}. \tag{139}$$

This correction is a weak function of the reemitted temperature. For 1 ns pulses, the source temperature is about 10 eV higher than the re-emission temperature for most cases of interest.

Equations (125), (130), and (131) can be used to calculate the expected hohlraum temperatures for the Nova experiments. The solid lines in Fig. 51 are for constant x-ray conversion efficiencies, $\eta_{\text{c.e}}$, of 60% and 70%. Also shown are the results of detailed numerical calculations.

The experimentally measured hohlraum temperature time history—shown in Fig. 52 for a typical 1 ns, constant-power pulse in a gold hohlraum—implies an x-ray conversion efficiency that increases with time during the pulse. If we assume that

$$\eta_{\text{c.e}}=0.70\,\tau(\text{ns})^{0.12}, \tag{140}$$

and use this in Eq. (124), we obtain $P=0.15$ or $T=T_0t^{0.15}$, where T_0 is the temperature at 1 ns. As shown in Fig. 52, this gives a good fit to the measured hohlraum temperature-versus-time profile. The temperature history in Fig. 52 is a wall reemission temperature obtained by using the Dante[150] x-ray diode array to measure x rays emitted from a diagnostic hole. As shown in Fig. 53, detailed numerical calculations also predict an x-ray conversion efficiency that increases with time. Equation (140), which is consistent with the numerical model results for a 1 ns pulse, is also plotted in Fig. 53.

The analysis used for Eq. (132) can be generalized for hohlraums with more complex geometric structure.[151] The single temperature analysis of Eq. (132) applies to hohlraums that have a single chamber containing all x-ray sources and sinks. More complex multichambered geometries, such as those shown in Fig. 54, frequently are used in ICF experiments. In the two chambered geometries shown in Fig. 54,

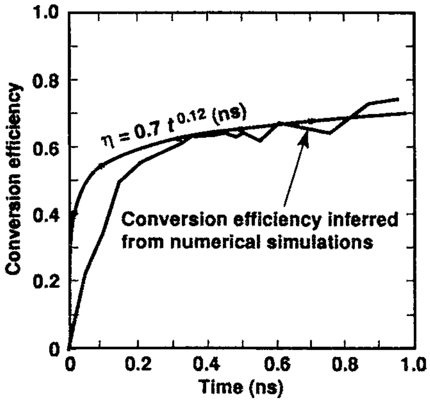

FIG. 53. The conversion efficiency η inferred from hohlraum simulations is consistent with η derived from T_r and wall loss measurements.

we define a production or primary chamber (p), and a sink or secondary chamber (s). Although both chambers generally can have both sources and sinks, the p chamber is defined to be the chamber with the dominant source of energy, such that net energy flow is from p to s so that s has the lower temperature. Because the internal structure in these hohlraums significantly retards radiation flow between chambers, it is necessary to describe these more complex geometries with two temperatures T_p and T_s.

Both hohlraums in Fig. 54 have more surface area, because of the internal baffles, than would an empty hohlraum of the same size. Since the baffles absorb energy, one might conclude that the capsule in both cases would see a lower temperature. This is true for the hohlraum in Fig. 54(b). In this case, the capsule is in the sink chamber. The added heat loss of the baffles plus the reduced x-ray transport result in a lower temperature at the capsule.

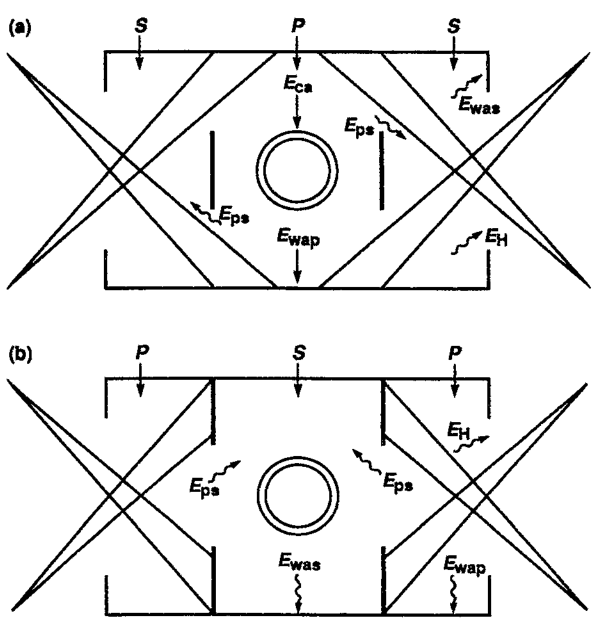

FIG. 54. A multichambered hohlraum can be described as having a production chamber (P) and a sink chamber (S). In (a) the capsule is in the x-ray production chamber, where the light is absorbed. In (b) the capsule is in the sink chamber, which is separated from the laser absorption and x-ray production chamber by baffles.

In the hohlraum in Fig. 54(a), however, the capsule is in the x-ray production chamber. Although the baffles absorb energy, they also retard energy transport to the sink chamber, which acts to increase the temperature of the production chamber. This effect can more than compensate for the added heat capacity of the baffles.

To be more quantitative in this case, we write the energy balance equation for the production and sink regions as

$$\eta E_{lp} = E_{wap} + E_{ps} + E_{\mathrm{ca}} \tag{141}$$

and

$$\eta E_{ls} + E_{ps} = E_{was} + E_h, \tag{142}$$

where E_{ca} and E_h are the capsule and LEH energies, respectively, and are given by Eq. (131) for a constant temperature. Here E_{was} and E_{wap} are the sink and production wall energies, which are given by Eq. (125) for constant temperature with $T_r = T_s$ in the sink chamber and $T_r = T_p$ in the production chamber. Here E_{ps} is the energy transported from the production chamber to the secondary and, for constant temperature, is approximated by

$$E_{ps} = 10^{-2} A_{ps} (T_p^4 - T_s^4), \tag{143}$$

where A_{ps} is the area of the transport opening between the production and sink chamber. The x-ray conversion efficiency is given by η as before. Here E_{lp} is the laser energy deposited in the production chamber and E_{ls} is the laser energy deposited in the sink chamber. If the radiation temperature is not constant, then the energy terms must be calculated as integrals over the time history, as in the example below.

Hohlraums such as that shown in Fig. 54(a), which have been referred to as "shimmed hohlraums," have been fielded on Nova as part of the hohlraum symmetry studies. Figure 78 in Sec. IX shows the results of such an experiment. Without the shims, Nova hohlraums of this size, irradiated with 20 KJ of light in a constant-power, 1 ns pulse, achieve peak drive temperatures of about 230 eV. With the shims, the primary chamber reaches a temperature of 240 eV, and the capsules systematically have a yield that is about a factor of 2 higher.[152] The following solution to Eqs. (141) and (142) below for this specific example reproduces this result.

The cylindrical hohlraum in Fig. 78 has a radius of 0.8 mm, a LEH 0.6 mm in radius, and a length of 2.3 mm. The shims are 0.325 mm in radius and are placed on axis 0.65 mm from the hohlraum midplane. The capsule radius is 0.275 mm. Thus, the area of the primary walls (A_p), from shim to shim along the hohlraum wall, including the shim disk area, is 0.072 cm^2, the area of the two secondary chambers (A_s) is 0.074 cm^2, the capsule area (A_c) is 0.0094 cm^2, and each LEH area (A_h) is 0.009 cm^2. About 20% of the laser energy (E_s) is deposited along the cylinder wall between the axial position of the shim and the end of the hohlraum. The other 80% of the laser energy is E_p. We use η=0.7, as discussed in Fig. 51.

As discussed in Fig. 52, for a constant-power, 1 ns pulse, the hohlraum temperature increases in time as $T=T_0(t/t_0)^{0.15}$, so that

$$E_h=10^{-2}A_h\int_0^t\left[T_s\left(\frac{t}{t_0}\right)^{0.15}\right]^4 dt$$

$$=6.25\times10^{-3}A_hT_s^4\left(\frac{t^{1.4}}{t_0}\right). \quad (144)$$

In Eq. (144), T_s is the temperature of the secondary region at a time $t_0=1$ ns. Also, since the pulse is 1 ns long, the last term is unity, and we have

$$E_h=6.25\times10^{-3}A_hT_s^4. \quad (145)$$

Similarly, we have

$$E_{\rm ca}=6.25\times10^{-3}A_cT_p^4 \quad (146)$$

and

$$E_{ps}=6.25\times10^{-3}A_{ps}(T_p^4-T_s^4). \quad (147)$$

The primary and secondary chamber wall losses, from Eq. (124) with $P=0.15$, are given by

$$E_{wap}=4.4\times10^{-3}A_pT_p^{3.3}\left(\frac{t}{t_0}\right)^{1.12}=4.4\times10^{-3}A_pT_p^{3.3} \quad (148)$$

and

$$E_{was}=4.4\times10^{-3}A_sT_s^{3.3}. \quad (149)$$

If we define $T_s/T_p=y$, we can write Eqs. (141) and (142) as

$$\eta E_{ls}=4.4\times10^{-3}A_pT_p^{3.3}+6.25\times10^{-3}A_{ps}T_p^4(1-y^4)$$
$$+6.25\times10^{-3}A_cT_p^4 \quad (150)$$

and

$$\eta E_{ls}+6.25\times10^{-3}A_{ps}(1-y^4)$$
$$=4.4\times10^{-3}A_sT_p^{3.3}y^{3.3}+6.25\times10^{-3}A_hT_p^4y^4. \quad (151)$$

By adding Eqs. (150) and (151), we obtain

$$\eta E_1=\eta(E_{lp}+E_{ls})$$
$$=4.4\times10^{-3}A_p[1+(A_s/A_p)y^{3.3}]T_p^{3.3}$$
$$+6.25\times10^{-3}A_c[1+(A_h/A_c)y^4]. \quad (152)$$

Inserting the values of the areas and energies into Eqs. (151) and (152) gives

$$140=3.2T_p^{3.3}(1+y^{3.3})+0.6T_p^4(1+1.9y^4) \quad (153)$$

and

$$28=2.14T_p^4(1-y^4)=3.2T_p^{3.3}y^{3.3}+0.57T_p^4y^4. \quad (154)$$

Equations (153) and (154) can be solved iteratively to give $T_p=242$ eV and $y=0.87$ or $T_s=211$ eV.

For simple geometry with no shims, we use Eq. (130):

$$\eta E_1=4.4\times10^{-3}A_wT^{3.3}+6.25\times10^{-3}A_hT^4$$
$$+6.25\times10^{-3}A_cT^4. \quad (155)$$

With the total hohlraum wall area $A_w=0.134$ cm^2 and A_h and A_c the same as above, we obtain

$$140=5.9T^{3.3}+0.86T^4, \quad (156)$$

which yields the solution $T=230$ eV.

These calculations show that, although the shims absorb about 500 J of x rays, the primary chamber of the shimmed hohlraum in Fig. 78 is expected to be about 10 eV hotter than the unshimmed hohlraum, as seen experimentally and in more detailed LASNEX hohlraums. This occurs because the shine shield restricts radiation flow to the secondary chambers, which are 30 eV colder than the primary chamber. Because of this effect, the flux onto the capsule in the shimmed hohlraum is increased by $(242)^4/(230)^4=1.225$. In other words, the shimmed hohlraum is 22.5% more energy efficient than is the unshimmed hohlraum. Although ignition target designs (discussed in Sec. XIII) have not yet used such shimmed hohlraums, they also, in principle, provide a means of increasing the coupling efficiency to the capsule at this scale.

Since the hohlraum temperature depends on both the x-ray conversion efficiency and the hohlraum wall loss, we need an independent measurement of the wall loss in order to be confident of both elements of the hohlraum energetics model. Two independent tests of the hohlraum wall loss have been obtained in Nova experiments. In one technique,[153] a thin patch of gold is placed on the wall of the hohlraum. The burnthrough time of soft x rays is a measure of the wall loss, which scales approximately as $(K_0)^{-0.47}$ from Eq. (128). A second, less sensitive technique, uses a wedge of gold or a series of gold steps of different thicknesses placed in the wall of the hohlraum. The shock velocity generated in the gold is approximately proportional to $(K_0)^{-0.25}$. Both techniques have been used on Nova.

Figure 55 shows the results of Nova experiments[154,155] using a thin gold patch that has 1, 2, and 3 μm thick sections and an open hole. Emission through the open hole tracks the laser pulse while emission from the gold patch is delayed. The analytical results plotted in Fig. 55 use $P=0.15$, as discussed previously, in Eq. (128). The predicted burnthrough rate is slightly greater than observed, corresponding to about a 10 eV temperature difference. Also shown are the results of detailed numerical simulations, which accurately match the observed burnthrough rate.

Hohlraum temperatures have proven to be reproducible at the major indirect-drive experimental facilities. Figure 56 is a plot of hohlraum temperature versus P_L/A_w for experiments from GEKKO XII,[27] Phebus,[28] and Nova.[149] Here P_L is the laser power. The line is $T^{3.3}$ from the scaling in Eq. (126).

The x-ray conversion efficiency in hohlraums for pulses 1 ns or longer is, in general, significantly greater than that measured on flat high-Z disks in open geometry.[156] Figure 57 shows the x-ray conversion efficiency for a flat disk measured on Nova for 1 ns pulses. For intensities of a few times 10^{14} W/cm^2 to about 10^{15} W/cm^2 (the intensities on the hohlraum wall for the data in Fig. 51), the x-ray conversion on disks is clearly lower than for hohlraums and is more intensity sensitive. On a gold-coated sphere illuminated with the

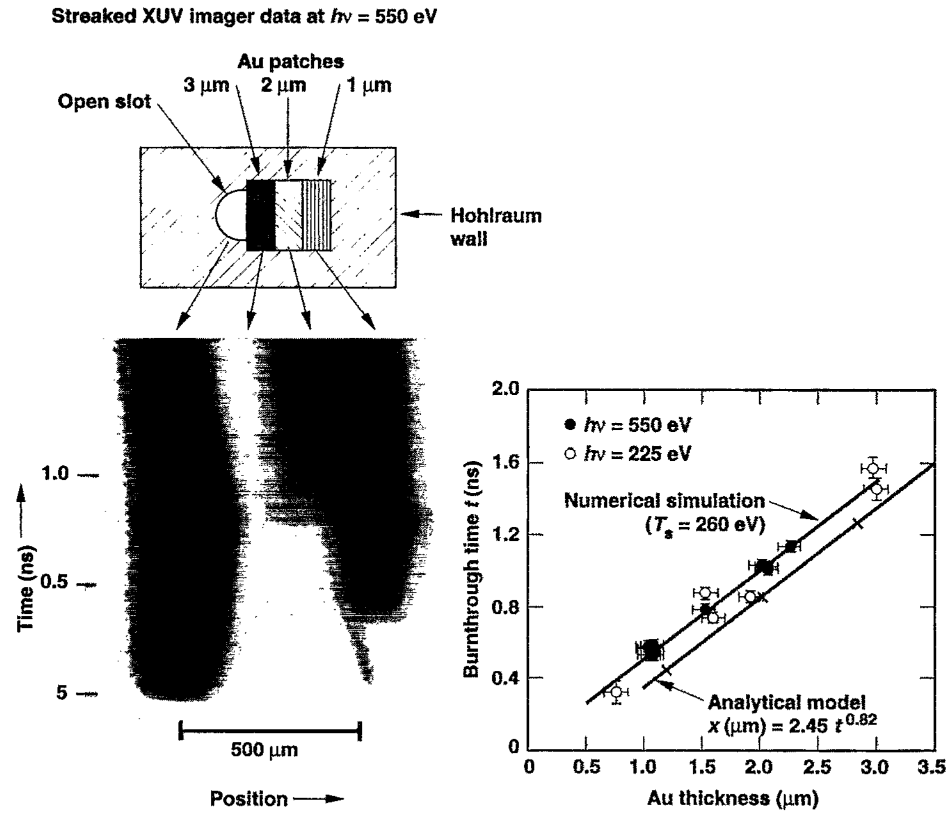

FIG. 55. The radiation-wave burnthrough measurements in thin gold foils agree well with numerical simulations and analytical models.

24 beams of the Omega laser, conversion efficiencies comparable to those in a hohlraum were obtained,[157] as indicated in Fig. 57. When only six beams from Omega were focused onto a sphere, a conversion efficiency comparable to those seen on Nova flat targets was obtained. These results in open geometry are not well understood theoretically. Although the results obtained in hohlraums are calculated accurately over a fairly wide range of conditions, the inability to predict the results accurately from open-geometry experiments is a continuation of the historical difficulty of calculating the conditions in laser-irradiated, low-Z disks.[158]

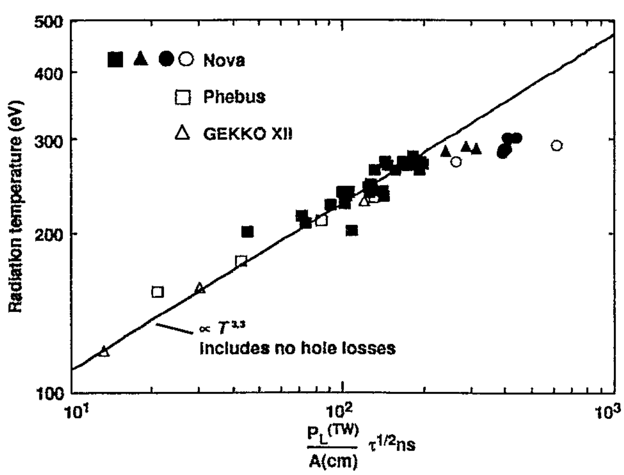

FIG. 56. Submicrometer-laser-wavelength hohlraum drive experiments from various facilities show general agreement.

The soft x-ray emission region around a laser spot in a hohlraum becomes significantly larger than the incident spot during the laser pulse, as shown in Fig. 58. These data are taken by cutting a slot in the hohlraum and imaging the soft x-ray emission around a laser spot on the opposite wall[159] with a soft x-ray framing camera (SXRFC).[160] The SXRFC can take four frames in each of three different x-ray energy channels. Figure 58 shows the spot size measured at energies of 450 and 1200 eV. The data shown are from three shots with nominally the same conditions. A typical error bar on the spot-size measurements is 20%–30%, based on uncertainty in film calibration and the flat-field response of the instrument. As shown in Fig. 58, postprocessed calculations of the emission spot size in hohlraums are consistent with the observed size increase. This increase in size is not seen for a 1 ns pulse in open geometry. Experimentally, the open-geometry data are taken simultaneously with the hohlraum data by focusing one of the laser beams on the outside of the hohlraum. The brightnesses of the laser spot outside the hohlraum and the hohlraum laser spot are roughly equal, so that the increase in hohlraum x-ray conversion efficiency is consistent with this increase in the x-ray emission region.

Experiments by Sigel *et al.*[161] at 300 ps did not show this increase in conversion efficiency relative to disk measurements. Figure 59 shows the reemitted flux from their spherical cavity experiments (obtained from x-ray emission through a diagnostic hole) versus the source flux (based on disk measurements) in the hohlraum. The theoretically predicted reemitted flux, as shown, is consistent with the disk

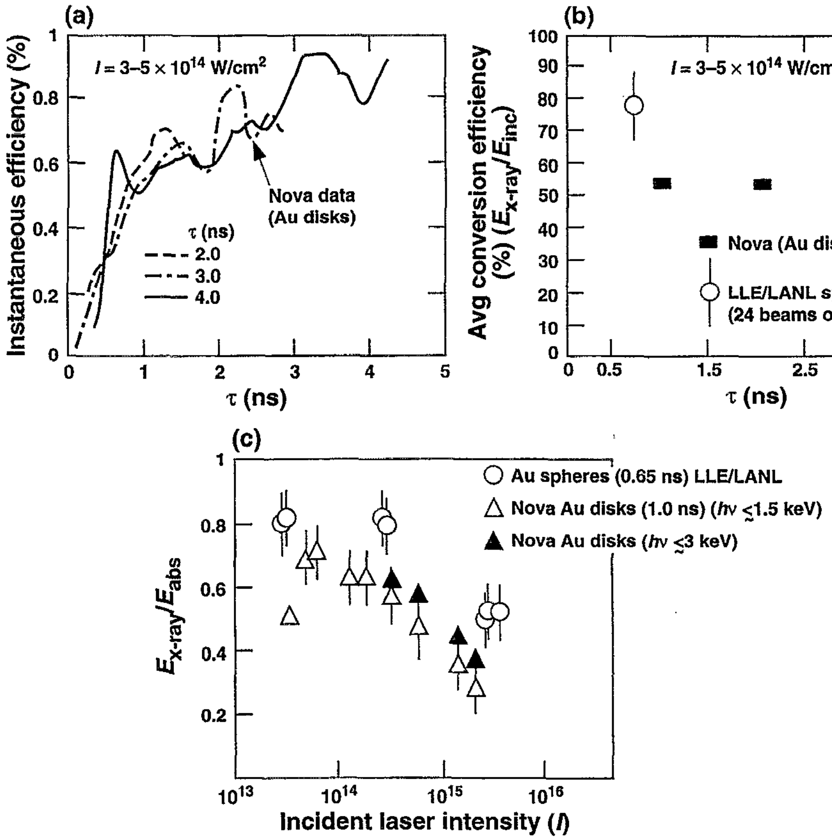

FIG. 57. Time-resolved and time-integrated x-ray measurements from open-geometry experiments show an increase in x-ray conversion efficiency with increasing laser pulsewidth and a decrease with increasing intensity.

conversion efficiency and not with a much higher efficiency. The equivalent Nova experiments have not been done.

It is difficult to obtain drive measurements to an absolute accuracy better than about 10 eV or 15%–20% in x-ray flux. First, the x-ray diodes of the Dante system are calibrated only to an accuracy of about 20%, and the Dante measurements are subject to diagnostic hole closure, which is difficult to fully account for. Also, because of the current placement technique in the hohlraum wall, there are geometric shadowing effects on the witness plate, which can reduce the apparent temperature.

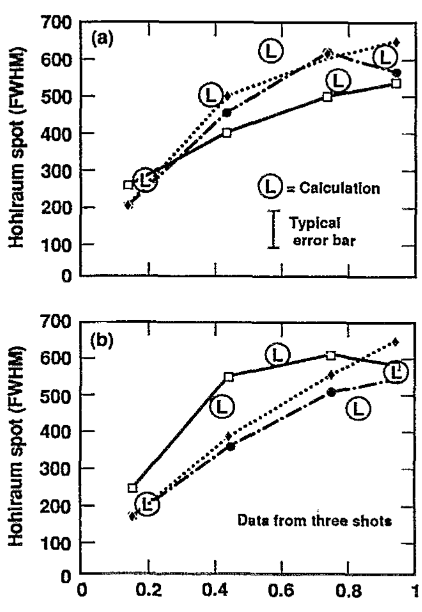

FIG. 58. Data and postprocessed calculations (circled L) indicate that x-ray source size in hohlraums increases with time: (a) spot size at 452 eV; (b) spot size at 1200 eV.

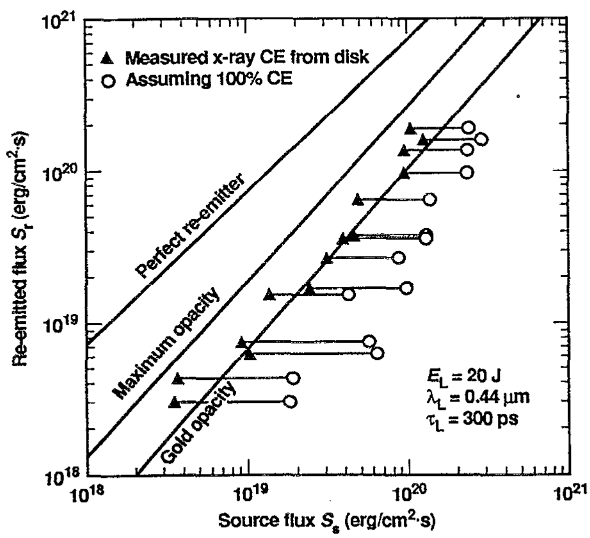

FIG. 59. Experiments at Garching with low energy and short pulses do not see significant enhancement of x-ray production in hohlraums compared to open-geometry measurements.

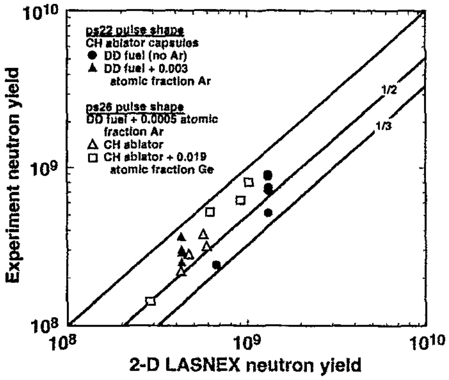

FIG. 60. Experimental yields for pulse-shaped implosions are one-half to one-third those predicted by current 2-D LASNEX calculations.

Because capsule yields are sensitive to the drive, they provide additional data for evaluating drive. Figure 60 compares the measured to calculated yields for the ps22 symmetry experiments discussed in Sec. IX and the ps26 implosion experiments shown in Fig. 47. The observed yields are about a factor of 2 lower than calculated, which is consistent with about a 10 eV lower temperature[162] or to 15%–20% lower flux if the discrepancy is entirely the result of reduced drive. The calculations were integrated, two-dimensional (2-D) hohlraum calculations that included the capsule, so the effects of flux asymmetry discussed in Sec. IX are included. Detailed mix calculations do not predict any significant yield reductions from hydrodynamic instabilities for these experiments, but it is possible that the yield reduction is coming from some effect other than drive. For example, Nova, with only five beams in each ring of beams, has a five-fold azimuthal asymmetry, which is a three-dimensional (3-D) effect, and cannot be included in 2-D calculations. Also, residual random pointing and power variations between beams result in 3-D perturbations, which are not calculated. ICF3D,[163] a new code currently being developed for ICF applications, will be able to address issues such as these in three dimensions. Experiments are currently being conducted to better quantify the drive.

Most current calculations do not include the effects of self-generated magnetic fields. Although energy transport in hohlraums is dominated by radiation, magnetic field effects in the vicinity of the laser absorption could affect x-ray production. The importance of self-generated magnetic fields in hohlraum plasmas is complex both theoretically and experimentally. Theoretically, simple scaling arguments can produce fields on the order of a megagauss (MG). Megagauss fields have been observed in open-geometry experiments.[164] However, magnetic fields are affected by several source and loss terms of comparable importance, which vary differently in different parts of the plasmas. Consequently, it is not clear from scaling arguments alone where these fields are in relation to the regions of large heat flux or radiation generation.

The emission spot-size data and calculations in Fig. 58 for pure gold hohlraums on Nova show agreement without including magnetic fields. In symmetry experiments discussed in Sec. IX, using hohlraums filled with a variety of gases showed that, except for a time delay compared to pure gold, the x-ray hot-spot image size and the contrast ratio of the hot spot to the background wall depended only weakly on hohlraum fill.[165] Hence, the potential effects of self-generated magnetic fields on the laser spot are not readily evident in Nova experiments. However, it is valuable to estimate the potential importance of magnetic fields for NIF targets.

In LASNEX calculations, it is possible to include the effects of magnetic fields by including the Braginskii transport coefficients[166–168] and the magnetic induction equation. The equation for the magnetic field B used in LASNEX is given by[169]

$$\frac{\partial B}{\partial t}=\nabla\times\left[V\times B+\frac{c}{en_e}\left(\nabla P_e-\frac{J\times B}{c}-R\right)\right], \tag{157}$$

$$J=\frac{c}{4\pi}\nabla\times B, \tag{158}$$

$$R=\frac{1}{en_e}(\alpha_\perp J_\perp+\alpha_\wedge J\times b)+\beta_\perp\nabla_\perp T_e+\beta_\wedge b\times\nabla T_e. \tag{159}$$

If we just consider the $\nabla\times(1/n)\nabla P$ source term, we have

$$\frac{\partial B(\mathrm{MG})}{\partial t(\mathrm{ns})}=10^{-4}\frac{1}{n_e}\nabla n_e\times\nabla T_e\ (\mathrm{keV}), \tag{160}$$

with distance in cm. For nanosecond time scales and gradients typical of ICF targets, megagauss fields are obtained. The cross-field electron conduction coefficient $K_\perp$ is given by[166–169]

$$K_\perp^e=\frac{n_eT_e\tau_{ei}}{m_e}\frac{\gamma_1'\chi^2+\gamma_0'}{\chi^4+\delta_1\chi^2+\delta_0}, \tag{161}$$

where n_e is the electron density and m_e is the electron mass and $\chi=\Omega\tau_{ei}$. The δs and γs depend on z. The electron cyclotron frequency $\Omega=1.76\times10^{13}B(\mathrm{MG})$, and the electron–ion collision frequency $\tau_{ei}=(1.09\times10^{-11})T_e^{3/2}/[z\ln\Lambda(n_e/10^{21})]$, so that

$$\chi=\Omega\tau_{ei}=1.92\times10^2\frac{B(\mathrm{MG})T_e^{3/2}(\mathrm{keV})}{z\ln\Lambda(n_e/10^{21})}. \tag{162}$$

In the limit of $\chi\gg1$, the transport from Eq. (161) is reduced by a factor

$$\frac{K_\perp(\chi\gg1)}{K(\chi=0)}=\frac{\gamma_1'/(\gamma_0'/\delta_0)}{(\Omega\tau_{ei})^2}\approx\frac{1}{(\Omega\tau_{ei})^2}. \tag{163}$$

One way to estimate the importance of magnetic field effects on NIF relative to Nova targets is to examine how the terms in the magnetic field generation equation scale. Since the NIF target has nearly the same plasma densities, temperatures, and fluid velocities as discussed in Sec. XI, the scaling of the terms in the induction equation (157) is given by $\nabla\times(1/n)\nabla P\approx(1/n)\nabla n\times\nabla T$ source term $\sim1/\mathrm{scale}^2$, $\nabla\times J$ diffusion term $\sim1/\mathrm{scale}^2$, $\alpha,\beta\sim$nonlinear functions of B, $V\times B$ convection term $\sim1/\mathrm{scale}$, $J\times B$ Hall term $\sim1/\mathrm{scale}^2$, and ∇T terms $\sim1/\mathrm{scale}^2$.

The source terms and dissipation terms have nearly the same $1/\mathrm{scale}^2$ dependence. The time available for the magnetic fields to develop is proportional to scale. If the gradient scale for the magnetic fields is proportional to the hohlraum scale, one would expect NIF to have smaller magnetic fields than Nova targets. However, in some regions of the hohlraum, the gradient scale depends only weakly on the hohlraum size.

As a quantitative test of the importance of magnetic fields on NIF targets, we have included the magnetic field equation in a detailed LASNEX NIF hohlraum calculation[170] for the baseline PT target described in Sec. XIII. This calculation was run for the duration of the high-power part of the NIF pulse. Throughout the pulse in this calculation, $\Omega\tau_{ei}<1$ in the region of heat flow and radiation generation. Magnetic fields had less than a 5% effect on the energy delivered to the capsule. There are regions in the hohlraum with $\Omega\tau_{ei}>1$, although not in places where electron heat flow to the hohlraums walls is significant.

These results are obviously quite preliminary. However, there is no evidence that magnetic fields cause significant transport effects on Nova or will cause major problems on NIF. Even if magnetic fields became large enough to affect the size of the hot spot or the x-ray production region, they would not affect radiation transport significantly. As discussed in Sec. IX, the radiation distribution in a hohlraum is quite insensitive to the laser spot size, as long as its centroid is well defined.

IX. HOHLRAUM RADIATION UNIFORMITY

The optimal choice for the ratio of hohlraum case area to capsule area is strongly affected by the need to achieve a very high degree of flux uniformity on the capsule. From Eq. (2), we have, approximately,

$$\frac{\delta v}{V} \approx \frac{\delta R}{R} < \frac{1}{4}\frac{r}{R} \approx \frac{3}{4}\frac{\delta I}{I}, \tag{164}$$

where the intensity dependence comes from the rocket equation, Eq. (53), for a radiation-driven rocket. Since $20 \leqslant R_{cap}/r \leqslant 40$ is typical, we require energy fluxes to the capsule that are uniform to about 1%. The tolerable degree of asymmetry depends on the ignition margin available. For the NIF ignition capsules, we have allowed a factor of 2 in implosion energy to account for the degradation expected from both asymmetry and mix. For asymmetry alone, these capsules will ignite with an imploded fuel that has $\delta R > r/2$. However, in order to tolerate both the effects of hydrodynamic instability and mix, we specify $\delta R < r/4$.

If the case radius is large compared to the capsule radius, hohlraums are very effective at smoothing all but the longest-wavelength perturbations. Analytical results can readily be obtained for the example of a spherical capsule of radius R_{cap} inside a spherical case of radius R_{wall}.[171,172] If a Legendre polynomial perturbation of order l is applied on the inside of the case, the resultant perturbation on the capsule is as shown in Fig. 61. If the case radius is about four times the capsule radius, all modes but the P_2 component are smoothed by about two orders of magnitude. When $R_{wall}/R_{cap}=5$, P_4 passes through zero. If a capsule is chosen so that it passes through this value as it implodes, very small

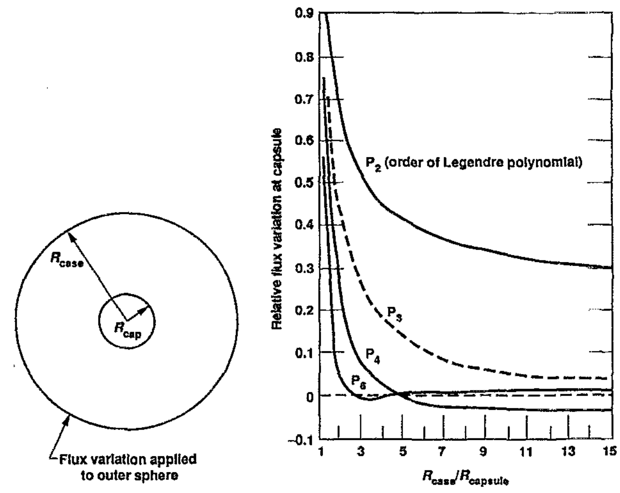

FIG. 61. Hohlraums with $R_{wall}/R_{capsule}$ from about 3–5 effectively smooth all but the P_2 Legendre polynomial flux variations.

average levels of P_4 can be achieved. The reason for smoothing short-wavelength modes is easy to understand. If we assume that the channel is thin to radiation transport, then any point on the surface of the capsule averages flux from a large fraction of the hohlraum solid angle. In this process, all high-spatial-frequency modes are averaged out. In practice, a desire to maximize hohlraum coupling efficiency often results in $R_{wall}/R_{cap}<4$, at least at early times. Therefore, both P_2 and P_4 can be issues. For nonspherical hohlraums, the situation is somewhat more complicated because coupling between modes[173] occurs for finite-size capsules. If a pure P_2 is applied to the case, P_2 and all higher modes appear at the capsule. This occurs because different points on the capsule see different solid angles and hence have different smoothing factors. This changes the shape of the perturbation, which is equivalent to adding harmonics of the applied mode. Figure 62 shows the coupling[174] between P_2 and P_4 for a cylindrical hohlraum that has a length-to-diameter ratio of 1.75, typical of laser-driven hohlraums on Nova or an ignition experiment. Figure 62(a) shows the P_2 and P_4 at the capsule for a $P_2(P_4)$ applied at the case. The principal effect of this coupling is to slightly shift the optimal pointing location for capsule symmetry in the discussion below.

In Fig. 61, all odd harmonics have been ignored because of an assumed left–right symmetry to the hohlraum. This imposes a power balance and pointing accuracy specification on the laser. (In Sec. XIII, Figs. 116 and 117 show the RMS flux asymmetry in all modes as a function of power balance and pointing accuracy for the NIF ignition targets.)

The long-wavelength P_2 component must be smoothed by choosing either the appropriate hohlraum geometry or laser geometry. With N rings of beams, it is possible[175] to exactly eliminate all the Legendre moments with $1<l<2N-1$. If the number of beams in each ring is equal to $2N-1$ or more, then the spherical harmonic modes Y_l^m with $m<2N-1$ are eliminated as well. In a hohlraum with no holes, the rings must be placed at the zeros of the Legendre polynomial of order N. The beams in each ring must be uniformly spaced around the ring, and the intensities of the

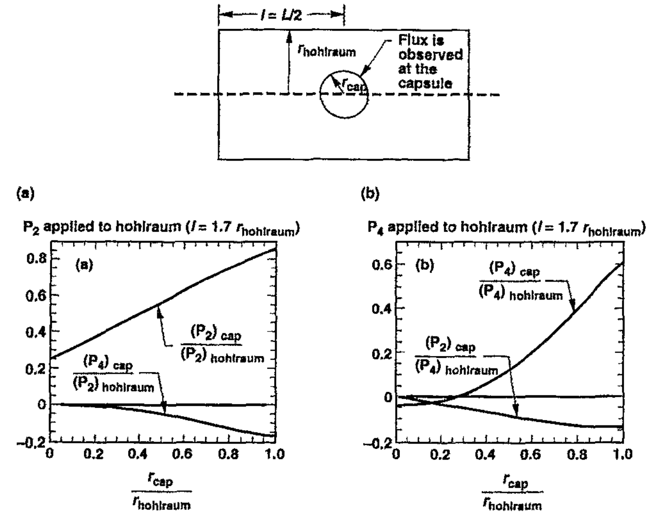

FIG. 62. Coupling occurs between Legendre polynomial spatial harmonic modes in nonspherical hohlraums.

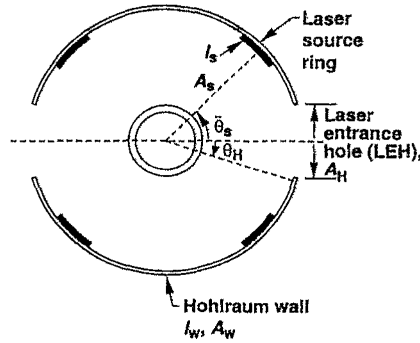

FIG. 63. A simplified spherical hohlraum is used to analyze hohlraum symmetry.

rings must be proportional to the Gaussian quadrature weight for that angle.

Holes in a hohlraum wall can be treated as a negative source, and a very similar analysis applies. For example, if the hohlraum wall is heated and the laser beams are suddenly turned off so that no flux comes from the beams, then a significant negative P_2/P_0 occurs because of the holes. For a typical laser hohlraum, holes covers about 5% of the solid angle, and $P_2/P_0=-0.227$ from the holes. To balance this asymmetry,the centroid of the laser emission must move toward the LEHs. Because the hohlraum wall has a time-varying albedo and because of plasma blowoff from the hohlraum wall, which changes the angular position of the laser beams relative to the capsule, symmetry in hohlraums also is time varying.

Because the interior of an ICF hohlraum is initially empty or filled with a low-density, optically thin gas and remains largely optically thin during the laser pulse, the diffusion approximation used for losses into the hohlraum wall in Sec. VIII does not apply to transport within a hohlraum.

When blowoff from the hohlraum wall is important in determining the spatial distribution of sources and sinks of x-ray energy in the hohlraum, or when material in the hohlraum approaches an optical depth, the coupled hydrodynamics and radiation transfer equations[176] must be solved. Several models—including Monte Carlo, P_N, and S_N—have been developed to solve the radiative transfer equation. The Monte Carlo probabilistic methods, which have been considered as the main reference for comparing other approximations, were first applied by Fleck.[177] The spherical harmonic method, or P_N, method[178] is based on the expansion of the specific intensity into spherical harmonics. When only the first two terms of the expansion are used, the Eddington or diffusion approximation is obtained. The discrete ordinates, or S_N, method[179] solves the transport equation for a series of specific angles.

If blowoff is unimportant, a "view factor" calculation[180,181] can be used. This approximation assumes vacuum radiation transport between the surface coupled to a wall loss model, such as Eq. (124).

However, significant insight can be obtained from an even simpler analytical model that can be used to estimate the required location of the laser spots at various times, as well as the sensitivity of the symmetry to deviations from the optimal position.[182] The hohlraum is assumed to be spherical, although the analysis also can be done for cylinders.[183] For purposes of this discussion,the effect of the capsule on hohlraum symmetry is small and is ignored. Although the model is readily generalized, we also assume for most of the analysis that there is a single LEH and a single ring of laser beams on each side of the hohlraum, as shown in Fig. 63. The laser-beam ring is located at an angular location θ relative to the capsule axis. The position or relative powers for multiple rings would be chosen so that their power-weighted P_2 is the same as that for a single ring. The flux at any point on a capsule comes from both the laser-heated region and the x-ray-heated wall. Only the flux from the laser-illuminated region is sensitive to the pointing accuracy of the laser. The flux from the x-ray-heated wall is essentially independent of exactly where the laser hits the wall. As the wall albedo increases, so does the ratio of the pointing-insensitive flux from the x-ray-heated wall to that from the laser-heated regions.

We define I_s to be the x-ray source intensity provided by the laser, and the blackbody emission from the wall to be $I_w=10^{-2}T_r^4$, where T_r is in units of 10^2 eV, as before, and I_w, which is in units of 10^{15} W/cm^2, is assumed to be uniform throughout the hohlraum. Although this assumption is not strictly valid, the variations within the hohlraum are relatively small for typical laser-driven hohlraums. The laser spot intensity is the excess brightness of the wall directly heated by the laser. The excess flux from the laser spots must supply the energy lost to the hohlraum wall, LEHs, and capsule. To lowest order, this flux is independent of the size or solid angle of the laser sources, but I_s clearly depends on the size of the laser spots. A smaller spot must be more intense in order to produce the required energy. The ratio of the laser spot intensity to the wall intensity depends on the wall albedo and the sizes of the LEHs and the laser spot. If we ignore the capsule, we have

$$I_sA_s=\dot{E}_w+I_wA_H,$$

where A_s and A_H are the areas of the laser spots and LEHs.

The hohlraum wall loss for gold, E_w, is given by Eq. (124), and the flux into the wall for constant temperature is

$$\frac{dE_w}{dt}=\dot{E}_w=3.2\times10^{-3}\,\frac{T_r^{3.3}A_w}{\tau^{0.38}K_{0R}^{0.39}},\tag{165}$$

where E_w is in MJ, and A_w and τ are in cm^2 and ns as before. The ratio of the laser x-ray intensity to the wall radiation intensity is then

$$\frac{I_s}{I_w}=\frac{A_w}{A_s}\left(\frac{0.32}{T_r^{0.7}\tau^{0.38}K_{0R}^{0.39}}+\frac{A_h}{A_w}\right).\tag{166}$$

For a sphere, the ratio of the areas is the same as the ratio of the solid angles, so we can also write

$$\frac{I_s}{I_w}=\frac{\Omega_w}{\Omega_s}\left(\frac{1-\alpha}{\alpha}+\frac{\Omega_H}{\Omega_w}\right),\tag{167}$$

where Ω_w, Ω_H, and Ω_s are the fractional solid angles of the wall, LEHs, and laser source regions. The ratio of the total power from the wall to that from the laser spots, F, is given by

$$F=\frac{I_w\Omega_w}{I_s\Omega_s}=\left(\frac{1}{[(1-\alpha)/\alpha]+(\Omega_H/\Omega_w)}\right).\tag{168}$$

It is F that will determine the optimal pointing angle and the relaxation of the pointing requirements in a hohlraum. Adding a capsule to the analysis has the effect of adding a term $\Omega_{\rm cap}/\Omega_w$ to the denominator, where $\Omega_{\rm cap}$ is the solid angle of the capsule as seen from a point on the wall.

At $t=0$, the ratio of the wall emission to the laser spot emission is zero. But the total wall emission rapidly comes to dominate the emission from the laser spots. For example, for the ignition design, the drive temperature is about 300 eV, while most of the energy is being delivered, and the pulse width is about 3 ns. The drive temperature is about 100 eV during the foot, a duration of about 10 ns. Figure 64(a) is a plot of F versus time at 100 and 300 eV for a case with LEHs that cover 5% of the total solid angle. Even at 100 eV, the total flux from the wall exceeds that from the laser spot in less than 100 ps.

During an interval of a few hundred picoseconds, while the albedo and optimal pointing position are changing rapidly, the flux symmetry in hohlraums can vary greatly with time, but ignition capsules can tolerate a high degree of asymmetry for times this short (see Fig. 115 and the discussion in Sec. XIII for the baseline NIF ignition hohlraum).

In the case of a single ring of laser irradiation on each end of the hohlraum, the laser emission region will balance the P_2 from the hole if we have

$$\int_s I_s(x)P_2(x)dx+\int_w I_w(x)P_2(x)dx=0,\tag{169}$$

where $x=\cos\theta$. Assuming that the emission from the laser sources is uniform and that loss from the LEH is uniform, Eq. (169) is approximately equivalent to

$$P_2(\bar{X}_s)\Omega_sI_s=P_2(\bar{X}_H)\Omega_HI_w.\tag{170}$$

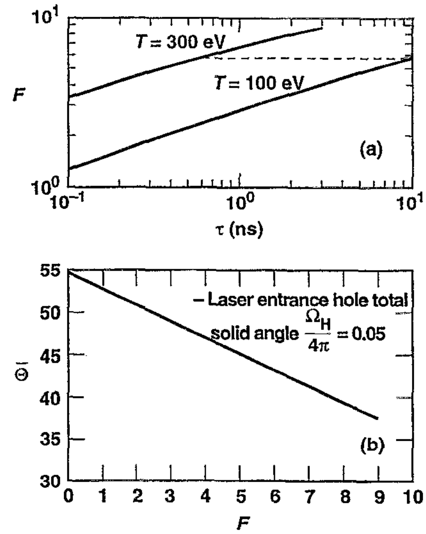

FIG. 64. (a) The hohlraum smoothing factor F versus pulse length. Here F is the ratio of the x-ray flux from the hohlraum wall to the flux from the laser hot spots. (b) The required laser source angular location $\bar{\Theta}$ to zero P_2 versus hohlraum smoothing parameter F. As the hohlraum wall flux increases, the laser spot must be closer to the laser entrance hole (LEH) to compensate for the deficit in flux from the LEH.

This expression is accurate to terms of order $\Omega^3/4$ in the fractional solid angles of the laser sources and LEHs. In Eq. (170), $\bar{X}$ is the average value of $\cos\theta$ for the LEH or the laser source location. Using the expression for F from Eq. (168), we have

$$\begin{aligned}P_2(\bar{X}_s)&=P_2(\bar{X}_H)\,\frac{\Omega_H}{\Omega_w}\,F\\&=P_2(\bar{X}_H)\left(\frac{\Omega_H/\Omega_w}{[(1-\alpha)/\alpha]+(\Omega_H/\Omega_w)}\right).\end{aligned}\tag{171}$$

The effect of the capsule could be included by adding another term, Ω_c/Ω_w, to the denominator in F, as discussed earlier. Figure 64(b) plots the required location of the center of emission for the two-ring case as a function of F for holes that cover 5% of the solid angle. This angle is measured relative to the center of the capsule, so 0° is the axis of the hohlraum. Only the angle of one of the two rings is given. The other ring is located symmetrically on the other end of the hohlraum. If the holes were smaller, the required shift in angle would be less. One effect that is apparent from Figs. 64(a) and 64(b) is that a rapid change in hohlraum temperature results in a rapid shift in the optimal pointing angle (or power balance for multiple rings). This occurs because there is a drop in albedo, or F, which accompanies a rapid temperature change. For example, as seen in Fig. 64(a), it would take 600 ps at 300 eV to reach the albedo, or value of F, that was achieved after 10 ns at 100 eV.

Equation (171) can be generalized to more rings of laser sources and to higher-order perturbations. With two rings per side, we can generalize F to be

$$F=\frac{I_w\Omega_w}{I_{s1}\Omega_{s1}+I_{s2}\Omega_{s2}}.\tag{172}$$

The condition for balancing P_2 is then given by

$$P_2(\bar{X}_{s1})\epsilon + P_2(\bar{X}_{s2})(1-\epsilon) = P_2(\bar{X}_H)\,\frac{\Omega_H}{\Omega_w}\,F = h_2, \tag{173}$$

where ϵ and $1-\epsilon$ are the fractional powers in each ring. With two rings per side, the power in each ring can be varied in time so that the location of the centroid of emission is always at the angular location required to eliminate the P_2 flux variation. If the initial ring positions are at the zeros in P_3, at $\theta=39.23°$ and 90° relative to the capsule center, then P_4 as well as P_2 can be zeroed at time zero. For these locations, the expression for ϵ is given by

$$\epsilon = \frac{10}{9}\left(0.4 - P_2(\bar{X}_H)\,\frac{\Omega_H}{\Omega_w}\,F\right). \tag{174}$$

At time zero, the relative powers in the beams must be the Gaussian quadrature weights. To satisfy this requirement, the ratio of the power in the inner ring from each side to that in the outer ring on each side is 0.8 at $t=0$. Then, P_2 is controlled by changing ϵ and can be zerod as long as the required emission location does not move to a lower angle than the location of the outer ring.

The time-varying albedo discussed previously causes a time variation in the optimal pointing angle for the laser beams—or a time variation in capsule flux symmetry—for a fixed pointing angle. Plasma blowoff from the hohlraum wall has the effect of changing the source angle in time, relative to the capsule, for a fixed pointing direction. As plasma blows off the wall, the laser absorption and x-ray emission also move off the wall. This has the effect of moving the angle of the laser source relative to the capsule back toward the LEH. Although the position of the critical surface never moves very far from the original hohlraum wall, the absorption position can move far from the original wall. Inverse bremsstrahlung is very efficient at absorbing the laser light in high-Z material, even at densities well below the critical density. The inverse bremsstrahlung absorption length is given approximately by[184]

$$\lambda_{\text{I.B.}}(\text{cm}) = \frac{0.56\lambda^2 T_e^{3/2}(\text{keV})}{(n/n_c)^2 z \ln \Lambda}, \tag{175}$$

where λ is the laser wavelength in micrometers. In gold or other high-Z hohlraum wall material, the absorption length is less than 0.1 cm for $n/n_c=0.1$ at a temperature of 4 keV, which is typical for the laser propagation channel, as discussed below. This is comparable to the scale of a Nova hohlraum, but only about $\frac{1}{4}$ the scale of an ignition-scale hohlraum. Absorption lengths in gold near $n/n_c \approx \frac{1}{4}$ seldom exceed $\sim$100 μm for a laser with $\lambda=0.35$ μm.

For both the NIF hohlraum and the Nova experiments described above, the density along much of the laser propagation path has $n/n_c \approx 0.1$, and the electron temperature $T_e \approx 3$–5 keV. In both cases, the laser intensity $I \approx 1$–2×10^{15} W/cm^2. For Nova-scale hohlraums, the laser is able to propagate through this plasma, even in gold, and most of the laser light is absorbed fairly close to the wall in higher-density, lower-temperature gold near $n/n_c \approx \frac{1}{4}$. In NIF-scale hohlraums, which are about four times the size of those on Nova,

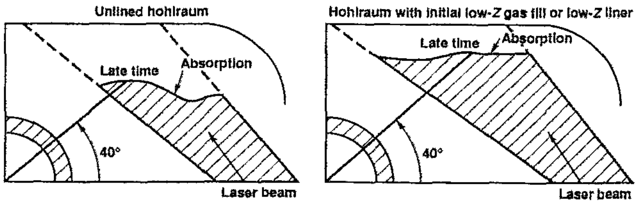

FIG. 65. Ignition-scale hohlraums use low-Z liners or gas fill to eliminate excessive wall spot motion.

inverse bremsstrahlung in gold at $n/n_c \approx 0.1$ is large enough that the laser absorption and x-ray emission region movement from the original wall makes it very difficult to maintain radiation symmetry.

The fix for this effect, recognized in 1978 at LLNL,[185] is to displace the high-density gold blowoff with lower-density material. Two approaches to this have been tried: (1) a low-Z liner on the gold, which blows off to fill the hohlraum interior with low Z[186,187] and (2) an initial gas fill of the hohlraum.[185,187,188]

The effect of such low-Z material is indicated schematically in Fig. 65. With an all-gold hohlraum, the location of the emission region moves below the 40° minimum angle required to balance the negative P_2 from the hole, so it would not be possible to achieve symmetry at a late time. With either a low-Z liner or gas fill, the motion of the emission location off the initial hohlraum wall is limited to an acceptable degree. Neither of these approaches stop the high-density gold blowoff, but they displace the low-density gold blowoff (below a density of $n/n_c \approx 0.1$ on NIF target designs), so the laser beam can propagate close to the initial wall position on NIF targets. As in Nova targets, most of the absorption then occurs in a thin gold layer near $n/n_c \approx \frac{1}{4}$. Low Z has little effect on Nova targets because the beam already could propagate to a position near the wall. Initial NIF target designs[187] and Nova experiments to test these designs used a low-Z liner that was viewed as a simpler fabrication approach. As expected from calculations, the Nova experiments with a liner showed the same asymmetry versus pointing as an unlined gold hohlraum with the same pulse length.[189] The principal purpose of the Nova experiments was to see if any adverse plasma coupling effects would be seen when the laser propagated through the low-Z plasma rather than a gold plasma.

However, detailed modeling of the NIF targets showed that the NIF capsule symmetry was adversely affected by a hydrodynamic pressure pulse, which was generated by stagnation of the liner blowoff on the axis of the hohlraum. Our code, LASNEX, is cylindrically symmetric and may exaggerate this stagnation. Hohlraums also could be designed to prevent a focused axial stagnation. This or other hohlraum modifications may result in a target with a liner that can provide a low-Z fill in NIF hohlraums.

Because a gas-filled hohlraum, the original approach used in the 1978 calculations,[185] does not have this stagnation problem, it was adopted as the NIF baseline design. This approach also was evaluated in 1988 for the proposed Laser Microfusion Facility (LMF) targets.[188]

Capsules being designed for ignition can tolerate some time variation in symmetry without performance degradation, but the magnitude of the symmetry swings must be kept below a maximum that depends on the temporal history of the time variations. Without introducing initial spatial variations in composition or thickness, capsules with a time-varying P_2 cannot be corrected simultaneously in velocity and position. Azimuthal variations in radial velocity introduce azimuthal pressure variations, which generate azimuthal mass flow. For small-amplitude or short-duration intensity variations, these effects are largely reversible if the sign of the flux variations is reversed to give a uniform time-averaged flux. However, after an azimuthal flux variation that persists for a substantial fraction of the pulse, subsequent reversal of the flux nonuniformity will not entirely remove the effects of the earlier asymmetry. If the effect of the P_2 is tuned so that the capsule is spherical at ignition, then velocity and density generally will vary from pole to waist. If the capsule is tuned to minimize velocity and density variations at ignition, then the implosion will be asymmetric. As discussed in the Introduction, an asymmetric implosion converts less of the available kinetic energy into internal energy, resulting in lower peak pressure and a higher ignition threshold.

The effect of time-dependent, long-wavelength asymmetry was examined in 1988 for the proposed LMF capsules. This work prompted us in 1988 to propose a system (for the LMF and later for the NIF) with two cones of beams on each side in order to ensure control of time-dependent P_2 asymmetry. Work on NIF ignition capsule implosions was initiated in 1990, when the NIF was proposed, and continues today. Excessive time-dependent asymmetry can cause jetting of material in the radial direction. Such jetting was seen in 1990 NIF target calculations, in which a single cone of beams per side was used instead of two. In this case, the time-varying P_2 and P_4 asymmetry are bad enough to cause capsule failure. The early-time, positive asymmetry drives material to the waist, and then, upon deceleration, this material falls as a curtain on the waist plane, quenching ignition.[190] This issue is discussed in more detail in Sec. XIII.

There are several possible techniques for controlling time-dependent symmetry. For example, a slot could be cut in the waist of the hohlraum to exactly balance the P_2 effect of the hole. The optimum location of the beam spots is then independent of time. This strategy would cost about 20%–30% in energy. The same effect also could be accomplished by reducing the albedo over a somewhat larger area near the waist of the hohlraum. Alternately, one could put a high-Z disk in the hohlraum between the capsule and the entrance hole. In the limit that this disk has the same albedo as the rest of the hohlraum and shields the entire capsule from the hole, this eliminates P_2 caused by the LEH and again gives a time-independent solution to the optimal beam location. However, neither of these approaches, by itself, eliminates the effect of the time-dependent location of the emission region. Other approaches—such as layered hohlraum walls—to provide a space- and time-varying albedo are possible, and additional internal structure can be added to eliminate P_4, if necessary, to optimize hohlraum coupling efficiency.[185]

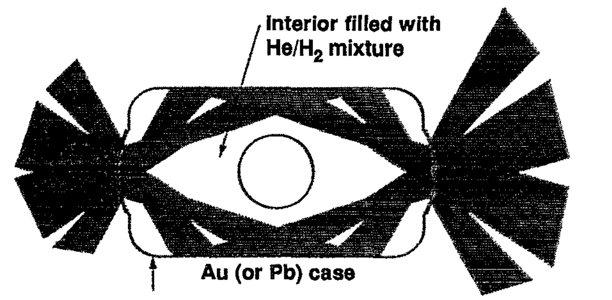

FIG. 66. To provide the required capsule flux uniformity, the NIF will use a large number of beamlets arrayed in two concentric cones on each side of the hohlraum.

As shown schematically in Fig. 66, for the NIF laser, which has 192 beams in 48 clusters of 4, we intend to control the time-varying flux symmetry by using two rings per side in the hohlraum and by varying the power ratio between the two rings.[191] This approach has been called "beam phasing." The current baseline hohlraum design uses a 0.8 mg/cm^3 He/H_2 gas fill to minimize the motion of the laser spot and to minimize laser absorption in the propagation path of the laser. This design is discussed in more detail in Sec. XIII.

To estimate the magnitude of the asymmetry at the hohlraum wall, which would occur from a pointing error, $(P_2/P_0)_{\rm wall}$ can be written as

$$\left(\frac{P_2}{P_0}\right)_{\rm wall}=\frac{5[P_2(\bar{X}_s)-P_2(\bar{X}_H)(\Omega_H/\Omega_w)F]}{1+F}. \tag{176}$$

The error introduced by deviations from the optimal angle are reduced by the factor $1+F$, compared to those that would occur at $t=0$ ($F=0$) or with no hohlraum. For the two-ring example used here, at $F=0$, $P_2/P_0=1\%$ for a pointing error $\delta\theta_0=0.08°$. For the case of two rings per side, the required pointing angle of the centroid of emission is obtained by varying the ratio of power in the two rings so that a pointing error corresponds to a power imbalance between the two rings.

For the NIF ignition capsule design (see Fig. 107 in Sec. XIII), the time integral of P_2/P_0 must be reduced below about 1%. Because most of the energy is delivered while $1+F\approx 10$, this corresponds to about a 1° placement error in the average position of the rings. For the NIF hohlraum (see Fig. 106 in Sec. XIII), a 1° ring placement error corresponds to about a 100 μm movement of the ring along the wall at the initial radius for a ring at 50° relative to the capsule. Since many beams will make up the laser rings, the pointing accuracy for individual beams is further relaxed from the average aiming accuracy by a factor of 2 or more, depending on how the pulse shaping is carried out. (Detailed calculations for the NIF ignition targets are discussed in Sec. XIII.)

The symmetry for an ignition capsule would be iterated by a variety of techniques, such as imaging the shape of a shock front propagating through a foam ball, as described below, or symmetry capsules specially designed to sample flux uniformity during varying fractions of the ignition-

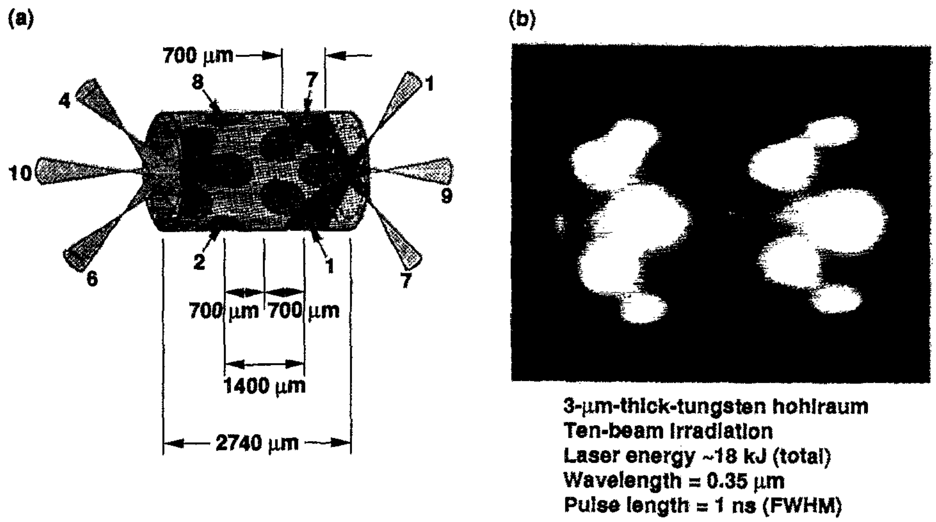

FIG. 67. X-ray imaging of thin-wall hohlraums shows high absorption and little spot motion or beam spreading for 1 ns pulses (1986 Nova data): (a) relative beam pointing for a scale-1.0 hohlraum (ten beams); (b) relative beam spot positions, as imaged with a ~50 μm resolution pinhole camera.

capsule laser pulse. The power ratio of the rings would be adjusted to obtain symmetry for each of a succession of symmetry capsules that would sample successively longer portions of the entire pulse. The beam placement specifications discussed in Sec. XIII are chosen to provide the reproducibility required for such an iterative technique.

In addition to direct capsule measurements of symmetry, experimental measurements of the x-ray spot motion and

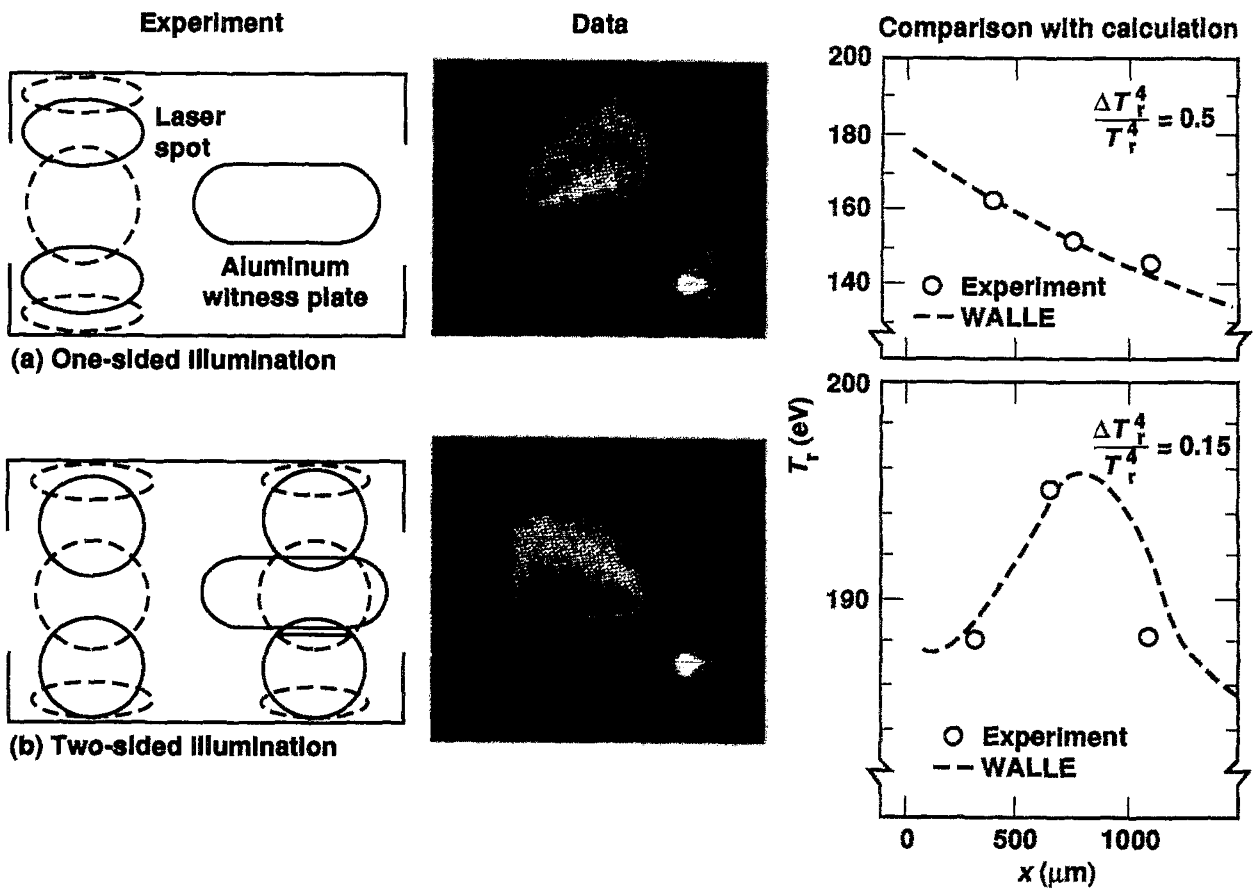

FIG. 68. Knowledge of laser deposition and radiation transport makes possible accurate modeling of wall heating uniformity.

hohlraum wall albedo provide significant information on time variation of the capsule symmetry. These experiments, in effect, specify the functional form of the time-dependent symmetry from the LEH and wall motion. The implosion experiments then determine the time average of this functional form. Wall-loss experiments, such as those discussed in Fig. 55, are related—through Eqs. (134), (168), and (171)—to the desired angular location of the x-ray emission. Experiments, such as those on Nova discussed below, can also measure the actual location of the laser-generated hot spots and their motion due to wall blowoff and refraction. With the constraints imposed by such measurements, a time-integrated measurement of implosion symmetry for the ignition experiments may be adequate to ensure that the time variations are acceptable. For example, the uncertainty in the wall opacity obtained from wall-loss experiments will result in an uncertainty in the power or pointing required for optimal symmetry in an ignition hohlraum. However, a 30% uncertainty in opacity would result in only about a 1° uncertainty in the optimal location of the average laser hot-spot position or a 1% uncertainty in the time-dependent asymmetry at the peak of the laser pulse. This is well within tolerable limits if the time-integrated flux is uniform. The Nova spot-motion experiments discussed below have an error bar of about 50 μm on the measurement of the centroid of x-ray emission. Experiments with this level of accuracy on an ignition experiment would result in a <1% uncertainty in the time-dependent asymmetry from spot motion. With two rings of beams per side, as proposed for the NIF, the relative brightness of the two rings also would have to be determined to a few percent, as indicated in Table VIII in Sec. XIII.

A wide variety of experiments have been carried out on Nova to test the control of hohlraum symmetry. Thin-walled hohlraums, which transmit x rays with $h\nu$>3–5 keV were used to determine the location of laser light absorption.[91] Figure 67 shows the results of a thin-walled hohlraum experiment with a 1 ns pulse. This experiment demonstrated high absorption and little spot motion at the geometric position of the laser beam spot. More recent experiments on Nova,[192] which use a time-gated x-ray framing camera, can be used to obtain time-resolved information about the high-energy x-ray emission from pulse-shaped hohlraums.

Uniform-thickness witness plates also were placed in the hohlraum wall[91] in early Nova experiments to measure temperature gradients. As shown in Fig. 68, the time variation in shock breakout is related to the temperature gradient. For a hohlraum with a single ring of beams, the gradient is very large. With two rings, the gradient along the aluminum plate is only a few electron volts. Both results were as expected from calculations.

Since Nova has only a single ring of beams per side, as shown schematically in Fig. 10, it is possible to eliminate only the average of P_2. The residual time variation in flux uniformity produces the lateral mass motion described above. On Nova, these effects become significant for convergence ratios greater than about 10. Since the purpose of the Nova symmetry experiments was to determine only average flux uniformity, convergence ratios were limited to about 10, sufficient for a 1% average flux measurement without the added complexity of the distortion generated by the time dependence of the flux uniformity.

Beginning with experiments in 1986,[92] the time-averaged symmetry on Nova has been demonstrated by imploding capsules and imaging the imploded fuel volume. The fuel is imaged by using either an x-ray pinhole framing camera[193] or a time-integrated ring aperture microscope (RAM).[194] The RAM uses penumbral imaging with a ring slit to obtain about ten times better signal-to-noise ratio than a pinhole camera with a comparable resolution. The framing camera consists of a series of as many as 16 pinholes that image onto a microchannel plate (MCP). When a 100 ps voltage pulse is propagated across the MCP, the image from any given pinhole is recorded during the time this pulse is propagating across that portion of the MCP that is receiving photons from that pinhole. The time between individual images can be adjusted independently in the camera used to take the images shown in Fig. 69. Capsules used in these experiments are the same as those shown in Fig. 42.

The sign and magnitude of P_2 can be varied by changing either the hohlraum length or the beam pointing. Figure 70 shows the results of changing the beam pointing. We define the capsule pole as the portion of the capsule on the axis of rotation. The waist is the portion of the capsule along the hohlraum midplane. When the hohlraum is elongated, as in the left image, the position of the laser beams is closer to the LEH than is required to achieve uniform average flux, resulting in a "pancake" implosion. As the hohlraum is shortened, as shown in the right image, the illumination from the two rings of laser beams approaches the capsule waist, and the average flux delivered to the waist begins to exceed that delivered to the poles, resulting in a "sausage" implosion. Between these two extremes, the laser spots are at the optimum position for which the average P_2 component is zero, and the implosion appears spherical. The center image is spherical within the measurement accuracy of a few percent in flux. An interesting feature of the sausage image is the rotation of the image axis away from the hohlraum axis. This

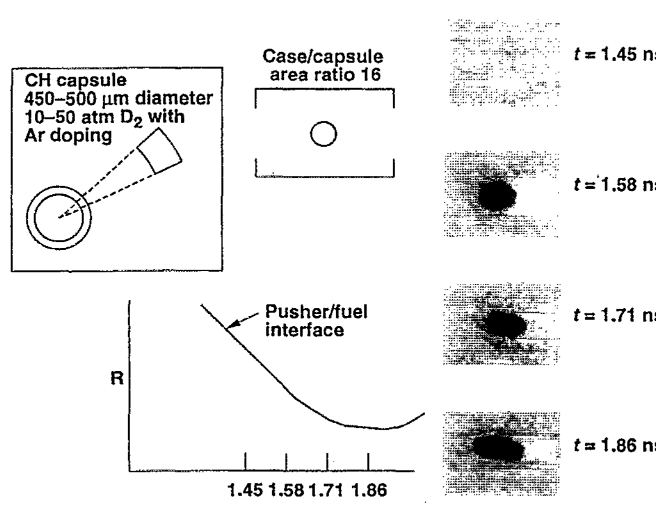

FIG. 69. The 100 ps resolution, x-ray framing cameras are used to observe the imploding capsule and to infer hohlraum drive symmetry.

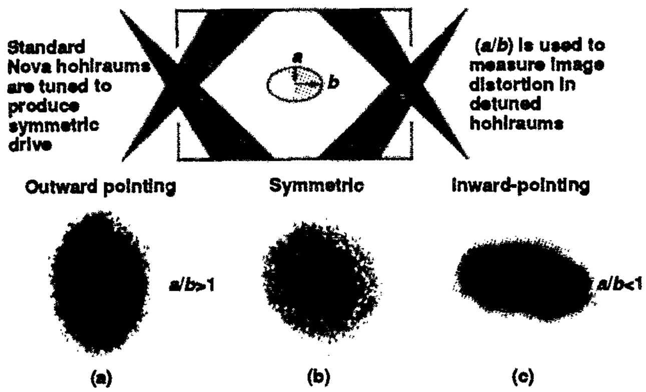

FIG. 70. Nova experiments have used x-ray imaging of imploding capsules to test the modeling of hohlraum drive asymmetries. Observed x-ray image shapes confirm the calculated variation of the implosion shape with beam pointing: (a) outward-pointing shifts produce pole-high fluxes or "pancake" images; (b) symmetric; (c) inward-pointing shifts produce waist-high fluxes or "sausaged" images. The tilted axis in (c) shows the effects of beam imbalance and pointing errors prior to the Precision Nova improvements.

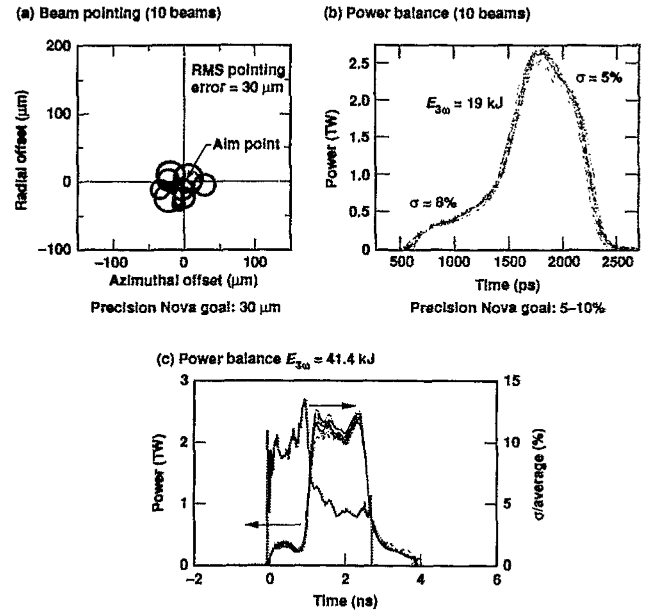

FIG. 71. The Nova laser power balance and beam pointing were improved by a factor of 2–3 in the Precision Nova project. These improvements were required for high-precision symmetry experiments and high-convergence implosions.

type of nonaxial distortion occurred frequently on Nova prior to the power balance and pointing improvements achieved in the "Precision Nova" Project. The pointing accuracy and power balance goals specified for Precision Nova recently have been achieved,[100] with pointing accuracy improved from about 100 μm to the Precision Nova goal of 30 μm [see Fig. 71(a)]. The power balance has been improved about a factor of 2, to 5%, during the high-power part of the pulse and to less than 10% during the low-power foot of the pulse [see Fig. 71(b)] for the 20 kJ pulse shape used for the high-density, high-convergence HEP-1 implosions described in Sec. X. With these specifications, Nova implosions can be carried out repeatedly within a 1% variation in the average flux uniformity. Figure 71(c) shows that Nova is now capable of meeting the Precision Nova power balance specifications for a pulse having a 10:1 contrast ratio and delivering more than 40 kJ.

Table III lists the different types of pulse shapes and hohlraums that have been used in symmetry experiments. Constant-power, 1 ns pulses; the 3:1-contrast, 2.2 ns, ps22 pulse; and the 8:1-contrast, ps23 pulse have all been used. [The last two pulse shapes and their witness-plate shock trajectories were shown in Figs. 40(c) and 40(d).] Gold hohlraums without liners, hohlraums with CH and nickel liners, and hohlraums with methane gas fill have been tested. Most of the symmetry experiments were carried out with ps22, which produces plasma conditions and spot motion that are very close to those of NIF target designs.

The symmetry experiments with liners were carried out before choosing a gas-filled hohlraum as the baseline target for the NIF. Symmetry experiments on gas-filled hohlraums began on Nova during the summer of 1994 and are continuing. Because the presence of low-Z material in the hohlraum during the high-power part of the pulse did not adversely affect the low-Z liner experiments, any difference between the lined and gas-filled hohlraums are expected to result primarily from startup effects. The gas-filled hohlraums present more of a computational challenge because of the presence of a window on the hohlraum LEH to contain the gas and because of a transient as the laser beam initially propagates through the window and gas. Gas-filled hohlraums also have been used for the plasma scaling experiments described in Sec. XI.

For all the Nova experiments discussed below, the hohlraums were 1600 μm in diameter with a 1200 μm LEH. Pointing positions refer to the distance between the hohlraum midplane and the plane at which the central ray of all the beams on one side would intersect as they pass through the axis of the hohlraum, as shown schematically in Fig. 72. This distance fixes the angle between the capsule axis and the x-ray emission region and is the principal determinant of the resultant implosion symmetry. In "normal focusing" for most Nova implosion experiments, all beams pass through the origin in the plane of the LEH. For a given LEH size, this gives the greatest clearance between the laser beams and the hohlraum wall. This is the focusing for experiments in which symmetry is changed by varying the hohlraum length. As indicated in Table III, experiments also have been done with constant-length hohlraums in which symmetry is changed by varying the beam focal position relative to the LEH. These two types of experiments give essentially the same results until the laser beams for the constant-length hohlraum experiments begin strongly interacting with plasma from the LEH.

Most of the symmetry experiments and modeling discussed hereafter were carried out on Nova between 1991 and 1993 as a joint effort by Livermore and Los Alamos.[192,189] Similar experiments have been carried out on the GEKKO XII laser.[27]

To date, hohlraums driven with ps22 have been tested under the widest range of different hohlraum and pointing

TABLE III. An extensive hohlraum symmetry database has been developed on Nova.

	Au, fixed length, variable focus	Au, variable length, fixed focus	Ni-line Au, fixed length, variable focus	Ni-lined Au, variable length, fixed focus	CH-lined Au, variable length, fixed focus	CH_4 gas-filled, variable length, fixed focus
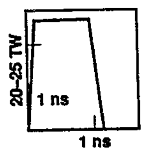	X	X	X	X		
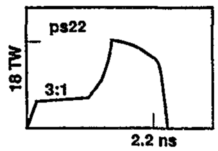	X	X	X	X	X	X
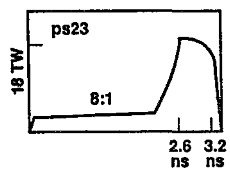	X					

variations. Figure 72 shows the results of experiments and calculations for ps22 in hohlraums lined with 150 nm of nickel. For these experiments, the beam crossing position was in the plane of the LEH, so the beam-pointing position is also the hohlraum half-length, and symmetry is plotted versus hohlraum half-length. The capsule distortion is the ratio of the capsule waist dimension to that along the hohlraum axis. The log of distortion is linearly proportion to average flux nonuniformity. For ps22 implosions, a 2:1 distortion of the fuel corresponds to a 5% average asymmetry. As seen in Fig. 72, the agreement between experiment and the LASNEX calculations is quite good.

Most of the data for the symmetry experiments were collected before the Precision Nova improvements were completed, and typical experiments with nominally the same conditions could have a shot-to-shot symmetry variation of several percent. However, with Precision Nova improvements, experiments reproducible to within 1% in average asymmetry are possible, as shown in Fig. 73 (again for ps22 experiments). The yield from these Precision Nova experiments is also highly reproducible, as shown in Fig. 74. At a temperatures of 1–2 keV produced in these implosions, the approximate factor-of-2 shot-to-shot yield variation corresponds to a reproducibility within $\pm 10\%$ in ion temperature.

The focus of gas-filled hohlraum experiments has been on the ps22 pulse in hohlraums filled with 1 atm of methane.[195] When ionized, this gas has a density $n/n_c \approx 0.03$, about the same as the NIF baseline hohlraum (see Fig. 106 in Sec. XIII). At a later time, the gas compresses to $n/n_c \approx 0.1$, also comparable to the NIF targets (see Fig. 90 in Sec. XI).

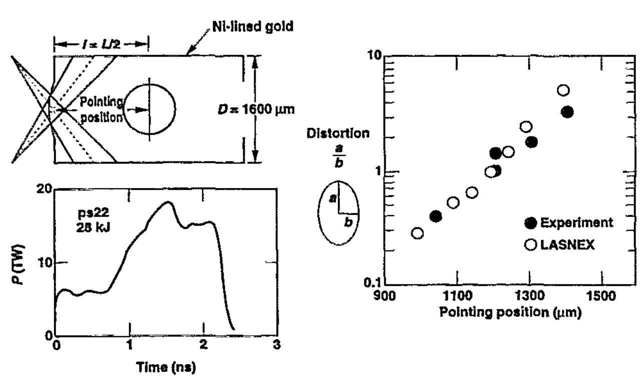

FIG. 72. LASNEX calculations do an excellent job of modeling symmetry for experiments in which laser pointing is kept fixed at the plane of the LEH as the hohlraum length is varied for pure-gold and lined hohlraums.[189]

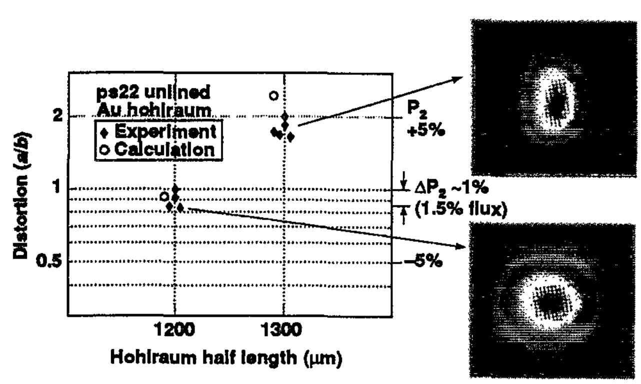

FIG. 73. Precision Nova implosions have shown excellent reproducibility of symmetry.

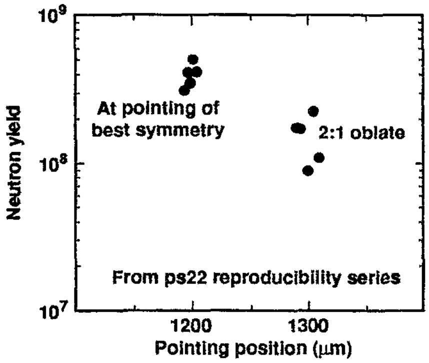

FIG. 74. At best pointing, the scatter in the Precision Nova ps22 yields imply average T_i is reproducible to less than $\pm 10\%$.

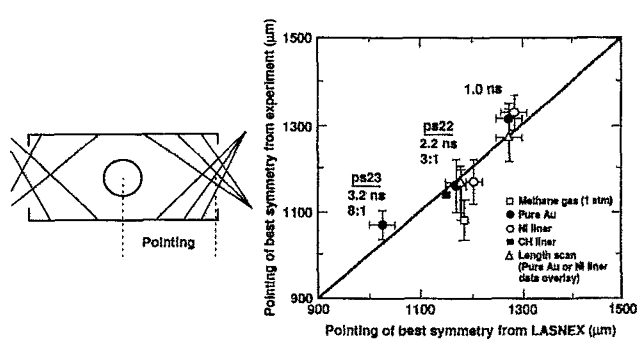

FIG. 76. LASNEX successfully predicts the pointing of best symmetry for almost all symmetry experiments. Beams must be moved inward for longer pulses to compensate for spot motion caused by hohlraum wall blowoff. The experimental pointing of best symmetry is offset from the calculations by ~150 μm for the methane-gas-filled hohlraums. The cause of this offset is being investigated.

The work on gas-filled hohlraums is still being analyzed and the symmetry results discussed below are preliminary. Detailed analysis[196] of the gas hohlraum energetics experiments, indicates that no significant surprises are observed compared to the earlier lined hohlraums when measured levels of SBS and SRS are taken into account.

A variation of capsule symmetry with hohlraum length for gas-filled hohlraums is reproducible and behaves the same as for lined and unlined hohlraums. However, as shown in Fig. 75, the gas-filled hohlraums have optimal symmetry for a target that is 10%–15% shorter than for the lined or unlined Nova hohlraums. Hohlraums with the standard polyimide 6500 Å windows and no gas fill also have optimal symmetry with a 10%–15% shorter hohlraum, as shown in Fig. 75. Optimal symmetry for a thinner, 3500 Å window and no gas fill falls between the two cases. LASNEX calculations correctly predict the slope of distortion versus pointing position, but are offset from the data by about 150 μm, about 15%–20% of the laser spot diameter. At a given pointing position, the symmetry shift is equal to about 5% in flux. Such a change in hohlraum length would cause no change in the NIF laser specifications. A promising explanation for this enhanced spot motion effect is refraction of laser beam filaments caused by flow of hohlraum plasma transverse to the laser beam propagation direction.[197] As a laser beam filament is forming, plasma is ejected at the sound speed from the

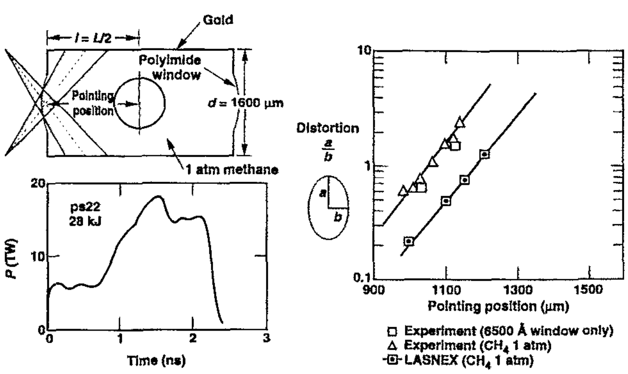

FIG. 75. Symmetry experiments with gas-filled hohlraums show the same variations with pointing position as empty hohlraums, but the data are offset from the current LASNEX calculations by 150 μm.

filament region. Without transverse flow, this process is symmetric and the beam propagation direction is unaffected. With transverse flow, the formation process is asymmetric, effectively resulting in a density gradient transverse to the beam which causes beam deflection. The effect is largest near the sonic point, where matter trying to propagate in the upstream direction, persists for a long time. In hohlraums, the sonic point in the flow generally occurs near the laser entrance hole. For Nova's unsmoothed beams, which are currently used for the symmetry experiments, this plasma is calculated to be unstable to filamentation essentially throughout the pulse for the gas-filled hohlraums. Initially empty hohlraums on the other hand, do not develop enough gain for filamentation until late in the pulse. Experiments are in progress that are designed to determine the source of the shift.

A convenient way of portraying the correspondence between experiment and calculation for the symmetry experiments is shown in Fig. 76. This figure compares the calculated and experimentally measured pointing of best symmetry for all of the combinations of hohlraums and pulse shapes tested. An interesting feature of Fig. 76 is the fact that, as the pulse length increases, the pointing of best symmetry moves toward the capsule waist. This occurs because of the increased spot motion caused by the wall blowoff, as the pulse length is increased. To compensate for this increased motion, the initial pointing location must be moved inward.

This motion of the x-ray emission region also has been measured directly in Nova experiments by cutting a slot in the hohlraum wall and looking at the axial location of the x-ray emission, from a beam on the opposite wall, as a function of time.[189,198] Figure 77 shows a comparison of the observed and calculated locations of the emission for a ps22 experiment at an x-ray energy of 450 eV. The observed axial spot motion of about 200 μm agrees with the calculated value. This motion corresponds to a shift in the angular position of emission relative to the capsule center of about 15°, comparable to that calculated for the individual cones of beams on the NIF target.

As shown in Fig. 78, Nova experiments also have been

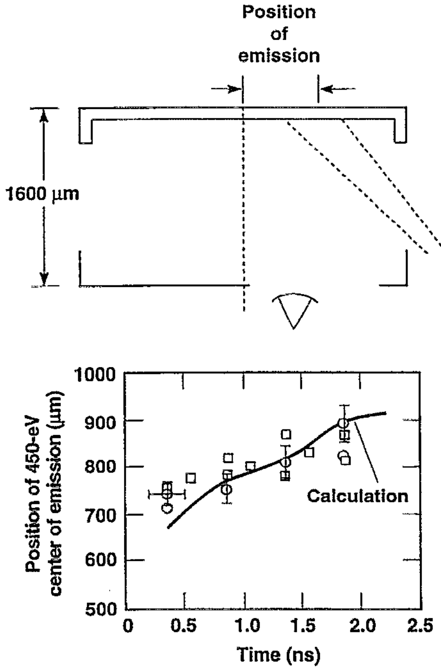

FIG. 77. The observed axial motion of the centroid of emission for ps22 is close to that calculated. In calculations, Nova beams are assumed to have a Gaussian profile, whereas the actual beam has significant structure, which makes identification of the beam centroid ambiguous.[96]

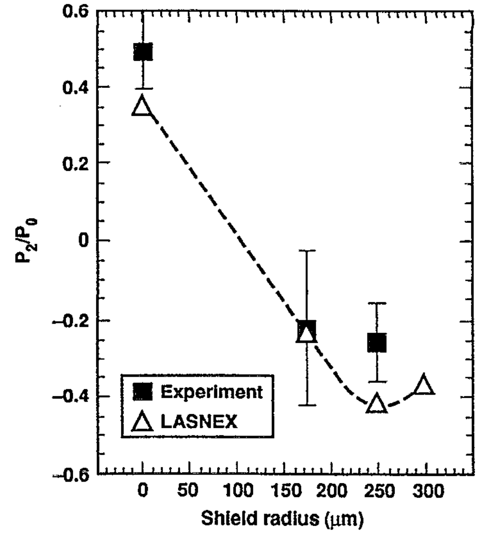

FIG. 79. The effect of LEH shields on Nova hohlraums can be modeled quantitatively.

used to determine the effects of putting a high-Z disk between the LEH and the capsule.[152] As discussed earlier, the high-Z disk reaches about the same temperature as the hohlraum wall, effectively eliminating the negative P_2 from the hole. Hence, a beam pointing in a standard hohlraum that gives a sausaged implosion produces a nearly spherical implosion when the disk is inserted. Figure 79 shows P_2/P_0 for the imploded shape as a function of the shield radius. Because of spot motion, which is largely unaffected by the presence of the disk, these implosions still have a time variation in symmetry. It may be possible to balance the effects of spot motion—which results in a progressively larger flux to the capsule pole—by using a shaped disk or entrance hole that becomes more lossy at late times.

The results shown in Figs. 73–79 represent a time-integrated measure of asymmetry. However, for the reasons discussed above, an implosion that has a time-average uniform flux will have a flux at any instant that may be either pole high or waist high. Figure 80 shows a typical variation for a 1 ns, constant-power pulse. Very early in time, for the pointing chosen, the flux is pole high. Then, as the wall albedo increases, significant flux starts to come from all areas of the hohlraum wall except for the LEHs, and the flux becomes waist high. As the hohlraum heats up, plasma blows

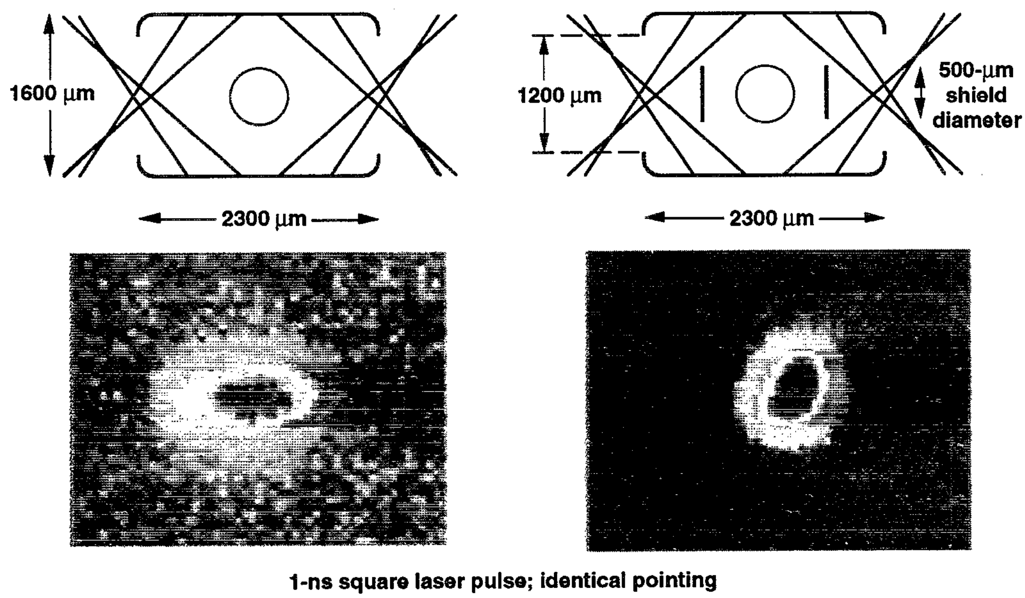

FIG. 78. Internal radiation shields modify implosion symmetry, in agreement with calculations.

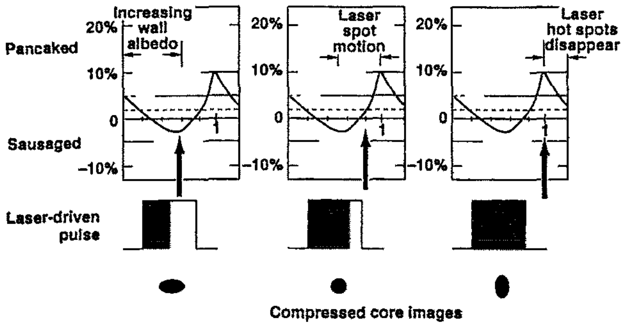

FIG. 80. Time-dependent symmetry from a 1 ns pulse. Symmetry capsules that implode at different times in the pulse show different asymmetries.

off the hohlraum walls, and the laser absorption region and x-ray production move inward, moving the x-ray emission more toward the pole, thus again making the flux on the capsule more pole high. Finally, when the laser beams shut off, there is no source to balance the holes, and the flux becomes waist high again. In Sec. XIII, Fig. 115 shows the equivalent time variation for a NIF target without using the "beam phasing" described previously to remove the time dependence.

Several techniques are being developed to obtain time-dependent symmetry information. One approach uses the full pulse with a series of capsules designed to implode at different times during the pulse. Those capsules that implode early see only the early-time asymmetry, and a record of the evolution of asymmetry can be obtained as indicated in Fig. 80. Los Alamos has begun work on this approach,[192] as shown in Fig. 81 for Nova experiments that used ps22.

A second technique replaces the capsule with a uniform sphere of material, as shown in Fig. 82. The x-ray flux in the hohlraum will drive a shock into this material, which can be imaged by x-ray backlighting. When an appropriate combination of sphere composition and density and x-ray backlighter energy are chosen, a large opacity contrast is obtained at the shock. With different choices of x-ray energy or material, the ablation front rather than the shock front is more easily imaged.

Distortion of the shock front is approximately related to the drive pressure nonuniformity by

$$\frac{d}{dt}(r_{\text{equator}}-r_{\text{pole}}) \approx \frac{1}{2}\sqrt{\frac{\bar{P}}{\rho}}\left(\frac{P_{\text{pole}}}{P_{\text{equator}}}-1\right). \tag{177}$$

For ps22, Fig. 82 shows the calculated ratio of $P_{\text{pole}}/P_{\text{equator}}$, which can then be compared with the measurement. The average pressure $\bar{P}$ can be obtained from the shock velocity. Figure 83 shows the results from a Nova experiment.[199] In this figure, A_2 is the second Legendre coefficient of the position of the shock trajectory and A_0 is the average distance moved by the shock. The numerical calculation and the data are in agreement for this experiment. Calculations[200] show that, with the current resolution of about 2 μm in the shock position, time variations in NIF target fluxes can be obtained to about 2%.

A technique that can be used to obtain early-time symmetry information is the reemission ball.[201] In this technique, a nonimploding, high-Z sphere is placed at the capsule location. Reemission from this sphere is related to the incident flux. Figure 84 shows the result of a Nova experiment that used a bismuth-coated sphere and a 2:1 beam asymmetry in the two Nova rings of beams.[192,202]

Symmetry experiments on Nova have been a good test of many of the features that will affect symmetry on the NIF.

(i) The minimum case-to-capsule ratio (ratio of hohlraum radius to initial capsule radius) is comparable on Nova (2.8) and the NIF (2.5). As described in Figs. 61 and 62, this ratio determines the geometric smoothing of source flux nonuniformities in a hohlraum. It also determines the coupling efficiency of x rays to the capsule, as described by Eq. (132).

(ii) The LEH effect on the flux uniformity at the capsule is comparable on Nova experiments and the NIF hohl-

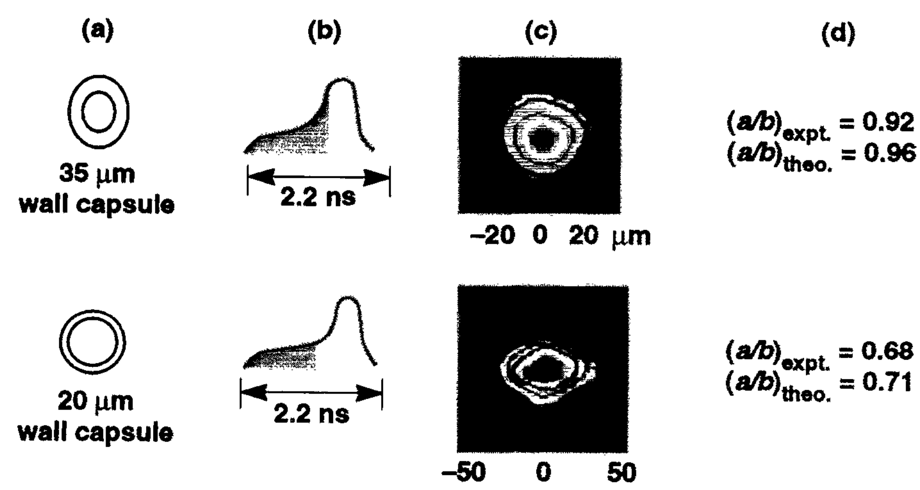

FIG. 81. Data from ps22 using the variation in implosion time of capsules with different wall thickness: (a) initial capsule configuration; (b) shaded portion of the drive represents the effective sampling interval for the implosion for the two cases; (c) implosion image data taken orthogonal to the hohlraum axis; and (d) comparison of the measured capsule eccentricity with the calculated value.

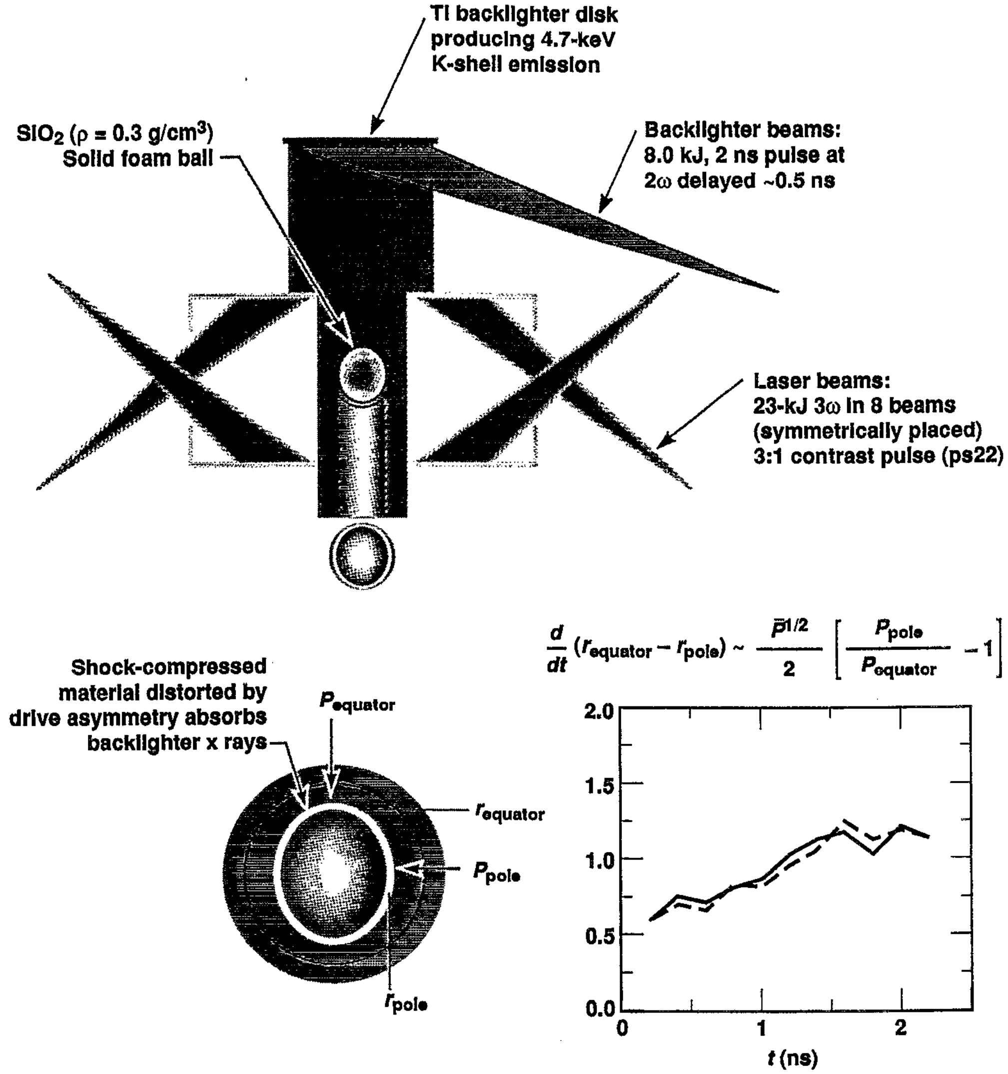

FIG. 82. X-ray radiography can be used to infer time-dependent asymmetry from imaged shock distortion.

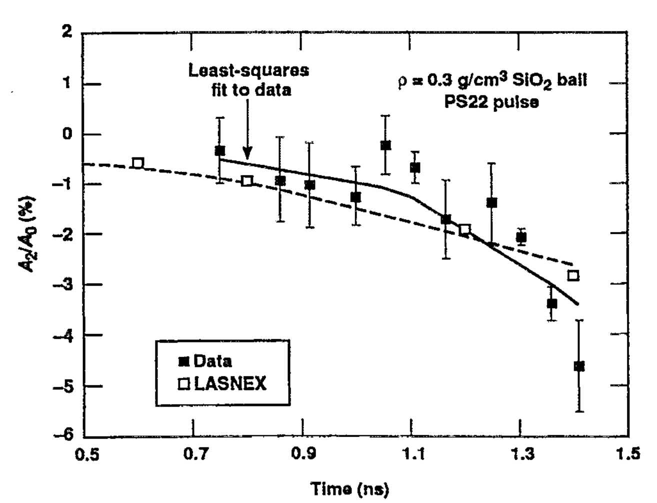

FIG. 83. The foam witness ball technique can measure pressure asymmetries with nearly 10% accuracy on Nova. Here A_2 is the second Legendre coefficient of the shock trajectory. Here A_0 is the average shock position.

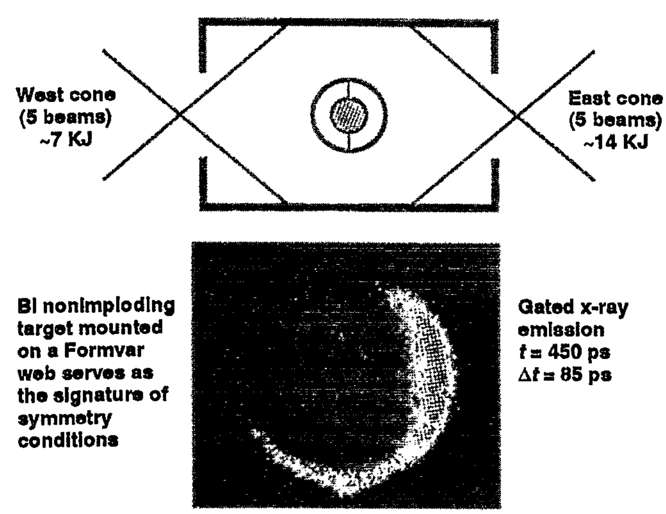

FIG. 84. Reemission from a high-Z coated sphere is sensitive to incident flux asymmetry for $h\nu \gg T$. This technique was proposed by Suter (1984) and has been developed by Los Alamos (1991–1994).[192] The reemission concept is sensitive to asymmetry for early times ($t<1$ ns) in the Nova experiments.

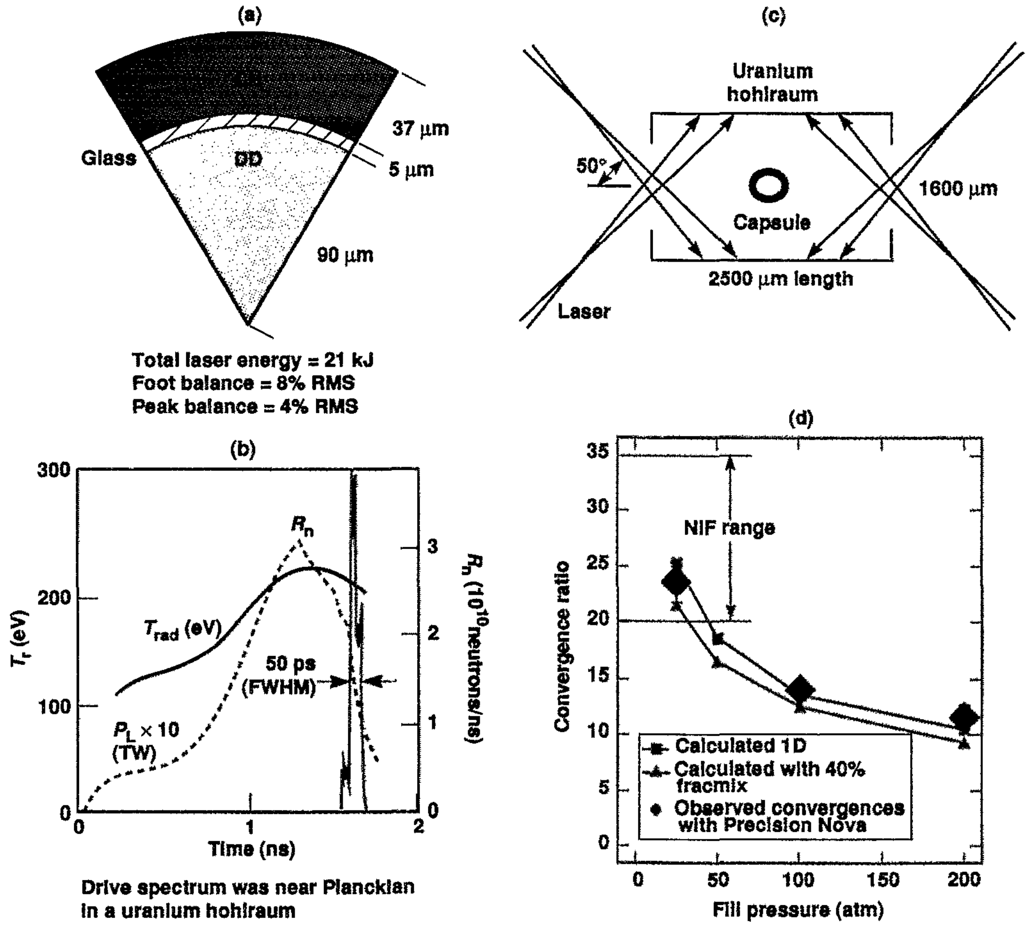

FIG. 85. HEP-1/Precision Nova shots have conservatively measured convergence ratios (from secondary neutron spectra) that are into the NIF range. The experimental measurements and calculations are in good agreement.[204] Fracmix in (d) is the mix width as a fraction of the distance between the fuel/pusher interface fall line and the unmixed interface postion.

raum (see Fig. 106 in Sec. XIII). The P_2/P_0 at the capsule, due to the LEH, is about 10% for the NIF design. Depending on the size of the LEH, this effect ranges from 10% to 20% for the Nova experiments.

(iii) The angular change in the location of the source emission due to wall blowoff, which determines the magnitude of flux asymmetry due to spot motion is about 10°–15° on both Nova experiments with the 2.2 ns ps22 pulse and for the gas-filled ignition hohlraum (see Fig. 106 in Sec. XIII).

(iv) Refraction effects for both the Nova experiments and the NIF hohlraum are generally fairly small. The refraction angle is given approximately by[203]

$$\frac{d\theta}{dx_s}=\frac{d}{dx_p}\sqrt{1-\frac{n}{n_c}}\Rightarrow\Delta\theta\approx\frac{1}{2}\frac{n}{n_c}\frac{L_s}{L_p}, \tag{178}$$

where $x_s(L_s)$ is distance (scale length) along the beam path and $x_p(L_p)$ is distance (scale length) perpendicular to the beam path. Because $n/n_c\approx 0.1$ and electron conduction results in $L_s\approx L_p$, refraction is limited to a few degrees.

(v) Implosion symmetry reproducibility for Precision Nova, as shown in Fig. 73 meets the 1% uniformity requirements for ignition experiment time-averaged flux.

(vi) Inward and outward pointing on Nova, as shown in Fig. 72, simulates the effects of the inner and outer rings on the NIF hohlraum (see Fig. 106 in Sec. XIII). Although the Nova experiments used only a single ring of beams per side, calculations indicate that the single-ring experiments are a good test of flux asymmetry from the individual ring positions.

X. COMBINED TESTS OF SYMMETRY AND HYDRODYNAMIC INSTABILITY

A goal of the NAS-mandated Nova Technical Contract (NTC) is implosions have levels of hydrodynamic instability growth and convergence ratios approaching those required for capsules on the NIF. Because Nova has only a single ring of beams per side, elimination of time-dependent symmetry effects has not been possible. Hence, the convergence ratio achievable on Nova is smaller than could be achieved on the NIF. However, hohlraums and capsules can be designed to minimize these effects on Nova. By the use of a smaller capsule-to-case aspect ratio, the higher-order flux asymmetries are further reduced. Also, a smaller capsule requires a shorter pulse, which results in less spot motion and less time-dependent asymmetry. Capsules being designed to vary hydrodynamic instability growth in a controlled way are described in Fig. 47.

In the HEP-1[204] experiments on Nova, we have made significant progress toward achieving the combined symmetry and stability-growth levels required for ignition targets by using the capsule shown in Fig. 85(a). This plastic-coated glass microballoon is about half the size of the typical Nova plastic capsule. Because of its small size, the HEP-1 capsule required the relatively short pulse shown in Fig. 85(b).

The glass inner shell of the HEP-1 capsule provided radiation preheat protection at this scale and was used for a neutron-activation measurement to determine the compressed pusher density. Also, as shown in Fig. 85(c), the capsule was placed in a uranium hohlraum, which further reduced preheat. Under the conditions of laser intensity and plasma temperature of this experiment, the uranium M-band radiation at about 4 keV was much smaller than the gold M-band radiation at about 3 keV from a standard Nova hohlraum.

Because the HEP-1 capsule was intended for high convergence-ratio experiments, it provided a particularly good test of precision Nova. The 8:1 contrast pulse shown in Fig. 85(b) was used for the Precision Nova power balance test shown in Fig. 71(b). The convergence ratio of these implosions was controlled by varying the initial fill density of the DD fuel from 200 to 25 atm. As seen in Fig. 85(d), the convergence ratio, as inferred from the ρr of the compressed fuel, varied from about 10 to 24. At the higher value, the convergence is comparable to that for some of the NIF ignition capsules designs discussed in Sec. XIII. The experimentally observed values of convergence in Fig. 85(d) were averaged over several implosions (2 at 200 atm, 6 at 100 atm, and 10 at 25 atm), and the errors were dominated by the statistical sample size of observed secondary neutrons. Without the improvements of Precision Nova, the achievable symmetry is inadequate, and the density of the implosions starts decreasing for fills below 100 atm. The ρr of the fuel in these implosions was obtained using the Large Neutron Scattering Array (LANSA)[205] array of 960 single-hit scintillator detectors. This detector measures neutrons from the secondary DT reactions that occur in DD fuel:

$$\begin{aligned} &\mathrm{D}+\mathrm{D}\rightarrow\mathrm{He}^3+\mathrm{N},\\ &\mathrm{D}+\mathrm{D}\rightarrow\mathrm{T}\ (1.01\ \mathrm{MeV})+P, \qquad (179)\\ &\mathrm{T}\ (0\text{--}1.01\ \mathrm{MeV})+\mathrm{D}\rightarrow\mathrm{He}^4+\mathrm{N}\ (11\text{--}17\ \mathrm{MeV}).\end{aligned}$$

The two DD reactions occur with equal probability. When the fuel ρr is less than the triton range, the probability of the DT reaction is proportional to the fuel ρr. The triton range depends on the fuel temperature, and, near the end of the range, the implied fuel ρr for a given secondary fraction is sensitive to temperature.[206]

Shown in Fig. 86 is the ratio of the DT-to-DD neutrons $R_{\mathrm{DT}}/R_{\mathrm{DD}p}$ as a function of fuel ρr at different fuel temperatures. The size of the HEP-1 capsule initially was chosen to minimize this problem by limiting the expected fuel ρr to a range in which the temperature-dependent effects were relatively small. In the HEP-1 experiments, fuel temperatures were 1–2 keV, and fuel ρr's were about 0.01–0.015 g/cm^2. As seen in Fig. 86, the inferred ρr is relatively insensitive to temperature in this range, and it is essentially linear in $R_{\mathrm{DT}}/R_{\mathrm{DD}p}$. Neutron energy depends on kinetics and the energy of the reacting triton, which slows down as it traverses the fuel. As the triton slows, the width of the neutron spectrum narrows.

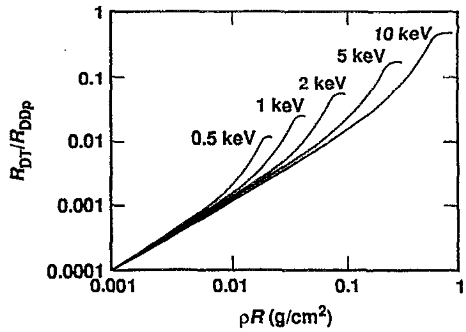

FIG. 86. We see $R_{\mathrm{DT}}/R_{\mathrm{DD}p}$ as a function of ρr for several fuel electron temperatures.[204] The model used assumes a large uniform density and temperature fuel region with a negligibly small central "hot spot," from which all tritons originate. Curves end at the value of ρr where the tritons have thermalized in the fuel. Fuel density used was 21 g/cm^3.

LANSA provides both a secondary neutron fraction and a neutron spectrum, so that the fuel ρr can be obtained without model-dependent assumptions regarding triton slowing.[207] Figure 87 shows the neutron spectrum obtained from summing the spectra from the ten 25 atm shots. Figure 87 also shows the LASNEX-calculated spectrum, including the effects of hydrodynamic instability estimated from the Haan mix model described earlier. From these measurements, we infer an average DT equivalent fuel density, assuming constant density versus radius, of about 20 g/cm^3.

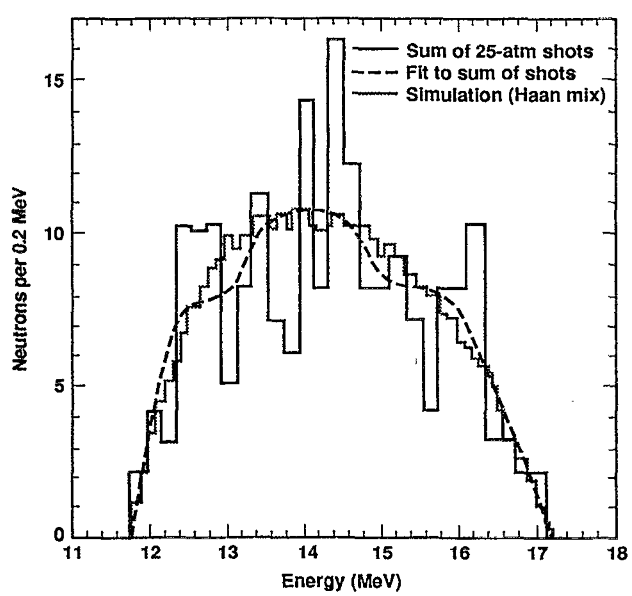

FIG. 87. Shape of composite neutron spectrum of 25 atm experiments (ten shots) is well modeled by simulation with the Haan mix model.[204]

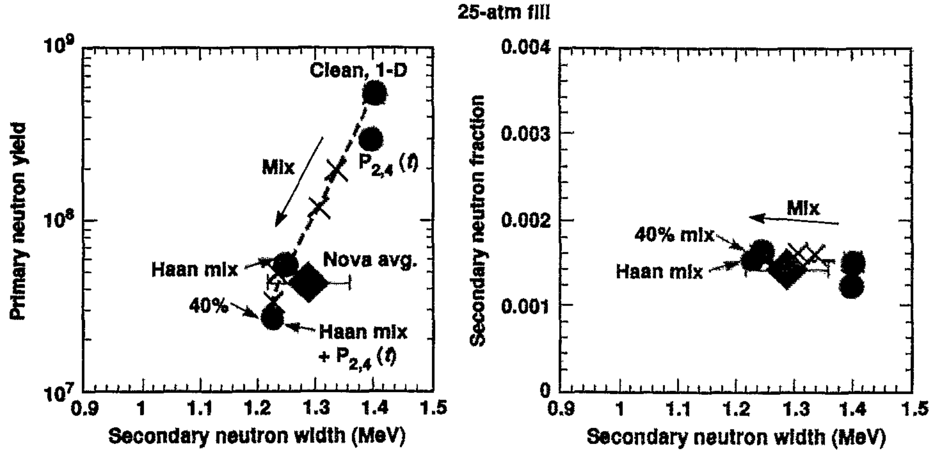

FIG. 88. The combination of the Haan mix model and drive asymmetry somewhat overestimates degradation of 25 atm fill capsules.

Figure 88 shows that the LASNEX calculations must add the effects of mix and asymmetry in order to reproduce the observed yield, secondary yield fraction, and secondary neutron-energy width. In these calculations, the P_2 and P_4 from residual pointing errors and beam imbalance were added to the calculations.

Also, two types of mix modeling were done. First were detailed 2-D calculations of the growth of a wide spectrum of individual modes. This growth, coupled with mode-saturation effects from the Haan model, was folded with the measured surface finish to obtain a mix depth as a function of time at the fuel–glass interface as the capsule decelerated. This analysis results in the point labeled "Haan mix." For comparison, another series of calculations simply mixed glass and fuel to a certain fraction of the distance between the interface and the "fall line" (i.e., the calculated position of the glass–DT interface if there had been no deceleration). The separation of the fall line and the glass–DT interface is the deceleration distance. Typically, a mix width will be some fraction ("fracmix" in Fig. 88) of this distance. For the calculations shown in Fig. 88, this mix width varied from 10% to 40%. The Haan mix analysis, for this capsule and surface finish, is essentially equivalent to a 40% mix width. Since the fall line is approximately at the origin at the time of peak neutron production, a 40% mix has the effect of mixing 40% of the fuel radius by the time of peak burn. As seen in Fig. 88, the Haan mix analysis plus the effects of asymmetry slightly overestimates the observed performance degradation.

In addition to the LANSA data used to obtain the fuel ρr, other experiments measured the glass pusher ρr. From these measurements, we obtain pusher densities of approximately 150±50 g/cm^3.

Table IV compares the measured and calculated values for convergence, fuel, and pusher density and yield. Also listed are the calculated hydrodynamic instability growth and the x-ray-pulse-shape contrast ratio. These quantities approach those required for a NIF capsule, as indicated.

XI. HOHLRAUM PLASMA CONDITIONS

To control symmetry, reproducible beam-propagation conditions are necessary in the laser channel, and these conditions must be consistent with accurate placement of the laser beams. Plasma parametric instabilities such as stimulated Brillouin scattering (SBS)[25] can result in an energy loss or possibly cause a random redirection of energy in the hohlraum. Stimulated Raman scattering (SRS), in addition to its

TABLE IV. For the Nova glass implosions, the calculated implosion parameters agree well with observed values and approach key NIF target requirements.

	Low-convergence fill pressure		High-convergence (25 atm) fill pressure		
	Observed	Calculated	Observed	Calculated	NIF
Convergence ($R_{\text{capsule}}/R_{\text{fuel}}$)	14±0.7	12.3	23.6±1.8	20.7	20–35
Density (g/cm^3) (hot spot model)	16±2.4	12.6	19.1±4.4	14	45–75
Pusher density mg/cm^2 (g/cm^3)	73±15	53 (140)	60±18	72 (170)	(700–1200)
Hydrodynamic instability growth	⋯	60–160	⋯	60–160	400
Pulse shape contrast (laser)	8	8	8	8	10–50
Yield (10^7 neutrons)	7.2±1	10	4.2±0.4	3.8	⋯

effects on the energy balance and symmetry, results in the generation of high-energy electrons, which can cause preheat, as described in Sec. XII.

Plasma that evolves into the hohlraum consists of radiation-driven blowoff and direct laser ablation. The radiation-ablated gold mass is approximated by Eq. (128). The mass ablated by direct laser electron conduction is obtained from Eq. (48), in which the laser intensity used should be the intensity that is not converted to x rays. For an ignition hohlraum at a radiation temperature of 300 eV, the unconverted incident laser intensity is about 10^{15} W/cm^2 on about 20% of the hohlraum area. In this case, direct laser ablation contributes only a few percent of the mass injected into the hohlraum. However, at early times, since the temperature of the laser-heated material is higher, the expansion velocity into the hohlraum is higher, and plasma in the laser beam will be dominated by the laser-ablated material. For laser light with wavelengths of 1 μm and longer, hohlraum plasma conditions can reach a significant fraction of critical density, $n_c=(10^{21}/\text{cm}^3)/\lambda^2(\mu\text{m})$, during this early phase.

For all hohlraum experiments on Shiva and earlier 1 μm lasers, we found that, when hohlraums are calculated to develop large regions of plasma near $n_c/4$, they became very efficient at converting incident laser light into hot electrons and Raman-scattered light. As shown in Fig. 21, the fraction of energy left in the laser pulse when the hohlraum is calculated to reach $n_c/4$ corresponds closely to the energy in hot electrons. The observed hot-electron fractions, with a temperature of about 50 keV, approached 50% of the incident light, which is the maximum possible level from Raman scattering. A 50% hot-electron fraction is possible only if all of the incident light is scattered in a Raman process at $n_c/4$.

The $2\omega_{pe}$ process also occurs at $n_c/4$ and is an additional potential source of electrons. In this process, an incident photon decays into two plasma waves. The $2\omega_{pe}$ instability produces no direct electromagnetic signature and thus is hard to detect. Emission at $1.5\omega_{pe}$ can be produced by this instability. The $2\omega_{pe}$ process generally produces higher-energy electrons than Raman scattering, and may be responsible for a superhot tail with a temperature above 100 keV, which was generally seen in the Shiva experiments.

A model that reproduces the scaling of hot electrons in these 1 μm experiments is based on considering only the time that it takes the directly driven laser blowoff to fill the hohlraum volume to $n_c/4$ and then assuming that all remaining light in the pulse is Raman scattered with 100% efficiency.[69] Below critical density, the laser heats the blowoff to near isothermal conditions. The time required for sufficient material to accumulate to reach $n_c/4$ scales as $\tau_{1/4}\approx S/V_s$, where V_s is the isothermal sound velocity and S is the hohlraum scale size. Since $V_s \propto (ZT_e)^{1/2}$ and $Z\propto T^{1/2}$, then $V_s\propto T^{3/4}$. If the temperature in the laser-heated blowoff is determined by the electron flux limit, which is a good approximation for long laser wavelength at relevant intensities, then

$$I\propto n_c T_e V_e \propto n_c T_e^{3/2} \propto T_e^{3/2}/\lambda^2,$$

or

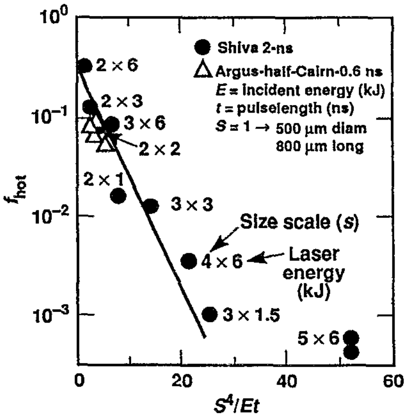

FIG. 89. Plots of f_{hot} vs S^4/Et for 2 ns Cairn experiments on Shiva. A scale-1.0 ($s=1$) hohlraum is 500 μm in diameter and 800 μm long.

$$T\propto (I\lambda^2)^{2/3}$$

and

$$V_s \propto T_e^{3/4} \propto (I\lambda^2)^{1/2},$$

where V_e is the electron thermal velocity. Using this scaling, we obtain

$$\frac{\tau_{1/4}}{\tau_L} \approx \frac{s}{V_s \tau_L} \propto \frac{S}{(I\lambda^2)^{1/2}\tau_L} \propto \left(\frac{S^4}{\lambda^2 E \tau_L}\right)^{1/2}, \tag{180}$$

where τ_L is the laser pulse length, E is the laser energy, and $I\propto E/s^2\tau_L$. This analysis predicts that there should be a time delay before the onset of hot-electron production. From Eq. (180), this time delay should scale with $E^{-1/2}$ for a fixed-size hohlraum and pulse length. This time delay and energy scaling were observed on Shiva, as shown in Fig. 22, which is a plot of the time delay in the production of high-energy x rays versus the energy into a scale-2.0 Cairn hohlraum in a 2 ns Gaussian pulse.

For closure times at the peak of the laser pulse or later, the fraction of energy left in a Gaussian laser pulse is proportional to the error function and scales approximately as $\exp(-\tau_{1/4}^2/\tau_L^2)$. Figure 89 is a semilog plot of f_{hot} vs S^4/E for various 2 ns experiments done to test this scaling. The first number listed near the data is the scale size, and the second number is the laser energy in kilojoules. The scaling is quite good, except for the lowest level point, with much less than 1% of the energy in hot electrons.

This plasma filling limited the hohlraum temperatures with low hot-electron levels, achievable with 1 μm laser light on Shiva,to between 130 and 140 eV. The NPIRE[71] implosion experiments discussed previously were designed for this temperature, and they worked essentially as calculated. The Cairn experiments discussed above, which were designed for higher radiation temperatures on both the Shiva and Argus lasers, were significantly degraded by hot-electron production.

For shorter laser wavelengths with higher critical densities, the blowoff plasma does not reach a significant fraction of critical density until significantly higher hohlraum temperatures are reached. At these higher hohlraum temperatures, particularly for shaped laser pulses of longer duration, the radiation-driven blowoff has time to fill the hohlraum and becomes the dominant source of plasma in the hohlraum. The interaction of the laser with the radiation blowoff determines the plasma conditions in the beam path. A combination of inverse bremsstrahlung absorption along the beam path, electron conduction from the beam path into the surrounding channel, and pressure equilibrium throughout the channel determines the beam-path density and temperature. By balancing these effects, a near equilibrium in temperature and density is established in the laser propagation channel. A simple model shows how these effects scale and reproduces the average temperature and density from numerical models.[99]

The inverse bremsstrahlung absorption power per unit volume, $P_{\mathrm{I.B.}}$, along the laser channel, is given by

$$P_{\mathrm{I.B.}}(\mathrm{TW/cm^3}) = \frac{P_L(\mathrm{TW})}{A_L L}\,(1 - e^{-L/\lambda_{\mathrm{I.B.}}}) \approx \frac{P_L(\mathrm{TW})}{A_L \lambda_{\mathrm{I.B.}}}, \tag{181}$$

where L is the propagation path length, and the absorption is assumed to be small. The inverse bremsstrahlung absorption length $\lambda_{\mathrm{I.B.}}$ is taken from Eq. (175). Here A_L is the cross-sectional area of the laser beams and P_L is the laser power in TW.

To estimate the electron conduction losses per unit volume from the channel, P_e, we use Eq. (27). Although the geometry of the laser beams can be complex, we approximate the conduction loss to be the loss from a sphere of radius r and obtain

$$P_e(\mathrm{TW/cm^3}) = \frac{16}{z \ln \Lambda}\,\frac{T_e^{7/2}}{r^2}\,S(Z), \tag{182}$$

where $S(Z)$ was defined in Eq. (27).

Letting $r^2 = A_L/\pi$ and equating the conduction loss with inverse bremsstrahlung heating, we have

$$P_L(\mathrm{TW}) = \frac{28\lambda^2 T_e^5(\mathrm{keV})}{z^2 \ln \Lambda^2 (n/n_c)^2}\,S(Z). \tag{183}$$

Relating laser power to laser energy using Eq. (92), we obtain the following relationship:

$$\frac{\lambda^2}{(n/n_c)^2}\,T_e^5 \approx 1.34 T_r^{1.93} E_L^{2/3} Z^2 \left(\frac{\eta}{0.15}\right)^{-0.15} \frac{\ln^2 \Lambda}{S(Z)}. \tag{184}$$

A second relationship between temperature and density is obtained by equating the pressure in the hohlraum outside the laser channel with the pressure inside the laser channel. The density in the hohlraum outside the laser channel is taken to be the radiation-ablated mass divided by the hohlraum volume. For a cylinder of radius R_{hohl}, the density is given by $\rho = 2m_r/R_{\mathrm{hohl}}$. We use Eq. (128) at constant radiation temperature for the radiation-ablated mass and relate time t to the laser energy by using Eq. (93). Assuming that the case-to-capsule-radius ratio is fixed at about 3 in order to achieve symmetry, we have, from Eq. (91a),

$$R_{\mathrm{hohl}}(\mathrm{cm}) = 1.04\,\frac{E_L^{1/3}(\mathrm{MJ})}{T_r^{1.03}}\left(\frac{\eta}{0.15}\right)^{1/3}. \tag{185}$$

Combining these equations, we have

$$\rho(\mathrm{g/cm^3}) = 0.0135 T_r^{1.86} E_L^{-0.153} K_0^{-0.46} \left(\frac{\eta}{0.15}\right)^{-0.153}. \tag{186}$$

For radiation temperatures typical of ICF, the average ionization $\bar{Z}$ of gold versus radiation temperature is given by

$$\bar{Z} = 23 T_r^{0.45}. \tag{187}$$

Combining these factors, we obtain the pressure outside the laser channel:

$$P(\mathrm{Mbar}) = 96\,\frac{Z}{A}\,\rho T = 0.15 T_{\mathrm{R}}^{3.3} E_L^{-0.153} K_0^{-0.46} \left(\frac{\eta}{0.15}\right)^{-0.153}. \tag{188}$$

The pressure in the laser channel can be written as

$$P(\mathrm{Mbar}) = 1.6\,\frac{(n/n_c)T_c}{\lambda^2}, \tag{189}$$

where λ is the laser wavelength in micrometers. Equating the two pressures yields

$$\frac{n}{n_c}\,\frac{T_e}{\lambda^2} = 0.09 T_{\mathrm{R}}^{3.3} E_L^{-0.153} K_0^{-0.4} \left(\frac{\eta}{0.15}\right)^{-0.153}. \tag{190}$$

Using Eqs. (184) and (190), we obtain the laser-channel density and temperature:

$$T_e = 0.55 \lambda^{2/7} Z^{2/7} (\ln \Lambda)^{2/7} K_0^{-0.137} \times \left(\frac{(\delta\epsilon)_{Z=1}}{(\delta\epsilon)_Z}\right)^{1/7} T_{\mathrm{R}}^{1.22} E_L^{0.051} \left(\frac{\eta}{0.15}\right)^{-0.09} \tag{191}$$

and

$$\frac{n}{n_c} = 0.16 \lambda^{12/7} Z^{-2/7} (\ln \Lambda)^{-2/7} K_0^{-0.323} \times \left(\frac{(\delta\epsilon)_Z}{(\delta\epsilon)_{Z=1}}\right)^{1/7} T_{\mathrm{R}}^{2.08} E_L^{-0.205} \left(\frac{\eta}{0.15}\right)^{-0.064}. \tag{192}$$

The assumptions used in this model break down for high-Z plasmas when the channel density exceeds about $10^{21}/\mathrm{cm}^3$. Reemission from the plasma becomes a major factor in the energy transport and the absorbed laser power required to maintain a given temperature increases. This fact is the primary reason that large-scale hohlraums must have low-Z fills to allow the laser to propagate to positions near the hohlraum wall, as required for symmetry.

Several interesting conclusions follow from Eqs. (191) and (192). First, the fraction of critical density in the channel scales nearly as the product of the laser wavelength squared and radiation temperature squared. So, for a fixed fraction of critical density, the achievable radiation temperature is inversely proportional to the laser wavelength. Also, at fixed hohlraum radiation temperature, the channel density is virtually independent of laser wavelength, since critical density scales as $1/\lambda^2$. This is seen in numerical calculations when the channel density remains well below critical density.[208]

TABLE V. A pressure balance model—in which inverse bremsstrahlung absorption and electron conduction establish conditions in the laser beam path, and radiation blowoff establishes conditions outside the laser channel—compares well with a wide variety of LASNEX hohlraum calculations for the hohlraum plasma conditions.

Cases examined			Pressure (Mbar)		Conditions in laser channel n_e/n_c		T_e (keV)	
Energy	T_r	Liner or gas fill	LASNEX calculation	Model	LASNEX calculation	Model	LASNEX calculation	Model
	Nova (0.35 μm)							
20 kJ	225 eV	Ni	3–4	4.3	0.055–0.075	0.08	3.8	3.6
25 kJ	240 eV	CH	4–5	5.5	0.08–0.11	0.12	3.0	2.9
	Ignition hohlraum (0.35 μm)							
1 MJ	300 eV	He gas	4–6	5.5	0.07–0.10	0.10	4–5	3.9
	LMF (0.35 μm)							
11 MJ	210 eV	LiH	1–1.2	1.25	0.028–0.04	0.035	2.2–2.5	3.0

The channel temperature is nearly linearly proportional to the radiation temperature and depends only weakly on laser energy, the laser wavelength, or the Z of the channel.

Equations (191) and (192) agree quite well with a variety of LASNEX calculations, as shown in Table V. For calculations using this model with liners, the Z of the liner is used in calculating the conditions in the laser channel. Gold is still used for calculating the mass in the channel outside the laser path, since the total mass of plasma in the hohlraum is still dominated by the gold blowoff. At 300 eV, the channel density for NIF hohlraums stays below $n/n_c \approx 0.1$. For the temperatures calculated, Landau damping is quite large under these conditions and plays an important role in the levels of parametric instabilities. For comparison, Fig. 90 shows contour plots of electron temperature and density at 14.4 ns from a LASNEX calculation for a NIF hohlraum. This hohlraum calculation had an initial 0.8 mg/cm^{3}He+H$_2$ gas fill inside the hohlraum (see Fig. 106 in Sec. XIII).

Using unsmoothed laser beams, SBS in the low-Z lined Nova hohlraums used for the pulse-shaped symmetry experiments is about 5% of the incident light.[209] Such hohlraums have extensive regions with $n/n_c \approx 0.1$ The observed scattering levels, although not a major energy drain, could impact hohlraum symmetry if scattering is significant at angles other than direct backscatter. A major element of the NTC has been the scaling and control of SBS to the larger plasmas of ignition hohlraums. Equations (191) and (192) can be used to estimate the scaling of gain for parametric instabilities as hohlraum radiation temperatures are varied. For SBS in a homogeneous plasma, the convective gain in the strong damping limit scales as[210,211]

$$Q_{\text{SBS}} = I\lambda^2 \frac{L}{\lambda} \frac{n/n_c}{T_e} \frac{\omega_a}{\nu_a}, \tag{193}$$

where L is the path length through the plasma and (ν_a/ω_a) is the ratio of the acoustic wave damping to its frequency. The damping is primarily Landau damping, which depends on material composition and the ratio of ion temperature T_i to electron temperature T_e, as shown in Fig. 91(a). For the NIF, where the ions and electrons have time to nearly equilibrate, $\nu_a/\omega_a \approx 0.2$–$0.4$, depending on how much hydrogen is in the hohlraum gas fill. The ion acoustic velocity, which is approximated by $\sqrt{(ZT_e+T_i)/m_i}$, is largely determined by the electron temperature and the mass m_i of the dominant ion species, while ions near the acoustic velocity provide the damping. Damping will be strong if the ion temperature is near the electron temperature, but it will be weak if the ions are cold. Also, the presence of a low-mass minority ion species increases the damping because these ions have a higher velocity, closer to the acoustic velocity. Hence, hydrogen as a minority species produces higher damping and lower SBS gains.[212] In the Nova "gasbag" experiments discussed below, plasmas with a significant hydrogen content generally had time-integrated SBS levels below about 1%, while plasmas without any hydrogen, such as pure CO_2, had average reflectivities as high as 15%–20%, as shown in Fig. 91(b). If we assume that L scales with the hohlraum radius given by Eq. (185) and use Eqs. (191) and (192) for n_e and T_e, we obtain

$$Q_{\text{SBS}} \approx I\lambda^{17/7} E_L^{0.077} T_{\text{R}}^{-0.17} Z^{-4/7} \eta^{0.359}. \tag{194}$$

Most of the radiation temperature and laser energy dependence of $(Ln/n_c)/T_e$ cancels. Thus, the gain depends on the radiation temperature through the higher intensity required for higher radiation temperature. For a fixed laser geometry, the required intensity scales approximately as T_r^4. Thus, the gain for SBS is a strong function of the radiation temperature.

The actual situation in a hohlraum plasma is far more complex than that represented by Eq. (193). Phase mismatch because of velocity gradients can reduce the gain length, and laser-beam filamentation can enhance the local intensity from the average intensity. Also, a variety of coherence control techniques—including random phase plates—and temporal smoothing—such as smoothing by spectral dispersion (SSD) developed at the University of Rochester[53] as part of the effort to control symmetry for direct drive—can break up coherent regions in the plasma to reduce the gain length. Figure 92 shows the focal spot of a Nova beam with and without a random phase plate. Although the peak speckle intensities are equally large, with and without a phase plate, the phase plate reduces the spatial scale of the speckles and produces a more uniform focal spot distribution. Distributing the laser energy over multiple frequencies also can be used to

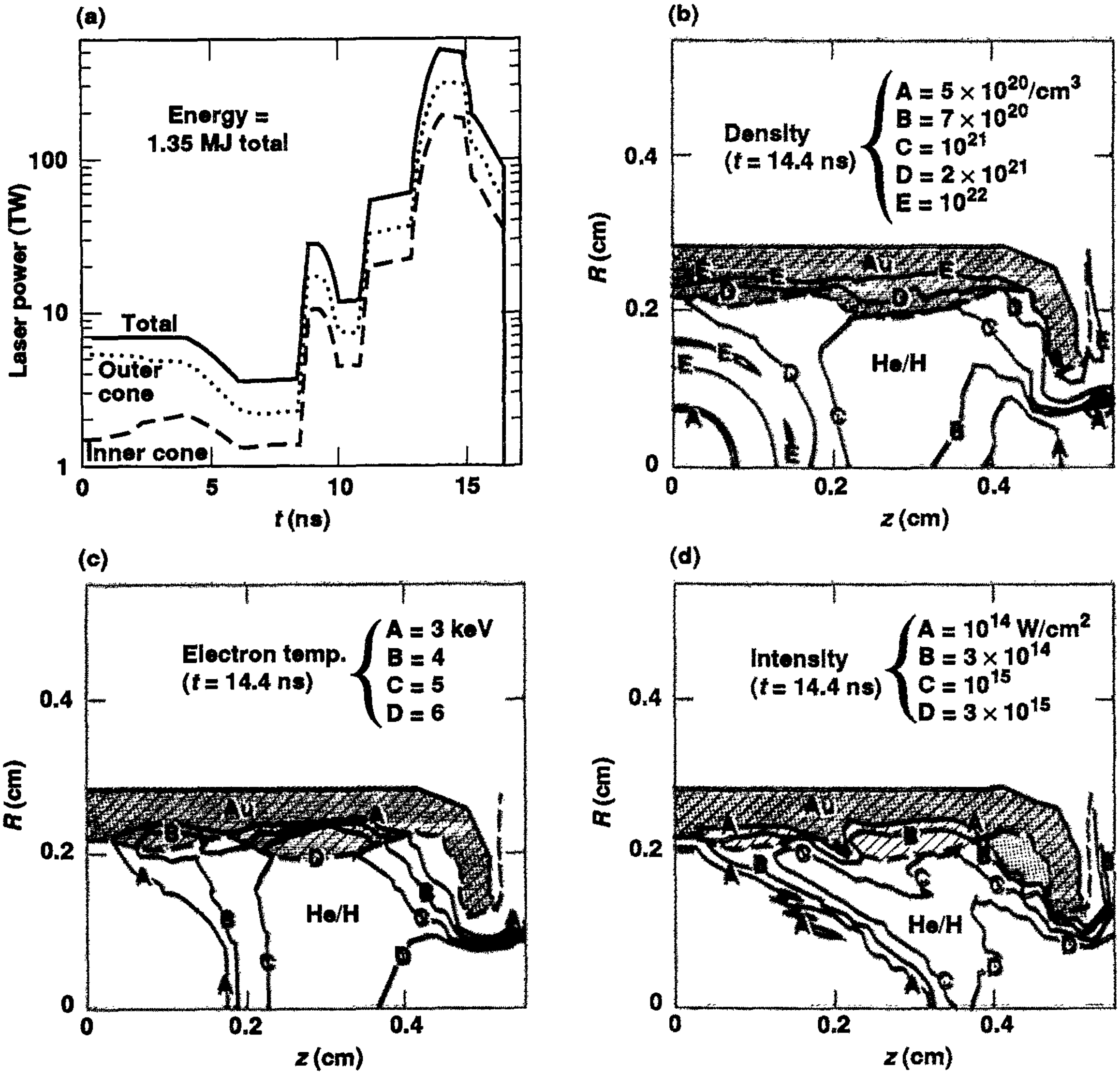

FIG. 90. Ignition-scale hohlraums at peak power have large regions in the laser channel with $n/n_c \approx 0.1$ and $T_e \approx 4$–6 keV.

control temporal coherence times. Detailed numerical models[213,214] have been developed to study the evolution of filamentation and SBS in the presence of such complex laser beam temporal and spatial characteristics.

The f number of the lens is important because the diameter and coherence length of the speckles is determined by the f number. A speckle diameter d_s is approximately equal to the diffraction-limited spot for the lens or $d_s \approx 2\ f\lambda$. The

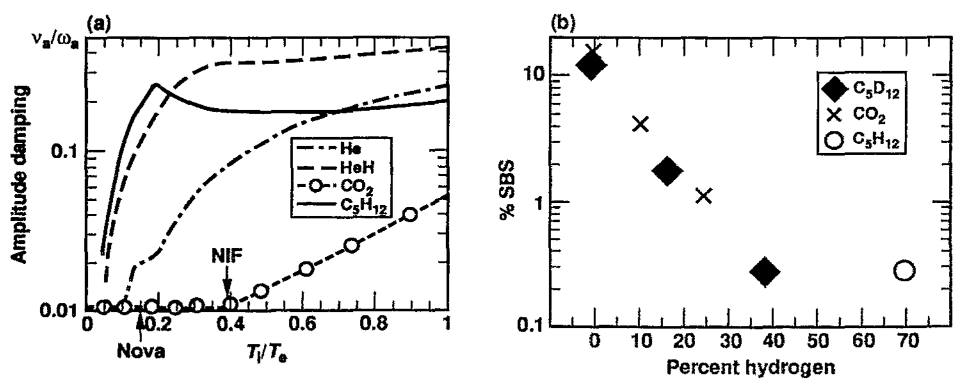

FIG. 91. Damping rates for helium–hydrogen mixtures in NIF are larger than for Nova CH mixtures: (a) 50/50 mixture of helium and hydrogen consistent with a 17 K cryogenic target; (b) protons mixed with CO_2 or C_5D_{12} reduced reflectivity in Nova experiments.

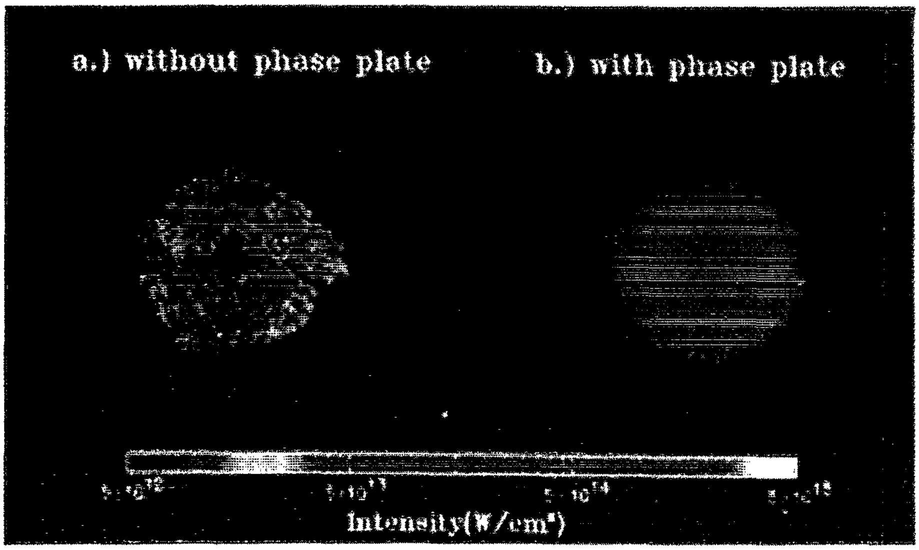

FIG. 92. Although speckle intensities are equally large with and without a random phase plate, a phase plate produces a more uniform focal spot distribution, as shown for a Nova beam.

coherence length of a speckle is approximately the Rayleigh range for the lens and is given by $l_{sp}=8f^2\lambda$. This effect is shown in the simulation [214] of an $f/4$ beam and an $f/8$ beam (see Fig. 93). Since filamentation and SBS will grow out of these speckles, the f number selects the size and coherence length for the most unstable growth regions in the plasma. If the spatial growth length for filamentation is greater than the length of the filaments, then filamentation is suppressed. This puts an upper limit on the f number, as given by[213,214]

$$f \lesssim \left(0.8\pi \frac{n}{n_c} \frac{I_{15}}{T_e(\text{keV})} G \right)^{-1/2} \Rightarrow f \lesssim 8, \quad \text{for NIF,} \tag{195}$$

where G is a factor that accounts for thermal effects. Filaments also will be stabilized if the growth rate γ is less than the bandwidth $\Delta\omega$, or equivalently,

$$\frac{\Delta\omega}{\omega} \gtrsim 0.05 \frac{n}{n_c} \frac{I_{15}\lambda^2}{T_e(\text{keV})} G \Rightarrow \frac{\Delta\omega}{\omega} \gtrsim 4\times 10^{-4}, \quad \text{for NIF.} \tag{196}$$

With a phase plate, the SBS signal levels dropped significantly in experiments at the University of Rochester, at Rutherford, and at Ecole Polytechnique.[215–217] Similar effects are seen in experiments currently being conducted on Nova. SSD experiments in which phase plates are combined with up to about 0.15% laser bandwidth have begun on Nova. Nova also has the ability to propagate four separate frequencies, separated by up to about 8 Å, through a single beamline. These techniques for beam smoothing can both be implemented on the NIF. These experiments are being done with both $f/4$ and $f/8$ lenses and with a variety of hohlraum

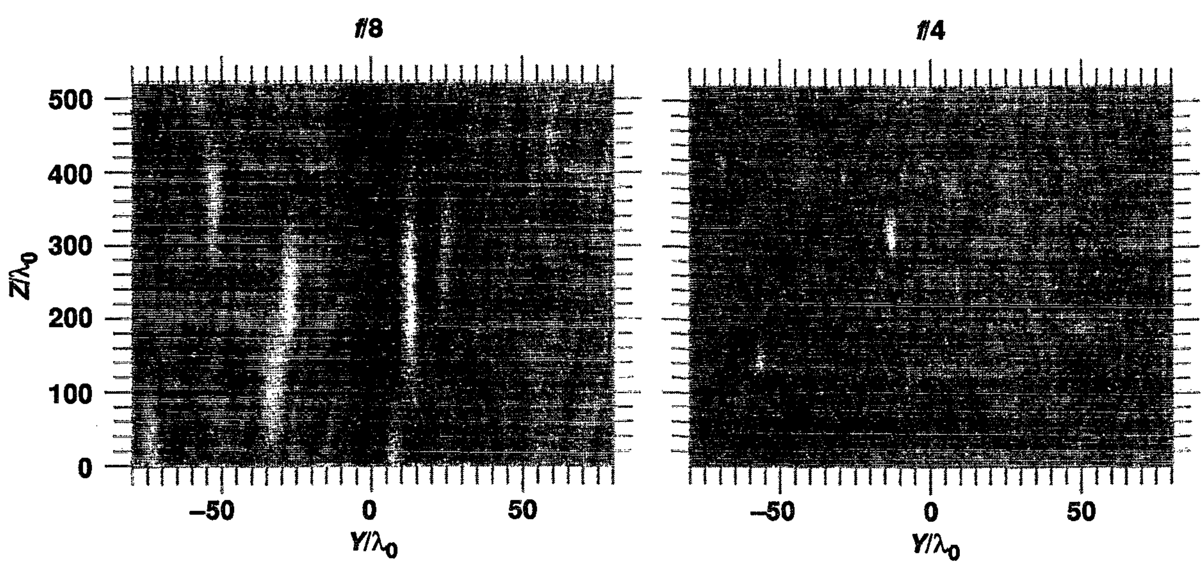

FIG. 93. Near "best focus," the field of a random phase-plate beam consists of long, narrow speckles whose size depends on lens f number and laser wavelength.

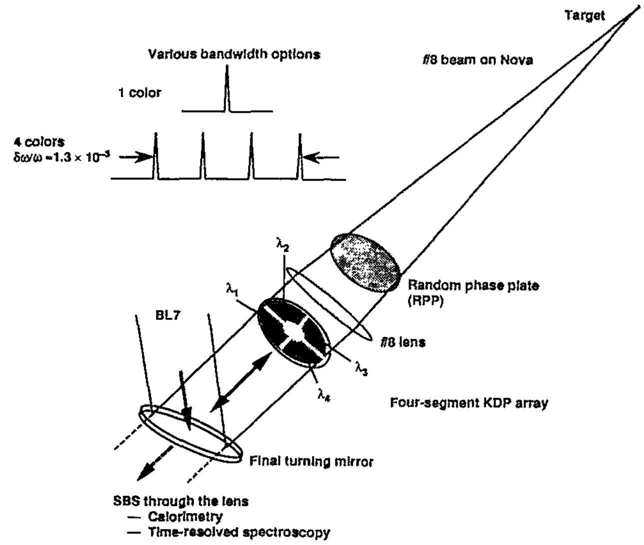

FIG. 94. One Nova beam has been converted to approximate the NIF focusing conditions for measuring SBS. The laser frequency in each of the four KDP segments can be separated by up to 8 Å (at 1 ω). SSD also can be implemented.

gas fills. The NIF laser design combines four $f/20$ beams propagating together as a single $f/8$ cluster. One beamline of Nova has been modified to simulate this configuration, as shown schematically in Fig. 94.

To evaluate the limits to the plasma conditions and laser intensities for ignition-scale hohlraums, experiments on Nova are being carried out both in open geometries and in hohlraums, as shown in Fig. 95. Open-geometry plasmas with the required dimensions and plasma density are being investigated by using "gasbag" targets,[218] in which the volume between two films of polyimide is filled with neopentane, deuterated neopentane, or CO_2 at about 1 atm. The gas-filled hohlraums[219,220] have a thin (<1 μm) plastic membrane covering the LEH and are filled with similar gases. Figure 96 and Table VI compare the plasma conditions calculated for the Nova experiments and for the NIF hohlraum.

Nine of Nova's ten beams are used to heat the plasma. The tenth beam is used as an interaction beam, delayed until the desired plasma conditions are reached, as shown in Fig.

TABLE VI. Detailed LASNEX calculations show that Nova plasmas are similar to those expected for the NIF.

	Nova		NIF	
	Gas bags	Hohlraums	Inner cone	Outer cone
Path length, l (mm)	~2	~2	~3	~2.5
$\int(n_e/n_c)dl$ (mm)	~0.2	~0.2	~0.3	~0.15
V_{flow} (cm/s)	$<10^7$	$<10^7$	$<10^7$	$<10^7$
L_v (mm)	>6	>6	>10	>6
T_iT_e	0.1–0.2	0.1–0.2	0.4	0.3–0.4

97. Figures 98 and 99 show calculated and observed 3 keV x-ray images of the gasbag and hohlraum targets. By about 500 ps, the plasma in the gasbag target is quite uniform. The hohlraum target, which has a ramped pulse, as shown in Fig. 97, has uniform conditions by about 800 ps. Hohlraum electron temperatures are obtained by using x-ray spectroscopy,[221] as shown in Fig. 100. Electron temperatures are 3–4 keV, in agreement with LASNEX simulations.

Time-integrated SBS reflectivities are less than 1% from C_5H_{12} plasmas for both open and closed geometries with $f/8$ focusing. Figure 101(a) shows the reflectivities for the gasbag[218] experiments. Peak reflectivities are about a factor of 2 larger. These levels are well within the goal of having less than 10% SBS on ignition targets.

The calculated linear SBS gain coefficients Q for the Nova experiments are comparable to or higher than those of NIF targets, as shown in Fig. 102. Without nonlinear saturation, the predicted SBS scattering, which scales as e^Q would be larger than that seen in the experiments. Current models usually include only pump depletion as a saturation mechanism. Additional nonlinear saturation mechanisms, such as limitations in the magnitude of ion particle-density fluctuations $\delta N/N$ caused by particle trapping,[222] are being evaluated.

A particular issue not addressed by these low-Z plasmas is the influence of the gold plasma near the hohlraum wall in the generation of SBS. Although most of the laser pathlength in NIF targets is through low-Z plasma, there is a 200–300 μm "shelf" of gold plasma with a density of $\sim 0.2n/n_c$ in the NIF targets. This scale length is set by inverse brems-

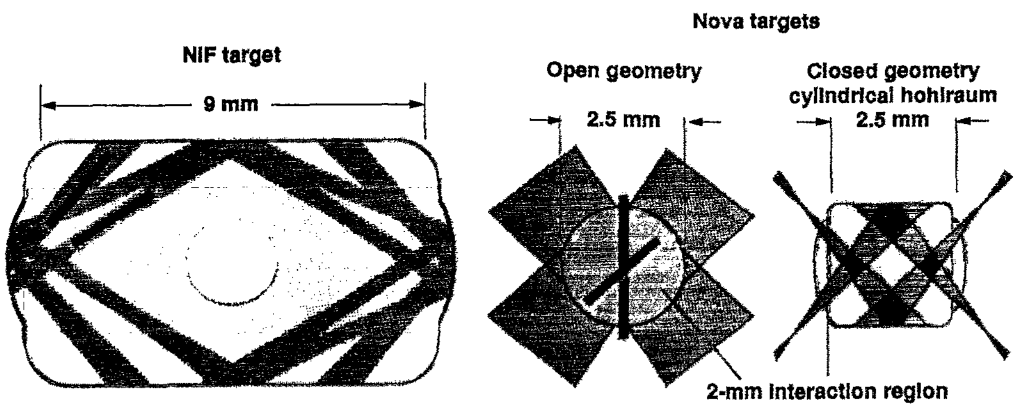

FIG. 95. Long-scale-length plasma experiments have been performed in both open and closed geometries.

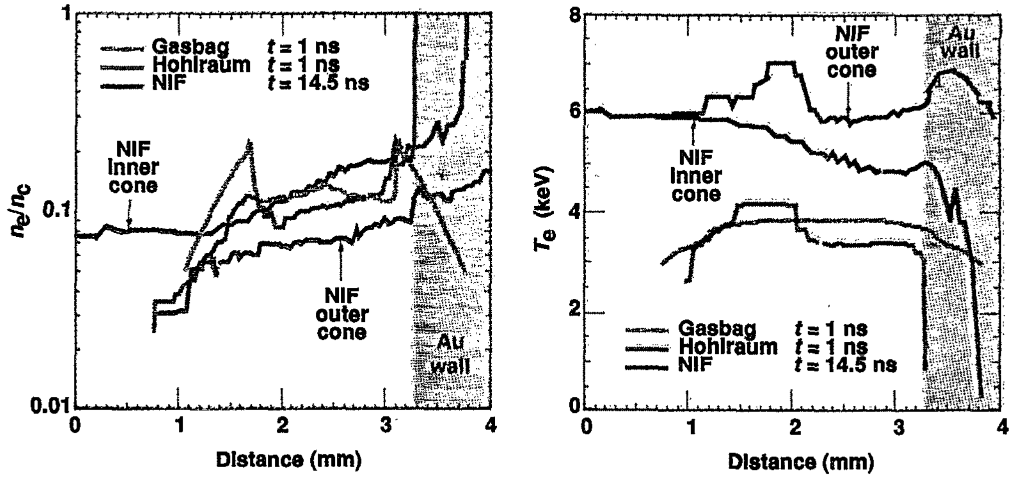

FIG. 96. Detailed LASNEX calculations show that Nova plasmas are similar to those expected for the NIF.

strahlung absorption and is about the same for NIF targets and current Nova hohlraums used for implosions. Although the scale lengths are small, the density is relatively high, the velocity gradients are small, and the ion Landau damping is weak, so that significant reflection, such as was seen in the CO_2 gasbag plasmas mentioned above, is possible. In fact, the several-percent levels of SBS seen in the Nova gas-filled hohlraum symmetry experiments are associated with the gold wall plasma. The SBS levels in these experiments drop to about 1% when the gold wall is removed. As was demonstrated for the CO_2 plasmas, calculations indicate that the level of SBS in the gold can be significantly reduced by doping the gold with a small amount of hydrogen (for example, the hydrogen could come in the form of CH_2 cosputtered with the gold when the hohlraum is constructed) or beryllium. Experiments to evaluate this effect will be carried out on Nova. Initial Nova experiments with alternating 78 Å Au and 32 Å Be layers show SBS levels reduced to about 1%.

The scattered-light experiments on Nova have been extended recently to include Raman-scattered light. These measurements indicate that the level of Raman scatter from $n/n_c<0.1$ can be larger than the SBS. For the range of intensities of interest to NIF ignition designs, 5×10^{14} to 2×10^{15} W/cm^2, the scattering levels are about 2%–5% with phase plates and 2 Å of SSD as shown in Fig. 101(b). This level is well within the NIF specification of <15% for energetics. Without SSD temporal smoothing, the level is about 10% at the upper end of the NIF intensity range, but still only about 2% at the lower end. The higher intensity of about

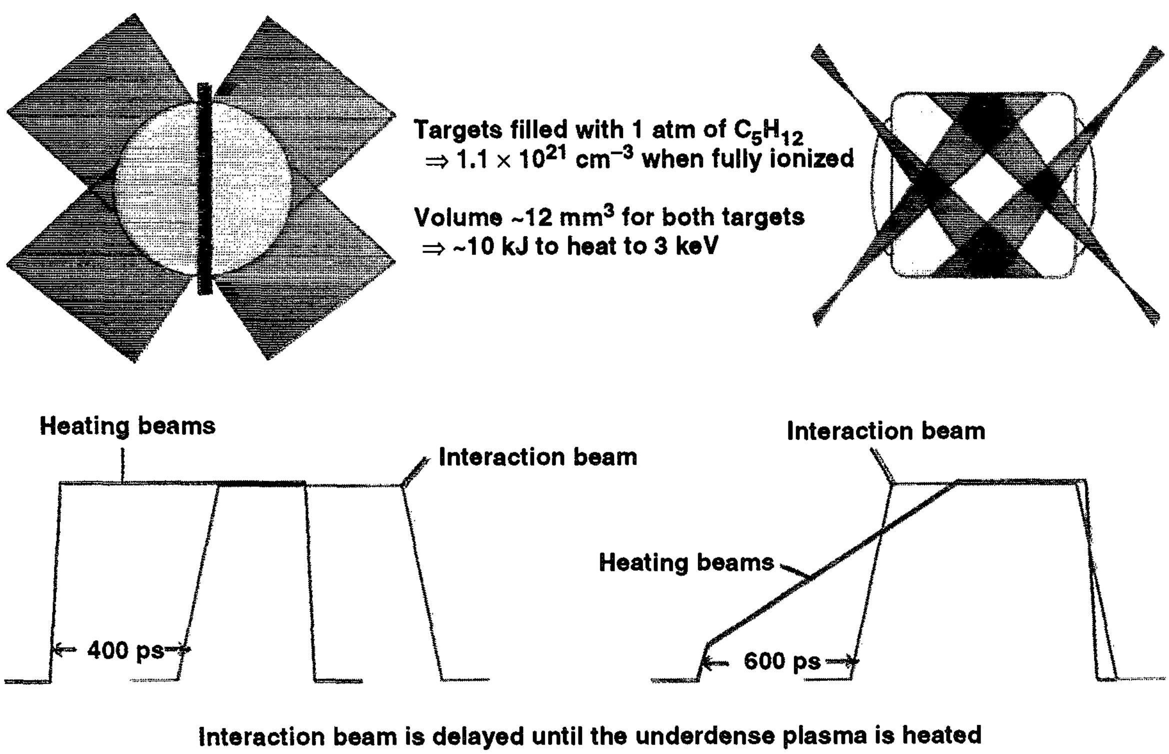

FIG. 97. Nine of Nova's beams are used to produce large scale-length plasmas. The interaction beam is delayed until the underdense plasma is heated.

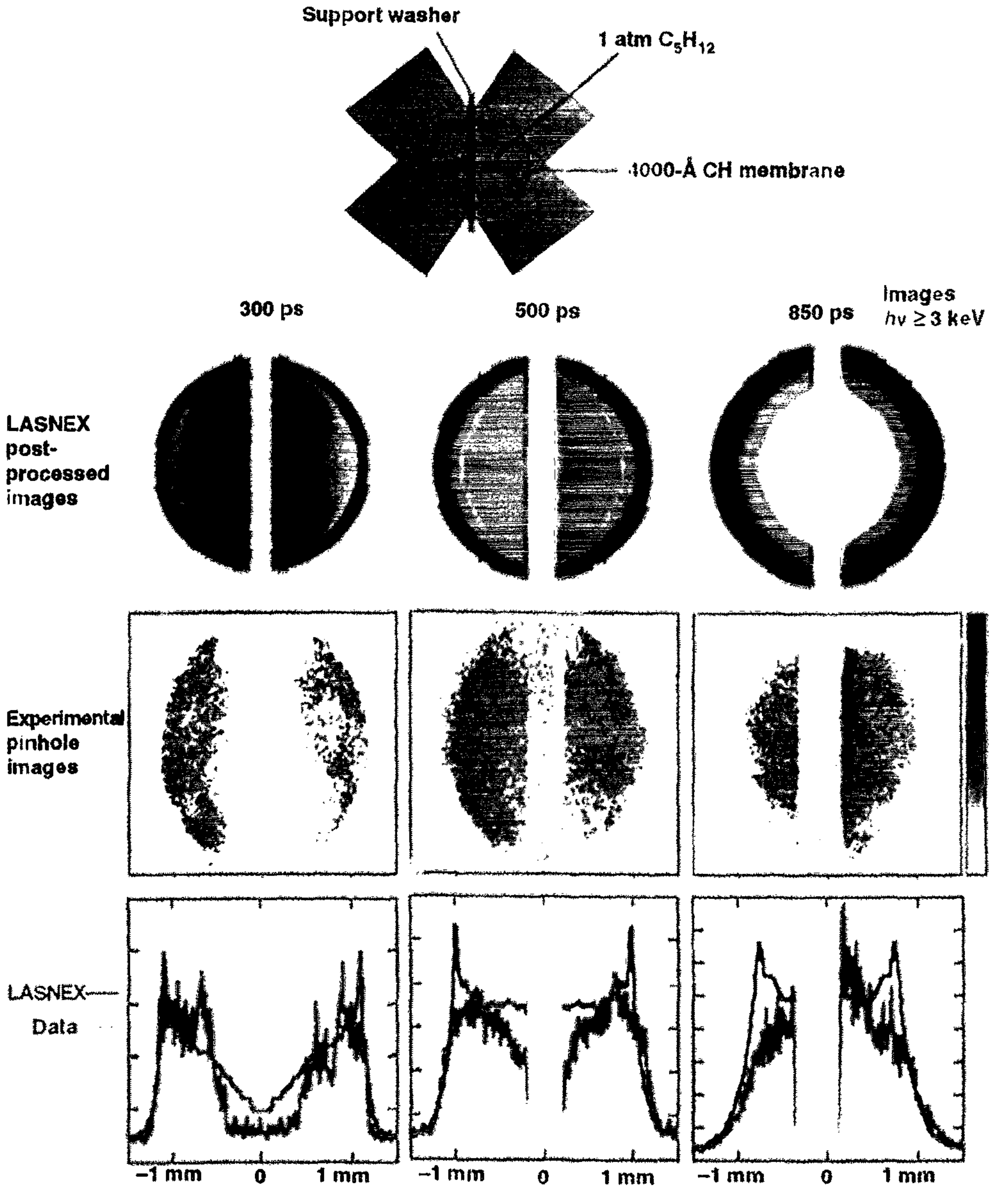

FIG. 98. X-ray images and calculations show that the long-scale-length plasmas are 1.5–2.0 mm in diameter during the time of the interaction beam.

2×10^{15} W/cm^2 applies to 300 eV peak hohlraum temperatures on NIF, whereas the lower intensity applies to 250 eV hohlraums. Ignition designs exist for both temperatures, but there is more margin for hydrodynamic instabilities at the higher hohlraum temperature. Raman scattering from these low densities produces hot-electron temperatures less than 20 keV. The NIF capsules have significant self-shielding for these energies, so the low-density SRS is not a preheat issue. The measured Raman scattering is narrowly collimated back into the $f/8$ incident lens. This observation is consistent with numerical calculations using the F3D code,[213] which integrate the Raman-scattering equations back through the plasma. The Raman gain is largest in the beam speckles, which geometrically favor scattering in a narrow backward direction. Because the SRS is directly back into the lens, this scattering does not adversely affect symmetry. As determined by high-energy x-ray measurements, the fraction of laser energy coupled into hot electrons with a temperature $\geq$50 keV, characteristic of Raman scattering or the $2\omega_{pe}$ instability near $n/n_c\approx\frac{1}{4}$, has been consistently less than about 1% for both the Nova implosion experiments and the large plasma experiments. Preheat from high-energy electrons is discussed in Sec. XII.

Further work on Nova is planned in order to more thoroughly evaluate Raman scattering levels and the role of laser-beam filamentation. These experiments will help to improve quantification of the range of plasma conditions that are accessible for ignition experiments.

XII. HOT ELECTRON PREHEAT

Understanding the behavior of Raman instability for ignition hohlraums is important because high-phase-velocity plasma waves produce very energetic electrons when they are damped in the hohlraum. These energetic electrons are a source of preheat, which can raise the fuel adiabat and make

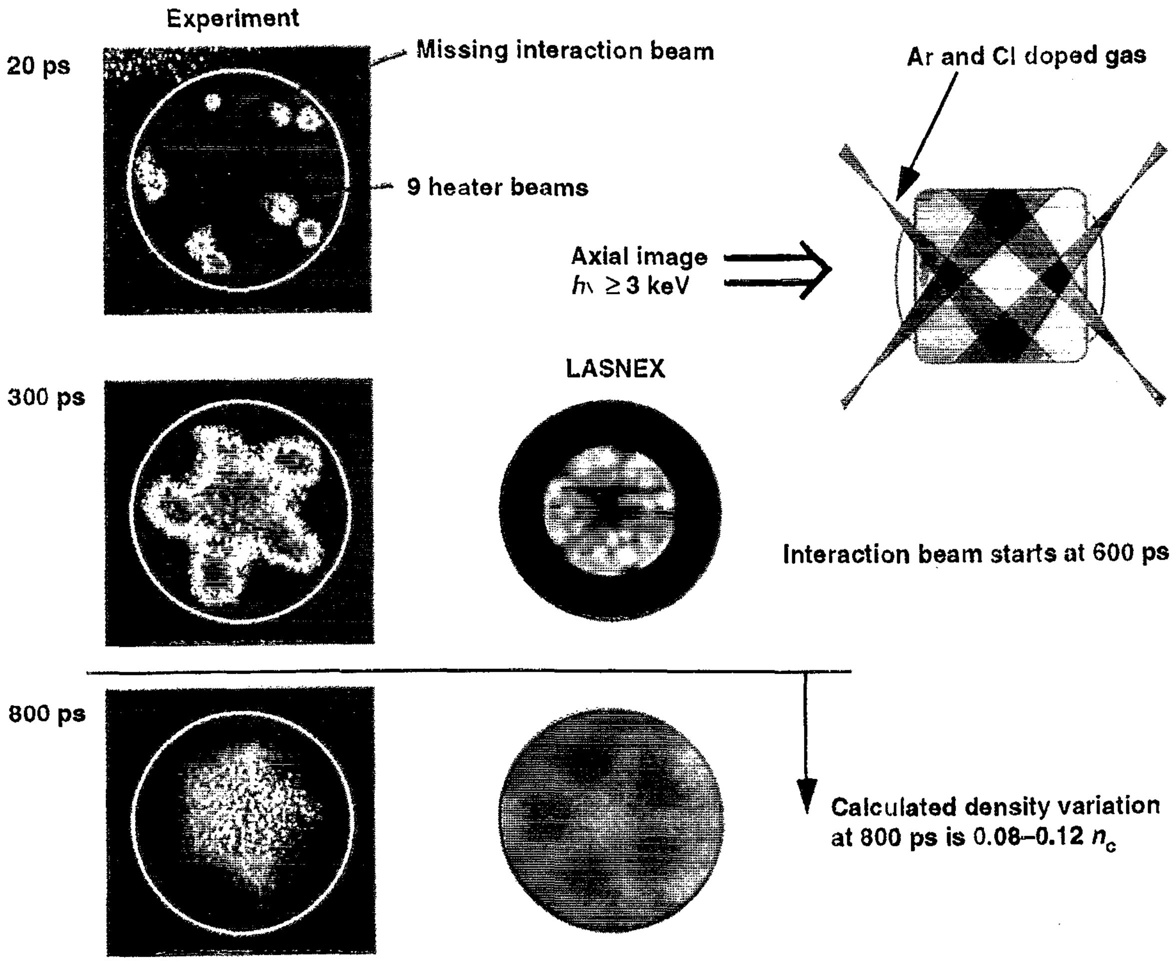

FIG. 99. Axial images of the hohlraum show uniform, underdense plasma during the interaction pulse.

the fuel less compressible, raising the ignition threshold. High levels of Raman scattering were the principal limitation to hohlraum experiments at 1 μm on the Shiva laser. Above hohlraum temperatures of 130–to 140 eV, significant levels of Raman scattering were observed. Preheat in the DT fuel must be limited to approximately the Fermi specific energy, ϵ_F (see Fig. 3), at the density of the fuel during the implosion. At this level of preheat, the pressure required to achieve a given density in the fuel doubles. Since the main fuel density during an implosion varies from a few to about 15 g/cm^3, the preheat must be limited to between 1 and 5×10^5 J/g. This preheating limit also can be expressed in terms of the fuel entropy, as presented in Sec. IV. If the preheat comes during the peak-power part of the implosion, while the capsule is at or near the peak ablation pressure, then the fuel is at the higher density and the higher preheat level is appropriate, as assumed below.

The preheat $\epsilon(x)$(J/g) inside an ablator of thickness x(g/cm^2) and area A(cm^2) caused by a Maxwellian distribution of electrons with a temperature $T_{\rm hot}$(keV) and energy $E_{\rm hot}$(J) is given by [223,224]

$$\epsilon(x)=\frac{E_{\rm hot}}{xA}\,y^{0.9}\,\exp(-1.65y^{0.4})=\epsilon_0 G(y), \qquad (197)$$

where $y=x/x_0$, where x is the thickness, in g/cm^2, of the ablator. Here x_0 is an approximate mean electron range, in g/cm^2, given by

$$x_0=\frac{3\times10^{-6}(A/Z)T_{\rm hot}^2}{Z^{1/2}}, \qquad (198)$$

where $T_{\rm hot}$ is the hot-electron temperature in keV and $G(y)$ is an attenuation factor that occurs because lower-energy electrons are absorbed in the ablator and do not reach the fuel. Here $G(y)$ is derived under the assumption that the hot electrons are not anomalously flux limited. Preheat on witness-plate experiments on Shiva[225] and Novette[226] were consistent with these assumptions, but these experiments were not carried out over a wide range of conditions.

Using Eq. (197), we can write the tolerable fraction of the laser energy into hot electrons as[227]

$$f_{\rm hot}=\frac{\epsilon_F M_F}{E_L G(y) D(r_{\rm source}/r_{\rm cap})}, \qquad (199)$$

where M_F is the fuel mass and E_L is the laser energy. $D(r_{\rm source}/r_{\rm cap})$ is a geometric dilution factor for the hot electrons. This factor is significant in hohlraums because the laser beams, where the hot electrons would be produced, are at some distance from the capsule. If hot electrons are isotropic,

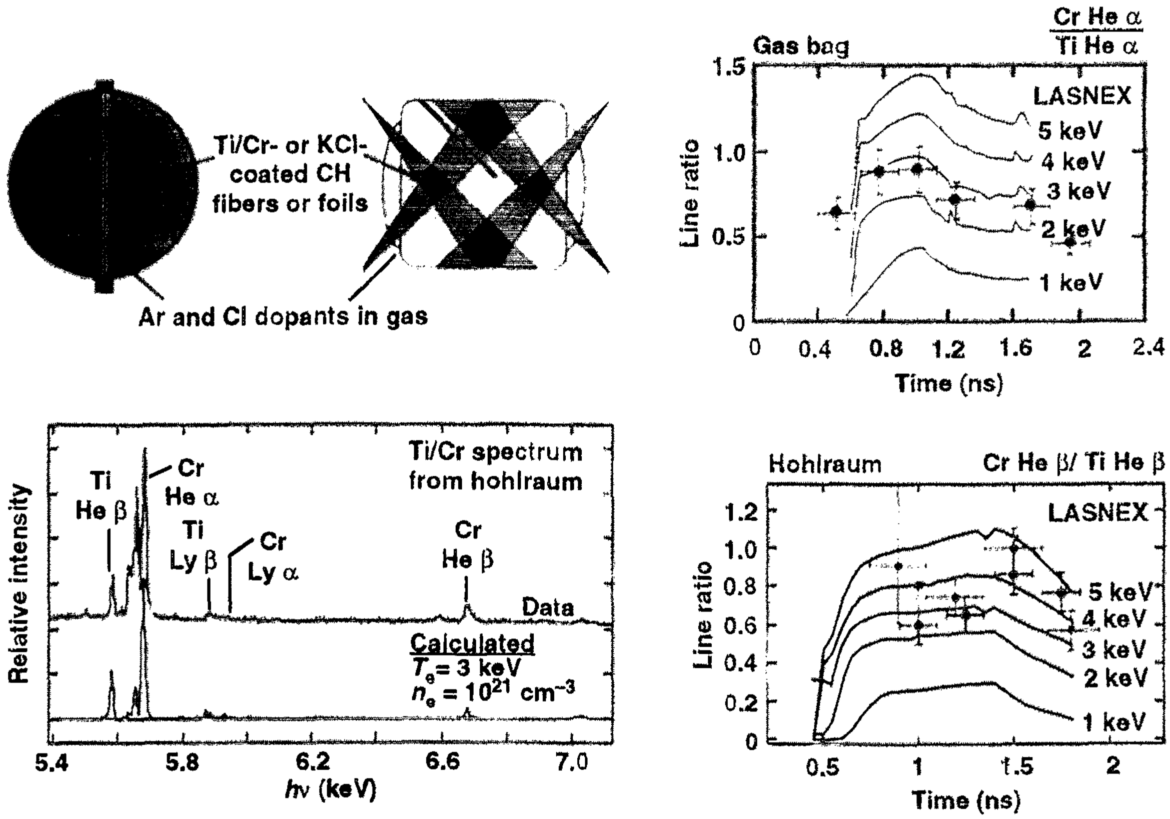

FIG. 100. X-ray spectroscopy indicates $T_e \geq 3$ keV for both open and closed geometries.

only those electrons that are in the solid angle subtended by the capsule will hit the capsule. If we take the average location of hot-electron production as the average case radius, the fraction of hot electrons hitting the case is equal to the ratio of the capsule area to the case area. Some of the electrons that miss the capsule will be reflected off the high-Z case and have another chance to intercept the capsule. For typical high-Z materials, about 50% of the incident electrons will be reflected with about 70% of their original energy. For the discussion below, $D=0.1$ is used. Figure 103 shows the hot-electron fraction that would result in fuel preheat equal to the Fermi specific heat as a function of the hot-electron temperature. The minimum tolerable level, for $40 \leq T_{\text{hot}} \leq 80$ keV, is about $f_{\text{hot}}=6\%$. If these hot electrons come from damping of plasma waves produced by Raman backscatter, the hot-electron temperature on the NIF is expected to be 20–40 keV. Raman forward scatter could produce much higher temperatures, but at reduced efficiency.

Nova hohlraum experiments with 0.35 μm light have all had hot-electron levels, based on high-energy bremsstrahlung emission, of about 1% or less. This includes the high-temperature, 300 eV hohlraums and hohlraums with long pulses. Experiments to measure Raman scattered light directly have begun on the NIF scale plasmas described in Sec. XI.

In the case of direct-drive capsules, the beams are absorbed in the immediate vicinity of the ablator, so there is very little geometric dilution of the hot electrons. In addition, direct-drive capsule have less ablator to provide preheat shielding for the fuel. Because of both of these factors, direct-drive capsules are more sensitive to preheat than are indirect-drive capsules. Figure 103 also shows the tolerable preheat fraction for a 1.8 MJ direct-drive capsule such as those now being investigated by LLE.[55,228,229] Direct-drive capsules likely will require an adiabat elevated by a factor of 3–4 over Fermi degeneracy to reduce hydrodynamic instability, as discussed in Sec. VI. In this case, direct-drive capsules could tolerate a fraction of hot electrons three to four times larger than indicated in Fig. 103 without further degradation in performance.

XIII. NATIONAL IGNITION FACILITY AND IGNITION TARGETS

The proposed National Ignition Facility (NIF) will use modern electro-optic technology, compact segmented amplifiers, and multipass laser architecture. Improvements in optical manufacturing will enable optical fluences greater than 2–4 times those used on Nova, substantially reducing the total laser aperture (and thus cost) required for ignition performance. Figure 104 is a schematic of the NIF from the recently completed conceptual design report.[230] Figure 105 is a schematic of the NIF target area.

The NIF, as currently proposed, is a 192-beam, frequency-tripled ($\lambda=0.35$ μm) Nd:glass laser system with routine on-target energy and power of 1.8 MJ and 500 TW,

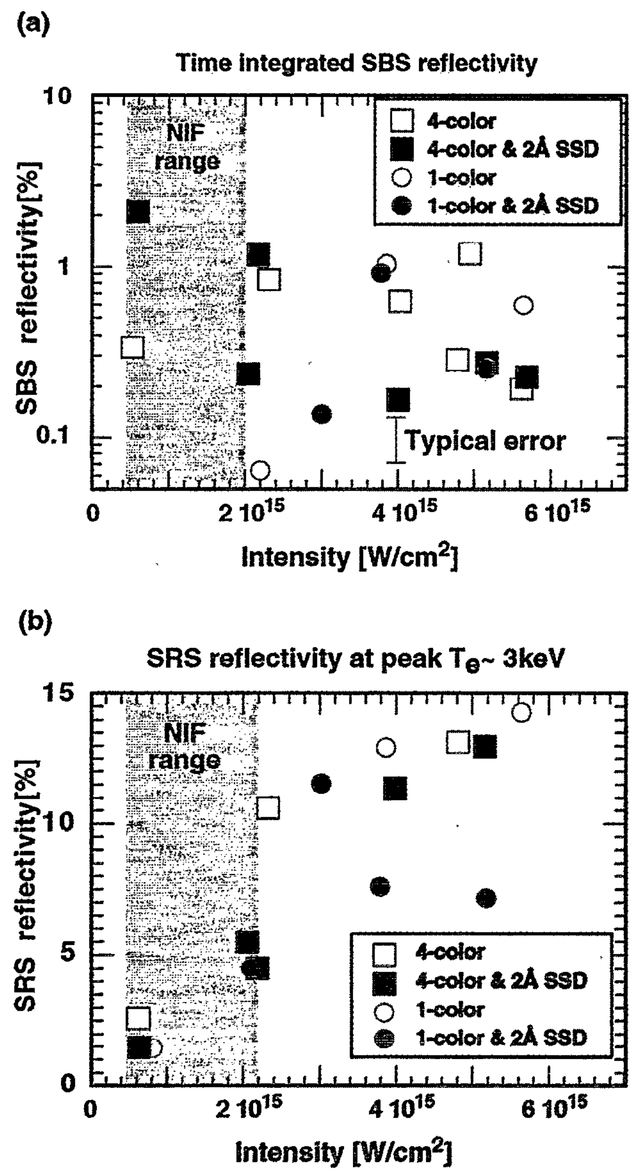

FIG. 101. (a) Time-integrated SBS reflectivities are 1% or less in energy from C_5H_{12} plasmas for both open (gasbag) and closed (hohlraum) geometries with $f/8$ focusing. Shown is the gasbag data. (b) For the range of intensities of interest to NIF ignition designs, SRS scattering levels are 2%–5% with phase plates and 2 Å of SSD. Without SSD temporal smoothing, the SRS level is about 10% at the upper end of the NIF intensity range, but still only about 2% at the lower end.

appropriately pulse shaped.[231] A scientific prototype of one of the NIF beams, the "Beamlet," is operational and has demonstrated most of the NIF laser requirements, including laser fluence and high-efficiency conversion to 0.35 μm light. The Beamlet will be used to continue to refine the NIF laser design before construction is initiated.[232,233]

The NIF system design requirements given in Table VII for indirect drive have been determined from the baseline target shown in Figs. 106 and 107. The hohlraum in Fig. 106 uses 1.35 MJ to drive the 150 kJ capsule in Fig. 107 at 300 eV.

As discussed in Sec. IX, the light coming in each LEH in Fig. 106 is in two cones, so we can minimize time-dependent

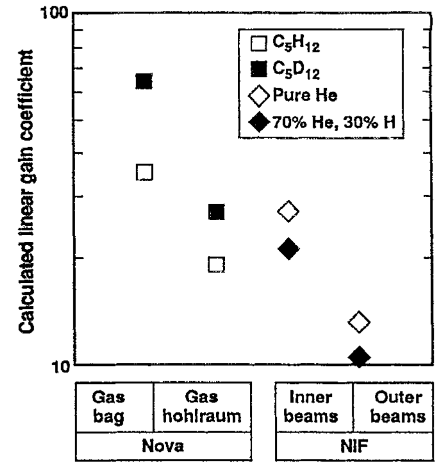

FIG. 102. Calculated linear SBS gain coefficients for the Nova experiments are comparable to those of NIF targets.

asymmetry in the x rays incident on the capsule by dynamically varying the relative brightness of the cones. About a third of the energy must go into the cones near the target midplane. The 192 beams are clustered in groups of 4, so that there are effectively 8 spots in each of the inner cones, and 16 in the outer cones. Each cluster of four beams combine to form an effective $f/8$ optic.

Each beam is focused to an elliptical spot, which reduces laser intensity without reducing LEH clearance. The spot has a shape approximating a flat top (probably a sixth-order super-Gaussian), again to minimize the peak intensity while maximizing LEH clearance. The nominal spot is 500 μm by 1000 μm at best focus. Such a spot can be made with recently developed kinoform phase plate techniques.[234,235]

The CH ablator in Fig. 107 contains 0.25 at. % bromine dopant. (The HEP-4 targets discussed in Sec. VI now use bromine-doped or germanium-doped CH.) The dopant, used to control the stability of the ablator/DT interface, reduces the preheat in the CH and eliminates an unstable density step at the CH/DT interface. As seen on current Nova targets, the CH is assumed to contain 5% oxygen as an incidental fabrication byproduct.

A convenient way to evaluate the laser requirements for ignition targets is shown in Fig. 108. For a given hohlraum

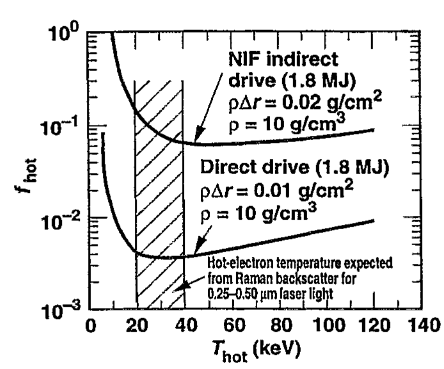

FIG. 103. The hot-electron fraction f_{hot} resulting in fuel preheat equal to Fermi energy varies from <1% for direct-drive ignition capsules to >5% for the indirect-drive capsules on the NIF.

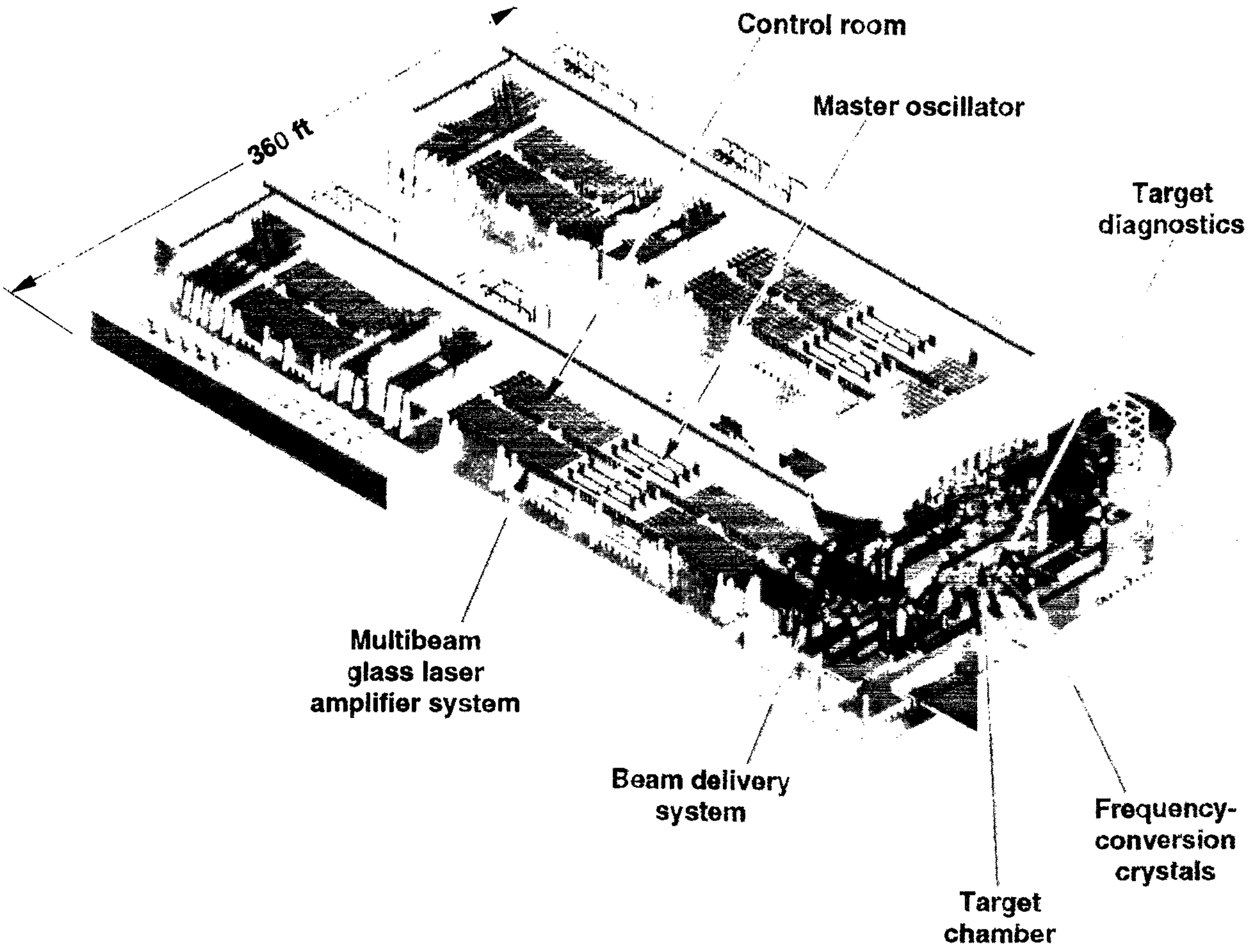

FIG. 104. The NIF is being designed to produce 1.8 MJ of 0.35 μm laser light with 500 TW for defense applications and inertial fusion ignition. The NIF will be able to explore ignition with both indirect-drive and direct-drive targets.

temperature T_r, Eq. (92) specifies the relationship between laser power and laser energy. Using the 11% hohlraum coupling efficiency calculated for the NIF hohlraum in Eq. (92), we obtain the set of curves labeled at different hohlraum temperatures in Fig. 108. Laser plasma coupling will limit the achievable hohlraum temperature. From Eq. (192), at 400 eV for the long pulses required for ignition capsules, the hohlraum plasma will approach $n/n_c \approx \frac{1}{4}$. Based on the hohlraum experimental results at 1 μm, this is probably an upper-limit temperature for ignition hohlraums. (For short pulses with reduced plasma filling, it should be possible to achieve higher temperatures.) We now are limiting peak hohlraum temperatures to about 300 eV, which limits the plasma densities to $n/n_c \approx 0.1$, as shown in Fig. 90.

The minimum capsule energy is proportional to $T_r^{-4.5}$, as given by Eq. (87). With a surface finish of about 10 nm, we require a margin in energy of about 1.5 above this minimum to ignite with the resultant mix. With a 100 nm surface finish, we require about a factor of 3 above the minimum energy. This gives the pair of curves, at these two different capsule surface finishes, which cut across the hohlraum temperature curves. Combining Eqs. (87) and (92), for a constant surface finish of 10 nm, gives

$$P_{\mathrm{laser}}(\mathrm{TW}) = 285 E_{\mathrm{laser}}^{0.23}(\mathrm{MJ}). \tag{200}$$

The region between the NIF laser design performance and the intersection of the achievable hohlraum temperature and achievable capsule surface finishes defines the operating space for ignition targets. We have evaluated a variety of capsules and hohlraums within this region, as indicated by the dots on Fig. 108. Most of the target analysis[236–238] has focused on the baseline 300 eV hohlraum and capsule shown in Figs. 106 and 107. Because this target design (referred to as the PT design) operates near the expected maximum hohlraum temperature, it is a good design to evaluate the laser power requirements. Also, because the laser–plasma coupling is more of an issue at the higher temperatures, as indicated in Sec. XI, it is important to investigate the high-temperature designs in detail. At 1.35 MJ, this point design is below the 1.8 MJ, 500 TW NIF laser design performance, and above the ignition energy minimum. This design allows for uncertainty in both laser–capsule coupling efficiency and ignition threshold.

The one-dimensional (1-D) capsule simulations described next are done with the LASNEX code,[51] using P_N radiation transport,[239] equations of state calculated in line

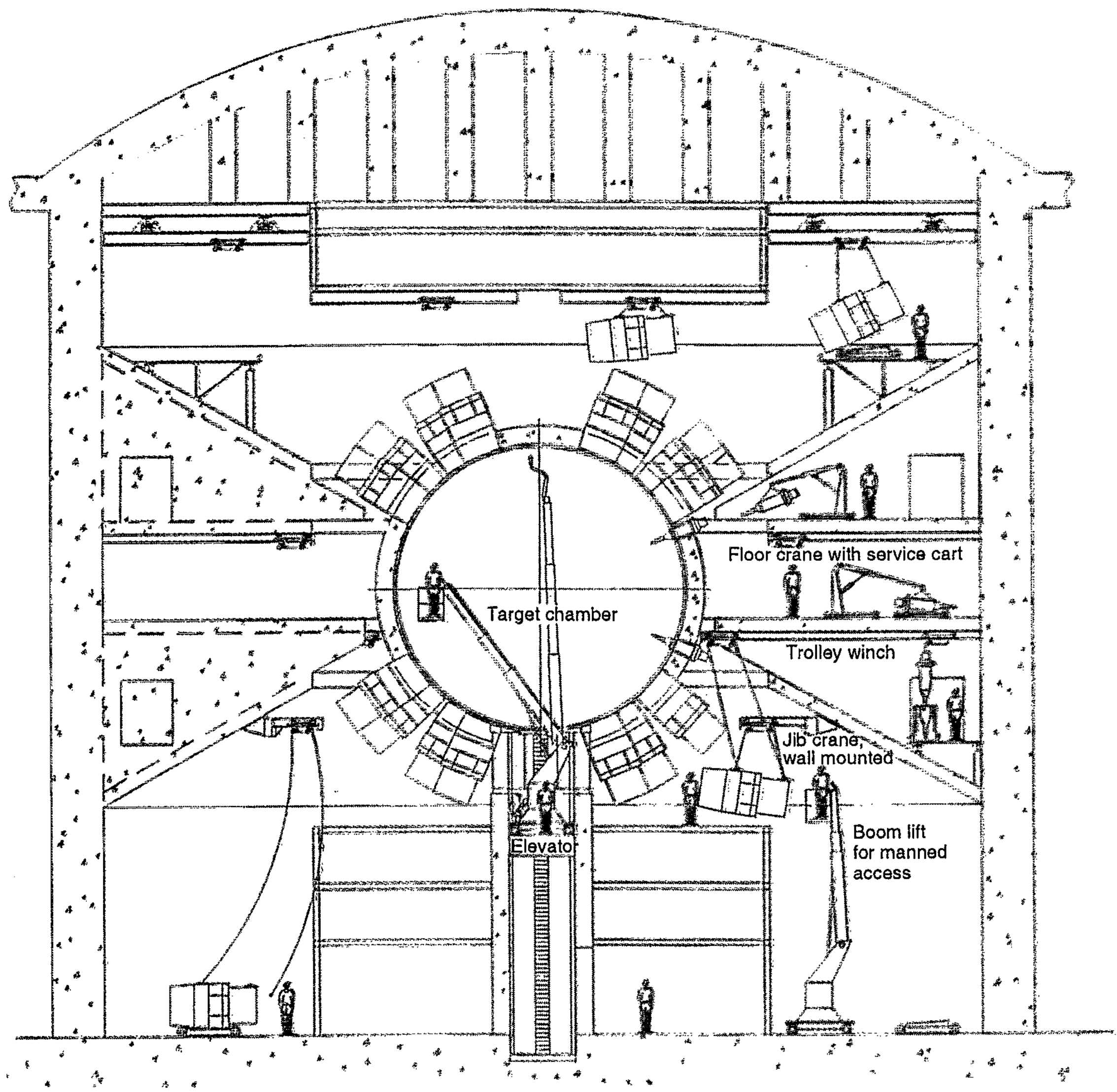

FIG. 105. The NIF target area is configured for accessibility and ease of maintenance for both laser operations and target experiments.

with a "Quotidian EOS" model,[240] and average-atom XSN opacities.[241] Other radiation-transport schemes predict the same capsule performance. As a source for implosion calculations, non-Planckian frequency-dependent radiation was determined from hohlraum simulations. The spectrum used affects the short-wavelength hydrodynamic instability growth. Other than this effect, which can change perturbation amplitudes by about a factor of 2, the spectrum has little effect on target characteristics. The deposition of α particles produced by the burn is normally calculated with the multigroup diffusion[242] model in LASNEX. Calculations[243] of the PT capsule using a Monte Carlo charged-particle transport model[244] produce ignition and burn that are essentially the same as produced by multigroup charged-particle diffusion.

The pulse shape shown in Fig. 106 creates four shocks. The final shock brings the ablator up to peak pressure with sufficiently low DT entropy, as previously shown in Fig. 37. The entropy requirement implies a corresponding requirement on pulse-shaping precision. For optimal performance, the shocks must be timed within about 200 ps. Given uncertainties in opacity and equation of state, adequate shock timing may not be predictable *a priori*, but it is achievable with an experimental program that uses techniques currently available on Nova.[108–110,149]

The capsule in Fig. 107 can tolerate moderate deviations from the optimal radiation temperature profile shown in Fig. 106. For example, Fig. 109 shows the yield as the early-time foot and peak drive temperatures are varied.

A lower temperature capsule design is shown in Fig. 110. This capsule was designed with a beryllium ablator, which develops a somewhat higher ablation pressure since it has a lower albedo in this temperature range. Hence, the capsule absorbs more flux at a given temperature, as discussed in developing equation (137). This is important at the lower temperature. Figure 111 shows the sensitivity of the beryllium capsule to pulse-shape variations. A higher-temperature foot to the pulse results in an overall shorter pulse but puts the capsule on a higher adiabat. This reduces the ignition margin and makes capsule performance more sensitive to hydrodynamic instabilities, the resultant mix, and

TABLE VII. Functional requirements for the indirect-drive NIF laser design.

Energy (measured at the entrance hole of the hohlraum)	1.8 MJ
Peak power	500 TW
Wavelength	0.35 μm
Pulse shape	Continuous or discrete pulses
Duration	20 ns
Dynamic range	
—Continuous	50:1
—Discrete	10:1
Capsule irradiation symmetry	Hohlraum illumination: Geometry: 2 concentric cones from each side Cone angles: 27° and 52° Beamlet distribution: $\frac{2}{3}$ on outer cone $\frac{1}{3}$on inner cone
Beamlet energy balance	8% RMS
Beamlet pointing accuracy	50 μm
Prepulse	$<10^8$ W/cm^2
Pulse simultaneity	<30 ps
Spot size	500 μm at the laser entrance hole
Beam smoothness	Kinoform phase plates at the output Centerline frequencies separated nominally by 1 nm at 1 ω in each beamlet of a 2×2 array 2×2 array of beamlets superimposed on target to control intensity fluctuations averaged over a 30 μm circle and 10 ps to less than 25% of average intensity

small deviations in the pulse. The shorter duration pulse in Fig. 111 is almost a direct geometric scale of ps22 used in most of the Nova symmetry experiments discussed previously. For the set of curves with the lower-temperature foot, the stepped temperature pulse and the middle continuous pulse give equivalent capsule performance.

The initial gas-fill density in the capsule, which can be controlled by varying the temperature of the cryogenic fuel, can be used in turn to control the capsule's convergence ratio, and hence its sensitivity to flux asymmetry. Figure 112 shows the result of varying the initial fill on the convergence ratio for the 300 eV baseline CH capsule. The yield decreases as the initial gas fill is increased because the total fuel ρr decreases. With a CH ablator, the convergence ratio can be decreased approximately from 35 to 25 before the yield drops below 1 MJ. With a 300 eV beryllium ablator capsule, the convergence ratio can be reduced further to about 20, as shown in Fig. 112.

As discussed previously, Nova capsules are made largely from plastic. A CH ablator was chosen for the baseline NIF capsule because developing, characterizing, and filling NIF capsules from this material would be more straightforward by means of techniques similar to those already developed for Nova capsules. Techniques are now being evaluated to develop high-quality beryllium shells.

All NIF targets require about a 100 μm cryogenic layer of DT. The physics and technology of thick cryogenic layer formation are quite complex. A prime candidate for thick layer formation is called β layering.[245,246] Because of tritium β decay, DT fuel produces heat at about 1 W/g. If a capsule partially filled with solid DT is held at uniform temperature, the DT will tend to form a uniform layer. If the layer is nonuniform, differential cooling will result in a higher surface temperature and a higher sublimation rate at the thicker part of the layer. Condensation will occur preferentially on the thinner and cooler parts of the layer. This technique produces uniform layers, but the surface quality of the layers depends on many variables that are still being investigated. Calculations indicate that the cryogenic layer must have a RMS surface finish of 0.5 μm or less in spectral modes below $l \approx 30$. Current estimates from cylindrical β-layer experiments carried out jointly by Los Alamos and LLNL indicate that a β layer will have a surface roughness about 2–4 times larger then this.[247] However, experiments also indicate that additional heating (either from Joule heating of free electrons in the DT driven by a microwave power source or from infrared absorption in the rotational and vibrational absorption bands of DT) can improve uniformity to the required level.[248] This latter technique also should apply to DD layers, which will be required for a variety of diagnostic experiments.

Alternatively, a uniform layer may be produced by applying a temperature gradient to a liquid cryogenic layer.[249] Because both surface tension and evaporation rates are temperature dependent, it is possible under some conditions to obtain a uniform layer by adjusting these two properties with an appropriate temperature gradient.

In a final technique, a low-density foam is used as a matrix for the cryogenic fuel layer.[250] A foam-filled fuel layer has a higher ignition temperature, which depends on the foam density and material composition. Hence, most foam designs require a thin layer of pure DT on the inside of the foam to aid ignition.

The Omega Upgrade laser will be used as a test bed for

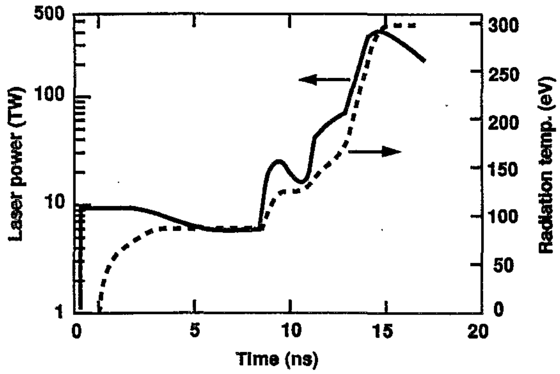

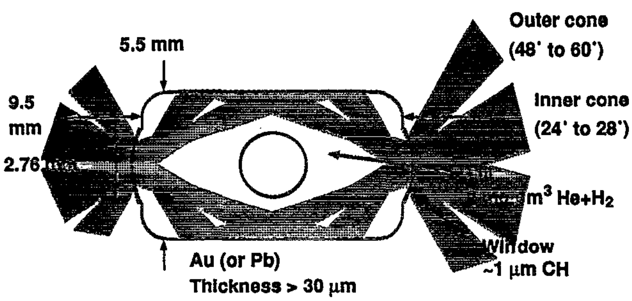

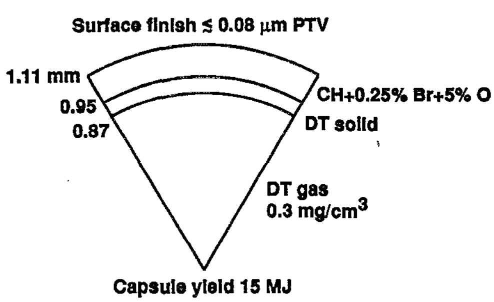

FIG. 106. Most of our modeling has concentrated on a 300 eV target, which absorbs 1.35 MJ of light.

developing targets with thick cryogenic layers. These experiments will begin in 1998.

As discussed in the Introduction, initiation of a self-sustaining burn wave constitutes ignition in ICF.

Beyond a threshold implosion velocity for a given capsule size, $P\,dV$ work can compress the hot spot to the ρr and temperature at which α-particle deposition can initiate a burn wave. This occurs when the hot spot's central temperature reaches about 10 keV with a ρr of 0.2–0.3 g/cm^2, as described in Sec. III. For NIF−scale capsules, threshold velocity is expected to be 3.5–4.0$\times 10^7$ cm/s.

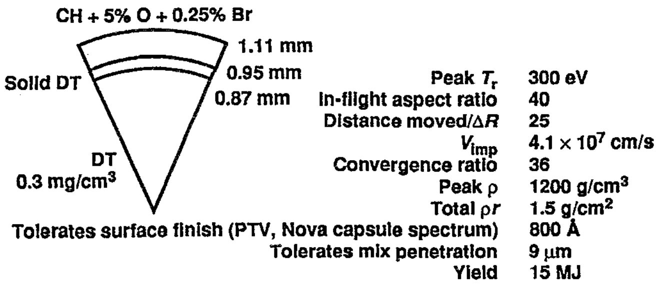

FIG. 107. A CH capsule is our ignition point design, and its features determine the requirements for symmetry, stability, and ignition.

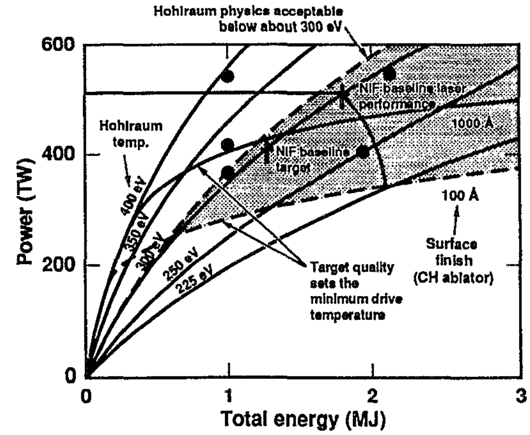

FIG. 108. For ignition targets, plasma-physics issues constrain the achievable hohlraum temperatures, and hydrodynamic instabilities establish the minimum required temperature. The shaded region constitutes the accessible region in power and energy space, where ignition with indirect-drive capsules is predicted.

Ignition results in a rapid increase in yield as implosion velocity is increased gradually beyond the ignition threshold velocity. Experimentally, the implosion velocity can be increased, while keeping the fuel on the same isentrope, by varying the peak drive temperature at the end of the pulse or by varying the length of the pulse.

As shown in Fig. 113 for the PT capsule, without α-particle deposition and the resulting burn propagation, NIF targets are expected to produce no more than 10–100 KJ, whereas a target with ignition and successful burn propagation will produce 1–20 MJ of thermonuclear energy, depending on capsule and hohlraum design.

Below a burn-averaged temperature of about 3 keV, negligible α-particle deposition occurs, and the observed increase in fusion yield with implosion velocity follows that expected for the purely hydrodynamic increase in the fusion cross section. By the time the fuel temperature doubles due to α-particle deposition, the fusion burn rate has increased by an order of magnitude or more beyond what could be achieved with pure hydrodynamic compression. Target performance below a central temperature of a few keV will provide an experimental baseline for determining the purely hydrodynamic increase in fuel temperature as a function of implosion velocity against which the measured departure due to α-particle deposition can be determined.

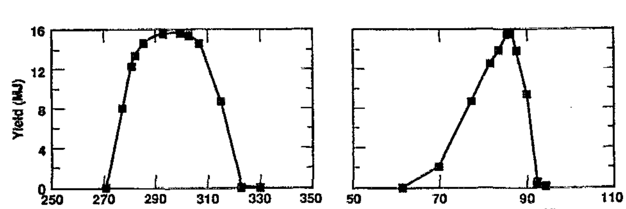

FIG. 109. The NIF capsule point design readily tolerates 6% swings in peak or foot temperatures (25% changes in flux).

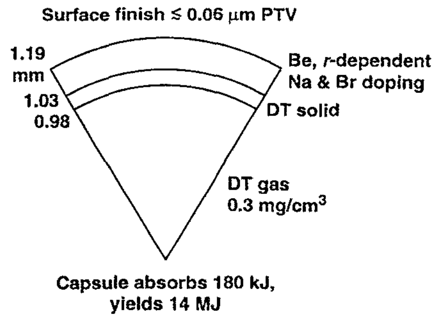

FIG. 110. A capsule with 250 eV peak drive provides a different tradeoff between hydroinstabilities and laser–plasma effects. A slightly higher-energy capsule can be driven by the same laser since the peak power requirement is lower. Beryllium is a superior ablator material at 250 eV. This design can tolerate surface perturbations of ~600 Å, compared to ~800 Å for CH/300 eV (both peak-to-valley, within the range of current Nova capsules). The peak intensity drops from 2×10^{15}–7×10^{14} W/cm^2, which reduces the gain for laser–plasma instability. The convergence ratio is about the same as for a CH capsule at 300 eV.

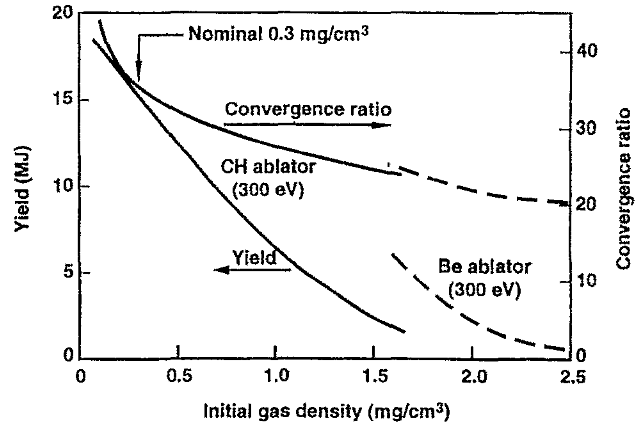

FIG. 112. Capsule gas fill provides direct control of convergence ratio. Increasing the initial gas fill reduces convergence ratio (and yield).

A complementary set of experiments could be done with a nonigniting fuel layer. For example, above or below some ratio of D to T, the targets will not ignite at any implosion velocity reached on the NIF. Assuming a comparable cryogenic layer quality and a slightly revised pulse shape to account for initial fuel density differences, a curve of yield versus implosion velocity with a nonigniting fuel mixture, normalized for cross section differences, would provide an additional baseline for comparison with the ignition experiments. Changing the D to T ratio could affect a cryogenic layering process, which would complicate direct comparison with the 50/50 DT case. For example, β layering will not work with a pure D_2 fuel layer but might work with a pure or nearly pure T_2 layer.

The NIF baseline capsule designs absorb 150 kJ, of which about 25 kJ ends up in the compressed fuel. As shown in Fig. 113, the central temperature gets to about 10 keV when the capsule has produced ~400 kJ. Therefore, ignition occurs when the fuel energy gain is about 16, or when the α-particle deposition is about three times the initial energy delivered to the compressed fuel. Since the NIF baseline targets are expected to yield up to 15 MJ, these targets would have a fuel energy gain of about 600. A factor of 5–10 higher-energy gain is required for ICF energy production, as discussed in Sec. XIV. ICF target gain requirements can be compared to the MFE power gain Q discussed in the Introduction.

The general approach to modeling the effects of hydrodynamic instabilities on ignition capsules was described in Sec. VI. The ignition targets are designed to remain in the linear or weakly nonlinear regime. Because of this, instability modeling is based on linear analysis that is as accurate as possible, with an extension into the weakly nonlinear regime

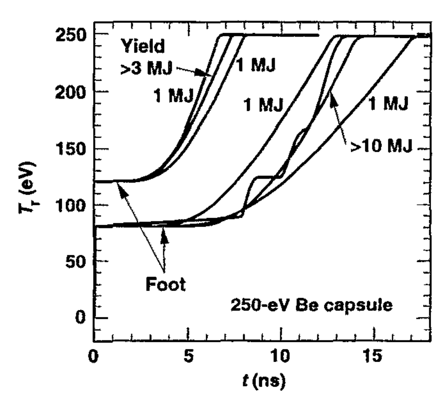

FIG. 111. Total pulse length can be varied by adjusting the power in the foot of the pulse. The capsule fails when the foot power is greater than about 130 eV because the fuel adiabat is too high.

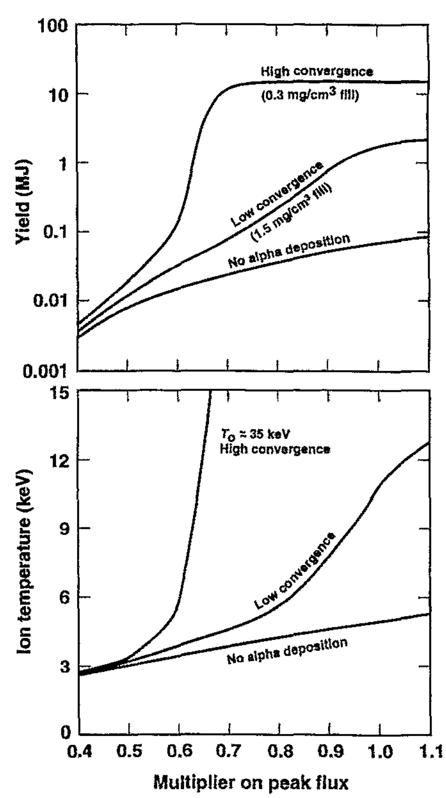

FIG. 113. Ignition could be diagnosed as an increase in yield and neutron-width burn temperature as drive is varied.

as necessary. The linear analysis is based on a decomposition of the surface perturbations into spherical harmonics, which are eigenmodes of the linear evolution. Single-mode growth is determined by running many 2-D simulations, each of one single mode in the linear regime throughout the simulation. This provides the most accurate calculation of all known effects, including ablation and density-gradient stabilization, Richtmyer–Meshkov[251] growth, and convergence effects. This set of calculations, combined with a nonlinear saturation model,[131] provides a spectrum of growth factors, as shown in Fig. 48 for the PT capsule. These growth factors are combined with an assumed initial surface spectrum to determine the ignition time perturbation.

To test the weakly nonlinear analysis, full simulations of multimode perturbations with realistic initial amplitudes are also run. Currently, simulations must be 2-D, and the number of modes that can be included is limited. A variety of multimode simulations have been run on several capsules, at solid angles ranging from relatively small conic sections to half-spheres. Results are consistent with this modeling, although further substantiation is an area of current work. Recent development of 3-D codes will allow testing of possible differences between 2-D and 3-D evolution.[252]

The effects of these perturbations on the hot spot are evaluated in a variety of ways. The unstable interface is between relatively cold, dense DT and the hot, lower-density DT of the hot spot. Material mixing of different elements does not occur, only thermal mixing. The actual perturbations are 3-D and multimode, and the weakly nonlinear perturbation growth analysis indicates that the spectrum is strongly dominated by modes around $l = 10–20$, as shown in Fig. 48. The 3-D character cannot be fully represented in any existing code; available 3-D codes do not include all of the relevant physical processes. There is 3-D calculational[252] and experimental[253] evidence that the multimode 3-D perturbation is probably an array of spikes penetrating in toward the hot-spot center surrounding approximately hexagonal bubbles. The effects of perturbations on the hot spot have been modeled in two dimensions in five ways.

(i) A single bubble of appropriate solid angle surrounded by a curtain of spikes falling along a reflecting boundary condition. The circular cone approximately represents a multifaceted 3-D cone of similar size and gross shape.
(ii) Perturbations with the opposite sign; i.e., a spike on axis surrounded by a circular bubble.
(iii) Perturbations on the waist that represent long circular ridges and curtains.
(iv) The multimode 2-D simulations mentioned above, continued through burn time.
(v) One-dimensional modeling in which the thermal mixing caused by the perturbation growth is represented as an enhanced thermal conductivity in the perturbed region.

All of these approaches give similar results as to how large a spike can be tolerated before ignition is quenched: the spikes penetrating the hot spot can be 10–15 μm in amplitude (for the PT), compared to a hot-spot radius of 30 μm. Combined with the modeling described above, this corresponds to a maximum tolerable initial ablator surface roughness of 50–80 nm RMS. This is to be compared with 20–30 nm RMS surface finish on current Nova capsules.

Analysis of the bubble penetration from the outside of the shell gives a surface-finish requirement for shell integrity during acceleration that is comparable to that for ignition. This equivalence depends weakly on the shape assumed for the spectrum of initial perturbations.

The modeling described so far pertains to surface perturbations that are initially on the outside of the ablator. Of course, there will be perturbations on the other interfaces, as well as material inhomogeneity and other fabrication defects. Any of these can be modeled in a conceptually identical way, using LASNEX simulations based on the assumption that the perturbation of interest exists. These calculations predict that the capsule tolerates perturbations initially on the other interfaces, which are much larger than tolerable perturbations initially on the outside. Perturbations on the DT/CH interface are very unlikely to be large enough to matter. Perturbations on the DT gas/solid interface need to be smaller than about 0.5 μm.

Currently, the best way to model radiation transport and coupling efficiency in ICF hohlraums is with detailed 2-D calculations using a radiation-hydrodynamics code. The calculations described here use LASNEX, with detailed radiation transport for the hohlraum/capsule coupling. The simulations are continued all the way through burn. The simulations track the laser beams, calculating inverse bremsstrahlung energy deposition and any refraction that occurs. The calculations typically use XSN non-LTE multigroup opacities,[241] although simulations with an opacity table derived from the STA opacity model are also done.[146] Any coupling to the capsule via hydrodynamic pressure or electron conduction is included.

Adequate symmetry and near 1-D burn performance has been achieved in such integrated simulations for a variety of designs at several sizes, including the PT, and beryllium designs driven at 250 and 300 eV. Figure 114 shows the 1-D and 2-D yield and burn temperature for the PT target and targets scaled from this design. The 1-D results are from hydrodynamically scaled targets with the required laser energy given by $E(\mathrm{MJ}) = 1.35s^3$, where s is the spatial scale factor compared to the PT.

To model asymmetry resulting from imperfect power balance and pointing of the laser beams, we must estimate the effects of fully 3-D asymmetry. This asymmetry and its effects have been modeled in a variety of ways. The asymmetry can be estimated analytically, using laser spot brightnesses and positions determined from the 2-D LASNEX simulations. Also, the asymmetry can be calculated in three dimensions with a view-factor code. We have used fully integrated calculations, as described above, to confirm the modeling and for some sensitivity studies. The actual 3-D asymmetry on the capsule must be estimated with 2-D simulations of the implosion driven with an asymmetric radiation source.

Calculations have been carried out with a wide variety of asymmetries on 2-D capsule implosions to ensure that the

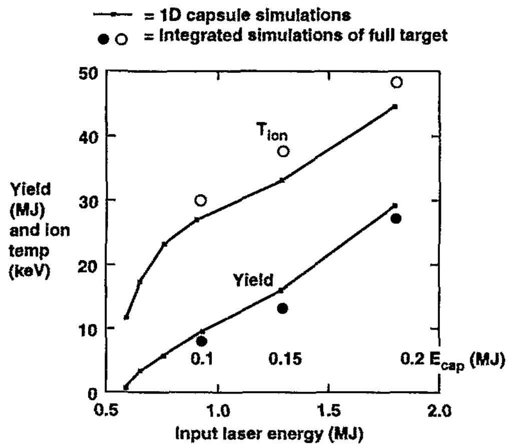

FIG. 114. Scales of the point design ignite above about 700 kJ. For the 1-D capsule simulations, capsule dimensions and times are scaled by s, and the effective laser energy is given by $E_{\text{eff}}(\text{MJ})=1.35s^3$, where $s=1$ is the PT design. For the integrated hohlraum and capsule simulations, dimensions and times are proportional to s, and powers are proportional to s^2.

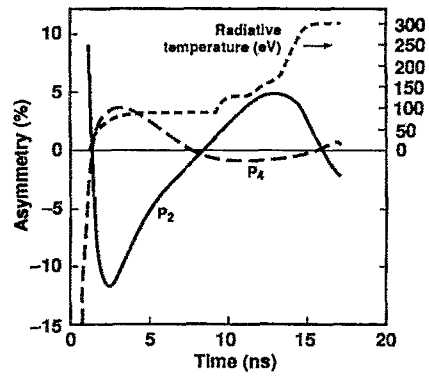

FIG. 115. With a constant power ratio (35% inner cone, 65% outer cone), NIF targets exhibit time-varying asymmetry in the P_2 and P_4 Legendre moments of flux. In detailed 2-D calculations, ignition capsules with this degree of time variation ignite and give yields near those seen for spherical implosions with uniform radiation drive. This degree of temporal variation in flux uniformity is near the maximum tolerable and would be reduced by "beam phasing" in which the power fraction in the inner and outer cones is varied in time.

specified asymmetry levels are acceptable. Asymmetry can affect ignition in a variety of ways: the obvious kinematic effects of differing velocities; initiation of RT instability growth, especially evident during deceleration; mass flow toward less-driven regions, seeding RT instability; irregular hot-spot compression, sometimes forming jets that protrude from the core and disrupt the imploded configuration, as discussed in Sec. IX; and delayed ignition, resulting in more RT growth.

The maximum tolerable asymmetry depends on temporal and spatial specifics. In detailed simulations, a P_2 asymmetry that varies between +4% (constant until switching) and −4% (for the duration of the pulse) produces a marginally acceptable implosion. (In this, and in all of the following, the P_2 coefficient is quoted so that the peak-to-valley asymmetry in flux is 1.5 times the number quoted.) If the switching time is chosen so that the average asymmetry is zero, the imploded configuration is, on average, round but shows a jet. With a swing from +2% to −2%, the asymmetry is small. In this case, the peak pressure generated in the fuel (when no thermonuclear burn is allowed) is reduced by about 12% compared to a perfectly spherical implosion. The yield (in a burn-on simulation) is not reduced by the asymmetry.

It is worth noting that, in this simulated implosion with a ±2% time-dependent asymmetry, the shell is as much as 10 μm out of round while at radii between 500 and 100 μm. It is as much as 10% out of round ($\Delta R=10$ μm for $R=100$ μm) toward the end of the implosion. This degree of asymmetry in the implosion could be measured with a backlighted imaging diagnostic similar to those that have been used on Nova. As mentioned in the Sec. IX discussion on time-dependent asymmetry, the roundness of an imploding shock in a foam shell can be determined on Nova to ~2 μm resolution.

The jetting asymmetry effect is maximized (at a given percent of peak flux asymmetry) by having the asymmetry be constant for the first part of the pulse and then switching to another constant value, with the opposite sign, for the remainder of the pulse. For that kind of time dependence, the baseline NIF capsule can tolerate 4% P_2 asymmetry, as described above. Typical detailed 2-D calculations have a more gradual variation in asymmetry with a lower average perturbation for a given peak, as indicated in Fig. 115.

If the period of the symmetry swings is shorter, such as would be the case in an experimental program that was designed to obtain a uniform average flux over some fraction of the implosion, still larger symmetry swings are tolerable. For example, with a P_2 of the form

$$A_2(t)=A_0(t)\epsilon_{20}\sin[\omega(t-t_0)], \tag{201}$$

where $A_0(t)$ is the total flux, $\omega=2\pi/(2\text{ ns})$ (a 2 ns period), implosion symmetry is tolerable with ϵ_{20} larger than 10%. The time t_0 must be such that the average asymmetry is about 1%. When t_0 is changed, the principal effect we see is the change in the average P_2. If the sinusoidally time-dependent asymmetry is too large, the failure mechanism for this short-duration asymmetry is a jet coming from the center of the implosion outward, as a result of irregular shock convergence in the center, rather than the azimuthal mass variation seen for the longer duration asymmetry described above.

Although NIF hohlraums certainly have time-dependent asymmetry, current detailed 2-D integrated calculations of NIF targets indicate that, with optimal placement of the two rings of laser beams per side, the time dependence is marginally tolerable for ignition targets, even without independent time histories for the individual rings. Figure 115 shows the time-dependent asymmetry for the PT target, with the two cones on each side having a constant power ratio. In this case, 35% of the laser power is in the inner ring and 65% is in the outer ring. The capsule in this integrated calculation achieved nearly the yield obtained in a perfectly spherical implosion. However, the time variation shown in Fig. 115 is near the maximum tolerable. Independent control of the

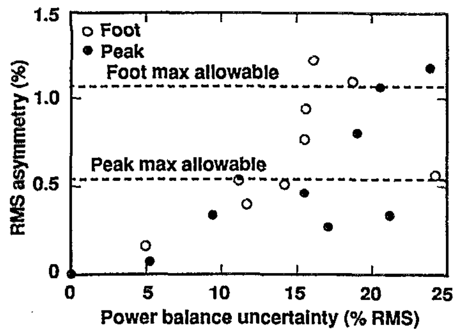

FIG. 116. Beam-to-beam energy balance errors can be as large as 15% if beamlet-to-beamlet fluctuations are uncorrelated.

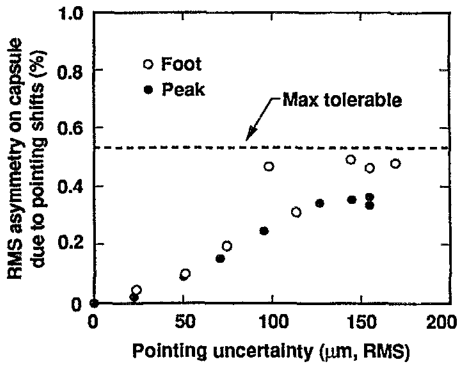

FIG. 117. Pointing errors can be as large as 200 μm RMS without degrading symmetry significantly.

power ratio in the separate rings, or "beam phasing," would be used to reduce the time-dependent asymmetry, as described in Sec. IX.

Since LEH effects and laser spot motion from refraction, wall blowoff, and laser–plasma interaction are the primary causes of time-dependent asymmetry, the issue for the NIF is whether uncertainty in these variations could lead to a failed implosion. Experimental measurements of the wall loss and laser spot position on Nova can establish the time-dependent asymmetry to a few percent, as discussed in Sec. IX. Similar experiments can be done on the NIF. As indicated in Fig. 115, this is well within the tolerable level of time variation for NIF capsules. Further, as described in Sec. IX, several techniques are being developed on Nova that would apply to the NIF for directly measuring the time-dependent asymmetry onto the capsule.

We do not find very much variation in sensitivity to asymmetry among the various targets we have designed. Smaller capsules are slightly more sensitive to asymmetries that couple to deceleration RT growth. The difference is not large, and symmetry sensitivity is not an issue that is important in deciding the overall tradeoffs of laser size and power. Varying the hohlraum size, with a given capsule, is the symmetry issue likely to be more important in the tradeoffs.

Three-dimensional Walle code[180,254] view factor calculations, as shown in Fig. 116, indicate that 10% RMS power imbalance between the beamlets results in less than 1% asymmetry at any given time on the capsule, provided the deviations are uncorrelated among the 192 beams. If the power imbalance varies in time, the tolerable power imbalance at any particular time can be much larger than this, depending on its time dependence. If correlations exist between the beams' powers, a much tighter power-balance requirement is necessary. For example, groups of eight correlated beams, with each group going into the same area of the hohlraum, must be balanced within about 3%. This increased precision requirement is consistent with the assumed reduction in the number of statistically independent power histories. Since the pulse shape can be adjusted for each of the 192 beamlets in the NIF design, any power variations should be statistical.

These requirements on the laser are well within current Nova performance parameters of 3% RMS energy imbalance, and 5%–10% power imbalance over time scales that are generally less than half the pulse length.[100] This does not mean that symmetry in Nova hohlraums is as good as in NIF hohlraums; the looser requirements for NIF are a result of the larger number of beams.

Three-dimensional Walle view factor calculations indicate that with nominal pointing errors—each beam is to point within 50 μm RMS of its nominal position, as specified in Table VIII—the resulting additional asymmetry on the capsule will be significantly less than 1%, as shown in Fig. 117. This pointing specification also ensures more than adequate clearance of the LEH. This requirement is similar to that met by the Nova laser (30 μm RMS on Nova[100] is 10 μrad, but 50 μm RMS on NIF is 7 μrad because of the longer focal length).

Both view factor and 2-D detailed integrated calculations have been carried out to evaluate the sensitivity of symmetry to changes in hohlraum geometry and beam cone positions. Table VIII gives the results for the view factor calculations, which are generally consistent with the analytical analysis presented in Sec. IX.

Figure 118 shows an example of the 2-D sensitivity determined from the integrated calculations, in this case for a beryllium-ablator target driven with a step laser power pro-

TABLE VIII. Several parameters are available to control symmetry with two cones of beams.

		P_2 (%)[a]	P_4 (%)[a]
Power balance inner versus outer			
change inner power/outer power by 5%	Foot	1.7	−0.4
	Peak	1.0	−0.1
Hohlraum aspect ratio (fixed hohlraum area and LEH, beams central in LEH)			
Make hohlraum 100 μm longer	Foot	1.8	1.6
	Peak	1.6	0.7
Make hohlraum 100 μm longer and use power to correct P_2 change	Foot	⋯	2.0
	Peak	⋯	0.8
Outer beam pointing			
Move spots 100 μm out	Foot	1.2	1.2
	Peak	1.2	0.5
Inner beam pointing			
Move spots 100 μm out	Foot	1.4	−1.2
	Peak	0.9	−0.5

[a]Estimates made using the Walle 3-D view factor radiation transport code.

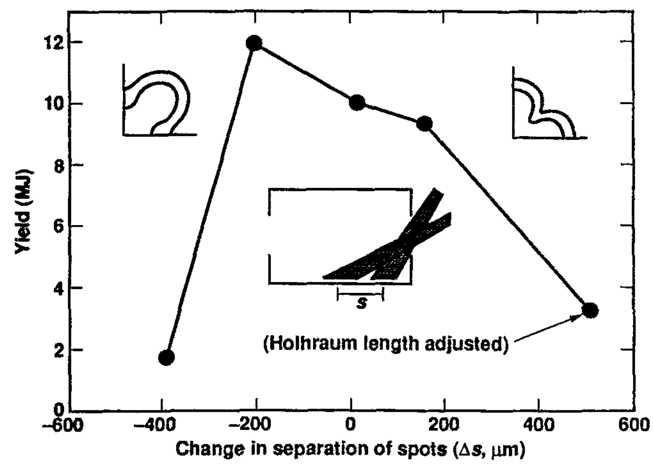

FIG. 118. Integrated calculations are being used to confirm acceptable sensitivity to pointing. Laser ring separation controls P_4. The pointing sensitivity is large enough that we can use it to control P_4 but small enough for the specified pointing accuracy.

file. The target can tolerate beam movement of the average ring location of ± 200 μm, well outside the expected deviation, given the pointing specification on the laser.

Figure 119 shows that the integrated calculations of the PT target can tolerate significant variations in the peak power pulse length at two hohlraum lengths, which differ by 400 μm.

Asymmetries might also arise from laser–plasma interaction processes, or other phenomena such as RT instability at the Au/He interface, which are currently predicted not to be significant, but for which uncertainty remains. Light can be scattered, or it can be absorbed more or less efficiently at different positions in the hohlraum. The effect in all cases is equivalent to a power balance change, a movement of the x-ray emission spots, or perhaps a spreading of the laser *deposition* spots (for small-angle side scattering). Difficulties could arise only if these effects are so large that their irreproducible part is larger than the limits described above. If any of these processes occur but are reproducible and not too large, the effect can be mitigated by changing the hohlraum design parameters. Estimates based on Nova experiments described in Sec. XI and modeling indicate that these processes can be kept within acceptable limits. If we cannot do this for the 300 eV PT target, our ultimate recourse will be to increase the hohlraum size, reduce the laser intensity, and correspondingly reduce the hohlraum drive temperature to the 250 eV design, which has significantly less plasma, as discussed in Sec. XI.

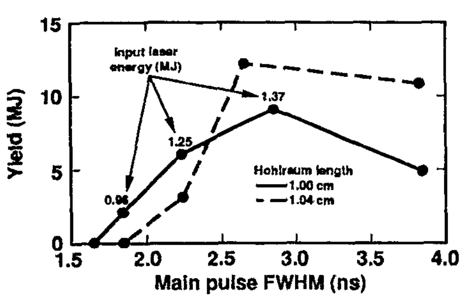

FIG. 119. Integrated calculations indicate that the high-power main pulse length can be varied by more than 0.5 ns.

The remaining uncertainties can be mitigated with changes in the target design that will be made after further Nova experiments, or after the NIF experiments begin. Some of the uncertainties that we have evaluated include the following.

(i) A factor of 2 in hydrodynamic instability growth (equivalent to a factor of 2 in surface finish or a factor of 2 in the acceptable size of the bang-time perturbations) shifts the ignition cliff from 0.8 to about 1.0 MJ. Improvements in surface finish could probably recover the original margin.

(ii) The combined uncertainties in x-ray conversion and hohlraum wall loss (energy) are less than about 20%.

(iii) Stimulated Brillouin scattering should be only a few percent, based on the experiments described in Sec. XI.

(iv) Depending on the accuracy of the 2-D integrated calculations, achieving the correct power balance between the inner and outer cones of beams may require reducing the power in one or the other so that it cannot run at its full power. This may result in a net energy loss of 10%–15%.

(v) An error in hohlraum optimization that requires increasing the LEH radius 50% would require an increase in laser energy of 15% to regain the same hohlraum temperature.

(vi) Similarly, increasing the hohlraum area by 35% increases the required laser energy by 15%.

Several other uncertainties are energetically insignificant. For example, the equation of state and opacity of the CH ablator are sufficiently uncertain that we expect to adjust the details of the pulse shape phenomenologically, but this will not significantly affect the performance requirements of the laser, or the target performance.

These errors, in combined effect, are consistent with the factor-of-2 margin provided by a 1.8 MJ, 500 TW laser. Based on all available data and detailed simulations, 1.8 MJ should be adequate for ignition.

Although indirect drive is the primary approach to ignition on the NIF, developments in direct drive have reached the point where this approach also looks quite promising. With the implementation of additional beam smoothing and more beam ports on the target chamber, the NIF can be configured to be capable of both indirect and direct drive. Figure 120(a) shows a schematic of the NIF target chamber with the 48 beam ports configured for indirect drive. By adding 24 more ports, as indicated in Fig. 120(b), and implementing 2-D SSD beam smoothing, the NIF would achieve the beam smoothing currently estimated by LLE[55] to be required for direct drive. The NIF will be able to shift rapidly (≤ 1 day) between these two geometries if a movable turning mirror is inserted in the NIF switch yard and the additional hardware required for the 24 new beam positions is installed.

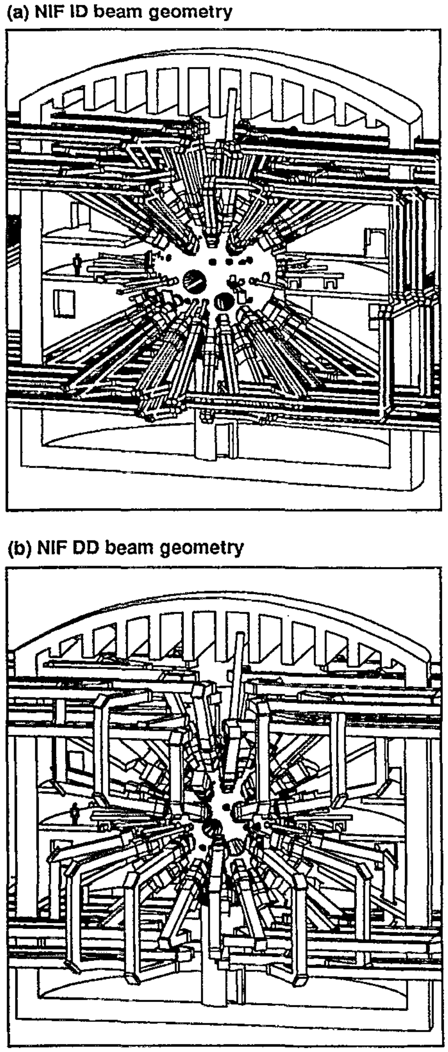

FIG. 120. The NIF target area beam geometry: (a) NIF baseline target area uses 48 clusters of 4 beams configured for indirect drive; (b) NIF target area building and beam transport system can be reconfigured for direct drive by switching 24 of the 4-beam clusters to alternate positions.

XIV. INERTIAL FUSION ENERGY

Experiments and analysis conducted over the course of nearly two decades of research have allowed us to establish the hydrodynamics, radiation transport, x-ray production requirements, and the plasma-physics limitations of indirect inertial fusion using laser drivers. A demonstration of ignition and burn propagation would set the stage for high-confidence development of the applications of ICF, including inertial fusion energy (IFE).

Because of their potential efficiency, durability, and rep rate, the NAS,[26] FPAC,[34] and FEAC[59] reviews concluded that, of the current ICF drivers, heavy-ion drivers have the greatest potential for future inertial fusion power plants. For both laser-driven and ion-driven indirect drive, the capsule is radiation driven so that the capsule implosion and burn physics are the same. If the ion-driven hohlraums are heated to the same radiation temperature T_r, then the requirements for hydrodynamic instability, implosion uniformity, and pulse shaping to drive the capsule can be applied directly. In addition, at the same radiation temperature, x-ray hohlraum wall losses, radiation-driven hohlraum wall motion, and radiation transport are also directly applicable. Because these are the primary issues that affect coupling efficiency and hohlraum symmetry, the laser-driven hohlraum physics program provides a solid base for calculating heavy-ion (HI) hohlraums.

Clear differences exist between HI and laser hohlraums, as indicated in Fig. 6. For example, unlike HI hohlraums, laser-driven hohlraums have holes that affect symmetry, and lasers must contend with laser–plasma parametric instabilities and spot motion, which limit hohlraum plasma conditions.

In current NIF hohlraums, temporal and spatial control of the power is used in a large number of beams to control hohlraum symmetry, whereas in the HI hohlraum in Fig. 6, only two radiators are used. As stated earlier, this geometry is attractive from the point of view of fusion chamber design[38] because it is compatible with a variety of protected-wall fusion chambers. Symmetry is obtained by adjusting the internal structure and shape of the hohlraum.[72,255] The HI hohlraum in Fig. 6 controls P_2 asymmetry by controlling the size, shape, and position of the shield directly inside of each radiator, such as in the Nova experiments described in Figs. 78 and 79. Higher-order components to asymmetry, except for P_4, are controlled by having a relatively large hohlraum. For hohlraum designs that attempt to maximize coupling efficiency, control of P_4 is also required. That is accomplished by an additional shield, as shown in Fig. 6. By using the data and calculational techniques developed for laser-driven hohlraums, it is possible to calculate the impact of the geometric differences between ion and laser hohlraums. To test the transport issues directly, it is also possible to do laser experiments with geometries that mock up HI hohlraums.

The physics of ion stopping in hot matter and x-ray production from a volume-heated radiator are unique to ion hohlraums. Ion stopping in hot matter has been studied by many investigators. [35,36] The physics is believed to be well understood, and the experiments to date,[256] although not at the required matter temperature, match theory. The body of data being developed in the light ion program conducted at Sandia National Laboratories is being extended to higher matter temperatures as the ion-beam intensity on the PBFA II machine is increased. If Sandia is successful in raising the intensity from the current 1–2 TW/cm^2 to about 5 TW/cm^2, PBFA II should be able to reach temperatures of 100 eV. An investigation of a wide range of beam–plasma instabilities,[257] which could be driven by the ion beam as it propagates through the low-density target corona, also has failed to uncover any mechanism that could transfer a significant fraction of the beam energy.

Simulations of the absorber/radiator geometries shown in Fig. 121 indicate that an x-ray conversion efficiency of 50%–80% can be achieved under appropriate conditions.[37] Ion beams generally are absorbed in a relatively low-Z material that heats up and then radiates like a blackbody if the radiator has an optical depth approximately equal to a Planck mean-free path. The energy balance equation for an ion beam can be written as

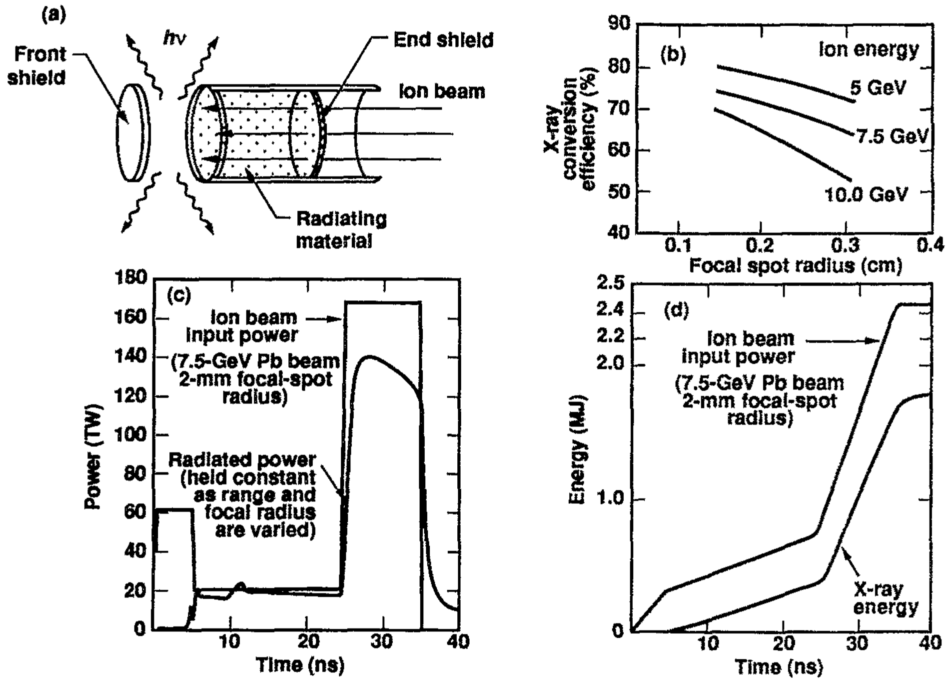

FIG. 121. With properly designed radiation converters, heavy-ion beam energy can be efficiently converted to x rays.

$$I=R\frac{d\epsilon}{dt}+\frac{dE_k}{dt}+\sigma_r T_r^4, \tag{202}$$

where R is the ion range in g/cm^2, ϵ is the specific energy of the absorber, and E_k is the kinetic energy of expansion of the absorber. The heat capacity term, $R(d\epsilon/dt)$, which is proportional to the temperature T_r, is the dominant term at low temperature. At high temperature, the radiative term dominates. The kinetic-energy term generally can be made small by appropriate choice of absorber material. If the intensity is too low, the absorber material never heats up sufficiently to become an efficient radiator before the pulse ends. At high intensity, the absorber heats up quickly and then radiates very efficiently. The intensity required for efficient conversion increases as the range increases because the longer range results in a higher heat capacity of the absorber and a longer time before radiation becomes efficient.

Figure 121 shows the results of calculations for a specific radiator geometry. In these calculations, the x-ray power required by a target was specified. As the ion-beam range and focal-spot size varied, the ion-beam power also was varied to achieve the required x-ray power.

Figure 122 shows the calculated gains (as a function of ion-beam focal-spot radius for two typical HI ranges) for targets with the geometry shown in Fig. 6. The gains given in Fig. 122 are based on an analytical model[258] for the various elements of the ion-beam-driven hohlraum. As indicated,

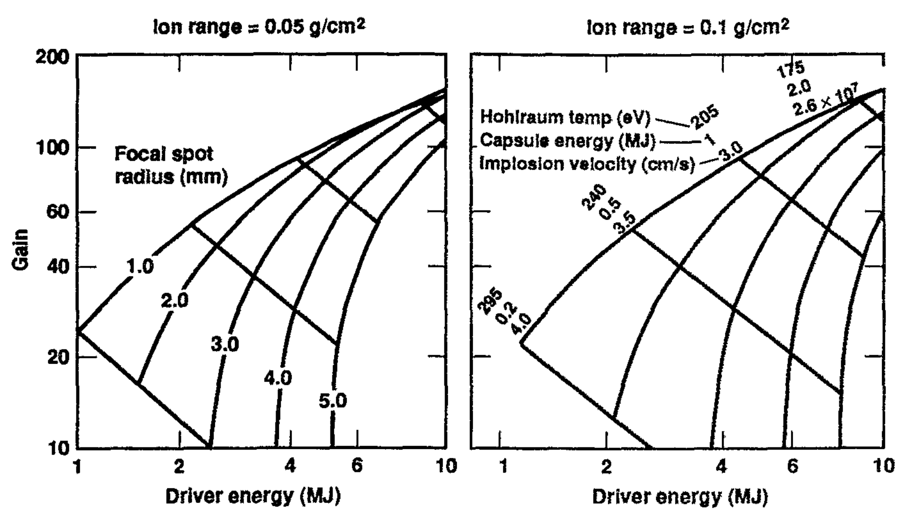

FIG. 122. Energy production using indirect-drive, heavy-ion targets may be feasible with a driver of 2–3 MJ.

these gain curves have used capsules with drive temperatures that vary in the way specified by Eq. (87), with a factor of 2 allowance for nonideal effects. The wall-loss model follows that given by Eq. (124), and the modeling of the radiator components is similar to that given by Ho.[37] Detailed 2-D integrated radiation-hydrodynamics calculations, using the modeling techniques developed for the Nova experiments and the NIF hohlraums, are being carried out. Initial calculations[259] of this type have achieved a gain of 50 at 8 MJ. Refinements of these calculations are expected to demonstrate gains comparable to those in Fig. 122.

As shown in Fig. 122, gains are critically dependent on the spot size of the ion beam when it is focused on the target radiators. This dependence arises from the energy required to heat the material in the x-ray converters to a temperature at which they will radiate efficiently. As the ion range decreases, less mass is heated at a given spot size. This results in a higher gain for a given spot size or a larger tolerable spot size for a given gain. As the range decreases, the radiators cover an increasing fraction of the hohlraum surface area. For some designs, such as those being pursued by Sandia for light ions and some recent HI target designs,[260] the ion beams cover the entire surface of the target. Such designs are feasible because the range of relevant ions is much greater than the thickness of high-Z material needed to contain the radiation. An optimal thickness exists for the high-Z case that comes from trading off (1) ion-beam energy lost as the ions penetrate and heat the case and (2) radiation containment. In general, such target designs have lower gain than that given in Fig. 122 for the two radiator designs.

The optimal choice of focal-spot size and range is largely an accelerator issue because targets with adequate gain are feasible over a wide range of these choices. In designs with larger spot size and lower intensity, the accelerator must be able to transport more current, and the focusing system must be able to focus more current, or the beams must be partially neutralized. Designs such as those shown in Fig. 6 are the current baseline HI designs because the longer range ions, which have lower beam current for a given driver energy, can be ballistically focused without current or charge neutralization. Ballistic focusing is well understood theoretically, although effects such as photoionization of the incoming beam by target x-ray emission must be addressed,[261] and it provides HI target point designs with a high-confidence focusing approach. This is viewed as important because of the present lack of data to conclusively support the feasibility of charge-neutralization schemes for focusing.

This situation could change because of work being done in the light- and heavy-ion beam programs to investigate charge-neutralization schemes. Beams being produced by the pulsed-power, light-ion beam machines have inherently high current and must rely on current and charge-neutralized focusing schemes.[262] The theoretical understanding being developed for these schemes, and the experiments being carried out and planned can provide the information required to base HI designs on neutralized focusing.

Since the ability to achieve the required beam intensity is the central issue for both HI and light-ion drivers, depending on the outcome of focusing and transport experiments, the optimal design for HI accelerators may well be ones that have higher-current, lower-energy beams and targets that can accept a lower intensity. The optimal accelerator architecture also could end up being a hybrid between today's light-ion machines with a single-step particle acceleration and the conventional HI accelerator concepts with a very large number of acceleration steps.

The following discussion of specific drivers is taken largely from the article by Hogan, Bangerter, and Kulcinski.[38]

There are two main approaches to HI drivers: radio frequency (RF) accelerators and induction accelerators. Physicists in Europe and Japan are studying the RF accelerator because of their large body of experience with the many existing high-energy physics accelerators. Physicists in the United States are examining the induction accelerator because of its simplicity and ability to handle high-current beams. In such accelerators, space-charge-dominated beams are accelerated periodically by induction cells and transported by a sequence of alternating-gradient quadrupoles.

HI-driven target chambers have the advantage that no material object important to beam propagation or focusing need be in a direct line of sight with the target. The beams can be bent out of the direct path with magnets that are themselves out of the line of sight. Line-of-sight "get lost" (nonreflective and nonscattering) dumps handle the x rays, neutrons, and debris, while fast-closing valves and differential pumps isolate the accelerator vacuum from the vapors in the target chamber.

Central to the economics of any inertial fusion power plant is the fusion cycle gain.[38] The fusion cycle gain is the product of the driver efficiency η (the ratio of the energy delivered to the target and the energy supplied to the driver), the target gain G (the ratio of the thermonuclear yield and the driver energy), the nuclear energy multiplier M (the energy change due to neutron reactions, principally in the lithium-bearing blanket used to produce tritium), and the thermal-to-electric energy conversion efficiency ε. In any inertial fusion power plant, the net electricity P_n is related to the gross electricity P_g through the power balance equation:

$$P_n = P_g - P_a - P_d = P_g(1 - f_a - 1/\eta G M \epsilon), \tag{203}$$

where P_a is the power used for auxiliary equipment and $f_a = P_a/P_g$ is typically a few percent of the gross electricity. Here P_d is the driver power, and the driver's recirculating power fraction P_d/P_g is the reciprocal of the fusion cycle gain $\eta G M \varepsilon$.

Since the nuclear energy multiplier M is typically 1.05–1.15, and the conversion efficiency ε is typically 0.35–0.45, the product ηG must be greater than about 10 to keep the recirculating power fraction below 20%–25%. If the recirculating power fraction much exceeds this fraction, the cost of electricity escalates rapidly.

Because of their projected high efficiency, HI accelerators can tolerate a significant uncertainty in the target gain that is ultimately achievable. HI accelerators are projected to have efficiencies of 20%–35%, and point designs for gigawatt reactors use drivers of 5–7 MJ. Figure 122 shows clearly that, in this range, HI-driven targets can tolerate a drop in gain of a factor of 2 or more and still meet the ηG requirements for energy production if the ion beam can be focused to a radius of 2–3 mm. This target margin is comparable to that of the NIF, which is being designed with approximately a factor-of-2 margin in energy, as indicated in Fig. 108. This margin is considered adequate, given the current state of knowledge about laser indirect-drive targets. HI targets should not have a larger uncertainty than laser targets, because part of the NIF margin is to account for uncertainties in coupling efficiency due to plasma-physics effects as the laser propagates through the hohlraum. Ion-beam targets will not have this problem. For ion beams, the primary uncertainty is the spot size achievable with a given accelerator design. It is generally believed that a conservative accelerator could be designed that would achieve the desired spot size with high confidence. However, the cost impact of such a conservative design could make energy production unattractive. The purpose of the HI driver development program funded by the Office of Fusion Energy (OFE), is to determine the requirements of an accelerator that would deliver the required beam power, energy, pulse shape, and focal spot at minimal cost.

Pulse-power technology can compress large quantities of electricity into reasonably short pulses efficiently and at relatively low cost. In a light-ion accelerator, an electrical pulse of the required energy is progressively shortened by a variety of pulsed-power techniques. The ions are generally accelerated in a single step, although multigap light-ion accelerators have been proposed. As stated earlier, obtaining the required focused intensity is the major challenge for light-ion beams.

Laser drivers also have been identified that are candidates for fusion energy production. Diode-pumped solid-state lasers (DPSSL) and KrF lasers both have the potential efficiency and rep rate required for power production.

Solid-state lasers initially were discounted for fusion energy production because of the characteristics of flashlamp-pumped Nd:glass lasers—in particular, their inefficiency and low pulse rate. However, the diode-pumped, gas-cooled, solid-state laser may overcome these problems.[263,264] One current candidate is an InGaAs diode array and an ytterbium-doped fluorapatite crystal—$Yb:Ca_5(PO_4)_3F$. The estimated wall-plug efficiency of such a laser could exceed 10%. For a DPSSL to be economical, the cost of the diode arrays must decrease from a current cost of between \$1 and \$10 per peak watt to between 1¢ and 10¢ per peak watt when they are produced in volume. The DPSSL laser has an attractive development path because it is highly modular, like the NIF. All of the operational features of the laser can be demonstrated at an aperture scale of only 10–15 cm.

In excimer lasers using gases such as KrF, the gaseous lasing medium is pumped by an electric discharge or an electron beam. The lasing gas flows through heat exchangers to remove waste heat. The 0.26 μm wavelength and broad bandwidth of KrF lead to good coupling to the target. The use of the KrF laser is complicated by its very short spontaneous emission lifetime—that is, it does not store energy in the excited state for times longer than the desired extraction time. Thus, for good efficiency, light must be extracted during the entire pumping time. The anticipated pumping time, as dictated by pulsed-power requirements, is several hundred nanoseconds. Therefore, the pulse must be shortened by about a factor of 100 by using such techniques as angular multiplexing, in which short seed pulses pass through the amplifier sequentially for the entire duration of the pumping, each at a slightly different angle. These beams are then transported through paths of different lengths so they arrive at the target simultaneously. Recent studies[265,266] of KrF lasers found net wall-plug efficiencies of 6%–8%.

The relatively low efficiency of both DPSSL and KrF lasers puts a premium on high target gain in order to achieve an $\eta G \approx 10$. As indicated by Fig. 7, the gain for indirect-drive targets is inadequate for a KrF laser unless the hohlraum coupling efficiency can be increased. The indirect-drive gain is marginal for the DPSSL laser, even at a driver energy of 10 MJ. The higher gains projected for direct drive, as shown in Fig. 44, are marginal for KrF and adequate for DPSSL lasers. If the effects of hydrodynamic instability are less severe than currently estimated, direct-drive target gains could be higher. The durability of optical components facing the neutrons, x rays, and debris from the fusion explosion also poses a major challenge for lasers. Since the NIF will be configured to test both indirect drive and direct drive, it will be able to test both target options for laser-driven IFE.

ACKNOWLEDGMENTS

A significant number of the references in this review are to Livermore or Los Alamos internal documents that are not yet publicly available (listed as "unpublished" in the reference list), but many are in the process of review for declassification as a result of the December 1993 decision by DOE to declassify large portions of the U.S. ICF Program. As in any large scientific undertaking, the work reported here required the efforts of many hundreds of people who are not mentioned in this document. In addition, for this document, I have had to select a small subset of the work on indirect drive that has been carried out over the past two decades. Most of the laser technology and diagnostic development required for the analysis and experiments discussed here is not covered at all, but that information is publicly available in other reports.

This work was performed under the auspices of the U.S. Department of Energy by the Lawrence Livermore National Laboratory under Contract No. W-7405-Eng-48.

[1] J. H. Nuckolls, L. Wood, A. Thiessen, and G. B. Zimmerman, "Laser compression of matter to super-high densities: thermonuclear (CTR) applications," Nature **239**, 129 (1972).

[2] K. A. Brueckner and S. Jorna, "Laser-driven fusion," Rev. Mod. Phys. **46**, 325 (1974).

[3] J. D. Lindl, R. L. McCrory, and E. M. Campbell, "Progress toward ignition and burn propagation in inertial confinement fusion," Phys. Today **45**(9), 32 (1992).

[4] R. M. White, D. A. Resler, and S. I. Warshaw, "Evaluation of charged-particle reactions for fusion applications," *Proceedings of the International Convergence on Nuclear Data for Science and Technology 1991*, Julich, Germany, edited by S. M. Qaim (Springer-Verlag, Berlin, 1992), p. 834.

[5] S. Chandrasekhar, *Hydrodynamic and Hydromagnetic Stability* (Oxford University Press, London, 1961).

[6] J. H. Nuckolls, "Laser-induced implosion and thermonuclear burn," *Laser Interaction and Related Plasma Phenomena*, edited by H. J. Schwarz and H. Hora (Plenum, New York, 1994), Vol. 3B, pp. 399–425.

[7] See National Technical Information Service Document No. UCRL-74116 (J. Nuckolls, L. Wood, A. Thiessen, and G. Zimmerman, "Laser implosion of DT to densities >1000 g/cm^3. Optimum pulse shape; fusion yield vs laser energy," Lawrence Livermore National Laboratory, Livermore, CA, UCRL-74116, 1972). Copies may be obtained from the National Technical Information Service, Springfield, VA 22161.

[8] J. J. Cordey, R. J. Goldston, and R. R. Parker, "Progress toward a tokamak fusion reactor," Phys. Today **45**, 22 (1992).

[9] J. D. Strachen, H. Adler, P. Alling, C. Ancher, H. Anderson, J. Anderson, D. Ashcroft, C. Barnes, G. Barnes, S. Batha, M. Bell, R. Bell, M. Bitter, W. Blanchard, N. Bretz, R. Budny, C. Bush, R. Camp, M. Caorlin, S. Cauffman, Z. Chang, C. Cheng, J. Collins, G. Coward, D. Darrow, J. DeLooper, H. Duong, L. Dudek, R. Durst, P. Efthimion, D. Ernst, R. Fisher, R. Fonck, E. Fredrickson, N. Fromm, G. Fu, H. Furth, C. Gentile, N. Gorelenkov, B. Grek, L. Grisham, G. Hammett, G. Hanson, R. Hawryluk, W. Heidbrink, H. Herrmann, K. Hill, J. Hosea, H. Hsuan, A. Janos, D. Jassby, F. Jobes, D. Johnson, L. Johnson, J. Kamperschroer, H. Kugel, N. Lam, P. LaMarche, M. Loughlin, B. LeBlanc, M. Leonard, F. Levinton. J. Machuzak, D. Mansfield, A. Martin, E. Mazzucato, R. Majeski, E. Marmar, J. McChesney, B. McCormack, D. McCune, K. McGuire, G. McKee, D. Meade, S. Medley, D. Mikkelsen, D. Mueller, M. Murakami, A. Nagy, R. Nazikian, R. Newman, T. Nishitani, M. Norris, T. O'Connor, M. Oldaker, M. Osakabe, D. Owens, H. Park, W. Park, S. Paul, G. Pearson, E. Perry, M. Petrov, C. Phillips, S. Pitcher, A. Ramsey, D. Rasmussen, M. Redi, D. Roberts, J. Rogers, R. Rossmassler, A. Roquemore, E. Ruskov, S. Sabbagh, M. Sasao, G. Schilling, J. Schivell, G. Schmidt, S. Scott, R. Sissingh, C. Skinner, J. Snipes, J. Stevens, T. Stevenson, B. Stratton, E. Synakowski, W. Tang, G. Taylor, J. Terry, M. Thompson, M. Tuszewski, C. Vannoy, A. von Halle, S. von Goeler, D. Voorhees, R. Walters, R. Wieland, J. Wilgen, M. Williams, J. Wilson, K. Wong, G. Wurden, M. Yamada, K. Young, M. Zarnstorff, and S. Zweben, "Fusion power production from TFTR plasmas fueled with deuterium and tritium," Phys. Rev. Lett. **72**, 3526 (1994).

[10] K. Huang, *Statistical Mechanics* (Wiley, New York, 1967), pp. 224–252.

[11] S. P. Lyon and J. D. Johnson, "Sesame: The Los Alamos national laboratory equation of state database," Los Alamos National Laboratory, Los Alamos, NM, LA-UR-92-3407 (1992) (unpublished).

[12] J. D. Lindl, "Physics of ignition for ICF capsules," *International School of Plasma Physics Piero Caldirola: Inertial Confinement Fusion (1988)*, edited by A. Caruso and E. Sindoni (Editrice Compositori, Bologna, Italy, 1988), pp. 617–631.

[13] C. Longmire, *Elementary Plasma Physics* (Wiley, New York, 1967), p. 203.

[14] G. S. Fraley, E. J. Linnebur, R. J. Mason, and R. L. Morse, "Thermonuclear burn characteristics of compressed deuterium–tritium microspheres," Phys. Fluids **17**, 474 (1974).

[15] W. M. Manheimer and D. G. Colombant, "Steady-state planar ablative flow," Phys. Fluids **25**, 1644 (1982).

[16] J. Bunkenberg, J. Boles, D. Brown, J. Eastman, J. Hoose, R. Hopkins, L. Iwan, S. Jacobs, J. Kelly, S. Kumpan, S. Letzring, D. Lonobile, L. Lund, G. Mourou, S. Refermat, W. Seka, J. Soures, and K. Walsh, "The Omega high-power phosphate-glass system: Design and performance," IEEE J. Quantum Electron. **QE-9**, 1620 (1981).

[17] J. M. Soures, R. Hutchison, S. Jacobs, L. Lund, R. McCrory, and M. Richardson, "Omega: A short-wavelength laser for fusion experiments," *Proceedings of the 10th Symposium on Fusion Engineering*, edited by C. C. Hopkins, D. M. Pulyer, J. N. Stacy, and K. E. Wakefield (Institute of Electrical and Electronic Engineers, New York, 1983), p. 1302.

[18] J. L. Emmet, W. F. Krupke, and J. B. Trenholme, "Future development of high-power solid-state laser systems," Sov. J. Quantum Electron. **13**, 1 (1983).

[19] J. T. Hunt and D. R. Speck, "Present and future performance of the Nova laser system," Opt. Eng. **28**, 461 (1989).

[20] C. Yamanaka, Y. Kato, Y. Izawa, K. Yoshida, T. Yamanaka, T. Sasaki, M. Nakatsuka, T. Mochizuki, J. Kuroda, and S. Nakai, "Nd-doped phosphate glass laser systems for laser-fusion research," IEEE J. Quantum Electron. **QE-9**, 1639 (1981).

[21] J. M. Soures, R. McCrory, T. Boehly, R. Craxton, S. Jacobs, J. Kelly, T. Kessler, J. Knauer, R. Kremens, S. Kumpan, S. Letzring, W. Seka, R. Short, M. Skeldon, S. Skupsky, and C. Verdon, "Omega Upgrade laser for direct-drive target experiments," Laser Part. Beams **11**, 317 (1991).

[22] R. L. McCrory, J. Soures, C. Verdon, T. Boehly, D. Bradley, R. Craxton, J. Delettrez, R. Epstein, R. Hutchison, P. Jaanimagi, S. Jacobs, R. Keck, J. Kelly, T. Kessler, H. Kim, J. Knauer, R. Kremens, S. Kumpan, S. Letzring, F. Marshall, P. McKenty, S. Morse, W. Seka, R. Short, M. Skeldon, S. Skupsky, and B. Yaakobi, "Direct-drive laser fusion target physics experiments," *Plasma Physics and Controlled Nuclear Fusion Research 1992* (International Atomic Energy Agency, Vienna, 1993), Vol. 3, p. 31.

[23] S. E. Bodner, R. Lehmberg, S. Obenschain, C. Pawley, M. Pronko, J. Sethian, A. Deniz, J. Hardgrove, T. Lehecka, O. Barr, I. Begio, S. Ozuchlewski, D. Hanson, N. Kurnit, W. Leland, J. McCleod, E. Rose, and G. York, "Krypton-fluoride laser fusion development in the USA," in Ref. 22, p. 51.

[24] S. P. Obenschain, S. Bodner, R. Lehmberg, A. Mostovych, C. Pawley, M. Pronko, J. Sethian, J. Stamper, A. Deniz, T. Lehecka, and J. Shipman, "Nike KrF laser development for direct drive laser fusion," *Plasma Physics and Controlled Nuclear Fusion Research 1990* (International Atomic Energy Agency, Vienna, 1991), Vol. 3, p. 51.

[25] W. L. Kruer, *Physics of Laser Plasma Interactions* (Addison–Wesley, Redwood City, CA, 1988).

[26] *National Academy of Sciences Review of the Department of Energy's Inertial Confinement Fusion Program, Final Report* (National Academy Press, Washington, DC, 1990).

[27] H. Nishimura, H. Shiraga, H. Takabe, Y. Kato, S. Miyamoto, M. Takagi, T. Morimatsu, T. Yamanaka, T. Jitsuno, M. Nakatsuka, and S. Nakai, "High convergence uniform implosions by cannonball targets with Gekko XII blue laser," *14th International Conference on Plasma Physics and Controlled Nuclear Fusion Research*, Würzburg, Germany, 1992, Nuclear Fusion Research 1992 (International Atomic Energy Agency, Vienna, 1993), Vol. 3, p. 97.

[28] C. Bayer, J. L. Bourgade, H. Dumont, J. P. Garconnet, J. P. Jadaud, D. Juraszek, A. Richard, and M. Rostaing, "Indirect drive implosion experiments," 23rd ECLIM, St. John's College, Oxford, England (private communication, 1994).

[29] G. G. Kockemasov, "Laser fusion investigations on high power iodine laser ISKRA in Arzamas-16," in Ref. 28.

[30] G. D. Tsakiris and R. Sigel, "X-ray generation in a cavity heated by 1.3 or 0.44 mm laser light: II. Time-resolved measurements," Phys. Rev. A **38**, 5769 (1988).

[31] *Inertial Confinement Fusion and High Power Laser Technology*, 2nd Collection, edited by P. Xie (Publishing House of China Academy of Engineering Physics, Beijing, 1992).

[32] J. P. Vandevender, and D. L. Cook, "Inertial confinement fusion with light ion beams," Science **232**, 831 (1986).

[33] D. Cook, R. Adams, J. Aubert, L. Bacon, J. Bailey, D. Bloomquist, J. Boyes, G. Chandler, R. Coats, J. Corley, J. Crow, M. Cuneo, D. Derzon, M. Derzon, M. Desjarlais, R. Dukart, D. Fehl, A. Filuk, R. Gerber, T. Haill, D. Hanson, D. Humphreys, T. Hussey, H. Ives, D. J. Johnson, D. L. Johnson, W. Johnson, R. Kensek, M. Kiefer, R. Leeper, R. Lemke, T. Lockner, J. Maenchen, M. Matzen, D. McDaniel, P. McKay, E. McGuire, T. Mehlhorn, C. Mendel, L. Mix, A. Moats, W. Nelson, C. Olson, R. Olson, T. Pointon, J. Poukey, J. Quintenz, J. Ramirez, T. Renk, G. Rochau, P. Rockett, S. Rosenthal, D. Rovang, C. Ruiz, D. Schmitt, D. Seidel, S. Slutz, R. Stinnett, W. Stygar, M. Sweeney, G. Tisone, and J. Vandevender, "Light ion driven inertial confinement fusion," *Plasma Physics and Controlled Nuclear Fusion Research 1992*, Würzburg, Germany, 1992 (International Atomic Energy Agency, Vienna, 1993), Vol. 3, pp. 63–71.

[34] *Fusion Policy Advisory Committee Final Report*, DOE/S-0081 (U.S. Department of Energy, Washington DC, 1990).

[35] J. D. Lindl, R. O. Bangerter, J. W.-K. Mark, and Y. L. Pan, "Review of target studies for heavy ion fusion," *Heavy Ion Inertial Fusion*, edited by M. Reiser, T. Godlove, and R. Bangerter, AIP Conf. Proc. 152 (American Institute of Physics, New York, 1986).

[36] M. Murakami, J. Meyer-Ter-Vehn, and R. Ramis, "Thermal x-ray emission from ion-beam-heated matter," J. X-Ray Sci. Technol. **2**, 127 (1990).

[37] D. D.-M. Ho, J. D. Lindl, and M. Tabak, "Radiation converter physics and a method for obtaining the upper limit for gain in heavy-ion fusion," Nucl. Fusion **34**, 1081 (1994).

[38] W. Hogan, R. Bangerter, and G. Kulcinski, "Energy from inertial fusion," Phys. Today **45**(9), 42 (1992).

[39] B. G. Levi, "Veil of secrecy is lifted from parts of Livermore's laser fusion program," Phys. Today **47**(1), 17 (1994).

[40] J. H. Nuckolls, *Laser Interaction and Related Plasma Phenomena*, edited by G. H. Miley and H. Hora (Plenum, New York, 1992), Vol. 10, pp. 23–24.

[41] N. G. Basov and O. N. Krokhin, "The conditions of plasma heating by the optical generator radiation," *Proceedings of the 3rd International Conference on Quantum Electronics*, Paris, 1963, edited by P. Grivet and N.

Bloembergen (Columbia University Press, New York, 1964), pp. 1373–1377.
[42]J. Meyer-Ter-Vehn, "On energy gain of fusion targets: The model of Kidder and Bodner improved," Nucl. Fusion **22**, 561 (1982).
[43]See National Technical Information Service Document No. DE84017287/XAB (M. D. Rosen, J. D. Lindl, and A. R. Thiessen, "Model for gain versus laser energy in direct drive targets," Laser Program Annual Report—83, Lawrence Livermore National Laboratory, Livermore, CA, UCRL-50021-83). Copies may be obtained from the National Technical Information Service, Springfield, VA 22161.
[44]W. K. Levedahl and J. D. Lindl, "Energy scaling of ICF targets for ignition and high gain," Lawrence Livermore National Laboratory, Livermore, CA, CLY-95-0004, 1990 (unpublished).
[45]J. H. Nuckolls, "Initiation of fusion by lasers," Lawrence Livermore Laboratory, Livermore, CA, UCID-15997, 1972 (unpublished).
[46]G. S. Fraley and R. J. Mason, "Preheat effects on microballoon laser-fusion implosions," Phys. Rev. Lett. **35**, 520 (1975).
[47]G. Charatis, J. Downward, R. Goforth, B. Guscott, T. Henderson, S. Gildum, R. Johnson, K. Moncur, T. Leonard, F. Mayer, S. Segall, L. Siebert, B. Solomon, and C. Thomas, "Experimental study of laser-driven compression of spherical glass shells," *Plasma Physics and Controlled Nuclear Fusion Research* (International Atomic Energy Agency, Vienna, 1975), Vol. II, p. 317.
[48]E. K. Storm, H. G. Ahlstrom, M. J. Boyle, D. E. Campbell, L. W. Coleman, S. S. Glaros, H. N. Kornblum, R. A. Lerche, D. R. MacQuigg, D. W. Phillion, F. Rainer, R. Reinecker, V. C. Rupert, V. W. Slivinsky, D. R. Speck, C. D. Swift, and K. G. Tirsell, "Laser fusion experiments at 4 TW," Phys. Rev. Lett. **40**, 1570 (1978).
[49]M. D. Rosen and J. H. Nuckolls, "Exploding pusher performance—A theoretical model," Phys. Fluids **22**, 1393 (1979).
[50]J. D. Lindl and W. C. Mead, "Two-dimensional simulation of fluid instability in laser-fusion pellets," Phys. Rev. Lett. **34**, 1273 (1975).
[51]G. B. Zimmerman and W. L. Kruer, "Numerical simulation of laser-initiated fusion," Comments Plasma Phys. **2**, 51 (1975).
[52]Y. Kato, K. Mima, N. Miyanaga, S. Arinaga, Y. Kitagawa, M. Nakatsuka, and C. Yamanaka, "Random phasing of high-power lasers for uniform target acceleration and plasma-instability suppression," Phys. Rev. Lett. **53**, 1057 (1984).
[53]S. Skupsky, R. W. Short, T. Kessler, R. S. Craxton, S. Letzring, and J. M. Soures, "Improved laser-beam uniformity using the angular dispersion of frequency-modulated light," J. Appl. Phys. **66**, 3456 (1989).
[54]R. H. Lehmburg, A. J. Schmitt, and S. E. Bodner, "Theory of induced spatial incoherence," J. Appl. Phys. **62**, 2680 (1987).
[55]C. Verdon, "High-performance direct-drive capsule designs for the National Ignition Facility," Bull. Am. Phys. Soc. **38**, 2010 (1993).
[56]S. Nakai, "Progress in inertial confinement fusion in Japan," *Proceedings of the IAEA Technical Committee Meeting on Drivers for Inertial Confinement Fusion*, Osaka, Japan, 1991, edited by D. Banner and S. Nakai (International Atomic Energy Agency, Vienna, 1991), pp. 19–22.
[57]M. Nakatsuka, K. Yoshida, Ta. Jitsuno, T. Sasaki, and S. Nakai, "Upgrade for ignition with direct drive," in Ref. 6, pp. 130–133.
[58]J. D. Lindl, "Preliminary target design and spectral output for Shiva Nova," Lawrence Livermore National Laboratory, Livermore, CA, COPD 76-106, 1976 (unpublished).
[59]Fusion Energy Advisory Committee, *Advice and Recommendations to the U.S. Department of Energy in Response to the Charge Letter of September 18, 1992* (U.S. Department of Energy, Washington, DC, 1993).
[60]National Technical Information Service Document No. UCRL 5002175 (E. S. Bliss, J. A. Glaze, K. R. Manes, J. E. Murray, and F. Rainer, "Cyclops laser system," Laser Program Annual Report—1975, Lawrence Livermore National Laboratory, Livermore, CA, pp. 69–74). Copies may be obtained from the National Technical Information Service, Springfield, VA, 22161.
[61]J. D. Lindl, K. Manes, and K. Brooks, "'Forerunner,' First observation of laser-induced thermonuclear fusion and radiation implosion," Lawrence Livermore National Laboratory, Livermore, CA, UCRL-52202, 1976, pp. 88–98 (unpublished).
[62]W. W. Simmons, D. R. Speck, and J. T. Hung, "Argus laser system: Performance summary," Appl. Opt. **17**, 999 (1978).
[63]D. R. Speck, E. S. Bliss, J. A. Glaze, J. W. Herris, F. W. Holloway, J. T. Hunt, B. C. Johnson, D. J. Kuizenga, R. G. Ozarski, H. G. Patton, P. R. Ruppert, G. J. Suski, C. D. Swift, and C. E. Thompson, "The Shiva laser-fusion facility," IEEE J. Quantum Electron. **QE-9**, 1599 (1981).
[64]M. Rosen, "Half-Cairn physics experiments on Argus," Laser Program Annual Report, 1978, Lawrence Livermore National Laboratory, Livermore, CA, UCRL-50055-78, pp. 4-42–4-51 (unpublished).
[65]W. C. Mead, "Intermediate density targets," in Ref. 64, pp. 2-16–2-59 (unpublished).
[66]M. Boyle and E. Storm, "Review of the Argus 10× to 100× experimental program," in Ref. 64, pp. 4-5–4-42 (unpublished).
[67]J. M. Auerbach, E. M. Campbell, N. M. Ceglio, C. W. Hatcher, S. M. Lane, R. A. Lerche, L. N. Koppell, D. L. Matthews, K. R. Manes, W. C. Mead, R. H. Price, W. M. Ploeger, and J. C. Stevens, "10× and 100× Cairn experiment on Shiva," Laser Program Annual Report, 1979, Lawrence Livermore National Laboratory, Livermore, CA, UCRL-50055-79, pp. 5-1–5-31 (unpublished).
[68]E. M. Campbell, W. M. Ploeger, P. H. Lee, and S. M. Lane, "Exploding-pusher-tamper areal density measurement by neutron activation," Appl. Phys. Lett. **36**, 12 (1980).
[69]J. D. Lindl, "Cairn hohlraum scaling study—analysis of two-nanosecond experiments," in Ref. 67, pp. 5-80–5-88 (unpublished).
[70]J. M. Auerbach, K. R. Manes, and D. W. Phillion, "Cairn scaling study—The experiments," in Ref. 67, pp. 5-62–5-79 (unpublished).
[71]L. J. Suter and J. M. Auerbach, "NPIRE experiments," Laser Program Annual Report, 1980, Lawrence Livermore National Laboratory, Livermore, CA, UCRL-50055-80, pp. 2-37–2-45 (unpublished).
[72]J. D. Lindl, "Apollo targets for Nova and KrF-driven reactors," in Ref. 67, pp. 2-77–2-88 (unpublished).
[73]E. Storm, "Laser program overview," in Ref. 67, pp. 1-1–1-4 (unpublished).
[74]D. L. Youngs, "Numerical simulation of turbulent mixing by Rayleigh–Taylor instability," Physica D **12**, 32 (1984).
[75]B. W. Weinstein, "1979 Apollo targets," in Ref. 67, UCRL-50055-79, pp. 4-8–4-9 (unpublished).
[76]J. M. Auerbach, S. M. Lane, and K. G. Tirsell, "Experiments with Apollo intermediate-density targets," in Ref. 71, pp. 4-29–4-33 (unpublished).
[77]Y. L. Pan, "Analysis of Apollo intermediate-density targets," in Ref. 71, pp. 4-33–4-37 (unpublished).
[78]W. Seka, S. D. Jacobs, J. E. Rizzo, R. Boni, and R. S. Craxton, "Demonstration of high efficiency third harmonic conversion of high power Nd-glass laser radiation," Opt. Commun. **34**, 469 (1980); R. S. Craxton, *ibid.* **34**, 474 (1980).
[79]E. M. Campbell, R. E. Turner, L. V. Griffith, H. N. Kornblum, E. W. McCauley, W. C. Mead, B. F. Lasinski, D. W. Phillion, and B. L. Pruett, "Argus scaling experiments," Laser Program Annual Report, Lawrence Livermore National Laboratory, Livermore, CA, UCRL-50055-81/82, 1982, pp. 4-2–4-26 (unpublished).
[80]S. Sakabe, R. Sigel, G. D. Tsakiris, I. B. Foldes, and P. Herrmann, "X-ray generation in a cavity heated by 1.3 or 0.44 mm laser light. I. Time-integrated measurements," Phys. Rev. A, **38**, 5756 (1988).
[81]J. D. Lindl and G. E. McClellan, "Reactor target gain and symmetry calculations," in Ref. 69 pp. 2-10–2-22 (unpublished).
[82]J. D. Lindl, "A strategy for determining the driver requirements for high-gain ICF implosions utilizing hydrodynamically equivalent capsules on the Nova laser," Laser Program Annual Report, 1981, Lawrence Livermore National Laboratory, Livermore, CA, UCRL-50055-80/81, pp. 2-49–2-57 (unpublished).
[83]Draft of *Ad Hoc* Experts Group on Fusion Report (October 1979), 70-ETG-28 (unpublished).
[84]E. M. Campbell, J. T. Hunt, E. S. Bliss, D. R. Speck, and R. P. Drake, "Nova experimental facility," Rev. Sci. Instrum. **57**, 2101 (1986).
[85]F. Ze, L. Suter, E. M. Campbell, R. L. Kauffman, and D. W. Phillion, "Results of the Novette implosion experiments," Laser Program Annual Report 1983, Lawrence Livermore National Laboratory, Livermore, CA, UCRL-50055-83, pp. 4-21–4-30 (unpublished).
[86]L. J. Suter, "Analysis of Novette compression series," in Ref. 85, pp. 4-30–4-48 (unpublished).
[87]D. W. Phillion and S. V. Weber, "Radiation drive scaling at 2ω and 4ω," in Ref. 85, pp. 4-7–4-21 (unpublished).
[88]*Review of the Department of Energy's Inertial Confinement Fusion Program* (National Academy Press, Washington, DC, 1986).
[89]R. Kauffman, H. Kornblum, R. Turner, F. Ze, B. Lasinski, and R. A. Thiessen, "Nova holhlraum experiments," Laser Program Annual Report, 1985, Lawrence Livermore National Laboratory, Livermore, CA, UCRL-50055-85, pp. 4-1–4-6 (unpublished).
[90]See National Technical Information Service Document No. DE93014373 [*Laboratory Microfusion Capability Study: Phase II Report* (U.S. Department of Energy, Washington, DC, DOE/DP-0017, 1993)]. Copies may be

obtained from the National Technical Information Service, Springfield, VA 22161.

[91] R. L. Kauffman, F. Ze, L. J. Suter, R. P. Drake, W. G. Halsey, H. N. Kornblum, B. F. Lasinski, D. W. Phillion, and A. R. Thiessen, "Laser driven hohlraums," Laser Program Annual Report, 1986/87, Lawrence Livermore National Laboratory, Livermore, CA, UCRL-50055-86/87, pp. 4-2–4-25 (unpublished).

[92] R. E. Turner, L. J. Suter, R. L. Kauffman, J. Z. Grens, and D. W. Phillion, "Results from the Symmetry-I experimental series on Nova," in Ref. 91, pp. 4-25–4-34 (unpublished).

[93] J. D. Kilkenny and V. C. Rupert, "Preliminary Rayleigh–Taylor experiments on Nova," in Ref. 91, pp. 4-64–4-89 (unpublished).

[94] D. H. Munro, "LASNEX shell stability modeling of the Nova Rayleigh–Taylor experiments," in Ref. 91, pp. 2-82 to 2-90 (unpublished).

[95] L. J. Suter and R. E. Turner, "Analysis of pulse-shaped Nova implosions," ICF Program Annual Report 1988/1989, Lawrence Livermore National Laboratory, Livermore, CA, UCRL-LR-116901-88-89, pp. 2-8–2-18 (unpublished).

[96] S. P. Hatchett, S. M. Lane, S. W. Haan, M. D. Cable, D. R. Kania, R. A. Lerche, and B. A. Remington, "High-density, pulse-shaped implosions," in Ref. 95, pp. 2-19–2-27 (unpublished).

[97] C. J. Keane, D. Kania, B. A. Hammel, O. L. Landen, B. A. Remington L. J. Suter, and R. L. Turner, "High temperature implosion experiments on Nova," *Los Alamos National Laboratory 1991 Topical Conference: The Physics of Radiatively Driven ICF Targets*, Lost Alamos National Laboratory, Los Alamos, NM, LA-CP-91-400, pp. 68–74 (unpublished).

[98] J. D. Lindl, "Progress on ignition physics for ICF and plans for a Nova Upgrade to demonstrate ignition and propagating burn by the year 2000," *Fusion to Light Surfing*, edited by T. Katsouleas (Addison–Wesley, Redwood City, CA, 1991), p. 177.

[99] J. D. Lindl, "Progress on ignition physics for ICF and plans for a National Ignition Facility to demonstrate ignition and propagating burn," ICF Quart. Rep. **3**, 9 (1993), Lawrence Livermore National Laboratory, Livermore, CA, UCRL-LR-113687-93-1 (unpublished).

[100] See National Technical Information Service Document No. DE94010835 (Precision Nova ICF Quart. Rep. **4**, edited by H. T. Powell, Lawrence Livermore National Laboratory, UCRL-LR-105821-94-1, 1994). Copies may be obtained from the National Technical Information Service, Springfield, VA 22161.

[101] See National Technical Information Service Document No. SAND792454 (M. M. Widner, "Fuel energy balance studies of pellet ignition requirements," Sandia National Laboratories, SAND-79-2454). Copies may be obtained from the National Technical Information Service, Springfield, VA 22161.

[102] R. C. Kirkpatrick and J. A. Wheeler, "The physics of DT ignition in small fusion targets," Nucl. Fusion **21**, 389 (1981).

[103] L. Spitzer, *Physics of Fully Ionized Gases*, 2nd Rev. ed. (Interscience, New York, 1967), p. 145.

[104] M. D. Rosen (private communication, 1988).

[105] S. P. Hatchett and J. D. Lindl, "Design studies of single-shell ICF capsules for Nova," in Ref. 85, pp. 2-28–2-35 (unpublished).

[106] J. W. Bond, K. M. Watson, and J. A. Welch, *Atomic Theory of Gas Dynamics* (Addison–Wesley, Redwood City, CA, 1965).

[107] J. Nuckolls, J. Lindl, W. Mead, A. Thiessen, L. Wood, and G. B. Zimmerman, "Laser-driven implosion of hollow pellets," *Controlled Nuclear Fusion Research 1974* (International Atomic Energy Agency, Vienna, 1975), Vol. 3, pp. 535–542.

[108] E. M. Campbell, J. D. Kilkenny, D. R. Kania, P. M. Young, S. M. Lane, S. G. Clendinning, D. W. Phillion, C. B. Darrow, R. L. Kauffman, J. D. Lindl, L. J. Suter, S. P. Hatchett, W. L. Kruer, D. H. Munro, S. W. Haan, R. J. Wallace, C. W. Hatcher, R. S. Upadhye, D. T. Kyrazis, G. L. Hermes, D. R. Speck, C. Bibeau, R. B. Ehrlich, D. L. Matthews, B. J. MacGowan, M. D. Rosen, and M. S. Maxon, "Recent results from the Nova Program at LLNL," Laser Part. Beams **9**, 209 (1991).

[109] C. B. Darrow, "Drive and laser characterization for shaped-pulse hohlraum interactions," in Ref. 95 pp. 171–179 (unpublished).

[110] C. Darrow, L. Suter, H. Kornblum, D. W. Phillion, R. Thiessen, and R. L. Kauffman, "Recent indirect drive experiments on Nova," Los Alamos National Laboratory 1991 Topical Conference: The Physics of Radiatively Driven ICF Targets, Los Alamos National Laboratory, Los Alamos, NM, LA-CP-91-400, pp. 25–33 1991 (unpublished).

[111] B. A. Hammel, C. J. Keane, M. D. Cable, D. R. Kania, J. D. Kilkenny, R. W. Lee, and R. Pasha, "X-ray spectroscopic measurements of high densities and temperatures from indirectly driven inertial fusion capsules," Phys. Rev. Lett. **70**, 1263 (1993).

[112] B. A. Hammel, C. J. Keane, T. R. Dittrich, D. R. Kania, J. D. Kilkenny, R. W. Lee, and W. K. Levedahl, "K- and L-shell x-ray spectroscopic measurements and pusher dopants in indirectly driven ICF implosions," J. Quant. Spectrosc. Radiat. Transfer **51**, 113 (1994).

[113] H. Griem, *Plasma Spectroscopy* (McGraw-Hill, New York, 1964), pp. 63–101.

[114] R. L. McCrory and R. L. Morse, "Dependence of laser-driven compression efficiency on wavelength," Phys. Rev. Lett. **38**, 544 (1977).

[115] C. E. Max, J. D. Lindl, and W. C. Mead, "Effect of symmetry requirements on the wavelength scaling of directly driven laser fusion implosions," Nucl. Fusion **23**, 131 (1983).

[116] S. M. Pollaine and J. D. Lindl, "Effect of capsule aspect ratio on hydrodynamic efficiency," Nucl. Fusion **26**, 1719 (1986).

[117] S. P. Hatchett and M. D. Rosen, "Analysis of radiation-driven rocket efficiency," Laser Program Annual Report 1981/1982, Lawrence Livermore National Laboratory, Livermore, CA, UCRL-50055-81/82, pp. 2-15–2-20 (unpublished).

[118] M. D. Rosen and J. D. Lindl, "Model for gain vs laser energy for x-ray driven targets," in Ref. 85 pp. 2-17–2-20 (unpublished).

[119] See National Technical Information Service Document No. DE92006882 (S. Hatchett, "Ablation gas dynamics of low-Z materials, illuminated by soft x-rays," Lawrence Livermore National Laboratory, Livermore, CA, UCRL-JC-108348, 1991). Copies may be obtained from the National Technical Information Service, Springfield, VA 22161.

[120] J. D. Lindl, "Hydrodynamic and plasma stability limitations on the choice of laser wavelength for radiation driven ICF implosions," in Ref. 85, pp. 2-40–2-46 (unpublished).

[121] M. Tabak, D. H. Munro, and J. D. Lindl, "Hydrodynamic instability and the direct drive approach to laser fusion," Phys. Fluids B **2**, 1007 (1990).

[122] See National Technical Information Service Document No. DE86002577 (R. Lelevier, G. Lasher, and F. Bjorklund, "Effect of a Density Gradient on Taylor Instability"). Copies may be obtained from the National Technical Information Service, Springfield, VA 22161.

[123] D. Munro, "Analytic solutions for Rayleigh–Taylor growth rates in smooth density gradients," Phys. Rev. A **38**, 1433 (1988).

[124] H. Takabe, K. Mima, L. Montierth, and R. L. Morse, "Self-consistent growth rate of the Rayleigh–Taylor instability in an ablatively accelerating plasma," Phys. Fluids **28**, 3676 (1985).

[125] S. Bodner, "Rayleigh–Taylor instability and laser-pellet fusion," Phys. Rev. Lett **33**, 761 (1974).

[126] S. G. Glendinning, S. Weber, P. Bell, L. DaSilva, S. Dixit, M. Henesian, D. Kania, J. Kilkenny, H. Powell, R. Wallace, and P. Wegner, "Laser driven planar Rayleigh–Taylor instability experiments," Phys. Rev. Lett. **69**, 1201 (1992).

[127] M. Katayama, H. Azechi, A. Nishiguchi, M. Nakai, and S. Nakai, "Observation of hydrodynamic instabilities in planar foils accelerated with amplified spontaneous emission," *ILE Quarterly Progress Report-92*, No. 43 (Institute of Laser Engineering, Osaka University Press, Osaka, Japan, 1992), p. 27.

[128] J. Kilkenny, "Experimental results on hydrodynamic instabilities in laser accelerated planar packages," Phys. Fluids B **2**, 1400 (1990).

[129] B. A. Remington, S. W. Haan, S. G. Glendinning, J. D. Kilkenny, D. H. Munro, and R. J. Wallace, "Large growth Rayleigh–Taylor experiments using shaped laser pulses," Phys. Rev. Lett. **67**, 3259 (1991).

[130] B. A. Remington, S. V. Weber, S. W. Haan, J. D. Kilkenny, S. G. Glendinning, R. J. Wallace, W. H. Goldstein, B. G. Wilson, and J. K. Nash, "Laser driven hydrodynamic instability experiments," Phys. Fluids B **5**, 2589 (1993).

[131] S. Haan, "The onset of non-linear saturation for Rayleigh–Taylor growth in the presence of a full spectrum of modes," Phys. Rev. A **39**, 5812 (1989).

[132] D. Layzer, "On the stability of superposed fluids in a gravitational field," Astrophys. J. **122**, 1 (1955).

[133] S. Haan, "Weakly nonlinear hydrodynamic instabilities in inertial fusion," Phys. Fluids B **3**, 2349 (1991).

[134] B. A. Remington, S. V. Weber, M. M. Marinak, S. W. Haan, J. D. Kilkenny, R. Wallace, and G. Dimonte, "Multimode Rayleigh–Taylor experiments on Nova," Phys. Rev. Lett. **73**, 545 (1994).

[135] T. Dittrich, B. A. Hammel, C. J. Keane, R. McEachern, R. E. Turner, S. W. Haan, and L. J. Suter, "Diagnosis of pusher-fuel mix in indirectly driven Nova implosions," Phys. Rev. Lett. **73**, 2224 (1994).

[136] C. J. Keane, O. L. Landen, B. A. Hammel, T. R. Dittrich, S. P. Langer,

and D. H. Munro, "Nova high growth factor implosion experiments: Modeling and analysis," Bull. Am. Phys. Soc. **39**, 1686 (1994).
[137]O. L. Landen, B. A. Hammel, C. J. Keane, T. J. Murphy, R. G. Hay, R. A. Lerche, M. B. Nelson, M. D. Cable, J. D. Kilkenny, T. R. Dittrich, W. K. Levedahl, L. Suter, S. W. Haan, S. P. Hatchett, R. McEachern, R. Cook, and R. J. Wallace, "High growth-factor ICF implosions," Bull. Am. Phys. Soc. **39**, 1686 (1994).
[138]T. Endo, K. Shigemori, H. Azechi, A. Nishiguchi, K. Mima, M. Sato, M. Nakai, S. Nakaji, N. Miyanaga, S. Matsuoka, A. Ando, K. Tanaka, and S. Nakai, "Dynamic behavior of rippled shock waves and subsequently induced areal-density-perturbation growth in laser-irradiated foils," Phys. Rev. Lett. **74**, 3608 (1995).
[139]R. C. Cook, T. P. Bernat, G. Collins. S. A. Letts, R. McEachern, G. E. Overturf, and R. E. Turner, "Production and characterization of ICF capsules," *Plasma Physics and Controlled Nuclear Fusion Research* (International Atomic Energy Agency, Vienna, 1993), Vol. 3, p. 449.
[140]See National Technical Information Service Document No. DE 95000314 (R. J. Wallace, R. L. McEachern, and W. W. Wilcox, "Laser ablation machining of ICF capsules," ICF Quart. Rep. **4**, 79 (1994), Lawrence Livermore National Laboratory, UCRL-LR-105821-94-3). Copies may be obtained from the National Technical Information Service, Springfield, VA 22161.
[141]Ya. B. Zel'dovich and Yu. P. Razier, *Physics of Shock Waves and High-Temperature Hydrodynamic Phenomena* (Academic, New York, 1966), Sec. II.10.
[142]R. E. Marshak, "Effect of radiation on shock wave behavior," Phys. Fluids **1**, 24 (1958).
[143]M. D. Rosen, "Scaling law for radiation temperature," in Ref. 67 pp. 2-37–2-46 (unpublished).
[144]N. Kaiser, J. Meyer-ter-Vehn, and R. Sigel, "The x-ray driven heating wave," Phys. Fluids B **1**, 1747 (1989).
[145]R. Pakula, and R. Sigel, "Self-similar expansion of dense matter due to heat transfer by nonlinear conduction," Phys. Fluids **28**, 232 (1985).
[146]A. Bar Shalom, J. Oreg, W. H. Goldstein, D. Shvarts, and A. Zigler, "Super-transition-arrays: A model for the spectral analysis of hot, dense plasma," Phys. Rev. A **40**, 3183 (1989).
[147]J. D. Lindl, "Nova Upgrade has focused on target symmetry and hohlraum plasma conditions," presentation to NAS ICF Review Committee, Lawrence Livermore National Laboratory, Livermore, CA, XDIV-90-0045, 1990 (unpublished).
[148]M. Murakami and J. Meyer-ter-Vehn, "Indirectly driven target for inertial confinement fusion," Nucl. Fusion **31**, 1315 (1991).
[149]R. Kauffman, L. Suter, C. B. Darrow, J. D. Kilkenny, H. N. Kornblum, D. S. Montgomery, D. W. Phillion, M. D. Rosen, A. R. Thiessen, R. J. Wallace, and F. Ze, "High temperatures in inertial confinement fusion radiation cavities heated with 0.35 μm light," Phys. Rev. Lett. **73**, 2320 (1994).
[150]H. N. Kronblum and R. L. Kauffman, "Measurement of 0.1–3-keV x-rays from laser plasmas," Rev. Sci. Instrum. **57**, 2179 (1986).
[151]M. D. Rosen, "Scaling laws for specialized hohlraums," Lawrence Livermore National Laboratory, Livermore, CA, UCRL-ID-119916, 1994 (unpublished).
[152]See National Technical Information Service Document No. DE95000314 (T. J. Murphy and P. A. Amendt, "X-ray flux symmetry control in advanced Nova holhraum, " ICF Quart. Rep. **4**, 101 (1994) Lawrence Livermore National Laboratory, UCRL-LR-105821-94-3). Copies may be obtained from the National Technical Information Service, Springfield, VA 22161.
[153]R. Sigel, G. D. Tsakiris, F. Lavarenne, J. Massen, R. Fedosejevs, J. Meyer-ter-Vehn, M. Murakami, K. Eidman, S. Witkowski, H. Nishimura, Y. Kato, H. Takabe, T. Endo, K. Kondo, H. Shiraga, S. Sakabe, T. Jitsuno, M. Takagi, C. Yamanaka, and S. Nakai, "Experimental observation of laser-induced radiation heat waves," Phys. Rev. Lett. **65**, 587 (1990).
[154]J. Porter and A. R. Thiessen, "Summary of albedo experiment," Lawrence Livermore National Laboratory, Livermore, CA, CLY-92-059, 1992 (unpublished).
[155]See National Technical Information Service Document No. DE95011969 (J. L. Porter, T. J. Orzechowski, M. D. Rosen, A. R. Thiessen, L. J. Suter, and J. T. Larsen, "The albedo of gold at high temperatures," ICF Quart. Rep. **4**, 125 (1994); Lawrence Livermore National Laboratory, UCRL-LR-105821-94-4). Copies may be obtained from the National Technical Information Service, Springfield, VA 22161.
[156]See National Technical Information Service Document No. DE88014097, (R. L. Kauffman, "X-ray conversion efficiency," Laser Program Annual Report 1986, Lawrence Livermore National Laboratory, Livermore, CA, UCRL-50021-86). Copies may be obtained from the National Technical Information Service, Springfield, VA 22161.
[157]P. D. Goldstone, S. R. Goldman, W. C. Mead, J. A. Cobble, G. Stradling, R. H. Day, A. Hauer, M. C. Richardson, R. S. Marjoribanks, P. A. Jaanimagi, R. L. Keck, F. J. Marshall, W. Seka, O. Barnouin, B. Yaakobi, and S. A. Letzring, "Dynamics of high-Z plasmas produced by a short-wavelength laser," Phys. Rev. Lett. **59**, 56 (1987).
[158]M. D. Rosen, "Evidence of a laser intensity threshold for the onset of inhibited electron transport," Comments Plas. Phys. **8**, 165 (1984).
[159]F. Ze, R. Kauffman, J. Kilkenny, S. Langer, D. More, L. Powers, D. Ress, M. Rosen, L. Suter, R. Wallace, and J. Wiedwald, "Investigation of x-ray conversion efficiency in hohlraums," *1993 Topical Conference on Physics of Radiatively Driven ICF Targets*, 1993, Monterey, California, to appear in Def. Res. Rev. (unpublished).
[160]F. Ze, R. L. Kauffman, J. D. Kilkenny, J. Wiedwald, P. M. Bell, R. Hanks, J. Stewart, D. Dean, J. Bower, and R. Wallace, "A new multichannel soft x-ray framing camera for fusion experiments," Rev. Sci. Instrum. **63**, 5124 (1992).
[161]R. Sigel, R. Pakula, S. Sakabe, and G. D. Tsakiris, "X-ray generation in a cavity heated by 1.3 or 0.44 mm laser light III Comparison of the experimental results with theoretical predictions for x-ray confinement," Phys. Rev. A **38**, 5779 (1988).
[162]L. J. Suter (private communication, 1994).
[163]See National Technical Information Service Document No. DE95011969, (D. S. Kershaw, M. K. Prasad, and M. J. Shaw, "Three-dimensional, unstructured-mesh Eulerian hydrodynamics with upwind, discontinuous, finite-element method," ICF Quart. Rep. **4**, 160 (1994), Lawrence Livermore National Laboratory, UCRL-LR-105821-94-4). Copies may be obtained from the National Technical Information Service, Springfield, VA 22161.
[164]J. Stamper, E. A. McLean, and B. H. Ripin, "Spontaneous magnetic fields in laser-produced plasmas by Faraday rotation," Phys. Rev. Lett. **40**, 1177 (1978).
[165]D. Ress, L. V. Powers, F. Ze, L. J. Powers, and R. J. Wallace, "Soft x-ray emission spatial profiles in laser-driven hohlraums," Bull. Am. Phys. Soc. **39**, 1610 (1994).
[166]S. I. Braginskii, "Transport processes in a plasma," *Reviews of Plasma Physics* (Consultants Bureau, New York, 1965), Vol. 1, pp. 205–311.
[167]J. R. Sanmartin, "Electron heat conduction in ICF targets," *Nuclear Fusion by Inertial Confinement*, edited by G. Velarde, Y. Ronen, and J. M. Martinez-Val (CRC, Boca Raton, FL, 1993), Chap. 7.
[168]E. M. Epperlein and M. G. Haines, "Plasma transport coefficients in a magnetic field by direct numerical solution of the Fokker–Planck equation," Phys. Fluids **29**, 1029 (1986).
[169]See National Technical Information Service Document No. DE88016329 (P. D. Nielsen and G. B. Zimmerman, "Treatment of θ-directed magnetic fields in LASNEX," UCRL-53123, 1981). Copies may be obtained from the National Technical Information Service, Springfield, VA 22161.
[170]J. Hammer (private communication, 1994).
[171]S. W. Haan, "Radiation transport between concentric spheres," Lawrence Livermore National Laboratory, Livermore, CA, COPD 83-64, 1983 (unpublished).
[172]A. Caruso and C. Strangio, "The quality of the illumination for a spherical cavity enclosed in a radiating cavity," Jpn. J. Appl. Phys. **30**, 1095 (1991).
[173]L. J. Suter, "Cross talk between modes in cylindrical hohlraums," in Ref. 89, pp. 30–31 (unpublished).
[174]S. M. Pollaine (private communication, 1992).
[175]See National Technical Information Service Document No. DE86005297 (J. W. -K. Mark, "Reduction of deposition asymmetries in directly driven ion beam and laser targets," *1984 Laser Program Annual Report*, Lawrence Livermore National Laboratory, Livermore, CA, UCRL-50021-84, 1984, pp. 3-24–3-28). Copies may be obtained from the National Technical Information Service, Springfield, VA 22161.
[176]E. Minguez, "Radiation transport in ICF targets," in Ref. 16, Chap. 8.
[177]J. A. Fleck, Jr. and J. D. Cummings, "An implicit Monte Carlo scheme for calculating time and frequency dependent nonlinear radiation transport," J. Comput. Phys. **8**, 313 (1971).
[178]G. C. Pomraning, *Equations of Radiation Hydrodynamics* (Pergamon, New York, 1973), Chap. 5, Sec. 5.
[179]G. C. Pomraning, in Ref. 178, Sec. 6.
[180]R. C. Kirkpatrick, J. E. Tabor, E. L. Lindman, and A. J. Cooper, "Indirect solar loading of waste heat radiators," *Proceedings of Space 88*, edited by

S. W. Johnson and J. P. Wetzel (American Society of Civil Engineers, New York, 1988), pp. 964–973.
[181]M. Murakami and J. Meyer-ter-Vehn, "Radiation symmetrization in indirectly driven ICF targets," J. Nucl. Fusion **31**, 1333 (1991).
[182]J. D. Lindl, "Introduction to hohlraums," LLNL ICF Program (ICFAC/DP), Lawrence Livermore National Laboratory, Livermore, CA, CLY-92-094-VOL-1, pp. 5–54 (1992) (unpublished).
[183]M. Tabak, "Symmetry properties of reactor scale hohlraums," in Ref. 91, pp. 2-169–2-182 (unpublished).
[184]J. Dawson, P. Kaw, and B. Green, "Optical absorption and expansion of laser-produced plasmas," Phys. Fluids **12**, 875 (1969).
[185]J. D. Lindl, "Apollo targets for Nova and KrF-driven reactors," in Ref. 64, pp. 2-77–2-88 (unpublished).
[186]A. R. Thiessen, "Some aspects of LMF hohlraum design," *1988 Laser Program Annual Report: Target Design*, Lawrence Livermore National Laboratory, Livermore, CA, XDIV-90-0054 (unpublished).
[187]S. Pollaine, "Nova Upgrade symmetry design," 1990/1991 LLNL Laser Program Annual Report, Lawrence Livermore National Laboratory, Livermore, CA, UCRL-LR-116901-90/91, pp. 214–234 (unpublished).
[188]S. Pollaine, "Helium-filled hohlraum for foam-ablator capsules," in Ref. 186, pp. 246–259 (unpublished).
[189]L. J. Suter, A. A. Hauer, L. V. Powers, D. B. Ress, N. Delameter, W. W. Hsing, O. L. Landon, A. R. Thiessen, and R. E. Turner, "Modeling and interpretation of Nova's symmetry scaling data base." Phys. Rev. Lett. **73**, 2328 (1994).
[190]S. W. Haan, "Target design for national ignition facility," Presentation to ICFAC, 16–18 December 1992, Lawrence Livermore National Laboratory, Livermore, CA, CLY-92-094–Vol. 2, pp. 5–40 (unpublished).
[191]J. D. Lindl, "The physics of high gain ICF capsules is demanding but consistent with the Nova and Halite/Centurion data base," Presentation to DOE LMF Review, Lawrence Livermore National Laboratory, Livermore, CA, XDIV-88-0062, 1988 (unpublished).
[192]A. A. Hauer, "X-ray driven implosions in laser heated hohlraums," *Laser Plasma Interactions*, edited by M. Hooper and A. Cairns (Redwood Burn, Trowbridge, England, 1995), Vol. 5, pp. 5–24.
[193]J. D. Kilkenny, P. Bell, R. Hanks, G. Power, R. E. Turner, and J. Wiedwald, "High-speed gated x-ray imagers," Rev. Sci. Instrum. **59**, 1793 (1988).
[194]D. Ress, R. A. Lerche, and L. DaSilva, "Demonstration of an x-ray ring-aperture microscope for inertial confinement fusion experiments," Appl. Phys. Lett. **60**, 410 (1992).
[195]N. D. Delameter, E. L. Lindman, G. Magelssen, A. A. Hauer, J. B. Moore, and M. A. Salazar, "Symmetry experiments in gas-filled hohlraums at Nova," Bull. Am. Phys. Soc. **39**, 1610 (1994).
[196]L. J. Suter (private communication, 1995).
[197]R. W. Short, R. Bingham, and E. A. Williams, "Filamentation of laser light in flowing plasmas," Phys. Fluids **25**, 2302 (1982); H. Rose (private communication, 1994); D. Hinkel (private communication, 1995).
[198]L. V. Powers, D. B. Ress, L. J. Suter, and F. Ze, "LASNEX modeling of soft x-ray emission profiles in Nova Hohraums," in Ref. 159, (unpublished).
[199]P. Amendt, S. G. Glendinning, B. A. Hammel, R. G. Hay, and L. J. Suter, "Witness foam-ball diagnostic for Nova hohlraum time-dependent drive asymmetry," Rev. Sci. Instrum. **66**, 785 (1995).
[200]P. Amendt (private communication, 1995).
[201]L. J. Suter, "Diagnosing capsule drive symmetry with a re-emission ball," Laser Program Annual Report, 1984, Lawrence Livermore National Laboratory, Livermore, CA, UCRL-50055-84, pp. 2-19–2-26 (unpublished).
[202]N. D. Delameter, G. R. Magelssen, A. A. Hauer, L. J. Suter, and R. E. Turner, "Re-emission ball technique for symmetry measurements," Bull. Am. Phys. Soc. **38**, 1885 (1993).
[203]M. Born and E. Wolf, *Principles of Optics*, 5th ed. (Pergamon, New York, 1975), Sec. 3.2.1.
[204]M. Cable, S. E. Hatchett, J. A. Caird, J. D. Kilkenny, H. N. Kornblum, S. M. Lane, C. W. Laumann, R. A. Lerche, T. J. Murphy, J. Murray, M. B. Nelson, D. W. Phillion, H. T. Powell, and D. B. Ress, "Indirect driven, high convergence inertial confinement fusion implosions," Phys. Rev. Lett. **73**, 2316 (1994).
[205]M. B. Nelson, M. Cable, "LaNSA: A large neutron scintillator array for neutron spectroscopy at Nova," Rev. Sci. Instrum. **63**, 4874 (1992).
[206]E. G. Gamalii, S. Yu. Guskov, O. N. Krokhin, and V. B. Rozanov, "Possibility of determining the characteristics of laser plasma by measuring the neutrons of the DT reaction," JETP Lett. **21**, 70 (1975).
[207]M. D. Cable and S. P. Hatchett, "Neutron spectra from inertial confinement fusion targets for measurement of fuel areal density and charged particle stopping powers," J. Appl. Phys. **62**, 2233 (1987).
[208]J. D. Lindl, "LMF hohlraum design is based on experience gained from Nova and Halite/Centurion experiments," presentation to DOE LMF review, Lawrence Livermore National Laboratory, Livermore, CA, XDIV-88-0060, 1988 (unpublished).
[209]J. C. Fernandez, J. A. Cobble, C. C. Gomez, G. S. Schmidt, and D. A. Montgomery, "Hohlraum plasma dynamics experiments on the Nova laser," in Ref. 190, pp. 61–84 (unpublished).
[210]K. Nishikawa and C. S. Liu, *Advances in Plasma Physics,* edited by A. Simon and W. B. Thompson (Wiley, New York, 1976), Vol. 6, pp. 3–82.
[211]D. W. Phillion, W. L. Kruer, and V. C. Rupert, "Brillouin scatter in laser-produced plasmas," Phys. Rev. Lett. **39**, 1529 (1977).
[212]C. E. Clayton, C. Joshi, A. Yasuda, and F. F. Chen, "Dependence of stimulated Brillouin scattering on target material and f number," Phys. Fluids **24**, 2312 (1981).
[213]R. L. Berger, B. F. Lasinski, T. B. Kaiser, E. A. Williams, A. B. Langdon, and B. I. Cohen, "Theory and three-dimensional simulation of light filamentation in laser-produced plasma," Phys. Fluids B **5**, 2258 (1993).
[214]R. L. Berger, B. F. Lasinski, A. B. Langdon, T. B. Kaiser, B. B. Afeyan, B. I. Cohen, C. H. Still, and E. A. Williams, "The influence of spatial and temporal laser beam smoothing on stimulated Brillouin scattering in filamentated laser light," Phys. Rev. Lett. **75**, 1078 (1995).
[215]O. Willi, T. Afshar-rad, and S. Coe, "Study of instabilities in long scale-length plasmas with and without laser-beam-smoothing techniques," Phys. Fluids B **2**, 1318 (1990).
[216]C. Labaune, S. Baton, and T. Jalinaud, H. Baldis, and D. Pesme, "Filamentation in long scale length plasmas: experimental evidence and effects of laser spatial incoherence," Phys. Fluids B **4**, 2224 (1992).
[217]W. Seka, R. E. Bahr, R. W. Short, A. Simon, R. S. Craxton, D. S. Montgomery, and A. E. Rubenchik, "Nonlinear laser–matter interaction processes in long-scale-length plasmas," Phys. Fluids B **4**, 2232 (1992).
[218]B. J. MacGowan (private communication, 1995).
[219]L. V. Powers, R. E. Turner, R. L. Kauffman, R. L. Berger, P. Amendt, C. A. Back, T. P. Bernat, S. N. Dixit, D. Eimerl, J. A. Harte, M. A. Henesian, D. H. Kalantar, B. F. Lasinski, B. J. MacGowan, D. S. Montgomery, D. H. Munro, D. M. Pennington, T. D. Shepard, G. F. Stone, L. J. Suter, and E. A. Williams, "Low stimulated Brillouin backscatter observed from large, hot plasmas in gas-filled hohlraums," Phys. Rev. Lett. **74**, 2957 (1995).
[220]J. C. Fernandez, J. A. Cobble, W. W. Hsing, B. H. Wilde, B. H. Failor, R. G. Hockaday, P. L. Gobby, D. A. Montgomery, H. N. Kornblum, and J. L. Miller, "Laser–plasma instability in hohlraums," submitted to Phys. Rev. Lett.
[221]C. A. Back, "Measurements of electron temperature by spectroscopy in hohlraum targets," submitted to Phys. Rev. Lett.
[222]S. C. Wilks, W. L. Kruer, J. Denavit, K. Estabrook, D. E. Hinkel, D. Kalantar, A. B. Langdon, B. MacGowan, D. Montgomery, J. Moody, and E. A. Williams, "Nonlinear theory and simulations of stimulated Brillouin backscatter in multi-species plasmas," Phys. Rev. Lett. **74**, 5048 (1995).
[223]M. D. Rosen, "Electron transport and preheat," Laser Program Annual Report—79, Lawrence Livermore National Laboratory, Livermore, CA, UCRL-50021-79, pp. 5-91–5-96 (unpublished).
[224]M. D. Rosen, R. H. Price, E. M. Campbell, D. W. Phillion, K. G. Estabrook, B. F. Lasinski, and J. M. Auerbach, S. P. Obenshain, E. A. McLean, R. R. Whitlock, and B. H. Ripin, "Analysis of laser–plasma coupling and hydrodynamic phenomena in long-pulse, long-scale-length plasmas," Phys Rev. A **36**, 247 (1987).
[225]M. D. Rosen, "Investigations of IF target physics: Preheat, shock, and T_r scaling experiments with half-Cairn hohlraums," in Ref. 69 pp. 5-91–5-96 (unpublished).
[226]D. W. Phillion and M. D. Rosen, "Radiation-drive scaling at 2ω and 4ω," in Ref. 85, pp. 4-7–4-21 (unpublished).
[227]J. D. Lindl, "Tolerance of high-gain ICF capsules to preheat by high energy electrons," Laser Program Annual Report, 1984, Lawrence Livermore National Laboratory, Livermore, CA, UCRL-50055-84, pp. 2-38–2-39 (unpublished).
[228]R. McCrory and C. Verdon, *Short Wavelength Single Shell Direct Drive Pellet Designs*, edited by S. Skupsky (U.S. Department of Energy, Washington, DC, 1985), Vol. 23, pp. 125–140.
[229]R. McCrory and C. Verdon, "ICF computer simulations," *Computer Applications in Plasma Science and Engineering*, edited by A. Drobat (Springer-Verlag, Berlin, 1991), pp. 291–325.

[230]See National Technical Information Service Document Nos. DE95017671 through DE95017673 and DE95017676 through DE95017700 (J. A. Paisner, E. M. Campbell, and W. J. Hogan, *The National Ignition Facility Project*, UCRL-JC-117397 and UCRL-PROP-117093, May 1994). Copies may be obtained from the National Technical Information Service, Springfield, VA 22161.
[231]See National Technical Information Service Document No. DE94016700 (J. T. Hunt, K. R. Manes, J. R. Murray, P. A. Renard, R. W. Sawicki, J. B. Trenholme, and W. Williams, "Laser Design Basis for the National Ignition Facility," Lawrence Livermore National Laboratory, Livermore, CA, UCRL-JC-117399, 1994). Copies may be obtained from the National Technical Information Service, Springfield, VA 22161.
[232]B. M. Van Wonterghem, J. R. Murray, D. R. Speck, and J. H. Campbell, "Performance of the NIF prototype beamlet," Fusion Technol. **26**, 702 (1994).
[233]C. E. Barker, B. M. Van Wonterghem, D. R. Speck, B. W. Woods, D. F. Browning, S. C. Burkhart, W. C. Behrendt, J. R. Murray, J. H. Campbell, and I. C. Smith, "Third harmonic performance of a large aperture, multipass Nd-glass laser," *Advanced Solid State Lasers Conference*, Memphis, TN, 1995, Lawrence Livermore National Laboratory, Livermore, CA, UCRL-JC-118196 (unpublished); *Advanced Solid-State Lasers Proceedings*, edited by B. H. T. Chai and S. A. Payne (Optical Society of America, Washington, DC, 1995), Vol. 24, pp. 204–206.
[234]S. N. Dixit, J. K. Lawson, K. R. Manes, H. T. Powell, and K. A. Nugent, "Kinoform phase plates for focal plane irradiance profile control," Opt. Lett. **9**, 417 (1994).
[235]See National Technical Information Service Document No. DE95011969 (S. N. Dixit, I. M. Thomas, M. Rushford, R. Merrill, M. D. Perry, H. T. Powell, and K. A. Nugent, "Kinoform phase plates for tailoring focal plane intensity profiles," Lawrence Livermore National Laboratory, Livermore, CA, UCRL-LR-105821-94-4). Copies may be obtained from the National Technical Information Service, Springfield, VA 22161.
[236]S. W. Haan, "Design of targets for the national ignition facility," ICF Quart. Rep. **3**, 71 (1992), Lawrence Livermore National Laboratory, Livermore, CA, UCRL-LR-113687-93-1 (unpublished).
[237]S. W. Haan and S. M. Pollaine, "Target design for laser-driven thermonuclear ignition," LLNL Research Monthly 93-1 Lawrence Livermore National Laboratory, Livermore, CA, UCRL-50000-93-1, 1993, p. 5 (unpublished).
[238]S. W. Haan, S. M. Pollaine, J. D. Lindl, L. J. Suter, R. L. Berger, L. V. Powers, W. E. Alley, P. A. Amendt, J. A. Futterman. W. K. Levedahl, M. D. Rosen, D. P. Rowley, R. A. Sacks, A. I. Shestakov, G. L. Strobel, M. Tabak, S. V. Weber, G. B. Zimmerman, W. J. Krauser, D. C. Wilson, S. Coggeshall, D. B. Harris, N. M. Hoffman, and B. H. Wilde, "Design and modeling of ignition targets for the National Ignition Facility," Phys. Plasmas **2**, 2480 (1995).
[239]See National Technical Information Service Document No. DE95017708 (D. S. Kershaw, "Flux limiting in nature's own way," Lawrence Livermore National Laboratory, Livermore, CA, UCRL-78378, 1976). Copies may be obtained from the National Technical Information Service, Springfield, VA 22161.
[240]R. M. More, K. H. Warren, D. A. Young, and G. B. Zimmerman, "A new quotidian equation of state (QEOS) for hot dense matter," Phys. Fluids **31**, 3059 (1988).
[241]See National Technical Information Service Document No. UCRL-52276 (W. A. Lokke and W. H. Grasberger, "XSNQ-U: A Non-LTE emission and absorption coefficient subroutine," Lawrence Livermore National Laboratory, Livermore, CA, UCRL-52276, 1977). Copies may be obtained from the National Technical Information Service, Springfield, VA 22161.
[242]E. G. Corman, W. B. Loewe, G. E. Cooper, and A. M. Winslow, "Multigroup diffusion of energetic charged particles," Nucl. Fusion **15**, 377 (1975).
[243]S. P. Hatchett (private communication, 1993).
[244]See National Technical Information Service Document No. DE91009750 (G. B. Zimmerman, "Recent developments in Monte-Carlo techniques," Lawrence Livermore National Laboratory, Livermore, CA, UCRL-105616, 1990). Copies may be obtained from the National Technical Information Service, Springfield, VA 22161.
[245]J. K. Hoffer and L. R. Foreman, "Radioactively induced sublimation in solid tritium," Phys. Rev. Lett. **60**, 1310 (1988).
[246]See National Technical Information Service Document No. DE91017920 (T. P. Bernat, E. R. Mapoles, and J. J. Sanchez, "Temperature and age-dependence of redistribution rates of frozen deuterium–tritium," ICF Quart. Rep. **1**, 443 (1991), Lawrence Livermore National Laboratory, UCRL-LR-105821-91-2). Copies may be obtained from the National Technical Information Service, Springfield, VA 22161.
[247]J. K. Hofer, L. R. Foreman, E. R. Mapoles, and J. D. Simpson, "Forming a uniform shell of solid DT fusion fuel by the beta-layering process," *Nuclear Fusion Research 1992* (International Atomic Energy Agency, Vienna, 1993), Vol. 3, p. 443.
[248]G. W. Collins (private coummunication, 1995).
[249]K. Kim, L. Mok, M. J. Erlenborn, and T. Bernat, "Non-contact thermal gradient method for fabrication of uniform cryogenic inertial fusion targets," J. Vac. Sci. Technol. A **3**, 1196 (1985).
[250]R. A. Sacks and D. H. Darling, "Direct drive cryogenic ICF capsules employing D–T wetted foam," Nucl. Fusion **27**, 447 (1987).
[251]See National Technical Information Service Document No. DE91017542 (S. W. Haan, "Hydrodynamic instabilities on ICF capsules," Lawrence Livermore National Laboratory, Livermore, CA (UCRL-JC-107592), to be published in *Lecture Series on Inertial Fusion*, Department of Astrophysical Sciences, Princeton University, 1994). Copies may be obtained from the National Technical Information Service, Springfield, VA 22161.
[252]J. P. Dahlburg, "Three dimensional simulations of the ablative Rayleigh–Taylor instability," Bull. Am. Phys. Soc. **39**, 1576 (1994).
[253]M. M. Marinak, B. A. Remington, S. V. Weber, R. E. Tipton, S. W. Haan, K. Budil, O. L. Landen, J. D. Kilkenny, and R. Wallace, "Three-dimensional single-mode Rayleigh–Taylor experiments on Nova," UCRL-JC-120191, submitted to Phys. Rev. Lett.
[254]R. C. Kirkpatrick and C. A. Wingate (private communication, 1980); D. S. Bailey (private communication, 1981); D. H. Munro and G. B. Zimmerman (private communication, 1993).
[255]R. O. Bangerter, "Radiation-driven targets for heavy-ion fusion," in Ref. 67, pp. 2-28–2-30 (unpublished).
[256]D. Gardes, R. Bimbot, M. F. Rivet, A. Servajean, C. Fleurier, D. Hong, C. Deutsch, and G. Maynard, "Stopping of energetic sulfur and bromine ions in dense hydrogen plasma," Part. Accel. **37–38**, 361 (1992).
[257]D. W. Hewett, W. L. Kruer, and R. O. Bangerter, "Corona plasma instabilities in heavy ion fusion targets," Nucl. Fusion **31**, 431 (1991).
[258]R. O. Bangerter and J. D. Lindl, "Gain calculation for radiatively driven ion and laser targets," in Ref. 91, Lawrence Livermore National Laboratory, Livermore, CA, UCRL-50055-86/87, pp. 2-160–2-68 (unpublished).
[259]D. D.-M. Ho (private communication, 1995).
[260]M. Basko and J. Meyer-Ter-Vehn, "Hohlraum target for heavy ion inertial fusion," Nucl. Fusion **33**, 601 (1993).
[261]A. B. Langdon, "Reactor chamber propagation of heavy ion beams," Part. Accel. **37–38**, 175 (1992).
[262]C. Olson, D. Hinshelwood, R. Hubbard, M. Lampe, J. Neri, P. Ottinger, J. Poukey, D. Rose, S. Slinker, S. Stephanakis, D. Welch, and F. Young, "Physics of gas breakdown for ion beam transport in gas," *Proceedings of the International Symposium on Heavy Ion Inertial Fusion*, edited by S. Atzeni and R. A. Ricci, Nuovo Cimento A **106**, 1705 (1993).
[263]W. F. Krupke, "Solid state laser driver for an ICF reactor," Fusion Technol. **15**, 377 (1989).
[264]C. D. Orth, S. A. Payne, and W. F. Krupke, "A diode-pumped solid-state laser driver for inertial fusion energy," submitted to Nucl. Fusion.
[265]W. R. Meier, R. Bieri, and M. Monsler, *Osiris and Sombrero Inertial Fusion Power Plant Designs Final Report* (U.S. Department of Energy, Washington, DC, WJSA-92-01, DOE/ER/54100, 1992); also see W. R. Meier, R. Bieri, M. Monsler, C. Hendricks, P. Laybourne, K. Shillito, S. Ghose, L. Goldman, K. Auclair, C. Pang, R. Bourque, L. Stewart, E. Bowles, E. Hubbard, C. Von Rosenberg, Jr., M. McGeoch, I. Sviatoslavsky, R. Peterson, M. Sawan, H. Khater, L. Wittenberg, G. Kulcinski, G. Moses, E. Mogahed, J. MacFarlane, S. Rutledge, S. Humphries, Jr., and E. Cheng, "Results of inertial fusion reactor design studies: Osiris and Sombrero," *Proceedings of the 14th International Conference on Plasma Physics and Controlled Fusion Research* 1992, Würzburg, Germany (International Atomic Energy Agency, Vienna, 1993), Vol. 3, p. 339.
[266]L. M. Waganer, D. E. Driemeyer, and V. D. Lee, *Inertial Fusion Energy Reactor Design Studies* (McDonnell Douglas Aerospace, St. Louis, MO, U.S. Department of Energy, Washington, DC, 1992).